

Designing a Novel Drug Delivery System Based on Gold Nanoparticles for Breast Cancer Therapy



A thesis submitted to the School of Chemical & Physical Sciences, Faculty of Science & Engineering, at Flinders University of South Australia in fulfilment of the degree of

Doctor of Philosophy

August 2016

Zahrah Alhalili

Supervised by:

Professor Joseph G. Shapter (School of Chemical and Physical Sciences)

Co-supervised by:

Associate Professor Barbara Sanderson (School of Medical Science and Technology)

Table of Contents

Declaration.....	X
Acknowledgements.....	XI
Abstract.....	XIII
Publications.....	XV
List of figures.....	XVII
List of tables.....	XXVI
List of schemes.....	XXVIII
List of chemical structures.....	XXIX
List of abbreviations, symbols and units.....	XXXIX
Thesis guide.....	XLV
Chapter 1. Introduction and literature review	1
1.1 Synopsis	1
1.2 Breast cancer	2
1.2.1 Breast structure	2
1.2.2 Breast cancer types	3
1.2.2.1 Non-invasive breast cancer	3
1.2.2.2 Invasive breast cancer.....	4
1.2.2.3 Locally advanced breast cancer	4
1.2.2.4 Metastatic breast cancer.....	5
1.2.2.5 Rare types of breast cancer	5

1.2.2.5.1 Inflammatory breast cancer (IBC)	5
1.2.2.5.2 Triple-negative breast cancer.....	5
1.2.2.5.3 Paget’s disease of the nipple.....	5
1.2.2.5.4 Male breast cancer	6
1.2.3 Breast cancer treatment.....	6
1.2.3.1 Surgery.....	6
1.2.3.2 Radiation therapy.....	7
1.2.3.3 Chemotherapy.....	7
1.3 Paclitaxel (Taxol).....	8
1.3.1 Paclitaxel history.....	8
1.3.2 Paclitaxel structure and mechanism of action.....	8
1.3.3 Paclitaxel limitations.....	9
1.4 Targeted drug delivery for cancer treatment using nanotechnology	10
1.4.1 Passive targeting	15
1.4.2 Active targeting.....	15
1.5 Gold nanoparticles (AuNPs).....	19
1.5.1 History.....	19
1.5.2 Properties	19
1.5.3 Synthesis of gold nanoparticles.....	20
1.5.3.1 Synthesis of gold nanoparticles by chemical reduction methods	20
1.5.4 Surface functionalisation and bioconjugation of gold nanoparticles	22
1.5.4.1 Alkanethiols.....	23
1.5.4.2 In situ dithiocarbamate formation approach	25
1.5.4.3 Amino acids.....	26
1.5.5 Common bio-functional molecules conjugated onto AuNPs surface	27
1.5.5.1 Polyethylene glycol	27
1.5.5.2 Peptides.....	29

1.5.5.3 Oligonucleotides	29
1.5.5.4 Chemotherapeutic agents.....	30
1.5.6 Biomedical applications of gold nanoparticles	31
1.5.6.1 Gold nanoparticles in diagnostic applications	32
1.5.6.2 Gold nanoparticles for X-ray based imaging	33
1.5.6.3 Gold nanoparticles in therapeutic area for drug and gene delivery	33
1.5.7 Toxicity of gold nanoparticles	37
1.6 Cellular uptake of nanoparticles.....	38
1.6.1 Intracellular pathway	39
1.6.2 Cellular uptake of gold nanoparticles	40
1.6.3 Intracellular tracking of fluorescently labelled gold nanoparticles using confocal laser scanning microscopy	42
1.7 Antibodies	44
1.7.1 Structure and function.....	44
1.7.2 Monoclonal antibodies (mAbs) in therapeutic applications.....	47
1.7.3 Antibodies targeting tumour antigens	48
1.7.4 Antibody conjugation.....	48
1.7.5 Conjugation of antibodies to nanoparticles.....	49
1.8 Summary	52
Chapter 2. Experimental	54
2.1 Synopsis	54
2.2 Materials	55
2.2.1 Chemicals and reagents.....	55
2.3 Conjugation approaches	57
2.4 Non-covalent binding (hybrid preparation).....	58
2.4.1 Synthesis of gold nanoparticles (AuNPs)	58
2.4.2 Functionalisation of gold nanoparticles	60
2.4.3 Synthesis of PTX-thiol-AuNPs hybrid	61

2.4.4 Preparation of phosphate buffered saline (PBS)	62
2.5 Covalent binding (direct conjugate preparation)	63
2.5.1 Synthesis of PTX-thiol-AuNPs direct conjugate using EDC/NHS coupling reaction.....	63
2.6 Covalent binding (reverse conjugate preparation)	65
2.6.1 Synthesis of PTX-16-MHDA-AuNPs (reverse conjugation method).....	65
2.7 Preparation of fluorescently labelled AuNPs.....	67
2.7.1 Using covalent attachment (direct conjugate preparation).....	67
2.7.1.1 Synthesis of AuNPs-thiol-DAPI direct conjugate	67
2.7.1.2 Synthesis of PTX-thiol-AuNPs-thiol-DAPI direct conjugate.....	69
2.7.1.3 Synthesis of AuNPs-thiol-pyNH ₂ direct conjugate.....	71
2.7.1.4 Synthesis of PTX-thiol-AuNPs-thiol-pyNH ₂ direct conjugate	71
2.7.1.5 Synthesis of AuNPs-thiol-FB28 hybrid.....	72
2.7.1.6 Synthesis of PTX-thiol-AuNPs-thiol-FB28 direct conjugate	73
2.7.2 Using covalent attachment (reverse conjugate preparation)	75
2.7.2.1 Synthesis of AuNPs-16-MHDA-DAPI reverse conjugate.....	75
2.7.2.2 Synthesis of PTX-16-MHDA-AuNPs-16-MHDA-DAPI reverse conjugate ..	77
2.7.3 Synthesis of rhodamine B attached paclitaxel	81
2.8 Conjugation of antibodies.....	83
2.8.1 Synthesis of AuNPs-thiol-EpCAM direct conjugate	83
2.8.2 Synthesis of PTX-thiol-AuNPs-thiol-EpCAM direct conjugate.....	85
2.8.3 Synthesis of AuNPs-thiol-TARP direct conjugate.....	87
2.8.4 Synthesis of PTX-thiol-AuNPs-thiol-TARP direct conjugate	87
2.9 Characterisation techniques.....	88
2.9.1 Ultraviolet–Visible (UV-Vis) spectrophotometry.....	88
2.9.1.1 Sample preparation	88
2.9.1.2 Instrumentation and data acquisition	89

2.9.2 Transmission electron microscopy (TEM).....	89
2.9.2.1 Intracellular detection of AuNPs using transmission electron microscopy (TEM)	89
2.9.2.2 Sample preparation	90
2.9.2.3 Instrumentation and data acquisition	91
2.9.3 Dynamic light scattering (DLS).....	91
2.9.3.1 Sample preparation	91
2.9.3.2 Instrumentation and data acquisition	91
2.9.4 Fourier transform infrared (FT-IR) spectroscopy	92
2.9.4.1 Sample preparation	92
2.9.4.2 Instrumentation and data acquisition	92
2.9.5 Nuclear magnetic resonance spectroscopy (NMR).....	92
2.9.5.1 Sample preparation	93
2.9.5.2 Instrumentation and data acquisition	93
2.9.6 Fluorescence spectrophotometry.....	93
2.9.6.1 Sample preparation	93
2.9.6.2 Instrumentation and data acquisition	94
2.9.7 Confocal laser scanning microscopy.....	94
2.9.7.1 Sample preparation	96
2.9.7.1.1 Preparation of AuNPs samples without cells.....	96
2.9.7.1.2 Preparation of T47D cells treated with different AuNPs samples	96
2.9.7.2 Instrumentation and data acquisition	97
Chapter 3. Hybridisation of PTX with functionalised AuNPs	98
3.1 Introductory remarks	98
3.2 Description the synthesis of gold nanoparticles.....	99
3.3 Characterisation of PTX-thiol-AuNPs hybrid.....	102
3.3.1 UV-Vis spectrophotometry characterisation and data analysis.....	103
3.3.2 Analytical measurements of transmission electron microscopy (TEM)	105

3.3.3 Dynamic light scattering (DLS) measurement and analysis	107
3.3.4 FT-IR spectroscopy characterisation	110
3.3.5 ¹ H NMR spectroscopy characterisation of PTX-thiol-AuNPs hybrid.....	115
3.3.5.1 ¹ H NMR spectroscopy characterisation of gold nanoparticles	115
3.3.5.2 ¹ H NMR spectroscopy characterisation of LA attached AuNPs.....	117
3.3.5.3 ¹ H NMR spectroscopy characterisation of thiol functionalised AuNPs	119
3.3.5.4 ¹ H NMR spectroscopy characterisation of PTX-thiol-AuNPs hybrid	121
3.3.6 Drug loading studies of PTX-thiol-AuNPs hybrid.....	124
3.3.7 Cytotoxicity assay for PTX-thiol-AuNPs hybrid.....	129
3.4 Concluding remarks.....	131
Chapter 4. Chemical conjugation of PTX to functionalised AuNPs.....	132
4.1 Introductory remarks	132
4.2 Description of covalent conjugation between paclitaxel and gold nanoparticles	134
4.2.1 Description the synthesis of PTX-thiol-AuNPs direct conjugate.....	134
4.2.1.1 The function of EDC/NHS coupling reaction.....	135
4.2.2 Description the synthesis of PTX-16-MHDA-AuNPs reverse conjugate	137
4.2.2.1 The function of EDC/NHS coupling reaction.....	138
4.3 Characterisation techniques.....	139
4.3.1 Characterisation of PTX-thiol-AuNPs direct conjugate	139
4.3.1.1 UV-Vis analysis of PTX-thiol-AuNPs direct conjugate.....	139
4.3.1.2 TEM analysis of PTX-thiol-AuNPs direct conjugate	140
4.3.1.3 Dynamic light scattering (DLS) of PTX-thiol-AuNPs direct conjugate.....	141
4.3.1.4 FT-IR analysis of PTX-thiol-AuNPs direct conjugate.....	142
4.3.1.5 ¹ H NMR spectroscopy characterisation of PTX-thiol-AuNPs direct conjugate	145
4.3.1.6 Preparation of PTX-thiol-AuNPs direct conjugate for drug loading studies	150
4.3.1.7 Cytotoxicity assay for PTX-thiol-AuNPs direct conjugate	153

4.3.1.8 Comparison of cytotoxicity for PTX-thiol-AuNPs direct conjugate at different pHs.....	154
4.3.2 Characterisation of PTX-16-MHDA-AuNPs reverse conjugate.....	156
4.3.2.1 UV-Vis analysis of PTX-16-MHDA-AuNPs reverse conjugate	156
4.3.2.2 Dynamic light scattering (DLS) of PTX-16-MHDA-AuNPs reverse conjugate	158
4.3.2.3 FT-IR analysis of PTX-16-MHDA-AuNPs reverse conjugate.....	159
4.3.2.4 ¹ H NMR spectroscopy characterisation of PTX-16-MHDA-AuNPs reverse conjugate.....	161
4.3.2.5 Cytotoxicity assay for PTX-16-MHDA-AuNPs reverse conjugate.....	163
4.3.2.6 Comparison of cytotoxicity for PTX-16-MHDA-AuNPs reverse conjugate at different pHs	164
4.4 Concluding remarks.....	166
Chapter 5. Characterisation of conjugates based on fluorescent agents.....	167
5.1 Introductory remarks	167
5.2 Characterisation of fluorescently labelled AuNPs.....	171
5.2.1 UV-Vis analysis of fluorescently labelled AuNPs.....	171
5.2.2 Fluorescence spectroscopy analysis of fluorescently labelled AuNPs.....	173
5.2.3 TEM measurements of fluorescently labelled AuNPs	178
5.2.4 Dynamic light scattering (DLS) analysis of fluorescently labelled AuNPs.....	179
5.2.5 FT-IR spectroscopy characterisation of fluorescently labelled AuNPs	181
5.2.6 ¹ H NMR spectroscopy characterisation of fluorescently labelled AuNPs.....	190
5.2.7 Cytotoxicity evaluation of fluorescently labelled AuNPs.....	200
5.3 Characterisation of PTX-16-MHDA-AuNPs-16-MHDA-DAPI reverse conjugate	202
5.3.1 UV-Vis analysis of PTX-16-MHDA-AuNPs-16-MHDA-DAPI reverse conjugate	202
5.3.2 Fluorescence spectroscopy analysis of PTX-16-MHDA-AuNPs-16-MHDA-DAPI reverse conjugate	204

5.3.3 Dynamic light scattering (DLS) analysis of PTX-16-MHDA-AuNPs-16-MHDA-DAPI reverse conjugate	206
5.3.4 FT-IR spectroscopy characterisation of PTX-16-MHDA-AuNPs-16-MHDA-DAPI reverse conjugate	207
5.3.5 ¹ H NMR analysis of PTX-16-MHDA-AuNPs-16-MHDA-DAPI reverse conjugate	210
5.3.6 Cytotoxicity assessment of AuNPs-16-MHDA-DAPI reverse conjugate.....	212
5.4 Characterisation of paclitaxel conjugated to rhodamine B (PTX-RB conjugate)	213
5.4.1 UV-Vis analysis of PTX-RB conjugate	213
5.4.2 Fluorescence spectroscopy analysis of PTX-RB conjugate.....	215
5.4.3 FT-IR spectroscopy characterisation of PTX-RB conjugate	217
5.4.4 ¹ H NMR spectroscopy characterisation of PTX-RB conjugate	220
5.4.5 Cytotoxicity evaluation of free RB	223
5.5 Concluding remarks.....	224
Chapter 6. Intracellular uptake of gold nanoparticles	225
6.1 Introductory remarks	225
6.2 Cellular uptake of AuNPs by T47D breast cancer cells.....	227
6.2.1 CLSM analysis of AuNPs used as negative controls	228
6.2.2 CLSM analysis of fluorescently labelled AuNPs.....	230
6.2.3 CLSM analysis of free fluorescent dyes on T47D cells.....	232
6.2.4 Intracellular distribution of fluorescently labelled AuNPs with different dyes analysed by CLSM.....	234
6.2.5 TEM analysis of fluorescently labelled AuNPs	242
6.3 Concluding remarks.....	246
Chapter 7. Chemical conjugation of antibodies and PTX simultaneously to functionalised AuNPs nanocarriers	247
7.1 Introductory remarks	247
7.1.1 Overview of EpCAM and TARP antibodies.....	249

7.2 Characterisation of antibodies containing conjugates	251
7.2.1 UV-Vis analysis of antibodies containing conjugates	251
7.2.2 TEM analysis of antibodies containing conjugates.....	254
7.2.3 DLS analysis of antibodies containing conjugates.....	255
7.2.4 FT-IR analysis of antibodies containing conjugates	256
7.2.5 Cytotoxicity assay of antibodies containing conjugates	259
7.3 Concluding remarks.....	262
Chapter 8. Conclusions and recommendations	263
8.1 Synopsis	263
8.2 Conclusions	264
8.3 Future research directions.....	269
References	276
Appendices	316

Declaration

I certify that this thesis does not incorporate without acknowledgment any material previously submitted for a degree or diploma in any university; and that to the best of my knowledge and belief it does not contain any material previously published or written by another person except where due reference is made in the text.

Zahrah Alhalili on ____/____/____

Acknowledgements

First and foremost, praises and thanks to the God, for his infinite tenderness throughout my research work to complete the research successfully.

I would like to offer my sincerest gratitude to my supervisor Prof. Joseph Shapter for his guidance, encouragement and patience throughout the years. His dynamism, vision, sincerity and motivation have deeply inspired me. His guidance helped me throughout my research and writing of this thesis. It was a great privilege to work and study under his guidance.

I am extending my gratitude to my co-supervisor, Assoc. Prof. Barbara Sanderson at the Department of Health Medical Biotechnology-Flinders University for her continuous support during my PhD study, for her patience and nice cooperation. I would also like to thank Assoc. Prof. Martin Johnston, for giving training and assistance with NMR spectroscopy and taking the time to help me by running NMRs. Thanks to Dr. Rebecca Norman for her kind help with NMR related problems. Yvette DeGraaf at Flinders Microscopy was responsible for training me in the use of the confocal laser scanning microscopy at Flinders University. Lyn Waterhouse at Adelaide Microscopy-The University of Adelaide provided training and advice in the use of transmission electron microscopy (TEM) that has been vital to this project. I give thanks to Daniela Figueroa, Nur Hikmatul Auliya and Abeer Zaila from the Department of Health Medical Biotechnology-Flinders University for nice cooperation.

I would also like to thank the various support staff in the School of CaPS who have helped in my studies at Flinders in more ways than I was able to fully appreciate at the time. Special mention goes to David Vincent for technical/equipment and safety and members of Shapter's research group for their assistance and kindness.

I am extremely grateful to my parents for their love, prayers and caring.

My special thanks to my husband for his patience, support, help and encouragement. I am very much thankful to my daughter, Anwar, and my son, Abdullah, for their love, understanding and support to complete this research work. Also, I express my thanks to my sisters and brothers for their support and kind encouragement.

Abstract

Developing novel strategies to improve limitations of commercially available chemotherapeutics is critically important. This thesis details efforts toward the development of a novel drug delivery system based on anticancer drug paclitaxel (PTX) loaded gold nanoparticles that targets T47D breast cancer cells to attain a more efficient cancer treatment. By combining gold nanoparticles as nanocarriers, PTX as anticancer agent and alkanethiol acids (LA and 16-MHDA) as linkers, a novel drug delivery system was engineered. This thesis focuses on synthesis, functionalising and characterising gold nanoparticles complexes. The study shows that when functionalising the surface of gold nanoparticles with targeting ligands and the chemotherapeutic agent, their unique properties remain unchanged. Alkanethiol acids were used as linkers and stabilisers for gold nanoparticles to enhance their biocompatibility and suitability for intracellular delivery. The alkanethiol-gold nanoparticles platform was nontoxic. However, after loading the anticancer agent PTX onto the thiolated gold nanoparticles, significant cytotoxicity was induced. Different composites based on gold nanoparticles were used to determine cytotoxicity to T47D cells using the MTT assay. It was noticed that the synthetic method of PTX-AuNPs composites affects their toxicity. Significant reduction in cell viability was observed when T47D cells were exposed to PTX-thiol-AuNPs hybrid and the PTX-thiol-AuNPs direct conjugate. However, a reverse conjugate PTX-16-MHDA-AuNPs was less effective at killing cancerous cells. The designed PTX-thiol-AuNPs hybrid induced more cell death *in vitro* than the commercially available formulation of PTX used as a solution of PTX in ethanol. This means the PTX is extremely bioavailable

when a part of nanoparticle system and more efficient for breast cancer T47D cell treatment in comparison to the current PTX formulation. The intracellular uptake of gold nanoparticles by T47D cells was also evaluated by conjugating fluorescent dyes as probes with the thiolated gold nanoparticles. Gold nanoparticles were internalised via an endocytosis mechanism and taken up by the cells. Additionally, EpCAM or TARP antibodies conjugated to thiol-AuNPs in the presence and the absence of the anticancer agent, PTX, were synthesised using EDC/NHS coupling reaction and characterised to investigate their targeting ability against T47D cells. It was found that, antibodies conjugated thiolated AuNPs without PTX were nontoxic. However, the cytotoxicity of the cells exposed to antibodies and PTX attached simultaneously to the functionalised AuNPs shows that at low concentrations no significant reduction in cell viability was induced. However, when using high concentration the reduction of cell viability was significantly high. The number of cells killed by antibodies and PTX attached simultaneously to the functionalised AuNPs systems was significantly higher than that for cells killed by PTX-thiol-AuNPs direct conjugate system where no antibodies were used. The results indicate the effectiveness of combining EpCAM or TARP antibodies with PTX-thiol-AuNPs system to target T47D breast cancer cells.

Publications

Zahrah Alhalili, Daniela Figueroa, Martin R. Johnston, Barbara Sanderson, Joe Shapter
"Effect of modification protocols on the effectiveness of gold nanoparticles as drug
delivery vehicles for breast cancer cell killing" *Australian Journal of Chemistry*, **2016**.

Zahrah Alhalili, Abeer Zaila, Barbara Sanderson, Joe Shapter "Localisation and
uptake of fluorescently labelled gold nanoparticles by a T47D human breast cancer
cell line" *International Journal of Pharma and Bio Sciences (accepted)*.

Conference Proceedings

Zahrah Alhalili, Gold nanoparticles conjugated to paclitaxel for breast cancer
treatment. Oral presentation at the Engineering & Physical Sciences in Medicine
Conference (EPSM), Wellington, New Zealand, **2015**

Zahrah Alhalili, Designing a novel system of paclitaxel-gold nanoparticles conjugate
for breast cancer therapy. Oral presentation at the 4th International Conference on
Environment, Chemistry and Biology (ICECB), Auckland, New Zealand, **2015**

Zahrah Alhalili, Uptake of fluorescently labelled gold nanoparticles conjugate by a
human breast cancer cell line. Poster presentation at the Nanostructures for Sensors,
Electronics, Energy and Environment (NanoS-E3) International Workshop and
School on Nanotechnology, Kingscliff-New South Wales-Australia, **2015**

Zahrah Alhalili, Paclitaxel-gold nanoparticles conjugate designed for breast cancer
treatment. Poster presentation at the Royal Australian Chemical Institute (RACI)
National Congress, Adelaide, Australia, **2014**

Zahrah Alhalili, Paclitaxel-gold nanoparticles amalgamated for breast cancer
treatment. Poster presentation at the Australian Society for Medical Research
(ASMR), Adelaide, Australia, **2014**

List of Figures

Figure 1.1 Normal breast tissue [9].	3
Figure 1.2 Illustration of a woman's breast displays DCIS and invasive breast cancer [18].	4
Figure 1.3 Paclitaxel structure.	9
Figure 1.4 An illustration of some nanoparticles have been investigated for biomedical applications targeting cancer [2].	13
Figure 1.5 Overview of various targeting approaches for drug delivery to tumour cells. (A) intravenous administration of low-molecular-weight and conventional anti-tumour drug, which is usually removed rapidly from blood and shows accumulation in both cancerous and healthy cells. (B) passive targeting of nanomedicines to cancer cells based on the enhanced permeability and retention (EPR) effect. (C) active targeting of nanomedicines to tumour cells to improve cellular internalisation and cellular uptake of the nanomedicine. (D) active targeting to overexpressed receptors by angiogenic endothelial cells aims to reduce blood supply to tumours and thus prevent the cells from oxygen and nutrients [119].	18
Figure 1.6 TEM images of gold nanostructures: (a) nanospheres [151], (b) nanocages [151], (c) nanorods [151] and (d) inner nanoshell, consisting of a silica core layer and a gold shell layer [152].	21
Figure 1.7 Conjugation methods of AuNPs with different biomolecules [154].	23
Figure 1.8 Synthesis of Au-DHLA-luminol [160].	24
Figure 1.9 Synthesis of AuNPs–DTC–DNA conjugates [163].	25
Figure 1.10 Synthesis of gold nanoparticles reduced by glutamic acid bound to protein throughout the surface lysine residues of protein molecules [168].	27
Figure 1.11 Paclitaxel functionalised gold nanoparticles [188].	31
Figure 1.12 Biomedical applications of AuNPs. Image adapted from [194].	32
Figure 1.13 Schematic diagram of synthesis steps of AuNP-MPA-PEG-FITC [208].	34
Figure 1.14 Schematic representation of synthesis of AuNP-liposomes. (A) 90 nm-liposomes (B) AuNP–phospholipids are then exchanged into the lipid bilayer of the preformed liposomes [209].	35

Figure 1.15 PEGylated gold nanoparticles for gene delivery [138].....	36
Figure 1.16 Schematic diagram of preparing of DDAB-AuNPs/lipoplex complexes and the mechanism involved in the transfection enhancement [212].	36
Figure 1.17 Internalisation of nanoconjugate into the cells by receptor-mediated endocytosis mechanism [71].	41
Figure 1.18 Ig molecule's structure having two heavy and two light chains bound by disulfide bridges [260].	45
Figure 1.19 Illustration of structure of an immunoglobulin G (IgG) antibody molecule. Adapted from [263].	46
Figure 2.1 Optical properties of the colloidal gold prepared by the Turkevich's method as a function of time.	59
Figure 2.2 TEM images of gold nanoparticles trapped inside vesicles of a HeLa cell with sizes (A) 14 nm and (B) 30 nm. Adapted from [241] with some modifications.	90
Figure 2.3 Simplified diagram illustrating the light path in a confocal laser scanning microscopy [312].	95
Figure 2.4 Method of placing coverslips POC chamber to observe live cells under inverted microscope [315].....	97
Figure 3.1 UV-Vis spectra of (a) colloidal AuNPs (b) LA-AuNPs (c) thiol-AuNPs (d) PTX alone and (e) PTX-thiol-AuNPs hybrid.....	104
Figure 3.2 TEM images with size distribution histogram of (a) AuNPs (b) LA-AuNPs (c) thiol-AuNPs and (d) PTX-thiol-AuNPs hybrid.	106
Figure 3.3 DLS measurements for (a) AuNPs colloids (b) LA-AuNPs and (c) thiol-AuNPs.	108
Figure 3.4 DLS measurements for PTX-thiol-AuNPs hybrid at different mixing times.	109
Figure 3.5 FT-IR spectra of (a) trisodium citrate (b) AuNPs colloids (c) LA alone (d) LA-AuNPs (e) 16-MHDA alone (f) thiol-AuNPs (g) PTX alone and (h) PTX-thiol-AuNPs hybrid.....	113
Figure 3.6 ¹ H NMR spectra of AuNPs colloids.	116
Figure 3.7 ¹ H NMR spectra of (a) free LA molecules and (b) LA-AuNPs.	118
Figure 3.8 ¹ H NMR spectra of (a) free 16-MHDA and (b) thiol-AuNPs.	120
Figure 3.9 ¹ H NMR spectra of (a) PTX alone and (b) PTX-thiol-AuNPs hybrid.....	122

Figure 3.10 Experimental procedure for determining the composition of PTX-thiol-AuNPs hybrid after centrifugation.	124
Figure 3.11 UV-Vis spectra of (a) thiol-AuNPs (b) PTX-thiol-AuNPs hybrid and (c) normalised spectrum.	125
Figure 3.12 Subtracted UV-Vis spectra for PTX absorption on thiol-AuNPs at different times.	126
Figure 3.13 Loading curves for the hybrid AuNPs prepared using different interaction times between the AuNPs and PTX solution. The amount of PTX attached to the AuNPs is on the left axis (blue symbols) and the remaining free PTX (red symbols) is on the right axis.	128
Figure 3.14 Response of T47D cells to 24 h treatment with functionalised AuNPs (thiol-AuNPs) determined using the MTT assay. Data shown as mean, n:3, *: p≤0.05.	129
Figure 3.15 Response of T47D cells to 24 h treatment with (a) PTX and (b) PTX-thiol-AuNPs hybrid. Data shown as mean, n:3, *: p≤0.05.....	130
Figure 4.1 UV-Vis spectra of (a) AuNPs (b) LA-AuNPs (c) thiol-AuNPs and (d) PTX-thiol-AuNPs direct conjugate.	139
Figure 4.2 TEM image with size distribution histogram of PTX-thiol-AuNPs direct conjugate.	140
Figure 4.3 DLS size distribution (intensity graph) of PTX-thiol-AuNPs direct conjugate.	141
Figure 4.4 FT-IR spectra of (a) LA-AuNPs (b) thiol-AuNPs and (c) PTX-thiol-AuNPs direct conjugate.....	143
Figure 4.5 ¹ H NMR spectra of (a) LA-AuNPs (b) thiol-AuNPs and (c) PTX-thiol-AuNPs direct conjugate.....	148
Figure 4.6 UV-Vis spectra for PTX in supernatant of PTX-thiol-AuNPs direct conjugate samples at different times.	151
Figure 4.7 The amount of PTX left in the supernatant.	152
Figure 4.8 Response of T47D cells to treatment with PTX-thiol-AuNPs direct conjugate using MTT assay. Shown in concentration of PTX conjugated thiol-AuNPs (nM) versus relative survival (%) compared to the untreated control. Data shown as mean, n:3, *: p≤0.05.....	153

Figure 4.9 Response of T47D cell line to treatment with PTX-thiol-AuNPs direct conjugate at (a) pH 7.4 and (b) pH 6.5 using MTT assay. Shown in concentration of PTX in direct conjugate (nM) versus relative survival (%) compared to untreated control. Data shown as mean, n:3, *: $p \leq 0.05$ 155

Figure 4.10 UV-Vis spectra of (a) AuNPs (b) 16-MHDA-NHS (c) PTX-16-MHDA and (d) PTX-16-MHDA-AuNPs reverse conjugate. 157

Figure 4.11 DLS measurement for PTX-16-MHDA-AuNPs reverse conjugate. 158

Figure 4.12 FT-IR spectra of (a) 16-MHDA-NHS (b) PTX-16-MHDA and (c) PTX-16-MHDA-AuNPs reverse conjugate. 160

Figure 4.13 ^1H NMR spectra of PTX-16MHDA-AuNPs reverse conjugate. 162

Figure 4.14 Response of T47D cells to treatment with PTX-16-MHDA-AuNPs reverse conjugate using MTT assay. Data shown as mean, n:3, *: $p \leq 0.05$ 163

Figure 4.15 Comparison of response of T47D cell line to treatment with PTX-16-MHDA-AuNPs reverse conjugate at (a) pH 7.4 and (b) pH 6.5 using MTT assay. Shown in concentration of PTX in reverse conjugate (nM) versus relative survival (%) compared to untreated control. Data shown as mean, n:3, *: $p \leq 0.05$ 165

Figure 5.1 UV-Vis spectra of various fluorescent containing nanoparticles or their precursors. 1) DAPI 2) pyNH₂ and 3) FB28. 172

Figure 5.2 Fluorescence (a) excitation and (b) emission spectra of (A) free DAPI (B) AuNPs-thiol-DAPI direct conjugate and (C) PTX-thiol-AuNPs-thiol-DAPI direct conjugate. The excitation spectrum was recorded at an emission wavelength of 460 nm. The emission spectrum was recorded using an excitation wavelength of 358 nm. 175

Figure 5.3 Fluorescence (a) excitation and (b) emission spectra of (A) free pyNH₂ (B) AuNPs-thiol-pyNH₂ direct conjugate and (C) PTX-thiol-AuNPs-thiol-pyNH₂ direct conjugate. The excitation spectrum was recorded at an emission wavelength of 376 nm. The emission spectrum was recorded using an excitation wavelength of 342 nm. 176

Figure 5.4 Fluorescence (a) excitation and (b) emission spectra of (A) free FB28 (B) AuNPs-thiol-FB28 hybrid and (C) PTX-thiol-AuNPs-thiol-FB28 direct conjugate. The excitation spectrum was recorded at an emission wavelength of 435 nm. The emission spectrum was recorded using an excitation wavelength of 343 nm. 177

Figure 5.5 TEM images with size distribution histogram of (a) PTX-thiol-AuNPs-thiol-DAPI and (b) PTX-thiol-AuNPs-thiol-pyNH ₂ direct conjugates.	178
Figure 5.6 DLS measurements of various fluorescent containing nanoparticles. 1) DAPI 2) pyNH ₂ and 3) FB28.	179
Figure 5.7 FT-IR spectra of (a) DAPI alone (b) AuNPs-thiol-DAPI direct conjugate and (c) PTX-thiol-AuNPs-thiol-DAPI direct conjugate.	184
Figure 5.8 FT-IR spectra of (a) pyNH ₂ alone (b) AuNPs-thiol-pyNH ₂ direct conjugate and (c) PTX-thiol-AuNPs-thiol-pyNH ₂ direct conjugate.....	185
Figure 5.9 FT-IR spectra of (a) free FB28 (b) AuNPs-thiol-FB28 hybrid and (c) PTX-thiol-AuNPs-thiol-FB28 direct conjugate.	186
Figure 5.10 Chemical structure and proton numbering of DAPI alone.	190
Figure 5.11 Chemical structure of pyNH ₂	191
Figure 5.12 Chemical structure and proton numbering of FB28.	191
Figure 5.13 ¹ H NMR spectra of (a) DAPI alone (b) AuNPs-thiol-DAPI direct conjugate and (c) PTX-thiol-AuNPs-thiol-DAPI direct conjugate.	195
Figure 5.14 ¹ H NMR spectra of (a) pyNH ₂ alone (b) AuNPs-thiol-pyNH ₂ direct conjugate and (c) PTX-thiol-AuNPs-thiol-pyNH ₂ direct conjugate.	196
Figure 5.15 ¹ H NMR spectra of (a) FB28 alone (b) AuNPs-thiol-FB28 hybrid and (c) PTX-thiol-AuNPs-thiol-FB28 direct conjugate.	197
Figure 5.16 Cytotoxicity analysis of various fluorescent containing nanoparticles. 1) AuNPs-thiol-DAPI direct conjugate 2) AuNPs-thiol-pyNH ₂ direct conjugate and 3) AuNPs-thiol-FB28 hybrid in T47D human breast cancer cells. Results were tested by One-way ANOVA and statistical significance showing * at P<0.05.....	201
Figure 5.17 UV-Vis spectra of (a) 16-MHDA-DAPI (b) PTX-16-MHDA and (c) PTX-16-MHDA-AuNPs-16-MHDA-DAPI reverse conjugate.....	203
Figure 5.18 Fluorescence (a) excitation and (b) emission spectra of (A) 16-MHDA-DAPI reverse conjugate and (B) PTX-16-MHDA-AuNPs-16-MHDA-DAPI reverse conjugate. The excitation spectrum was recorded at an emission wavelength of 460 nm. The emission spectrum was recorded using an excitation wavelength of 358 nm.	205
Figure 5.19 DLS measurements for (a) AuNPs-16-MHDA-DAPI and (b) PTX-16-MHDA-AuNPs-16-MHDA-DAPI reverse conjugates.	206

Figure 5.20 FT-IR spectrum of PTX-16-MHDA-AuNPs-16-MHDA-DAPI reverse conjugate.	208
Figure 5.21 ¹ H NMR spectra of PTX-16-MHDA-AuNPs-16-MHDA-DAPI reverse conjugate.	211
Figure 5.22 Cytotoxicity analysis of AuNPs-16-MHDA-DAPI reverse conjugate in T47D human breast cancer cells. Results were tested by One-way ANOVA and statistical significance showing * at P<0.05.	212
Figure 5.23 UV-Vis spectra of (a) free PTX (b) free RB and (c) PTX-RB conjugate.	213
Figure 5.24 Spectrum after subtracting PTX-RB spectra from free RB spectra.....	214
Figure 5.25 Fluorescence (a) excitation and (b) emission spectra of (A) free RB and (B) PTX-RB conjugate. The excitation spectrum was recorded at an emission wavelength of 567 nm. The emission spectrum was recorded using an excitation wavelength of 540 nm.	216
Figure 5.26 FT-IR spectra of (a) RB alone and (b) PTX-RB conjugate.	218
Figure 5.27 Chemical structure of rhodamine B.	220
Figure 5.28 ¹ H NMR spectra of (a) free RB and (b) PTX-RB conjugate.	221
Figure 5.29 Cytotoxicity analysis of free RB in T47D human breast cancer cells. Results were tested by One-way ANOVA and statistical significance showing * at P<0.05.	223
Figure 6.1 Confocal fluorescence (left) ($\lambda_{ex} = 405 \text{ nm}$, $\lambda_{em} = 478-700 \text{ nm}$), bright field (middle) and overlaid (right) images of (a) AuNPs (b) thiol-AuNPs and (c) PTX-thiol-AuNPs direct conjugate. All images recorded at room temperature.	228
Figure 6.2 Fluorescence (left) ($\lambda_{ex} = 405 \text{ nm}$, $\lambda_{em} = 478-700 \text{ nm}$), bright field (middle) and overlaid (right) images of T47D human breast cancer cells (a) untreated cells (b) treated with AuNPs (c) treated with thiol-AuNPs and (d) treated with PTX-thiol-AuNPs direct conjugate.....	229
Figure 6.3 Fluorescence (left) ($\lambda_{ex} = 405 \text{ nm}$, $\lambda_{em} = 478-554 \text{ nm}$), bright field (middle) and overlaid (right) images of (a) AuNPs-thiol-DAPI direct conjugate (b) PTX-thiol-AuNPs-thiol-DAPI direct conjugate (c) AuNPs-thiol-pyNH ₂ direct conjugate (d) PTX-thiol-AuNPs-thiol-pyNH ₂ direct conjugate (e) AuNPs-thiol-FB28 hybrid and (f) PTX-thiol-AuNPs-thiol-FB28 direct conjugate at room temperature.....	230

Figure 6.4 Fluorescence (left) ($\lambda_{\text{ex}} = 405 \text{ nm}$, $\lambda_{\text{em}} = 478 \text{ nm}$), bright field (middle) and overlaid (right) images of T47D human breast cancer cells treated with free DAPI, free pyNH₂ or free FB28 (a, d and g) after 1 h of incubation (b, e and h) after 6 h of incubation and (c, f and i) after 24 h of incubation at room temperature. Original magnification was 63 \times . Scale bars = 20 μm233

Figure 6.5 Fluorescence (left) ($\lambda_{\text{ex}} = 405 \text{ nm}$, $\lambda_{\text{em}} = 478 \text{ nm}$), bright field (middle) and overlaid (right) images of T47D human breast cancer cells treated with (a) free DAPI or (b) AuNPs-thiol-DAPI direct conjugate after 6 h of incubation at room temperature. Original magnification was 63 \times . Scale bars = 20 μm235

Figure 6.6 Fluorescence (left) ($\lambda_{\text{ex}} = 405 \text{ nm}$, $\lambda_{\text{em}} = 478 \text{ nm}$), bright field (middle) and overlaid (right) images of T47D human breast cancer cells treated with AuNPs-thiol-DAPI direct conjugate, AuNPs-thiol-pyNH₂ direct conjugate or AuNPs-thiol-FB28 hybrid (a, d and g) after 1 h of incubation (b, e and h) after 6 h of incubation and (c, f and i) after 24 h of incubation at room temperature. Original magnification was 63 \times . Scale bars = 20 μm235

Figure 6.7 Fluorescence (left) ($\lambda_{\text{ex}} = 405 \text{ nm}$, $\lambda_{\text{em}} = 478 \text{ nm}$), bright field (middle) and overlaid (right) images of T47D human breast cancer cells treated with PTX-thiol-AuNPs-thiol-DAPI, PTX-thiol-AuNPs-thiol-pyNH₂ or PTX-thiol-AuNPs-thiol-FB28 direct conjugates (a, d and g) after 1 h of incubation (b, e and h) after 6 h of incubation and (c, f and i) after 24 h of incubation at room temperature. Original magnification was 63 \times . Scale bars = 20 μm236

Figure 6.8 Fluorescence (left) ($\lambda_{\text{ex}} = 405 \text{ nm}$, $\lambda_{\text{em}} = 478 \text{ nm}$), bright field (middle) and overlaid (right) images of T47D human breast cancer cells treated with (a) AuNPs-thiol-DAPI and (b) PTX-thiol-AuNPs-thiol-DAPI direct conjugates after 1 h of incubation at room temperature. Original magnification was 63 \times . Scale bars = 20 μm236

Figure 6.9 Fluorescence (left) ($\lambda_{\text{ex}} = 405 \text{ nm}$, $\lambda_{\text{em}} = 478 \text{ nm}$), bright field (middle) and overlaid (right) images of T47D human breast cancer cells treated with (a) AuNPs-thiol-DAPI (b) PTX-thiol-AuNPs-thiol-DAPI (c) AuNPs-thiol-pyNH₂ and (d) PTX-thiol-AuNPs-thiol-pyNH₂ direct conjugates after 1 h of incubation at room temperature. Original magnification was 63 \times . Scale bars = 20 μm238

Figure 6.10 Fluorescence (left) ($\lambda_{\text{ex}} = 405 \text{ nm}$, $\lambda_{\text{em}} = 478 \text{ nm}$), bright field (middle) and overlaid (right) images of T47D human breast cancer cells treated with AuNPs-

16-MHDA-DAPI or PTX-16-MHDA-AuNPs-16-MHDA-DAPI reverse conjugates (a and d) after 1 h of incubation (b and e) after 6 h of incubation and (c and f) after 24 h of incubation at room temperature. Original magnification was 63 \times . Scale bars = 20 μ m.....	239
Figure 6.11 Fluorescence (left) ($\lambda_{\text{ex}} = 405 \text{ nm}$, $\lambda_{\text{em}} = 526\text{-}700 \text{ nm}$), bright field (middle) and overlaid (right) images of (a) free RB and (b) PTX-RB at room temperature.....	240
Figure 6.12 Fluorescence (left) ($\lambda_{\text{ex}} = 405 \text{ nm}$, $\lambda_{\text{em}} = 526\text{-}700 \text{ nm}$), bright field (middle) and overlaid (right) images of T47D human breast cancer cells treated with free RB or PTX-RB conjugate (a and b) after 1 h of incubation (b and e) after 6 h of incubation and (c and f) after 24 h of incubation at room temperature. Original magnification was 63 \times . Scale bars = 20 μ m.	241
Figure 6.13 TEM images showing clusters and individual of AuNPs in cell cytoplasm of T47D cells exposed to 200 μ L of (a & b) AuNPs and (c) AuNPs-thiol-DAPI direct conjugate for 3-4 h. Scale bar = 500 nm.	243
Figure 6.14 TEM images showing clusters and individual of AuNPs in cell cytoplasm of T47D cells exposed to 200 μ L of (a) AuNPs-thiol-DAPI (b) PTX-thiol-AuNPs-thiol-DAPI (c) AuNPs-thiol-pyNH ₂ and (d) PTX-thiol-AuNPs-thiol-pyNH ₂ direct conjugates for 3-4 h. Scale bar = 500 nm.....	244
Figure 6.15 TEM images showing clusters and individual of AuNPs in cell cytoplasm of T47D cells exposed to 200 μ L of (a) AuNPs-thiol-DAPI direct conjugate (b) PTX-thiol-AuNPs-thiol-DAPI direct conjugate (c) AuNPs-thiol-FB28 hybrid and (d) PTX-thiol-AuNPs-thiol-FB28 direct conjugate for 3-4 h. Scale bar = 500 nm.	245
Figure 7.1 UV-Vis spectra of antibodies containing nanoparticles. 1) EpCAM and 2) TARP.....	252
Figure 7.2 TEM image with size distribution histogram of PTX-thiol-AuNPs-thiol-TARP direct conjugate.	254
Figure 7.3 DLS measurements of antibodies containing nanoparticles. 1) EpCAM and 2) TARP.	255
Figure 7.4 FT-IR spectra of (a) EpCAM antibody (b) AuNPs-thiol-EpCAM direct conjugate and (c) PTX-thiol-AuNPs-thiol-EpCAM direct conjugate.....	258
Figure 7.5 FT-IR spectra of (a) TARP antibody (b) AuNPs-thiol-TARP direct conjugate and (c) PTX-thiol-AuNPs-thiol-TARP direct conjugate.	258

Figure 7.6 Comparison of response of T47D cell line to treatment with gold nanoparticles conjugates containing antibodies and/ or PTX using MTT assay. Shown in concentration of the direct conjugates (nM) versus relative survival (%) compared to untreated control. Data shown as mean, n:3, *: $p \leq 0.05$260

Figure 7.7 Comparison of response of T47D cell line to treatment with gold nanoparticles conjugates with and without antibodies using MTT assay. Shown in concentration of the direct conjugates (nM) versus relative survival (%) compared to untreated control. Data shown as mean, n:3, *: $p \leq 0.05$. The PTX-thiol-AuNP direct conjugate data is reproduced from Figure 4.8 in Chapter 4, Section 4.3.1.7.261

Figure 8.1 TGA data measuring the loss of organic material corresponding to 4-mercaptophenol-coated AuNPs (red) and hybrid structure (blue) [189].271

Figure 8.2 pH dependent release of DOX from DOX loaded nanoparticles [452]...272

Figure 8.3 Intracellular uptake of AuNPs dependence on size [453].273

Figure 8.4 Intracellular uptake of 20 nm AuNPs dependence on incubation time [453].274

List of Tables

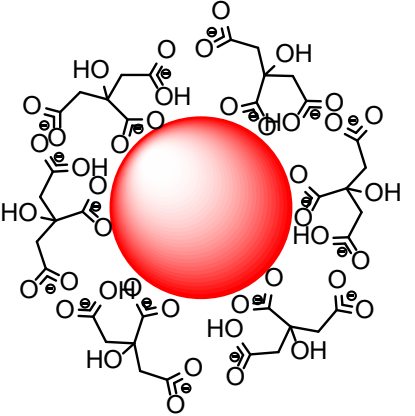
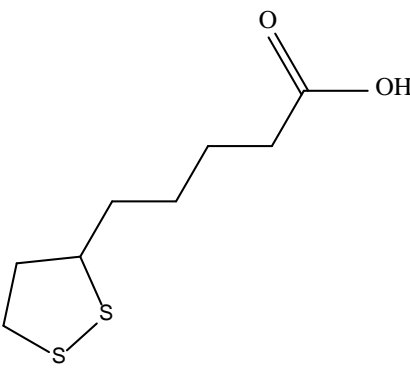
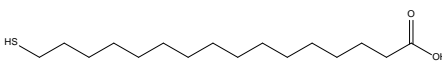
Table 1.1 Examples of nanomedicine based products for cancer approved by FDA and those undergoing clinical trials [108, 109].	14
Table 1.2 Some monoclonal antibodies approved by FDA and/or EMEA for human therapy [277-280].	47
Table 2.1 Chemicals and reagents.	55
Table 2.2 Exposure of T47D cells to various samples based on AuNPs.	97
Table 3.1 Particle size measurements of AuNPs, LA-AuNPs, thiol-AuNPs and PTX-thiol-AuNPs hybrid using TEM and DLS analytical techniques.	109
Table 3.2 DLS measurements of PTX-thiol-AuNPs hybrid at different mixing times.	109
Table 3.3 FT-IR peak positions of trisodium citrate, AuNPs, pristine LA, LA-AuNPs, pristine 16-MHDA, thiol-AuNPs, pristine PTX and PTX-thiol-AuNPs hybrid.	114
Table 3.4 Chemical shifts (δ /ppm) of LA functionalised AuNPs and free LA.	118
Table 3.5 Chemical shifts (δ /ppm) of free 16-MHDA and thiol-AuNPs.	120
Table 3.6 Chemical shifts (δ /ppm) of PTX alone and PTX-thiol-AuNPs hybrid.	123
Table 3.7 Drug loading for PTX-thiol-AuNPs hybrid samples.	126
Table 4.1 FT-IR peak positions of LA-AuNPs, thiol-AuNPs and PTX-thiol-AuNPs direct conjugate.	144
Table 4.2 ^1H NMR data (δ /ppm) for pristine LA and LA-AuNPs in CDCl_3 .	145
Table 4.3 Chemical shifts (δ /ppm) for thiol-AuNPs and free 16-MHDA.	146
Table 4.4 ^1H NMR chemical shifts (δ /ppm) for the protons of free PTX and PTX-thiol-AuNPs direct conjugate.	149
Table 4.5 Drug loading of PTX-thiol-AuNPs direct conjugate samples.	152
Table 5.1 Various fluorescent containing nanoparticles characterised by different techniques at different conjugation steps.	172
Table 5.2 DLS measurements of various fluorescent containing nanoparticles.	180
Table 5.3 FT-IR peak positions of DAPI alone, AuNPs-thiol-DAPI direct conjugate and PTX-thiol-AuNPs-thiol-DAPI direct conjugate.	187
Table 5.4 FT-IR peak positions of pyNH_2 alone, AuNPs-thiol- pyNH_2 direct conjugate and PTX-thiol-AuNPs-thiol- pyNH_2 direct conjugate.	188

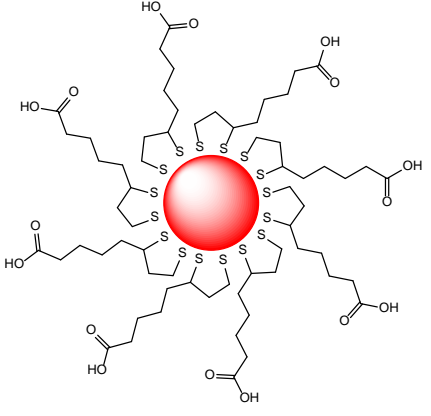
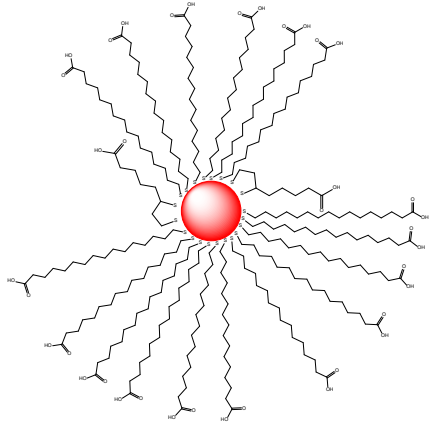
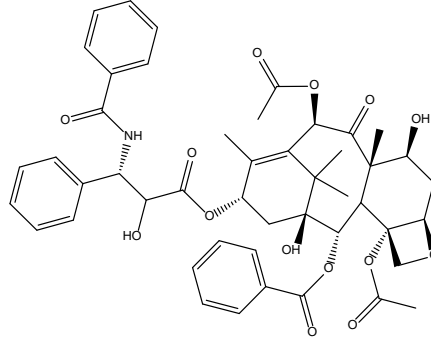
Table 5.5 FT-IR peak positions of FB28 alone, AuNPs-thiol-FB28 hybrid and PTX-thiol-AuNPs-thiol-FB28 direct conjugate.	189
Table 5.6 Chemical shifts (δ /ppm) for DAPI alone, AuNPs-thiol-DAPI direct conjugate and PTX-thiol-AuNPs-thiol-DAPI direct conjugate.	198
Table 5.7 Chemical shifts (δ /ppm) for free pyNH ₂ , AuNPs-thiol-pyNH ₂ direct conjugate and PTX-thiol-AuNPs-thiol-pyNH ₂ direct conjugate.....	198
Table 5.8 Chemical shifts (δ /ppm) for free FB28, AuNPs-thiol-FB28 hybrid and PTX-thiol-AuNPs-thiol-FB28 direct conjugate	199
Table 5.9 FT-IR peak positions of DAPI alone, free PTX and PTX-16-MHDA-AuNPs-16-MHDA-DAPI reverse conjugate.....	209
Table 5.10 FT-IR peak positions of RB alone and PTX-RB conjugate.....	219
Table 5.11 ¹ H NMR chemical shifts (δ / ppm) for RB alone and PTX-RB conjugate.	222
Table 6.1 Exposure of T47D cells to various samples based on AuNPs.	227
Table 6.2 Samples used for CLSM analysis in the presence or absence of cells.....	231
Table 7.1 Various samples based on AuNPs analysed using different techniques. ...	253
Table 7.2 DLS measurements of various antibodies containing nanoparticles.....	255

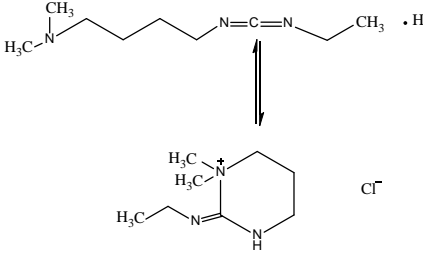
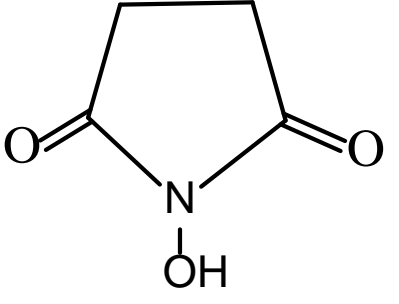
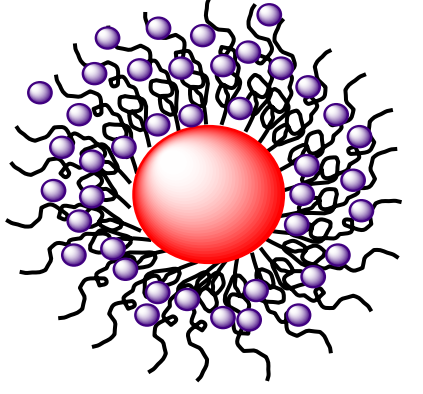
List of Schemes

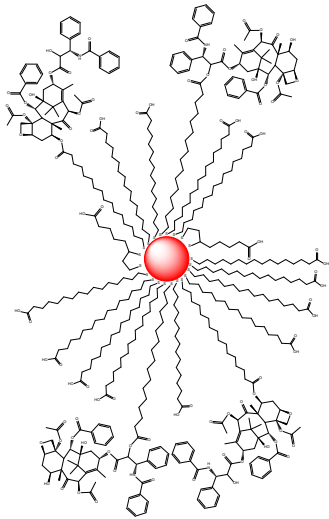
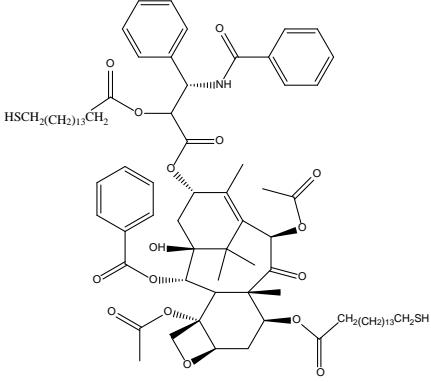
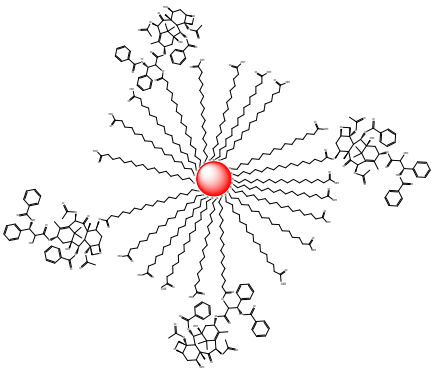
Scheme 2.1 Synthesis of citrate-stabilised gold nanoparticles (AuNPs).	59
Scheme 2.2 Functionalisation of gold nanoparticles using two-step ligand exchange method.....	60
Scheme 2.3 Synthesis of PTX-thiol-AuNPs hybrid.....	61
Scheme 2.4 Synthesis of PTX-thiol-AuNPs direct conjugate.....	64
Scheme 2.5 PTX-16-MHDA-AuNPs reverse conjugate.....	66
Scheme 2.6 Synthesis of RHN-thiol-AuNPs direct conjugate.....	68
Scheme 2.7 Synthesis of PTX-thiol-AuNPs-thiol-NH-R direct conjugate by covalent coupling reaction.	70
Scheme 2.8 Synthesis of AuNPs-thiol-FB28 hybrid.....	72
Scheme 2.9 Synthesis of PTX-thiol-AuNPs-thiol-FB28 direct conjugate.....	74
Scheme 2.10 Synthesis of AuNPs-16-MHDA-DAPI reverse conjugate.	76
Scheme 2.11 Synthesis of PTX-16-MHDA-AuNPs-16-MHDA-DAPI reverse conjugate.	80
Scheme 2.12 Synthesis of PTX-RB conjugate.....	82
Scheme 2.13 Synthesis of AuNPs-thiol-EpCAM direct conjugate.....	84
Scheme 2.14 Synthesis of PTX-thiol-AuNPs-thiol-EpCAM direct conjugate.	86
Scheme 3.1 The reduction of Au ⁺³ species [320].....	99
Scheme 3.2 Functionalisation of gold nanoparticles using two-step ligand exchange method.....	100
Scheme 3.3 Rapid exchange between hydrogens in citrate molecules.	115
Scheme 4.1 Schematic illustration of esterification process between the thiol-AuNPs and the anticancer PTX using EDC/NHS coupling reaction. An equivalent scheme can be drawn for the C ₇ position of PTX.	136
Scheme 4.2 Schematic illustration of esterification process between PTX and 16-MHDA using EDC/NHS coupling reaction; followed by adding AuNPs to form PTX-16-MHDA-AuNPs reverse conjugate. An equivalent scheme can be drawn for the C ₇ position of PTX.	138

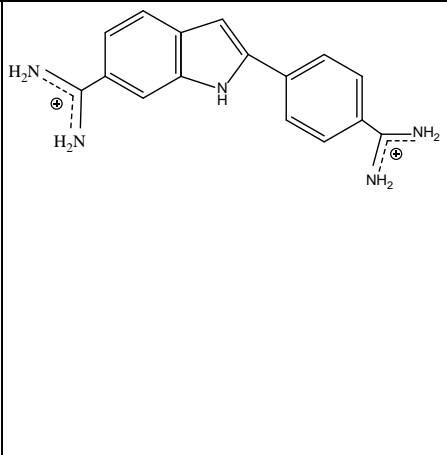
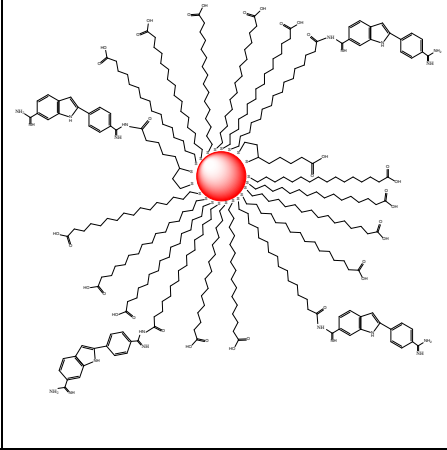
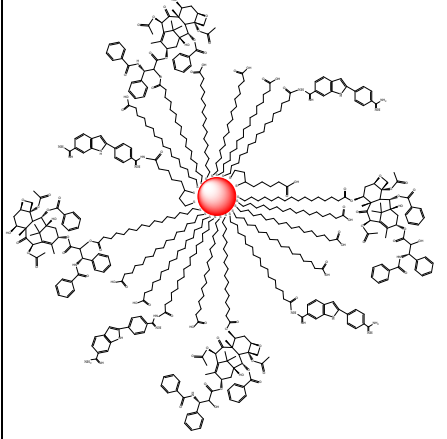
List of chemical structures

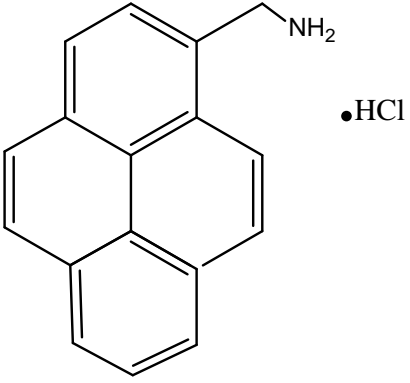
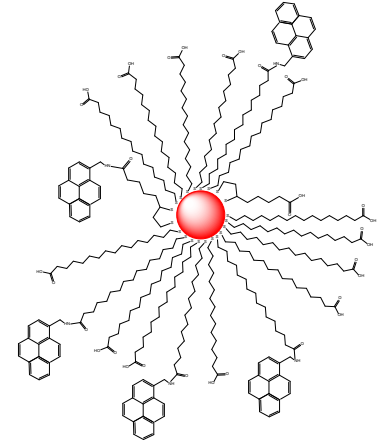
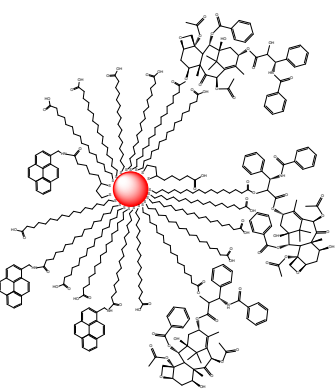
Abbreviation	Description	Structure
AuNPs	Gold nanoparticles. All sizes in this thesis will be given as diameters.	
LA	(\pm) - α -Lipoic acid.	
16-MHDA	16-Mercaptohexadecanoic acid.	

<p>LA-AuNPs</p>	<p>(±)-α-Lipoic acid functionalised gold nanoparticles.</p>	
<p>Thiol-AuNPs</p>	<p>(±)-α-Lipoic acid exchanged by 16-mercaptohexadecanoic acid functionalised gold nanoparticles.</p>	
<p>PTX</p>	<p>Paclitaxel.</p>	

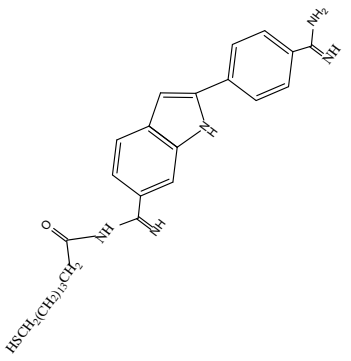
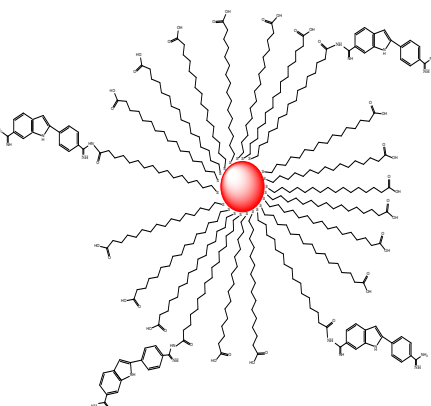
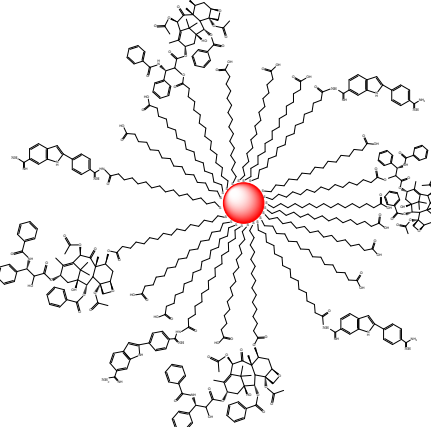
EDC	N-(3-Dimethylaminopropyl)-N'-ethylcarbodiimide hydrochloride.	 <p>The diagram shows the chemical structure of N-(3-Dimethylaminopropyl)-N'-ethylcarbodiimide hydrochloride. It consists of two parts: the carbodiimide form (top) and the zwitterionic form (bottom), connected by a double-headed equilibrium arrow. The carbodiimide form is $\text{H}_3\text{C}-\text{N}(\text{CH}_3)-\text{CH}_2\text{CH}_2\text{CH}_2-\text{N}=\text{C}=\text{N}-\text{CH}_2\text{CH}_3 \cdot \text{HCl}$. The zwitterionic form is a six-membered ring with a protonated nitrogen atom (N⁺) bonded to two methyl groups and a hydrogen atom, and a neutral nitrogen atom (N) bonded to an ethyl group and a hydrogen atom. A chloride ion (Cl⁻) is shown as the counterion.</p>
NHS	N-Hydroxysuccinimide.	 <p>The diagram shows the chemical structure of N-Hydroxysuccinimide, which is a five-membered ring containing one nitrogen atom and two carbonyl groups. The nitrogen atom is bonded to a hydroxyl group (-OH).</p>
PTX-thiol-AuNPs hybrid	(±)-α-Lipoic acid exchanged by 16-mercaptohexadecanoic acid functionalised gold nanoparticles mixed with paclitaxel.	 <p>The diagram illustrates a PTX-thiol-AuNPs hybrid. It features a central red sphere representing a gold nanoparticle (AuNP). This nanoparticle is surrounded by a dense layer of purple spheres, which represent thiol groups (-SH) that have been exchanged by 16-mercaptohexadecanoic acid. The thiol groups are further linked to a network of black wavy lines, representing the functionalized surface of the nanoparticles. The entire structure is shown as a spherical cluster.</p>

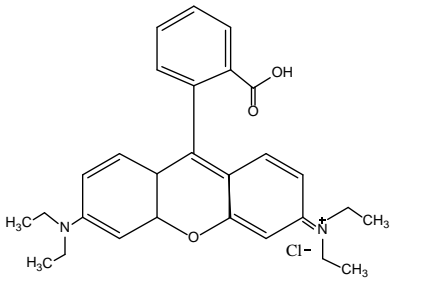
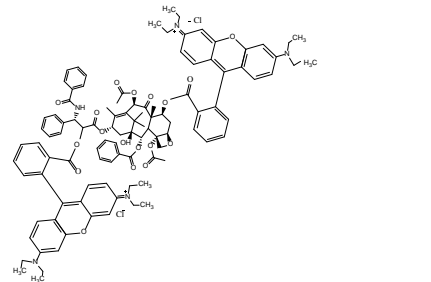
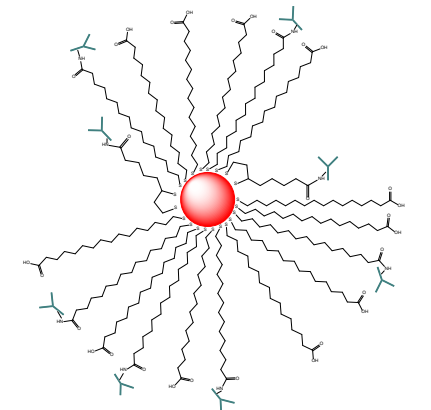
<p>PTX-thiol-AuNPs direct conjugate</p>	<p>(±)-α-Lipoic acid exchanged by 16-mercaptohexadecanoic acid functionalised gold nanoparticles covalently conjugated with paclitaxel using EDC/NHS coupling.</p>	
<p>PTX-16-MHDA</p>	<p>16-Mercaptohexadecanoic acid covalently attached to paclitaxel.</p>	
<p>PTX-16-MHDA-AuNPs reverse conjugate</p>	<p>16-Mercaptohexadecanoic acid covalently attached to paclitaxel via its carboxylic ends and then chemisorbed onto the surface of AuNPs via its thiols.</p>	

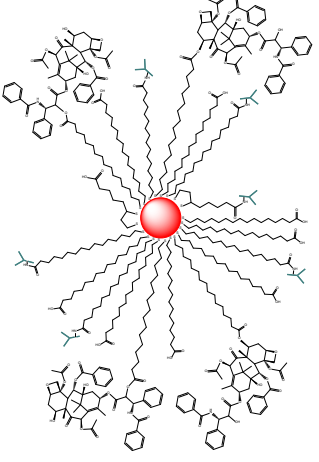
DAPI	2-(4-Amidinophenyl)-6-indolecarbamidine dihydrochloride.	
AuNPs-thiol-DAPI direct conjugate	(±)-α-Lipoic acid exchanged by 16-mercaptohexadecanoic acid functionalised gold nanoparticles covalently attached to 2-(4-amidinophenyl)-6-indolecarbamidine dihydrochloride.	
PTX-thiol-AuNPs-thiol-DAPI direct conjugate	(±)-α-Lipoic acid exchanged by 16-mercaptohexadecanoic acid functionalised gold nanoparticles covalently attached to 2-(4-amidinophenyl)-6-indolecarbamidine dihydrochloride and paclitaxel at the same time.	

PyNH ₂	1-Pyrenemethylamine hydrochloride.	
AuNPs-thiol-pyNH ₂ direct conjugate	(±)-α-Lipoic acid exchanged by 16-mercaptohexadecanoic acid functionalised gold nanoparticles conjugated with 1-pyrenemethylamine hydrochloride.	
PTX-thiol-AuNPs-thiol-pyNH ₂ direct conjugate	(±)-α-Lipoic acid exchanged by 16-mercaptohexadecanoic acid functionalised gold nanoparticles conjugated with 1-pyrenemethylamine hydrochloride and paclitaxel simultaneously.	

<p>FB28</p>	<p>Fluorescent brightener 28.</p>	
<p>AuNPs-thiol-FB28 hybrid</p>	<p>(±)-α-Lipoic acid exchanged by 16-mercaptohexadecanoic acid functionalised gold nanoparticles non-covalently interacted with fluorescent brightener 28.</p>	
<p>PTX-thiol-AuNPs-thiol-FB28 direct conjugate</p>	<p>(±)-α-Lipoic acid exchanged by 16-mercaptohexadecanoic acid functionalised gold nanoparticles non-covalently interacted with fluorescent brightener 28 and covalently attached to paclitaxel simultaneously.</p>	

16-MHDA-DAPI	16-Mercaptohexadecanoic acid covalently attached to 2-(4-amidinophenyl)-6-indolecarbamide dihydrochloride.	
AuNPs-16-MHDA-DAPI	16-Mercaptohexadecanoic acid covalently attached to 2-(4-amidinophenyl)-6-indolecarbamide dihydrochloride via its carboxylic ends and chemisorbed onto the surface of AuNPs via its thiols.	
PTX-16-MHDA-AuNPs-16-MHDA-DAPI reverse conjugate	16-Mercaptohexadecanoic acid covalently attached to paclitaxel via their carboxylic ends, and 16-mercaptohexadecanoic acid covalently attached to 2-(4-amidinophenyl)-6-indolecarbamide dihydrochloride via their carboxylic ends and then chemisorbed onto the surface of AuNPs via their thiols.	

<p>RB</p>	<p>Rhodamine B.</p>	 <p>The image shows the chemical structure of Rhodamine B. It consists of a central xanthene ring system. At the 4-position of the xanthene, there is a dimethylamino group (-N(CH₃)₂). At the 6-position, there is a diethylammonium group (-N⁺(CH₃)₂CH₂CH₃) with a chloride counterion (Cl⁻). At the 3-position, there is a phenyl ring substituted with a carboxylic acid group (-COOH).</p>
<p>PTX-RB</p>	<p>Paclitaxel covalently attached to rhodamine B.</p>	 <p>The image shows the chemical structure of Paclitaxel covalently attached to Rhodamine B. The structure is a complex hybrid of the two molecules. The paclitaxel core is linked to the rhodamine moiety through a covalent bond, specifically at the C-13 position of the taxane ring system. The rhodamine part of the structure is identical to the one shown in the first row.</p>
<p>AuNPs-thiol-antibody (EpCAM or TARP) direct conjugate</p>	<p>(±)-α-Lipoic acid exchanged by 16-mercaptohexadecanoic acid functionalised gold nanoparticles covalently attached to antibody (EpCAM or TARP).</p>	 <p>The image is a schematic diagram of a gold nanoparticle conjugate. It features a central red sphere representing the gold nanoparticle. Radiating from this sphere are numerous long, wavy lines representing 16-mercaptohexadecanoic acid chains. At the end of each chain, there is a blue Y-shaped structure representing an antibody molecule (EpCAM or TARP) covalently attached to the nanoparticle surface.</p>

<p>PTX-thiol-AuNPs-thiol-antibody (EpCAM or TARP) direct conjugate</p>	<p>(±)-α-Lipoic acid exchanged by 16-mercaptohexadecanoic acid functionalised gold nanoparticles covalently attached to antibody (EpCAM or TARP) and paclitaxel at the same time.</p>	
--	---	---

List of Abbreviations, symbols and units

Symbol/acronym/unit	Translation/explanation
CLSM	Confocal laser scanning microscopy
TEM	Transmission electron microscopy
DCIS	Ductal carcinoma in situ
LCIS	Lobular carcinoma in situ
IDC	Invasive ductal carcinoma
ILC	Invasive lobular carcinoma
LABC	Locally advanced breast cancer
IBC	Inflammatory breast cancer
HER2	Human epidermal growth factor receptor 2
PD	Paget's disease
%	Per cent
g mol⁻¹	Gram per mole
mg mL⁻¹	Milligram per millilitre
Cremophor EL	Polyethoxylated castor oil
mg/m²	Milligram per square meter
h	Hour
PEG	Polyethylene glycol
EPR	Enhancing permeability and retention effect

RES	Reticuloendothelial system
pH	Power of Hydrogen (per Hydrogen)
FDA	The U.S. Food and Drug Administration
DDSs	Drug delivery systems
L19	Human antibodies
ED-B	Extra-domain B of fibronectin
SPR	Surface plasmon resonance
HAuCl₄	Chloroauric acid
SERS	Surface enhanced Raman scattering
AuNRs	Gold nanorods
AuNSs	Gold nanoshells
PEG-SH	Thiol end polyethylene glycol
MPA	Mercaptopropionic acid
11-MUA	11-Mercaptoundecanoic acid
DHLA	Dihydrolipoic acid
CTAB	Cetyltrimethylammonium bromide
DTC	Dithiocarbamate
Zn²⁺	Zinc (II) ions
Ca²⁺	Calcium (II) ions
RCA120	Ricinus communis agglutinin
RGD	Arginine-glycine-aspartic acid peptide

Aβ1-16	β -amyloid peptide
5FU	5-Fluorouracil
BSA	Bovine serum albumin
FITC	Fluorescein isothiocyanate
DDAB	Didodecyldimethylammonium bromide
PAMAM	Polyamidoamine dendrimer
PDDA	Poly-diallyl dimethyl ammonium chloride
CT	Computed tomography
SERS	Surface-enhanced Raman spectroscopy
Chito6	Chitosan
TPPMS	Triphenylphosphine monosulfonate
AAS	Atomic absorption spectrometry
DC	Dendritic cells
PMT	Photomultipliers
APD	Assigning pseudocolors detector
Igs	Immunoglobulins
MAbs	Monoclonal antibodies
Abs	Antibodies
ADCC	Antibody-dependent cell-mediated cytotoxicity
CDC	Complement-dependent cytotoxicity

AFM	Atomic force microscopy
MRI	Magnetic resonance imaging
EMA	European Medicines Agency
PLGA	Poly(lactide-co-glycolide)
DSC	Disuccinimidyl carbonate
HCl	Hydrochloric acid
HNO₃	Nitric acid
HAuCl₄	Chloroauric acid
mL	Milliliter
mM	Millimolar
nm	Nanometre
kV	Kilovolts
DLS	Dynamic light scattering
UV-Vis	Ultraviolet-visible
FT-IR	Fourier transform infrared spectroscopy
¹H NMR	Nuclear magnetic resonance spectroscopy
NaOH	Sodium hydroxide
M	Molar
g	Gravity
NaCl	Sodium chloride
KCl	Potassium chloride

Na₂HPO₄	Sodium phosphate dibasic
KH₂PO₄	Potassium dihydrogen phosphate
PBS	Phosphate buffered saline
N₂	Nitrogen
RT	Room temperature
ε	Molar extinction coefficient
c	Concentration
ℓ	Path length
A	Absorbance
mm	Millimeter
CCD	A charge coupled device
DDD	Direct detection device
KBr	Potassium bromide
δ	Chemical shift
Δδ	Chemical shift differences
ppm	Parts per million
PMT	Photomultiplier tube
rpm	Revolutions per minute
T47D	Human ductal breast epithelial tumour cell line
EDTA	Trypsin-ethylene diamine tetra acetic acid

SDS	Sodium dodecyl sulfate solution
OD	Optical density
M_w	Molecular weight
nM	Nanomolar
MTT	3-(4,5-Dimethylthiazol-2-yl)-2,5-diphenyltetrazolium bromide
RPMI	Roswell Park Memorial Institute medium
FMC	Flinders Medical Centre
β-CD	Beta-cyclodextrin
DMEM	Dulbecco's modified Eagle's medium
WN	Wavenumber
EtOH	Ethanol
RDBC	Reconstituted dermal bovine collagen
n	Number of replicates
*p	Significance value of the test
EpCAM	Epithelial cellular adhesion molecule
PEI	Polyethyleneimine

Thesis guide

Objectives of the research

The main objective of this thesis was the development of a gold nanoparticle based drug delivery platform using a simple technique to increase the cellular uptake and hence effectiveness towards killing breast cancer cells as an alternative to conventional methods that use polyethylene glycol both as a linker and an antifouling agent due to its ability to resist fouling in biological systems. Potential drawbacks have emerged as adverse side effects by the polymer itself or by its derivatives need to be considered. It is hypothesised that having a biologically system that is comprised of gold nanoparticles (AuNPs) and a chemotherapeutic agent will demonstrate numerous significant advantages compared to their counterparts that use PEG. Therefore, new loading approaches and novel chemical attachments were investigated. The purpose of using different binding approaches to make the PTX loaded AuNPs is to investigate which approach leads to the most effective killing of breast cancer cells. The long-term goal of this area of research is to mitigate the side effects of PTX by specifically delivering the drug in a dose-effective way to malignant cells without damaging healthy cells. To achieve these aims, synthesis of the nanoconjugates was required. Descriptions of milestones were as following:

- 1- The long chain will increase the AuNP circulation time in biological systems by covering the surface to avoid serum protein binding. Thus, functionalisation of surface of AuNPs by (\pm)- α -lipoic acid (LA) as an intermediate for further functionalisation to control the kinetics followed by exchange with the long chain 16-mercaptohexadecanoic acid (16-MHDA) to increase the stability of functionalised AuNPs is carried out.
- 2- The first loading approach used was the physical binding (or non-covalent coupling) of paclitaxel to the surface of AuNPs that makes PTX extremely bioavailable and facilitates its release. Thereby, lower concentration of the drug will be needed leading to reduced side effects that result from current high dose treatment regimes.

- 3- The chemical attachment of PTX to the surface of AuNPs offers stronger interactions between the drug and the nanocarriers which may lead to an increase in the system stability and reduce premature drug detachment. However, the release of the drug in a controllable way using chemical binding regimes remains a challenge.
- 4- The use of an alternative synthetic method to chemically attach PTX to the modified AuNPs to investigate which chemical approach provides more benefits for biological use.
- 5- The high surface area of gold nanoparticles allows loading different fluorescent dyes which can be used to detect and track the fate of gold nanoparticles inside cells.
- 6- By exploiting the surface properties of gold nanoparticles, addition of targeting molecules (e.g., antibodies) could increase the interactions between the AuNPs and cancer cells to facilitate delivering and release of the drug in specific cells.

Layout of thesis

This thesis consists of eight chapters wherein [Chapter 1](#) provides an introduction to breast cancer, paclitaxel as a chemotherapeutic agent, the use of nanotechnology for cancer targeting, the use of gold nanoparticles (AuNPs) as delivery vehicles, cellular uptake of nanoparticles and a literature review of antibodies and their conjugation with nanoparticles. [Chapter 2](#) describes the materials, the experimental methods used throughout this study in addition to brief descriptions of the analytical instrumentation techniques used are provided. [Chapter 3](#) describes the synthesis mechanism and characterisation of AuNPs, the functionalisation of their surface with carboxylic acid-terminated alkanethiols, physical hybridisation of the particles with the anticancer agent, PTX, and the cytotoxicity assessment. [Chapter 4](#) describes the covalent conjugation of the chemotherapy drug, PTX, with the functionalised AuNPs using two methods. Characterisation of the conjugates and cytotoxicity evaluation are detailed herein. [Chapter 5](#) describes conjugation different fluorescent dyes onto the surface of AuNPs, analytical characterisation of these systems and results related to

cytotoxicity evaluation of conjugates containing fluorescent agents. Investigation of the intracellular uptake and localisation of AuNPs by T47D cells is described in [Chapter 6](#). [Chapter 7](#) discusses the conjugation of antibodies to the surface of gold nanoparticles to design systems capable to target specific sites of cancer cells. [Chapter 8](#) gives a conclusion for the previous chapters and discusses future work.

Chapter 1. Introduction and literature review

1.1 Synopsis

This chapter outlines the background information relevant to this thesis. Facts and statistics about breast cancer, including its types and some treatments used in breast cancer therapy, will be given. Specific attention will be paid to paclitaxel as anticancer drug, its structure, properties, function and its limitations. Then, a discussion on the progress of using nanotechnology for cancer targeting, which involves the current strategies used for targeting cancer intracellularly and nanoparticles applications in drug delivery, will be given. Particular focus will be given to gold nanoparticles (AuNPs) including their background, properties, synthesis methods, functionalisation and an overview of their biomedical applications will be provided with a specific focus on drug delivery systems. After that, attention will be focused on cellular uptake of nanoparticles, their pathway and the fate of those particles. The final section will be allocated to antibodies, their structure, function, conjugation with nanoparticles and their applications in biomedical field.

1.2 Breast cancer

Cancer is a group of diseases that start in any part of the body when the cells grow abnormally and out of control and spread to other tissues [1]. Cancer is a leading cause of death in developed countries and it is the second leading cause of mortality in the United States [2, 3]. Breast cancer can take place in any part of the breast including lobule, duct or connective tissues [4]. Breast cancer, apart from skin cancer, is the most common cancer among women in the United States, accounting for nearly 1 in 3 cancers [5]. It is also the second leading cause of cancer-related death among women after lung cancer [6]. In 2011, breast cancer was the third most common diagnosed cancer in Australia and it is predicted that it will remain the third most common diagnosed in 2015. In Australia in 2011, there were 14,568 new cases of breast cancer diagnosed; 103 cases for males and 14,465 cases for females. However, it is projected that the number of new cases diagnosed will rise to 15,740 cases, among them 145 cases for males, in 2015. Also, the mortality cases from breast cancer in 2012 in Australia were 2,819 and it is projected that this number will increase to 3,065 in 2015 [7].

1.2.1 Breast structure

The breast is mainly composed of two types of tissues which are glandular tissues and stromal (supporting) tissues. Glandular tissues contain the ducts for milk passageways and the glands (lobules) which are responsible for producing milk whereas stromal tissues are comprised of fatty and fibrous connective tissues. In addition, the breast has lymphatic and immune system tissues containing cellular fluids which are used for waste removal ([Figure 1.1](#)) [8].

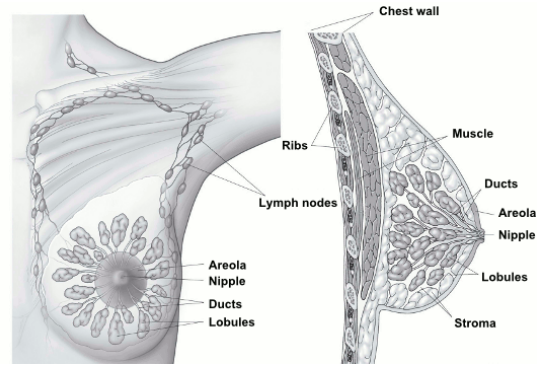


Figure 1.1 Normal breast tissue [9].

Breast cancer can start in different zones of the breast including ducts, lobules or in the tissue in between. Breast cancer can be classified into several types based on the part of the breast where it arises:

1.2.2 Breast cancer types

1.2.2.1 *Non-invasive breast cancer*

In this type of cancer, the breast cancerous cells are limited to milk ducts or lobules and do not spread to adjacent fatty connective tissues or other parts of the breast (Figure 1.2) [10]. Ductal carcinoma in situ (DCIS) forms the majority (90 %) of non-invasive breast cancer types. It involves clonal proliferation and cancerous cell accumulation inside the ducts without invasion to the surrounding parts of the breast [8]. DCIS includes varied lesions ranging from low-grade which are not life threatening to high-grade lesions which may eventually lead to histologic development to become invasive carcinoma [11, 12]. On the other hand, lobular carcinoma in situ (LCIS) includes proliferation of cancerous cells in the lobes of the breast and it is a less common type of non-invasive cancers. However, LCIS is considered an indicator of developing invasive breast cancer [8].

1.2.2.2 Invasive breast cancer

In this type of cancer, the breast cancer cells infiltrate from the duct and lobular walls and invade the adjacent fatty connective tissues of the breast [8] and may become metastatic by spreading to lymph nodes and other organs (Figure 1.2). Invasive ductal carcinoma (IDC) is the most common types of invasive carcinoma. It forms approximately 75 % of all breast cancers [13, 14]. Invasive lobular carcinoma (ILC) is the second most common breast cancer. Invasive lobular carcinoma forms approximately 10 % of all invasive breast cancer types [15]. Medullary carcinoma is a rare form of invasive ductal carcinoma. It forms approximately 3-5 % of all cases of breast cancer . Mucinous carcinoma of the breast is also a rare form of invasive ductal carcinoma accounting for approximately 1-6 % of all cases of breast cancer [16]. It is recognised by having a large amount of mucin [16]. Likewise, tubular carcinoma is a subtype of invasive ductal carcinoma. It is usually small and it consists of tube-shaped like structures. This type of cancer is called low-grade as the cells appear normal and they are likely to grow slowly. Tubular carcinoma accounts for approximately 1-4 % of all breast cancers [17].

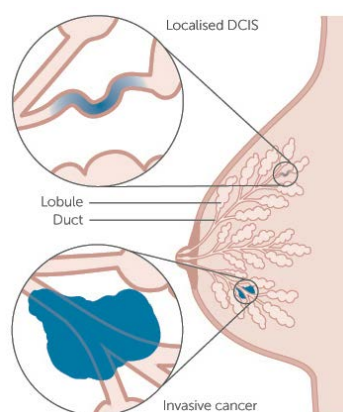


Figure 1.2 Illustration of a woman's breast displays DCIS and invasive breast cancer [18].

1.2.2.3 Locally advanced breast cancer

Locally advanced breast cancer (LABC) is an invasive and a common type of breast cancer in developing countries accounting for approximately 30 to 60 % of all breast cancers. It can be distinguished by the presence of a large primary tumour or the

involvement of a big area of lymph nodes with the absence of any evidence of distant metastases. Multidisciplinary therapy, which involves primary chemotherapy followed by locoregional therapy is currently a treatment of choice [19].

1.2.2.4 Metastatic breast cancer

In metastatic breast cancer, the cancerous cells have spread from their initial site to other parts of the body, which may include the lungs, liver, bones or brain, with continued growth [20]. Average survival of metastatic patients has been stated to range from 24 to 30 months with few surviving longer [21, 22].

1.2.2.5 Rare types of breast cancer

1.2.2.5.1 Inflammatory breast cancer (IBC)

Inflammatory breast cancer is a rare form of invasive breast cancer. The lymphatic vessels in the skin of the breast are affected by this type of cancer causing redness and inflammation of the breast [23, 24]. IBC accounts for 1 to 3 % of all breast cancers [23]. In IBC, the disease develops rapidly while the prognosis is poor [23]. The initial symptoms of the disease include painless swelling of the breast, feeling heavy and burning, redness and rash of the skin of the breast and pitted or dimpled skin [23, 24].

1.2.2.5.2 Triple-negative breast cancer

Triple-negative breast cancer is a type of breast cancer and it is characterised by the absence of estrogen, progesterone and HER2 receptors that usually found on the cells of breast cancer. It accounts for 15 % of all breast cancers. Triple-negative breast cancer can be treated by chemotherapy [25].

1.2.2.5.3 Paget's disease of the nipple

Paget's disease (PD) of the nipple is an uncommon subtype of breast cancer. It affects the nipple and the region around it. It is characterised by changes of the nipple and or areola including hard lumped or crusted lesions on the nipple and/ or areola, flatted out or turned inwards nipples, bleeding from the nipple in some cases and painful or

itchy skin in the area [26]. It forms 0.5-5 % of all breast cancers. This type of cancer is more common in postmenopausal women but it has been reported in patients aged between 24 and 90 [27].

1.2.2.5.4 Male breast cancer

Male breast cancer is an uncommon disease. The percentage of male breast cancer cases is less than 1 %. The behaviour of male breast cancer is similar to postmenopausal breast cancer in females. Risk factors related to male breast cancer include family history such as families with BRCA2 rather than BRCA1 mutations, hormones or obesity [28].

1.2.3 Breast cancer treatment

Choosing the appropriate treatment for breast cancer depends on several factors including breast cancer type, breast cancer stage, the area of breast cancer, the age and general health of the patient and whether the patient had a breast cancer before or not and what treatments were taken and the probable benefits and side effects of each treatment [29]. Generally, several sorts of treatments are used for breast cancer. Surgery, radiation therapy and chemotherapy are some of these therapies.

1.2.3.1 Surgery

Surgery is the initial therapy that most breast cancer patients receive to effectively remove tumour with negative margins to diminish a local recurrence risk [30]. Surgery treatment helps minimise the cancer growth and prevents its spread to other parts of the body. There are various types of surgery available which can be used individually or in combination with other treatments such as radiotherapy or chemotherapy [31]. Breast cancer patients are usually treated with breast-conserving surgery, which is the first type of operation, due to the limited size of most cancers and the possibility of reducing the size of large tumours using primary chemotherapy [31, 32]. Mastectomy, which is the second type of surgery, is used to remove the whole mammary gland. In addition, surgery is also used to remove the lymph nodes located under the armpit area depending on the degree or the level of lymph nodes affected and the cancer aggressiveness in each patient [30, 33]. This type of surgery is

applied if there are cancerous cells in the surgical margin, recurrence of breast cancer in the same breast or if radiotherapy was used before in that cancerous site [34].

1.2.3.2 Radiation therapy

Radiation therapy (radiotherapy) can be defined as the use of high energy X-rays to destroy cancer cells thus preventing them from continuing to grow. It is used to treat both the primary and progressive carcinomas [35]. Radiation therapy may be used individually or in combination with other treatments such as surgery and/or chemotherapy [35]. The main aim of using radiotherapy with other therapeutics is to remove any remaining breast cancerous cells that might have not been completely eradicated after surgery [36]. Using radiation therapy is recommended after breast-conserving surgery, after mastectomy in patients with a tumour larger than 5 cm or when the malignant cells spread into the lymph nodes [36]. Although radiation is very effective at killing cancer cells, developing resistance by some malignant cells has been reported resulting as a significant clinical problem [36]. Developing chemotherapy able to specifically sensitise the tumour to radiation is one solution to this obstacle. However, preparing such chemotherapeutics has attained limited success. Furthermore, detection levels of the resistance to the radiotherapy and its mechanism are lacking which increase the probability of failure of the treatment [36]. When using radiation therapy the normal, healthy cells might be damaged as well leading to adverse effects [37].

1.2.3.3 Chemotherapy

Chemotherapy is the use of cytotoxic chemical substances to destroy malignant cells or slow down their growth. Some of chemotherapeutics are extracted from natural sources while others are developed in the laboratory [38]. Chemotherapy is a treatment of choice for most classes of breast carcinomas [39]. Chemotherapy is used either separately by giving the patient several anticancer drugs at the same time or in some cases only one drug is given. It is used in combination with other treatments by applying it before or after surgery or radiation therapy, or together with radiation therapy [38]. The benefit of using adjuvant systemic chemotherapy is the killing or preventing undetectable micrometastasis after primary surgery then increasing the survival rate by reducing the recurrence. It has been shown that the use of adjuvant

chemotherapy to increase survival in both node-negative and node-positive is efficient. In addition, adjuvant chemotherapy may increase 10 year survival by 7 % – 11 % in premenopausal females with early stage breast cancer and by 2 % – 3 % in women aged over 50 [39]. Patients with locally advanced or large primary tumours are given neoadjuvant therapy to reduce the tumour and facilitate removal of invasive cancer via less surgery which may lead to a successful treatment [32]. Chemotherapeutic agents can be given intravenously or orally in a tablet [40]. The most commonly used chemotherapeutic agents for breast cancer treatment include paclitaxel, doxorubicin, docetaxel and cyclophosphamide [41].

1.3 Paclitaxel (Taxol)

Paclitaxel (PTX), also known as Taxol, is a hydrophobic and very efficient chemotherapeutic drug [42-44]. It is extracted from the bark of yew tree [45]. It is a white, crystal-like powder and its melting point is around 210 °C [44]. It is used alone or in combination with other treatment techniques [46] to treat different kinds of cancer cells such as breast [47], ovarian [48] and lung cancers [49].

1.3.1 Paclitaxel history

In the 1960s, the National Cancer Institute launched a program for screening and discovering new anti-tumour drugs and paclitaxel was one of them. The program involved examining anticancer activity for many plant extracts. A chemical extracted from the bark of *Taxus brevifolia* (Pacific or western yew) was included and screened and it showed anticancer activity against different cancer cell lines. This isolated chemical was called paclitaxel [50]. Paclitaxel has attracted great attention due to its unique mechanism of action displayed since its discovery in 1979 [51]. Two decades later, PTX has been approved in the United States as an anticancer drug for ovarian and breast cancers [50].

1.3.2 Paclitaxel structure and mechanism of action

Paclitaxel is a diterpenoid compound. Its chemical name is 5b,20-epoxy-1,2a,4,7b,10b,13a-hexahydroxytax-11-en-9-one-4,10-diacetate-2-benzoate 13 ester

with (2*R*,3*S*)-*N*-benzoyl-3-phenylisoserine with molecular formula of C₄₇H₅₁NO₁₄ and molecular weight 853.9 g mol⁻¹ [50]. PTX is composed of taxane structure with a four-membered oxetane ring and a homochiral ester side-chain at C13 (see [Figure 1.3](#)) [50].

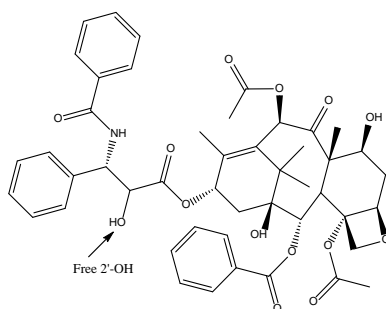


Figure 1.3 Paclitaxel structure.

Despite the achievement of total chemical synthesis of PTX, it is not considered to be suitable for commercial fabrication [52]. In addition, paclitaxel's structure provides a unique mechanism of action. It promotes polymerisation of tubulin dimers to form microtubules. PTX attaches to microtubule proteins through N-terminal 31 amino acids of the β -subunit of tubulin in the microtubule [53]. PTX has ability to stop cellular growth and induce apoptosis by blocking the replications of cells via stabilising the cellular microtubules and preventing depolymerisation [50, 51, 54, 55].

1.3.3 Paclitaxel limitations

The lack of permeability into cells and poor water solubility of paclitaxel (<0.03 mg mL⁻¹) have limited its utilisation in clinical applications [54, 56]. The commercially available form of paclitaxel drug, known as Taxol, is formulated in a mixture of Cremophor EL (polyethoxylated castor oil) and ethanol and it is given intravenously at doses of 135 or 175 mg/m² as a 3 or 24 h infusion every 3 weeks [50]. However, larger doses with a longer infusion period have been used as well [50, 57]. The use of Taxol formulation causes serious problems including short physical stability of the diluted formulation (it lasts between 12 and 24 h), danger of thrombosis and extravasation. Taxol formulations cause hypersensitivity reactions, nephrotoxicity, rash, neurotoxicity, chest ache, tachycardia and hypotension [58, 59]. As a result of

using Taxol formulation, the infusion time is prolonged and pre-treatment is needed. Moreover, unpredictable non-linear plasma pharmacokinetics are observed due to the changes that occur in pharmacokinetic profile of PTX *in vivo* because of the presence of Cremophor EL in combination with PTX [60]. Therefore, the current formulation of PTX has low therapeutic index [45]. PTX is a substrate of P-glycoprotein (P-gp). The P-gp reduces the bioavailability and facilitates the excretion of hepatobiliary by pumping the drug outside the cells leading to drug resistance [61, 62]. Several P-gp inhibitors, such as verapamil [63] and PSC 833 [64] were used with PTX. However, no successful results were attained due to their toxicity and/ or pharmacokinetic and biodistribution changes of PTX [44]. Therefore, developing an alternative formulation without using Cremophor EL is needed [46]. Current research focuses on developing drug based nanoparticles which are biodegradable and non-toxic carriers to solve the obstacles that exist in the commercially available anticancer drugs [65]. Combining drugs with nanoparticles could improve the drug solubility and reduce other drawbacks such as high toxicity and short circulation half-life within the body that exist in standard anticancer therapeutic drugs [44, 66].

1.4 Targeted drug delivery for cancer treatment using nanotechnology

The development of biopharmaceutics and pharmacokinetics began in 1950s. Biopharmaceutics studies the correlation between physical and chemical properties of drugs, the form of the dosage that could be given and the administration method and the pharmacological, toxicological or clinical effects that are observed after the administration of the drug [67]. While pharmacokinetics is the investigation of the time course of drug absorption, distribution, metabolism and excretion [67]. After that, efforts were directed to drugs targeting specific organs in the body [68]. At the present time, despite great developments in pharmacological research, the current cancer treatment lacks sufficient cancer diagnostic systems to predict the extent of treatment success [69]. Conventional anticancer drug delivery systems still have essential drawbacks including non-specific targeting of malignant cells as these agents can also be toxic and damage the healthy cells, poor water solubility, high sensitivity to biological environment, the need for high dosages to kill tumour cells

leading to increasing the toxicity and, because of inadequate drug distribution, resistance to the drug increases meaning that optimal treatment is difficult [68, 70, 71]. In addition, late diagnosis and treatment of cancer after it has been invasive and spread into other parts of the body make the cancer treatment outcomes unsatisfactory [68, 72]. Therefore, there is a need to develop a novel drug delivery system that has ability to overcome the limitations in conventional drug delivery systems (DDSs) [68], which refer to formulations, technologies or systems that transport a therapeutic agent in the body and enhance its efficiency by controlling the release of drugs in the body [73].

In the last few decades, nanotechnology has emerged with the potential to overcome limitations of current chemotherapeutics through designing drug based nanocarriers systems [74]. Nanotechnology is defined as the synthesis, design, characterisation and application of materials and devices through controlling shape and size at nanometre scales [75]. Cancer nanotechnology is a new multidisciplinary field combining various scientific disciplines; biology, chemistry, engineering and medicine; leading to significant progress in cancer detection, diagnosis and treatment [76]. When the size of bulk materials shrinks to nanometre size, these materials exhibit novel optical, electronic, magnetic and structural properties and these materials called nanomaterials [77-79]. Nanomaterials-based drug vehicles are small drug delivery systems ranging in size from 1 to 100 nm in two (include carbon-based nanomaterials (graphene, graphene oxide (GO)), silicate clays, layered double hydroxides (LDHs), transition metal dichalcogenides (TMDs) and transition metal oxides (TMOs) which are used for drug delivery) or three dimensions [75, 80] and have attracted great attention and emerged as novel promising systems for pharmaceutical and clinical applications. In the late 1960s, the first nanoparticles based drug delivery systems and vaccines were developed [68]. In comparison to large biological molecules such as enzymes, receptors and antibodies, nanoparticles can interact with biomolecules both on the surface of and inside cells leading to a revolution in diagnosis and treatment of cancer [2]. Nanomaterial based drug delivery systems are produced through different strategies including encapsulation and covalent or noncovalent attachment of a biomolecule to the nanoparticle [81]. In recent years, nanoparticles have been covalently attached to biological moieties such as peptides, proteins, nucleic acids, drugs and small-molecule ligands [82, 83]. Such

nanoparticles attached to biomolecules and used for medical applications are known as nanomedicines. Nanomaterials based drug delivery systems possess tremendous advantages compared to conventional drug delivery systems making them a promising alternative to overcome current problems in treating different diseases such as cancer, cardiovascular and neurodegenerative diseases [81]. One novelty of using nanotechnology in biomedicine applications is the possibility of designing materials and devices at nanometre size able to interact with cells and tissues at molecular level which was previously unmanageable [84]. In addition, nanotechnology has provided promising systems for early detection, diagnosis and treatment of diseases including cancer [85]. Imaging, drug delivery, biosensing and treatment of infectious diseases by controlling the biological, biophysical and biomedical obstacles have significantly improved using the features of nanotechnology [2].

Nanotechnology has led to significant improvement in pharmaceutical applications. The distinct properties of the nanoparticles allow the design of drugs or components of drugs providing systems with controlled release and drug targeting and delivery. For example, designing nano-polymers capsules that are able to release drugs at controlled rates or allowing release of the drug in different environments such as acid media to promote tumour uptake of the drug represents significant progress in pharmaceutical sector [86, 87]. Moreover, nanoparticles are promising platforms for targeted delivery of the drugs to cancerous cells. Using either passive or active targeting methods of nanoparticles (see [Chapter 1, Sections 1.4.1 and 1.4.2](#), respectively) can improve targeting tumour cells specifically by increasing the intracellular concentration of drugs in these sites without causing toxicity to normal cells [88]. Furthermore, nanoparticles can be used to increase the loading to deliver the drug at specific sites leading to reduced drug doses thus reducing the drug side effects [89]. Nanoparticles can also improve the solubility of the hydrophobic drugs [89]. For example, by conjugating of hydrophobic PXT with water-soluble polymers or by encapsulation of the drug into nanoparticles based lipid vehicles, the drug solubility has been improved significantly [90].

Additionally, nanoparticles can permeate easily into the cancerous sites due to their small size which leads to enhanced permeability and retention (EPR) enabling delivery of high doses of the therapeutic to specific tumour sites [90]. Furthermore,

coating the nanoparticle surface with different ligands, usually polyethylene glycol (PEG) can prevent the recognition then clearance of those particles by reticuloendothelial system (RES). As a result, more particles loaded with the drug can be internalised and localised in tumour cells [90]. Bioavailability of the conventional drugs is another obstacle where nanotechnology can provide probable solutions. The poor bioavailability of many conventional drugs has limited their use as oral formulations. However, nanotechnology with nano-sized materials is introducing novel therapies [91, 92]. In cases where the agents are susceptible at high pH to degradation or denaturation, formulations containing nanoparticles can protect these agents. Nanoparticles can prolong the drug exposure time by increasing retention of the formulation through improving bioadhesive interactions [93, 94]. Developing operative drug delivery systems able to carry and deliver the cargo safely to specific sites of the body can contribute significantly to enhancing the function of conventional drugs [95]. Therefore, current research has focused on producing novel nanoparticles functionalised with different biomolecules by covalent conjugation onto the surface, encapsulation or other strategies to target specific cancer cells [96]. These nanomaterials are able to interact with the cells at the surface of and inside the cells [97]. Many nanoparticle based carriers have been developed for targeting cancer cells including quantum dots [98], carbon nanotubes [99], paramagnetic nanoparticles [100], liposomes [101], polymeric nanoparticles [102], micelles, dendrimers, viral-based nanoparticles, metallic particles such as gold nanoparticles [103] and many others [97]. [Figure 1.4](#) shows some of these nanoparticle based carriers.

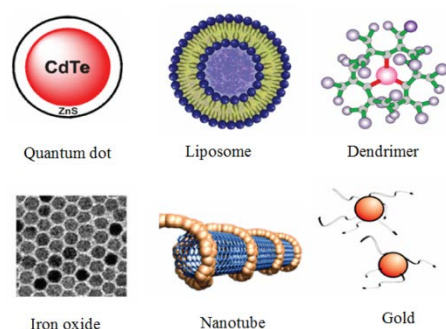


Figure 1.4 An illustration of some nanoparticles have been investigated for biomedical applications targeting cancer [2].

At present, various nanomedicines for cancer therapy have been already approved by the U.S. Food and Drug Administration (FDA) or under clinical trials [104] (see [Table 1.1](#)) including:

1. Abraxane®, human serum albumin nanoparticles conjugated paclitaxel targeting different cancers [65, 105].
2. Doxil (pegylated liposomal doxorubicin) which is the first nanodrug approved to be applied for treating several types of cancer such as metastatic ovarian cancer and AIDS-related Kaposi's sarcoma [106].
3. Myocet, which is used for the first-line treatment of metastatic breast cancer in combination with cyclophosphamide [106].
4. ThermoDox which is in clinical trial phase III to be used for liver cancer [106].

However, after approving any DDS, further clinical trials are applied before replacing the conventional free drug [74]. Many nanomedicine based products have been transformed from laboratory to clinical applications [107].

Table 1.1 Examples of nanomedicine based products for cancer approved by FDA and those undergoing clinical trials [108, 109].

Drug name	Active ingredient	Indications	Approval year/ clinical trial stage
Abraxane	Albumin-bound paclitaxel nanospheres Nab paclitaxel in combination with gemcitabine	Various cancers Metastatic pancreatic cancer	2013
Onivyde MM-398 (Merrimack)	Liposomal irinotecan (PEGylated)	Metastatic pancreatic cancer	2015
Onco-TCS	Liposomal Vincristine	Non-Hodgkin Lymphoma	In clinical phase I/II
LEP-ETU	Liposomal paclitaxel	Ovarian/breast/lung cancers	In clinical phase I/II
Aroplatin	Liposomal Cisplatin analog	Colorectal cancer	In clinical phase I/II
ThermoDox	Doxorubicin	Hepato cellular carcinoma	In clinical phase III

There are two main strategies, passive targeting and active targeting, used for delivering chemotherapeutic agents to malignant cells. These two types will be discussed in the following sections.

1.4.1 Passive targeting

Passive targeting is based on accumulation of nanoparticles and other macromolecules in and around tumour tissues that have unique characteristics such as leaky vasculatures with wide gaps between endothelial cells allowing extravasation of certain size of nanoparticles, as a result of the enhanced permeability and retention (EPR) phenomenon [110]. Some factors relevant to the tumour microvasculature and other factors associated with the nature of nanoparticles, such as size, shape and surface charge determine nanoparticle delivery to tumour sites [89, 110]. EPR relies on the nanoparticle's size and two basic phenomena which are the leaky vasculature and impaired lymphatic drainage of cancer tissues [111]. In passive targeting strategy, the pathophysiological state of malignant tissues directs the nanomedicines to tumour sites ([Figure 1.5.B](#)) [112]. Since solid tumours lack functional lymphatics and are incapable of removing extravasated nanocarriers, the vascular leakiness is increased allowing circulating nanomedicines to remain in the cells for longer times helping them accumulate in tumour sites [113]. Nanotechnological products can be delivered to the diseased or inflamed tissues and cells by exploiting the pathophysiological and anatomical changes that occur in the body [114]. Delivering a drug passively to a specific site can be accomplished by exploiting the anatomical changes that occur in diseased tissues. A typical drug targeting system should offer long circulating time within the body and adequate concentrations of the drug at the targeted site and it should maintain its therapeutic efficiency during the circulating time [115]. Enormous numbers of nanomedicines produced for drug delivery that targeted cancers rely on EPR ([Table 1.1](#)) [113].

1.4.2 Active targeting

In active targeting, specific interactions between specific ligands such as antibodies, proteins, lipoproteins, peptides, folate, saccharides and transferrin functionalised the surface of nanocarriers and specific receptors over expressed on the targeted cells

take place (Figure 1.5.C) [111]. An active targeting strategy is used to improve recognition of the targeted cells thus promoting the targeted cell uptake. EPR is responsible for enhancing tumour accumulation whereas the ligands attached to nanocarriers improve the specificity of delivering the cargo using nanocarriers. These interactions between the ligands functionalised nanocarriers and the receptors on cell membrane promote the internalisation of nanoparticles into the cells through an endocytosis mechanism [113]. Increased specificity of the interactions between a ligand functionalised nanocarriers and specific receptors on cell membrane requires selective binding between the ligand and the desired receptor with overexpression of that receptor [113, 116]. Significant development has been achieved at the preclinical trials for active targeting pathways. However, only few antibodies based nanomedicines such as Zevalin, Mylotarg, Ontak and Bexxar have been approved for clinical applications [113]. The failure to demonstrate active targeting molecule formulations such as liposomes, polymers and micelles at preclinical trial level can be attributed to the difficulties of passing physiological barriers, including the existence of additional cellular layers between endothelial and tumour cells, the high density of tumour cells and the high interstitial fluid pressure in cancerous sites. Additionally, after leaving the leaky vasculatures of tumour and before reaching the receptor sites on the membrane of cancerous cells, the antibodies bind to other species before reaching the target site [113]. Furthermore, barriers associated with binding site can lower the internalisation of actively targeted nanomedicines into the tumour sites as the nanomedicines penetrate into the cells using active targeting strategy have difficulties finding the targeted receptors at the tumour sites and binding to them [113, 117]. The main advantage of using actively targeted nanomedicines is their ability to penetrate and internalise efficiently into the cancerous cells higher than those internalised by passively targeting approach. Therefore, the active targeting strategy is valuable for delivering drugs intracellularly. Trials to get over the aforementioned problems regarding the use of active targeting to deliver a drug to tumour cells have been done. Researchers have developed formulations based on endothelial cell-targeted nanomedicines (Figure 1.5.D). For example, Borsi et al. [118] designed human L19 antibodies, which react with ED-B domain of fibronectin which is an angiogenic vasculature marker, as ligands to target drugs and other drug delivery systems to tumour blood vessels. The system is promising for solid tumours diagnosis and treatment [118]. In addition, another study showed conjugation of two

home selective to tumour blood vessel peptides containing an α_v integrin-binding Arg-Gly-Asp motif and the other an Asn-Gly-Arg motif, with the anti-tumour drug, doxorubicin, improved the efficiency of the drug against human breast cancer. The findings are encouraging for the development of novel targeted approaches that rely on specific expression of receptors in tumour vasculature [119]. The purpose of developing such formulations that rely on endothelial cell-targeted nanomedicines is to increase the potential of delivering drug to the tumour endothelium as nanomedicines targeted to the tumour vasculature do not rely on extravasation and permeation through pericyte, smooth muscle cell- and/or fibroblast-based cell layers. Due to the fact that endothelial cell-targeted nanomedicines can find their targeted receptors easier than nanomedicines targeted to cancer cells as these endothelial cells-targeted nanomedicines are not facing the dense tumour cells and the high interstitial fluid pressure, these targeted nanoparticles represent a good starting point for the development of such therapies [113]. Moreover, it can be projected that endothelial cell-targeted nanomedicines are promising in tumour targeting and therapy due to their ability to encounter, bind and kill their target sites. They can deny access of the tumour cells to oxygen and nutrients and there is a possibility of preparing endothelial cell-targeted nanomedicines able to release their cargo in the tumour vasculature by binding to tumour blood vessels. This way small drugs can penetrate into the tumour interstitium [113]. These observations with significant preclinical evidence regarding active targeting of the tumour blood vessels [118-120] coupled with the hopeful results from phase I trials for L19-targeted Interleukin-2 [121] and RGD-targeted adenoviruses [122] are raising expectations of the promising future of endothelial cell-targeted nanomedicines to enter clinical trials and then be approved for tumour therapy [113].

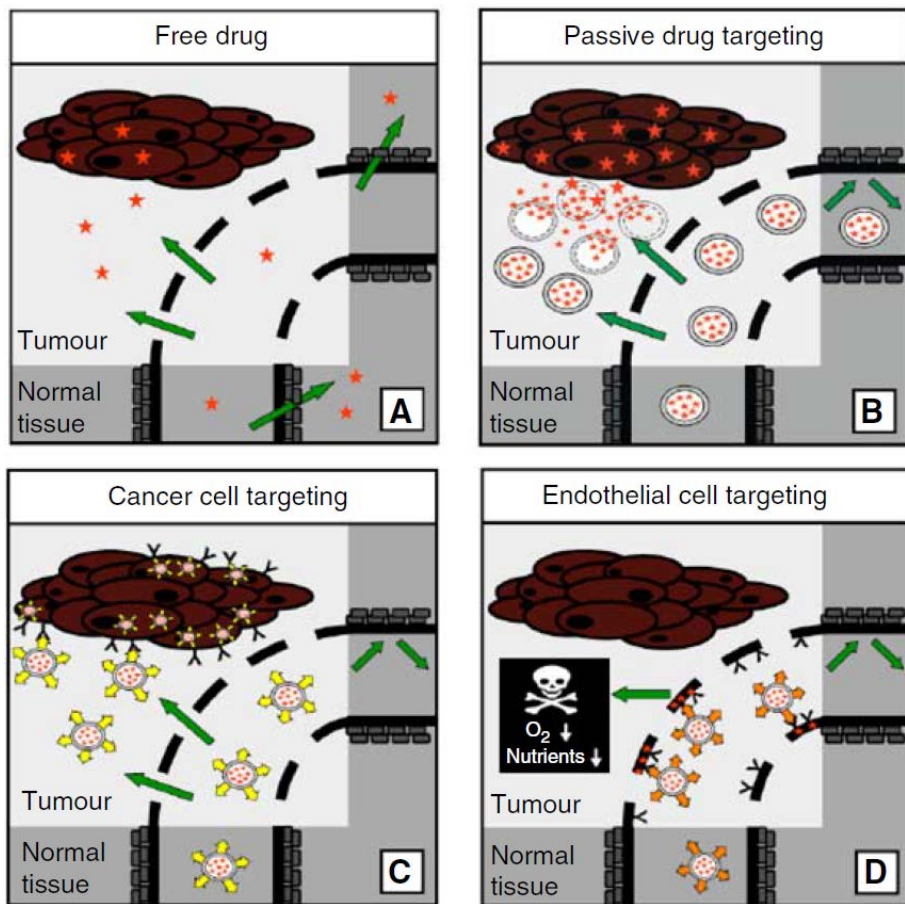


Figure 1.5 Overview of various targeting approaches for drug delivery to tumour cells. (A) intravenous administration of low-molecular-weight and conventional anti-tumour drug, which is usually removed rapidly from blood and shows accumulation in both cancerous and healthy cells. (B) passive targeting of nanomedicines to cancer cells based on the enhanced permeability and retention (EPR) effect. (C) active targeting of nanomedicines to tumour cells to improve cellular internalisation and cellular uptake of the nanomedicine. (D) active targeting to overexpressed receptors by angiogenic endothelial cells aims to reduce blood supply to tumours and thus prevent the cells from oxygen and nutrients [123].

This thesis will focus on gold nanoparticles as novel nanocarriers given their tremendous potential for cancer treatment.

1.5 Gold nanoparticles (AuNPs)

1.5.1 History

Gold nanoparticles, also known as colloidal gold, have been given extensive attention from ancient eras. In the 4th and 5th centuries B.C., Romans used gold nanoparticles to make the ruby red Lycurgus Cup for decoration [124, 125]. For therapeutic purposes gold colloids were used for different diseases such as heart problems, dysentery, epilepsy and tumours [125]. However, the first synthetic approach of colloidal gold nanoparticles (AuNPs) was reported by Faraday in 1857 [126]. Tetrachloroaurate solution was reduced by a phosphorus agent [127]. Then, Faraday investigated the optical properties and noticed the difference between colloidal gold and bulk material [128]. In the 20th century, different approaches of synthesising AuNPs have emerged [125].

1.5.2 Properties

Gold nanoparticles exhibit unique physical, chemical and biological properties that can be exploited to improve pharmaceutical applications. Unlike other nanoplatforms such as semiconductor quantum dots, magnetic and polymeric nanoparticles, plasmonic nanoparticles (such as gold nanoparticles and other noble metals) possess distinctive surface plasmon resonance (SPR). When exposing a molecule to light, a collective resonant oscillation of the free electrons of that particle is induced by the oscillating electromagnetic field of the light. Thereby, the electron oscillation around the surface of the particle will cause a charge separation and form a dipole oscillation along the direction electric field. When the maximum capacity of oscillation at a particular frequency is reached, this phenomenon is called surface plasmon resonance (SPR) [129, 130]. Many physicochemical properties of AuNPs are enhanced due to SPR [130]. Gold nanoparticles exhibit other unique properties placing them at the forefront of biological and clinical research. Gold nanoparticles are easy to synthesise with controllable sizes and shapes and can be surface functionalised with different biomolecules and ligands. AuNPs have high stability in physiological environments, high surface area, excellent biocompatibility and non-cytotoxicity properties [130, 131]. In addition, due to the high surface to volume ratio of AuNPs, they can be

exploited to increase drug loading which reduces the need for high doses and thus the toxicity to normal cells will be reduced [132].

1.5.3 Synthesis of gold nanoparticles

Generally, AuNPs can be obtained using physical or chemical methods. In physical methods such as metal-vapour synthesis [133] and laser ablation [134], bulk gold atoms are used to produce AuNPs with different size distribution. On the other hand, the most common chemical approach used to synthesise AuNPs is the reduction method which involves the use of gold compounds, usually chloroauric acid, as precursors in the presence of reducing agents [127]. Other chemical approaches such as photochemical methods [135], electrochemical methods [136], seeded-growth methods [137] and template synthesis [138] are also used for preparing AuNPs.

1.5.3.1 Synthesis of gold nanoparticles by chemical reduction methods

The most popular chemical method used to synthesise AuNPs with a relatively narrow size distribution is the reduction of chloroauric acid (HAuCl_4) using citrate as a reducing and stabilising agent in water [139, 140]. This method was first reported by Turkevitch [141]. The diameter of AuNPs can be controlled by changing the concentration of the salt, temperature and rate of addition of reagents. Different particles size ranging between 5 and 250 nm can be achieved by varying the parameters using this synthetic approach [142, 143]. By using this reduction method, the citrate capped AuNPs can be easily exchanged with other desired molecules or moieties [144]. For example, particles prepared by this method can be then easily functionalised by using thiol containing ligands followed by covalent attachment of various molecules to thiol modified AuNPs [145]. Another study reported the synthesis of high stability and uniformity AuNPs using L-Tryptophan as a reducing agent and polyethylene glycol (PEG) as a stabilising agent [146]. Ramezani et al. [147] reported the synthesis of environmental friendly AuNPs by using methanol extracts of *Eucalyptus camaldulensis* and *Pelargonium roseum* plants as a reducing agent [147]. Another study conducted by Ravindra et al. [148] showed the successful preparation of eco-friendly, monodispersed and stable AuNPs by using Serrapeptase as reducer and stabiliser [148]. In addition, different reducers stronger than citrate have been utilised to synthesise AuNPs. For example, the reduction of gold salt using

borohydride in the presence of an alkanethiol capping agent to produce AuNPs with small size 1-3 nm has been reported. This approach is called Brust-Schiffrin method [149, 150]. AuNPs can be synthesised by transferring AuCl_4^- from aqueous solution to toluene layer using tetra-octanyl ammonium bromide as a phase transfer reagent and sodium borohydride as a reducing agent [149]. Also, phosphanes and thiols were used as stabilisers in AuNPs synthesis due to the robust bonds formed between Au and P or S in those capping agents, respectively [127]. Gold nanoparticles can be synthesised in different shapes as well (Figure 1.6). For example, spherical AuNPs have been prepared with size ranging from 1 to 100 nm (Figure 1.6.a) [151]. Hexagon and boot shaped AuNPs were obtained and they exhibit different surface enhanced Raman scattering (SERS) making them promising in bio-labelling, bioassay, diagnosis and therapy applications [142]. Thomas et al. [152] synthesised six and eight faceted of gold nanoboxes [152]. Gold nanorods (AuNRs) (Figure 1.6.c) with longitudinal surface plasmon resonance bands in a wavelength range between 600 and 1100 nm were synthesised by a seed-mediated growth method. In this synthetic method, hydrochloric acid and silver nitrate were utilised as additives to control the shape and size of AuNRs [153]. Gold nanorods have potential applications in cancer imaging and photothermal treatment [153, 154]. Gold nanoshells (AuNSs) (Figure 1.6.d) consist of a core of silica and a shell of gold with spherical shape and diameter ranging between 50 and 150 nm were also synthesised. By adjusting the core diameter and the thickness of the thin layer of gold nanoshells, their optical properties can be controlled [151]. There are many other structures such as nanocages (Figure 1.6.b) [155] and nanoboxes [152].

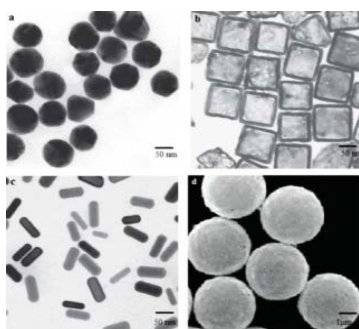


Figure 1.6 TEM images of gold nanostructures: (a) nanospheres [155], (b) nanocages [155], (c) nanorods [155] and (d) inner nanoshell, consisting of a silica core layer and a gold shell layer [156].

1.5.4 Surface functionalisation and bioconjugation of gold nanoparticles

The unique properties, such as facile synthesis and surface functionalisation, optical characteristics and biocompatibility of gold nanoparticles enable their use in a variety of biomedical applications, in particular in clinical diagnostics and therapy. Functionalisation the surface of AuNPs with one or several biomolecules (Figure 1.7) such as oligonucleotides, peptides, antibodies, fluorescent dyes, polymers (i.e., PEGs) and drugs is essential and dependent on the potential application. The conjugation approach of any biomolecule onto the surface of AuNPs depends on several factors such as particle size, shape and surface chemistry, the type of the ligand and functional groups that will be used for functionalisation, the type of biomolecule and the final application of the conjugate [142, 157]. Conjugation of gold nanoparticles with biomolecules can be done either by covalent chemistry or by non-covalent interactions (Figure 1.7) such as specific binding affinity, electrostatic interactions or hydrophobic interactions for biomedical applications [158]. When using a covalent strategy, stable and robust binding between biomolecules and nanoparticles is obtained. Biomolecules, that contain functional groups such as amines or thiols, can be directly conjugated to NPs through these groups and form stable conjugates [159]. However, some biomolecules do not contain reactive groups and should be functionalised prior to the conjugation. Using ligands as linkers or spacers, either by anchoring the ligand to the surface of the NPs first or by binding the ligand to the biomolecules primary, is one of the most common strategies to conjugate the biomolecules to the NPs [157].

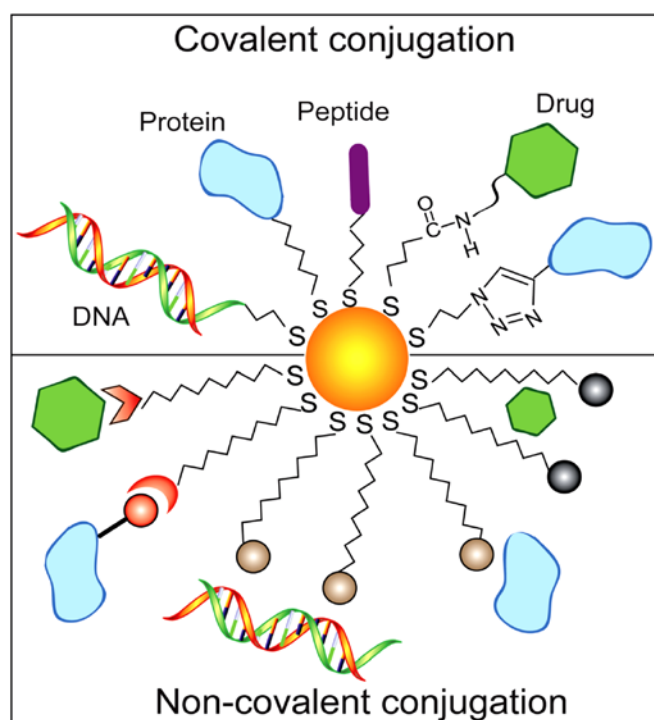


Figure 1.7 Conjugation methods of AuNPs with different biomolecules [158].

Compounds used as linkers anchored to the surface of AuNPs usually have sulfur (-SH), amine (NH_2) or phosphine (PH_3) due to the high affinity of these functional groups to AuNPs. Examples of ligands used as spacers and anchored directly to the surface of AuNPs are given in the following sections.

1.5.4.1 Alkanethiols

Modification the AuNPs surface with alkanethiols, which are the most commonly used ligands as linkers, can facilitate binding with biomolecules and provide a stable linkage [160]. Many studies have used thiol compounds to modify the AuNPs surface. Covalent binding of ligands to gold surface through Au-S bond is one strategy to functionalise the AuNPs surface and increase their stability. In this strategy, the nanoparticles are directly covalently functionalised with thiol molecules enabling attachment of different biomolecules to their surface using standard organic chemistry methods [145, 161]. For example, Brust et al. [149] reported a two-phase method for preparing thiol functionalised AuNPs then transferring the thiolated-AuNPs from an aqueous to an organic phase. The stability was improved due to the high affinity between Au and thiol. AuNPs were produced with small diameters

[149]. Gao et al. [162] reported the surface functionalisation of 17 nm AuNPs with several thiol compounds including glutathione, mercaptopropionic acid (MPA), dihydrolipoic acid and thiol ending polyethylene glycol (PEG-SH), through an Au-S bond. The study investigated the effects of the thiol ligands, buffer pH and salt concentrations on the AuNPs. The study found that the stability of AuNPs functionalised with PEG-SH was the highest compared to other thiol compounds [162]. Gupta's group [163] used 16-mercaptohexadecanoic acid (16-MHDA), which is a bifunctional ligand that acts as a surfactant, to modify the AuNPs surface. Uniform-sized and well-separated AuNPs were obtained after functionalising the surface with 16-MHDA using a cold synthesis approach [163]. Producing gold nanoconjugates with high stability can be achieved by using carboxylate-terminated alkanethiols such as thioctic acid (TA) or 11-mercaptoundecanoic acid (MUA) immobilised onto the surface of AuNPs. Such linkers contains sulfur atoms at one end that can be anchored on gold surface and they contain carboxyl groups in another end providing a reaction site for molecules having amino or alcohol groups to produce the nanoconjugates [164, 165]. For example, Roux et al. [164] used post-functionalisation method to prepare dihydrolipoic acid (DHLA) functionalised AuNPs followed by binding of electroluminescent luminol to carboxyl groups on Au-DHLA through amine coupling reactions (Figure 1.8) [164]. Similarly, Schiffrin's group reported immobilisation of His-tagged proteins onto the surface of thioctic acid modified AuNPs [165].

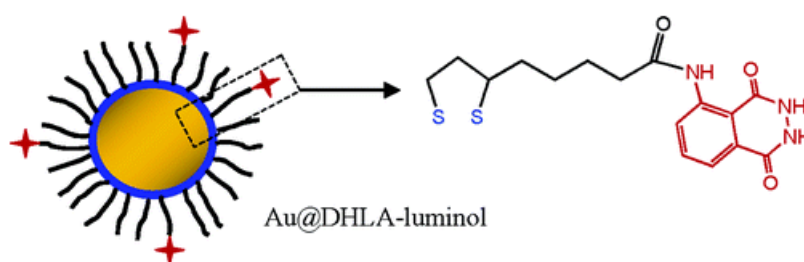


Figure 1.8 Synthesis of Au-DHLA-luminol [164].

1.5.4.2 *In situ* dithiocarbamate formation approach

The surface of AuNPs has been functionalised using an *in situ* dithiocarbamate approach which involves adding molecules containing amino group ends to AuNPs then converting them to dithiocarbamate by adding carbon disulfide [145]. Wei et al. [166] conjugated polyethylene glycol molecules with gold nanorods by dithiocarbamate formation. The prepared conjugates were stable in absence of cetyltrimethylammonium bromide (CTAB) opening up possibilities for biological applications [166]. Likewise, Liu's group [167] reported the conjugation of DNA with AuNPs by *in situ* dithiocarbamate (DTC) formation (Figure 1.9). This method provided more stability and robustness to the conjugates with resistance to ligand displacement. Such conjugates are rising the hopes of using them in diagnostic assays and other applications [167].

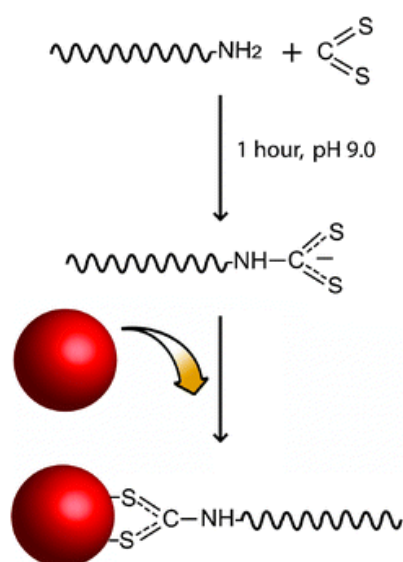


Figure 1.9 Synthesis of AuNPs–DTC–DNA conjugates [167].

Dithiocarbamate ligands bind to gold surface stronger than thiols. Their robustness makes them desirable in some applications. However, in drug delivery applications weaker bonds are needed to help release the drug [145]. Noncovalent interactions such as electrostatics, van der Waals forces and hydrophobic interactions can be applied for attaching molecules to AuNPs with weaker interactions which may be facilitate the drug release mechanism. Moreover, amino groups can be bound to

AuNPs with low binding energy of approximately ~ 6 kcal mol⁻¹ [145, 168]. Therefore, such linkers can facilitate the drug release [169].

1.5.4.3 Amino acids

Improving specificity and efficiency of delivery systems using nanoparticles can be achieved by modifying their surface with amino molecules. For example, Partha et al. [170] showed that DNA was bound effectively to amino acids such as lysine, polylysine and glycine functionalised AuNPs for gene delivery applications without showing cytotoxicity. In addition, they reported the dependency of delivering DNA effectively on the head group structure and its capability to condense DNA molecules [170]. In another example, Lee et al. [171] prepared amine functionalised AuNPs loaded siRNA-PEG conjugates to be used as delivery system to internalise therapeutic siRNA inside the cells. In this method, electrostatic interactions are developed between the positively charged AuNPs and the negatively charged siRNA attached polyethylene glycol (PEG) with cleavable disulfide bonds. The results showed the use of this conjugate against human prostate tumour cells prevented efficiently specific cancer genes [171]. Moreover, Wangoo's group [172] reported the synthesis strategy of monodispersed and stable carboxylated AuNPs using glutamic acid as the reducing and stabilising agent. The electrostatic interactions between negatively charged carboxyl groups of glutamic acid and the positively charged amino groups of the protein facilitate the conjugation of protein with carboxyl-terminated AuNPs (see [Figure 1.10](#)) [172].

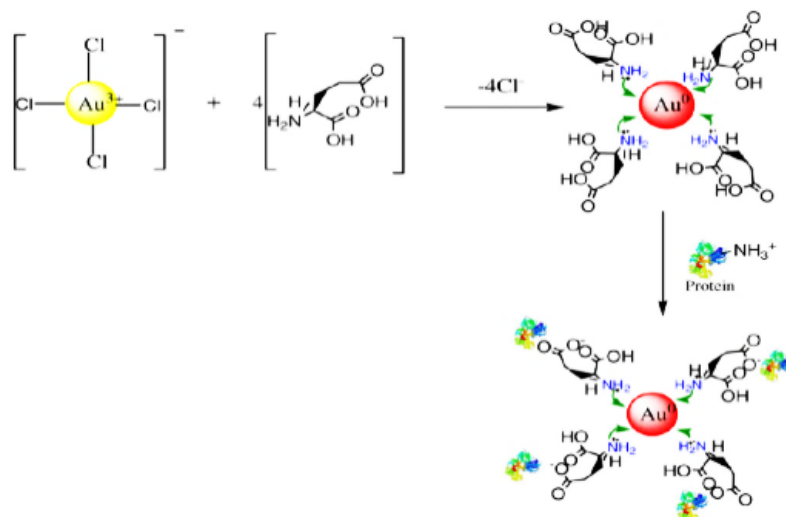


Figure 1.10 Synthesis of gold nanoparticles reduced by glutamic acid bound to protein throughout the surface lysine residues of protein molecules [172].

A brief summary of the most commonly used bio-functional molecules for functionalising the surface of AuNPs is given in the following sections.

1.5.5 Common bio-functional molecules conjugated onto AuNPs surface

1.5.5.1 Polyethylene glycol

Currently, PEGylation is the most common functionalisation technique used to modify the AuNP surface and other nanoparticles in pharmaceutical and biological research due to the ability of PEG to resist fouling in biological systems. PEGylation involves the use of PEG molecules alone or conjugated to other biomolecules such as biotin, peptides, oligonucleotides or drugs to coat the AuNPs or other nanoparticles and facilitate their internalisation to targeted cells [173, 174]. The PEGylated AuNPs can attach to cell membranes and thus, they can be used as drug carriers [142]. PEGylated AuNPs modified with a variety of biomolecules have been prepared. Takae et al. [175] synthesised PEGylated AuNPs functionalised lactose which were highly stable in physiological conditions [175]. Otsuka's group [176] reported the synthesis of PEGylated AuNPs. The HAuCl_4 aqueous solution was reduced by α -acetal- ω -mercapto-PEG. The synthesised PEG-Au was stable in physiological environments,

concentrated buffer solution and in serum solutions. In addition, lactose molecules immobilised on PEG-Au particles aggregated when exposed to *Ricinus communis* agglutinin (RCA120) and the colour changed from red to purple to red again. PEGylated AuNPs derivatives are expected to be used in different technological applications such as bioassays and bio-recognition [176]. Shimmin and co-workers [177] synthesised AuNPs functionalised with thiol-terminated PEG to study the effects of the polymer size and concentration on the size of prepared particles [177]. Despite the extensive use of PEG in coating nanoparticles for pharmaceutical and biological applications, its stability and functionality, which are influenced by its molecular weight, the ligands and the size of the NPs used and the capped functional groups in addition to other factors, still cause significant issues [142]. For example, Zhang's group [178] investigated the effectiveness of thioctic acid anchored PEGylated AuNPs system in the ablation of tumours in mice. They found that the intracellular of functionalised AuNPs is affected by nanoparticles size, PEG molecular weight and the ligand type anchored in PEGylated AuNPs [178]. In addition, potential drawbacks emerged as adverse side effects by the polymer itself or by its derivatives need to be considered. PEG has already shown a tendency to induce clotting and clumping of cells which may lead to embolism. This propensity is an indication of nonspecific interactions between PEG and blood [173]. Controversial observations reporting PEG genotoxicity have been published [179]. Some research groups have reported negative toxicity results for PEG while others reported positive results. For example, Mitchell et al. [180] have reported a negative response when using PEG 6000 in a mouse lymphoma assay, indicating no genotoxicity was induced when using PEG 6000 [180]. However, a positive response was reported for CHO cells exposed to tetraethylene glycol (TEG) at high doses that generated hyper-osmotic conditions where chromosomal damage was induced [179, 181]. PEG may also have some toxic side products from the polymerisation process. In addition, cellular uptake and endosomal escape are strongly hindered when using PEG molecules leading to significant reduction in the drug delivery activity [182]. Thus, it is important to seek approaches that do not rely on the presence of PEG.

1.5.5.2 Peptides

Functionalised AuNPs with peptides have been utilised in targeting cells. Sun's group [183] functionalised AuNPs with the peptide CALNN and its derivative CALNNGRRRRRRRRR (CALNNR8) for targeting intracellular components. The concentration of the peptide and the size of the AuNPs play a significant role in distribution of peptide modified AuNPs. In this study, AuNPs with a diameter of 30 nm showed interesting crossing of the cell membrane via endocytosis and micropinocytosis processes. Also, their affinity to DNA, RNA and the endoplasmic reticulum was high [183]. Likewise, Wang et al. [184] designed a colorimetric indicator of β -amyloid peptide (A β 1-16) functionalised AuNPs conjugated CALNNGK (biotin) G to investigate the interactions between β -amyloid peptide and metallic ions Zn²⁺ and Ca²⁺. It was suggested that A β 1-16 peptide-AuNPs conjugate is a promising optical sensor to be utilised in detecting A β 1-16 polymerisation. This gives an opportunity to develop new biosensors for clinical applications [184]. Bastús and co-workers [185] prepared several peptides conjugated to AuNPs to study their effects on macrophages. They concluded that peptides conjugated gold system could provide greater possibilities to deliver peptide molecules to the immune system making them promising adjuvant molecules for vaccine delivery [185]. In addition, the type of peptide used for conjugation to AuNPs and the type of cells could determine cellular and subcellular targeting of the nanoconjugate system [186]. For example, Kang's group [187] showed functionalisation of PEGylated AuNPs with arginine-glycine-aspartic acid peptide (RGD) and they reported signals from RGD and a lysine-lysine-lysine-arginine-lysine (KKKRRK) sequence (NLS) conjugated to AuNPs localised in the nucleus specifically targeting the nucleus of cancer cells. These results show the localisation of nanoparticles at the nucleus of cancer cells affect the functionality of the targeted cells and these observations could help dramatically improve nanomedicine and nanobiotechnology since they support understanding the interactions between nanomaterials and live organs [187].

1.5.5.3 Oligonucleotides

Functionalisation of nanoparticles, including AuNPs, with oligonucleotides has been reported by many research groups. For example, Pellegrino et al. [188] synthesised DNA conjugated to AuNPs using two approaches. Attaching specific numbers of

single-stranded DNA to phosphine-stabilised colloidal AuNPs through thiol-Au bonds is one way of synthesising this conjugate. The other way is saturation of gold surface using single stranded DNA molecules either particularly through thiol-Au bonds or by nonspecific adsorption [188]. Javier's group [189] reported the conjugation of aptamer antibody as a targeting agent to oligonucleotide functionalised AuNPs by hybridisation to be used in targeting prostate cancer cells. The results suggested the possibility of using this conjugate system for tracking and imaging of tumour cells [189].

1.5.5.4 Chemotherapeutic agents

Gold nanoparticles have been conjugated to a variety of antitumor drugs, such as cisplatin, doxorubicin or paclitaxel. Tomuleasa et al. [190] have conjugated AuNPs with conventional anticancer drugs for liver cancer treatment. In this method, the AuNPs were stabilised with L-aspartate and cytostatic drugs (doxorubicin, cisplatin and capecitabine) to be used as a complex cancer-targeting drug delivery system. Non-covalent conjugation was applied to conjugate the drugs with AuNPs-L-aspartate nanostructure. The cell viability was decreased significantly after treatment with the conjugate. The results reveal the potential use of this conjugate in the treatment of hepatocellular carcinoma [190]. Different research groups have reported the functionalisation AuNPs with paclitaxel using different approaches. Oh and co-workers [191] introduced a facile drug delivery system comprised of PTX loaded AuNPs electrostatically interacting with chitosan. In this situation, PTX was dispersed in AuNPs solution dissolved in tween 80. Then, chitosan was added to paclitaxel/gold nanoparticle system by inducing the ionic interactions. Afterward, the paclitaxel/gold nanoparticle/chitosan mixture was freeze-dried in the presence of pluronic F127 to form a powder. It was found that 90 % of PTX loaded AuNPs were released in approximately 12 days. The study concluded that the AuNPs composite (PTX loaded AuNPs/chitosan/pluronic F127) can be used as an efficient drug delivery system in cancer treatment [191]. Gibson et al. [192] reported the synthesis of paclitaxel conjugated AuNPs. The mercaptophenol covalently functionalised AuNPs were synthesised using the approach reported by Brust et al. [192]. Paclitaxel was linked to hexaethylene glycol linker at the C₇ position of PTX using carbodiimide-based esterification method. Then, the resulting analogue was attached

to the mercaptophenol-terminated AuNPs (Figure 1.11). The resulting conjugate was well characterised [193].

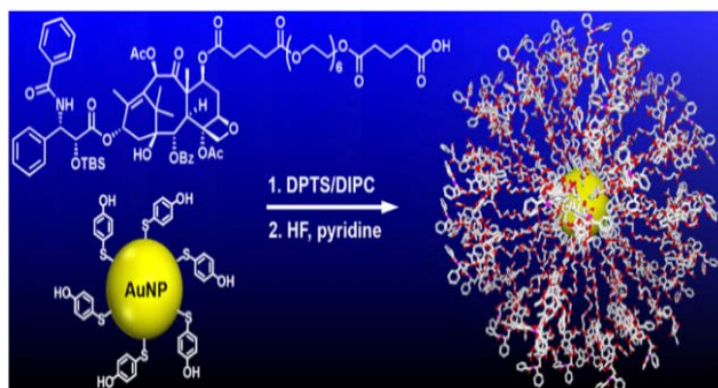


Figure 1.11 Paclitaxel functionalised gold nanoparticles [192].

Heo et al. [194] synthesised a drug delivery system that consists of AuNPs as platform, PTX as anticancer drug, PEG as an antifouling shell, biotin as cancer targeting ligand, rhodamine B as a fluorescent staining and β -cyclodextrin (β -CD) as a drug carrier for both PTX and rhodamine B. It was reported that the formulation was more effective at killing cancer cell lines HeLa human breast cancer cell lines, A549 human lung cancer cells and MG63 human osteosarcoma than the normal cells (NIH3T3) [194].

1.5.6 Biomedical applications of gold nanoparticles

The unique properties of AuNPs have been exploited in biomedical applications. For example, AuNPs have contributed significantly to understanding the behaviour of nanomaterials in both *in vitro* and *in vivo* and they have improved the diagnostic strategies [195, 196]. Functionalised AuNPs can be used in different biomedical applications such as drug and gene delivery [131, 197], diagnostics [198], biosensing [199], single molecule tracking [200], therapy [201] and transfection [202]. Also, since AuNPs have a high atomic number, they can absorb X-ray radiation and

enhance the contrast compared to other agents. Therefore, AuNPs are promising for detection of diseases by imaging [203].

The biomedical applications of AuNPs can be classified into imaging, diagnostic and therapeutic applications. Imaging applications are X-ray imaging, fluorescence, SERS, optical imaging and photoacoustics. Diagnostic applications are nucleic acid detection and protein detection whereas therapeutic applications of AuNPs are drug delivery, nucleic acid delivery, photothermal therapy and radiotherapy (see [Figure 1.12](#)). Some of these applications are discussed in the next sections.

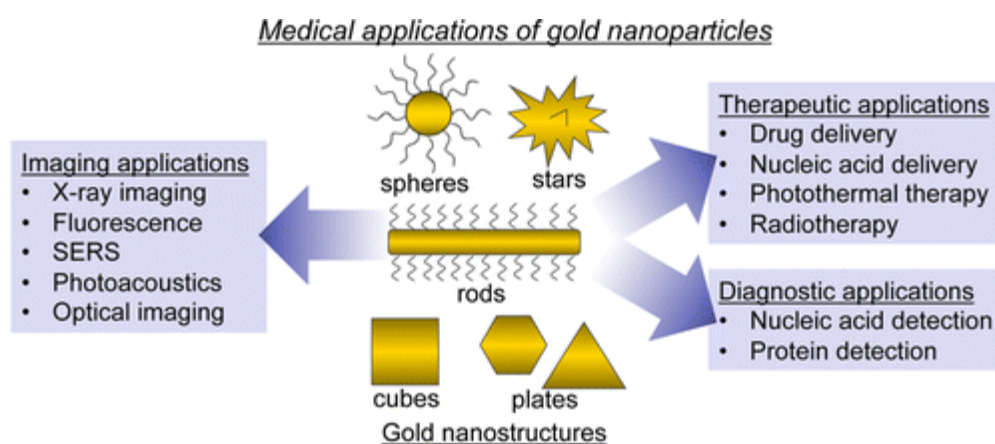


Figure 1.12 Biomedical applications of AuNPs. Image adapted from [198].

1.5.6.1 Gold nanoparticles in diagnostic applications

Development of innovative methods for the early detection of diseases is significant to increase survival rates and reduce effects of disease. AuNPs possess high surface area and can be functionalised to detect specific targets. Such properties offer high selectivity for diagnosis compared to conventional methods. A variety of analytes such as gases, ions, protein markers or DNA have been detected using AuNPs. You et al. [204] have developed protein sensors using six non-covalent gold nanoparticle–fluorescent polymer conjugates to detect, identify and quantify protein targets. It was found that in the absence of proteins, the polymer fluorescence was quenched by AuNPs. However, in the presence of proteins, the interactions between the polymer and the NPs were disrupted and distinctive fluorescence response arrays were produced. These results indicate the potential use of such sensors in medical

diagnostics [204]. Gold nanoparticles based electrochemical biosensors were extensively investigated for use in detection of specific biomolecules due to their ability to provide stable immobilised biomolecules, increase the conductivity of the electrodes and enable transfer of the electrons, consequently enhancing overall selectivity and sensitivity [205, 206]. For example, Qin et al. [207] detected choline by developing a highly sensitive, rapid and significantly effective biosensor comprised of choline oxidase, multi-wall carbon nanotubes, AuNPs and poly-diallyl dimethyl ammonium chloride (PDDA). Features such as high stability and selectivity and an excellent reproducibility of the developed choline based biosensor were observed [142, 207].

1.5.6.2 Gold nanoparticles for X-ray based imaging

AuNPs have high atomic number and electron density allowing them to absorb X-ray irradiation more efficiently than conventional iodine-based contrast agents at higher X-ray tube voltages, i.e. 90 kV, 120 and 140 kV, that are used in medical imaging [208]. AuNPs allow for prolonged imaging for tracking of cells and targeting specific ligands or cell types due to their ability to offer longer circulation times than conventional agents [209]. In addition to these characteristics, AuNPs show good biocompatibility meaning they can be used as contrast agents for X-ray based imaging methods such as computed tomography (CT) [210]. For example, Cai et al. [211] have prepared PEG modified AuNP as a blood pool contrast agent for X-ray computed tomography imaging in mice. The PEG-coated AuNPs were injected to mice and imaged with CT. Significant improvement in visualisation was observed in the tumour blood vessels structures of the mice. These results indicate the potential use of AuNPs as blood-pool agents for X-ray CT imaging [211].

1.5.6.3 Gold nanoparticles in therapeutic area for drug and gene delivery

The use of AuNPs as carriers in drug delivery systems is one of the most significant biomedical applications. Gu's group [212] conjugated AuNPs with NH₂-PEG-NH₂ through the amidation between NH₂ one side terminal groups on PEG and carboxyl terminal groups on a self-assembled monolayer of 3-mercaptopropionic acid (MPA) on the surface of AuNPs and NH₂ another side terminal group of PEG attached fluorescein isothiocyanate (FITC) (AuNP-MPA-PEG-FITC conjugate) (Figure 1.13).

PEG is used to enhance the stability of AuNPs, inhibit aggregation of the particles and adsorb protein which leads to improve the internalisation of the conjugate in the targeted cells. The biocompatibility and intracellular uptake of the prepared conjugate were evaluated *in vitro* in HeLa cell lines. The results showed the conjugate entered nucleus of the cells with no obvious cytotoxicity. Therefore, this nanomedicine conjugate is promising for use in nuclear drug delivery [212].

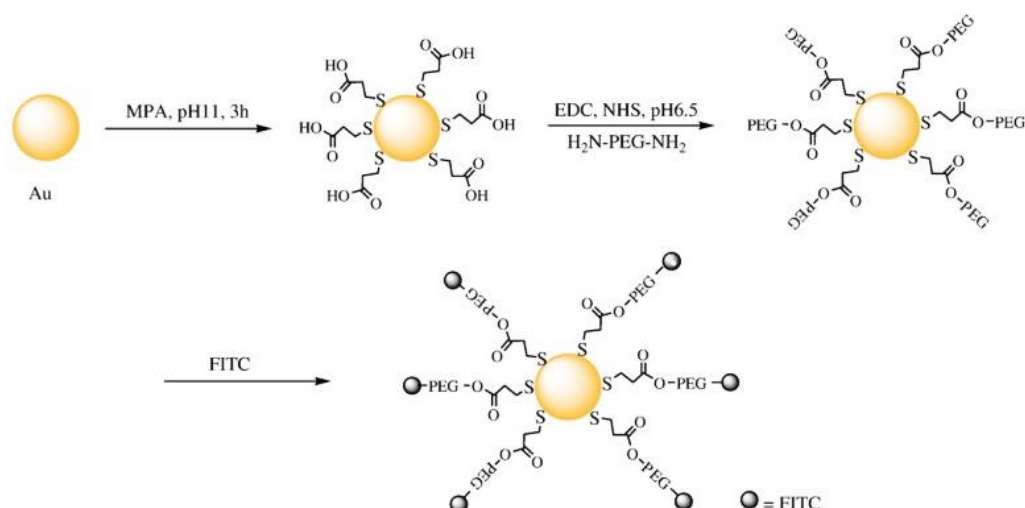


Figure 1.13 Schematic diagram of synthesis steps of AuNP-MPA-PEG-FITC [212].

Encapsulation of liposomes with AuNPs was investigated by Chithrani et al. [213]. They found a significant fraction of AuNPs about 1.4 nm in diameter were internalised and taken up by cells due to the liposome's efficiency of delivering small particles. Such conjugates are promising as active carriers in biomolecules delivery for targeted specific cells (Figure 1.14) [213].

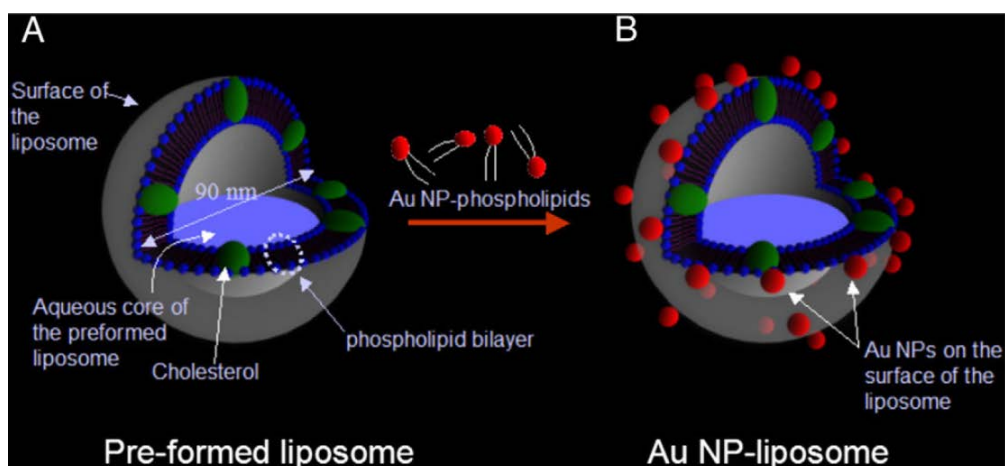


Figure 1.14 Schematic representation of synthesis of AuNP-liposomes. (A) 90 nm-liposomes (B) AuNP-phospholipids are then exchanged into the lipid bilayer of the preformed liposomes [213].

Mukhopadhyay et al. [214] synthesised a drug delivery system comprised of AuNPs as carriers, cetuximab as a targeting agent and gemcitabine as an anticancer drug to target three pancreatic cancer cell lines (PANC-1, AsPC-1 and MIA Paca2) *in vitro*. It was found that the nanoconjugate system (AuNPs bound to cetuximab and gemcitabine) was more affective at killing cancerous cells than the agents alone [214]. Kawano and co-workers [215] investigated PEGylated AuNPs for gene delivery. The cationic AuNPs were functionalised with PEG molecules loaded DNA. The transfection efficiency of the synthesised system by utilising a plasmid DNA mediated via electroporation was assessed. The results showed that when using DNA-PEGylated AuNPs conjugate, gene expression was about 100-fold greater than that with naked DNA after intravenous injection. In addition, stable transfection in circulation system and release of DNA at the targeted site were observed (Figure 1.15) [142, 215].

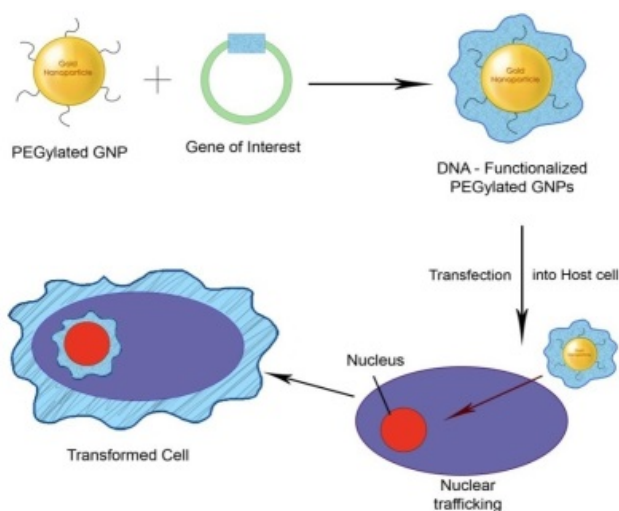


Figure 1.15 PEGylated gold nanoparticles for gene delivery [142].

Li's group [216] reported the synthesis of a cationic lipid, didodecyldimethylammonium bromide (DDAB), modified AuNPs for gene delivery. It was found that more DNA moieties bound to the lipoplexes after adding DDAB coated AuNP (Figure 1.16). Cellular uptake of DNA molecules was enhanced after transfection using this conjugate. A 48-fold enhancement of gene expression and an increase in green fluorescent protein was observed after transfection. Also, DDAB coated AuNPs reduced the liposomes cytotoxicity to cells. The results suggest the potential use of DDAB coated AuNPs for gene delivery [216].

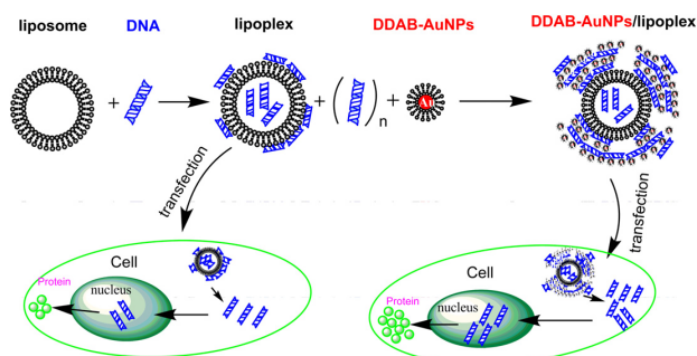


Figure 1.16 Schematic diagram of preparing of DDAB-AuNPs/lipoplex complexes and the mechanism involved in the transfection enhancement [216].

Zhou's group [217] reported the covalent conjugation of low molecular weight chitosan with AuNPs (Chito6-AuNPs) to be utilised as vectors for DNA vaccine delivery. The results showed significant improvement of serum antibody response up

to 10 times more than naked DNA vaccine after being delivered via intramuscular immunisation in BALB/c mice using Chito6-AuNPs conjugates [217].

Grace et al. [218] reported the detection of aminoglycosidic antibiotics such as streptomycin, gentamycin and neomycin using AuNPs as probes. Antibacterial activities of drugs loaded AuNPs against different probes of Gram positive and Gram negative organisms such as *Staphylococcus aureus*, *Micrococcus luteus*, *E.Coli* and *Pseudomonas aeruginosa* were assessed and the results showed the possibility of using AuNPs as carriers for drug delivery systems [218].

1.5.7 Toxicity of gold nanoparticles

Toxicity of various nanomaterials, including AuNPs, has been evaluated in many reviews [219-222] and contradicting studies regarding to the safety and the toxicity of AuNPs have been published. The toxicity of AuNPs is affected by five factors which are surface chemistry, size, shape, coating ligands and biological target assessed and various levels of toxicity have reported [223]. Many *in vitro* investigations showed that AuNPs are nontoxic for many types of cells. For example, Wyatt et al. [224] investigated the acute toxicity in human leukemia cells using AuNPs with different diameters (4, 12 and 18 nm) and different capping ligands (citrate, glucose, biotin, cysteine and cetyltrimethylammonium bromide (CTAB)). It was found that AuNPs are inherently nontoxic although some precursors of nanoparticles might cause toxicity [224]. Marche's group [225] studied the toxicity of citrate capped AuNPs in dendritic cells (DC). They found that the citrate capped AuNPs were non-cytotoxic and there was no activation of dendritic cells and no change of phenotype after introducing the nanoparticles [225]. On the other hand, some studies have shown that AuNPs can have cytotoxicity. For example, Rotello et al. [226] reported the toxicity of 2 nm positively and negatively charged surfaces of AuNPs using a fibroblast-like cell line and red blood cells. It was found that the cationic AuNPs were toxic to both cell lines at some concentrations. However, the anionic AuNPs were nontoxic at the same concentrations and using the same cell lines [226]. Pan's group [227] reported the effect of 1.4 nm AuNPs capped with triphenylphosphine monosulfonate (TPPMS). It was found that these AuNPs caused necrosis, an oxidative stress and mitochondrial damage in all cell lines examined. However, when using 15 nm

AuNPs, no cell damage was found [227]. Pan's group suggested that the AuNPs with small sizes may induce more cytotoxicity. Sastry's group [228] studied cytotoxic and immunogenic effects of 3.5 nm AuNPs on RAW264.7 macrophage cells and found that AuNPs were nontoxic [228]. According to these studies, there is a need to do more investigations on AuNPs with small diameters ranging between 1 and 10 nm using the same cell lines and the same preparation approaches [229].

Likewise, *in vivo* studies on cytotoxicity effect of AuNPs showed controversial results [230]. Chen et al. [231] injected naked AuNPs with different diameters ranging from 3 to 100 nm into BALB/C mice. It was found that, particles with small sizes (3 and 5 nm) and bigger sizes (50 and 100 nm) were nontoxic, However, AuNPs with sizes ranging from 8 to 37 nm showed harmful effects. It was reported that the toxicity of intermediate sized AuNPs caused damage mainly in liver, lungs and spleen [231]. Bar-llan et al. [232] assessed the toxicity of gold and silver nanoparticles with different sizes (diameters 3, 10, 50 and 100 nm) using zebrafish embryo screening platform. The results showed that AuNPs did not induce toxicity in zebrafish. However, when introducing equal size silver particles to zebrafish, the induced toxicity was high with 100 % mortality [232].

1.6 Cellular uptake of nanoparticles

Anticancer drugs tend to distribute intracellularly in both normal cells, where the interactions with the drug target are prevented, and cancer cells, where the interactions with drug target are promoted [233]. Successful design of nanoparticles as drug carriers requires understanding the internalisation mechanism and the intracellular transport of the drug and the nanoparticles. Small uncharged moieties such as O₂, CO₂ and H₂O can diffuse easily through cells membranes [234]. Ions and some small proteins and molecules such as glucose and amino acids are internalised throughout the cell membrane by specialised transporter proteins [235] while larger moieties such as nanoparticles are transported through an endocytosis mechanism [97, 236]. Endocytosis is a process that involves transport of the larger particles and vesicles, that are formed via infolding the plasma membrane, into cells [97, 235, 237] while exocytosis transports vesicles and other molecules from inside cells through the cell membrane to outside the cells [235, 237]. Endocytosis is usually divided into two

sorts called, phagocytosis and pinocytosis. Phagocytosis includes the uptake of large moieties up to a size of 20 μm by professional phagocytes such as, macrophages, neutrophils, monocytes and dendritic cells [97]. On the other hand, pinocytosis involves the uptake of fluids and solutes and this process occurs in all cell sorts. Pinocytosis can be categorised as clathrin dependent endocytosis and clathrin-independent endocytosis. The clathrin-independent endocytosis is further divided into caveolae-mediated endocytosis, clathrin- and caveolae-independent endocytosis and micropinocytosis. The macropinocytosis pathway is the internalisation of fluids and particles into cells non-specifically. Macropinocytosis is an actin reliant process. In this process, protrusions are formed at the exterior of cell membrane followed by fusion of these protrusions through the cell membrane by taking up bigger sizes of fragments [238]. Brandenberger et al. [239] reported the cellular uptake of 15 nm citrate-stabilised AuNPs by micropinocytosis and clathrin- and caveolin-mediated endocytosis pathways. This was attributed to the possible interactions with proteins or lipids and the agglomeration of the particles [239]. In addition, clathrin- and caveolae-independent pathways are classified as Arf6-dependent, flotillin-dependent, Cdc42-dependent and RhoA-dependent endocytosis [97, 240, 241]. Nanoparticles internalised and penetrate in cancer cells through pinocytosis [97].

1.6.1 Intracellular pathway

Rapidly formed vesicles will internalise inside the cell and fuse from Golgi complex to produce initial endosomes [235, 242]. The early endosomes (EE) develop to late endosomes (LE) and consequently these late endosomes fuse with lysosomes after 10 to 40 minutes of formation. This transformation process involves several changes such as a replacement of membrane components, a transfer to perinuclear site and a decrease in pH [243]. Then, the degraded contents of LEs in the lysosomes, which are the end point for many macromolecules and lipids, [243] can be delivered to specific sites or specific organs, removed from the cell by exocytosis or they can be released in cytosol. However, the possibility of nanoparticles conjugated drugs escaping from lysosomes and delivering drug to cytosol remains a big challenge [244]. For example, Gilleron's group [245] conjugated lipid nanoparticles (LNPs) with siRNAs for delivery targeting and investigated the cellular uptake and the conjugate pathways using different cell lines *in vitro* and in mouse liver using quantitative fluorescence

imaging and electron microscopy. The study concluded that only 1-2 % of siRNAs escaped from endosomes into the cytosol [245].

1.6.2 Cellular uptake of gold nanoparticles

Current research is focused on the interactions between AuNPs and mammalian cells, strategies of cellular uptake, the fate of AuNPs inside the cell and their removal from the cells then from the body [246]. The cellular uptake and the fate of AuNPs are highly affected by different factors including the particle size, shape and the surface functionalisation [246]. As an example of the effectiveness of particle size on cellular uptake of AuNPs, Chithrani and co-workers [247] have studied the cellular uptake of citrate AuNPs with average sizes of 14, 30, 50, 74 and 100 nm using HeLa cell lines. It was found that 50 nm AuNPs were the particles taken up by the cells the most [247]. It was expected that the penetration of the negatively charged citrate AuNPs in the negatively charged cells will be limited compared to the positively charged NPs. However, these findings can be understood by considering that after coating the cell-incubated citrate AuNPs with serum proteins from Dulbecco's modified Eagle's medium (DMEM) the charge effect was reduced. Moreover, the cell surface has many receptors for serum proteins which facilitate the uptake of AuNPs. It was concluded that the AuNPs internalised into the cells by a receptor-mediated endocytosis mechanism ([Figure 1.17](#)) [246, 247].

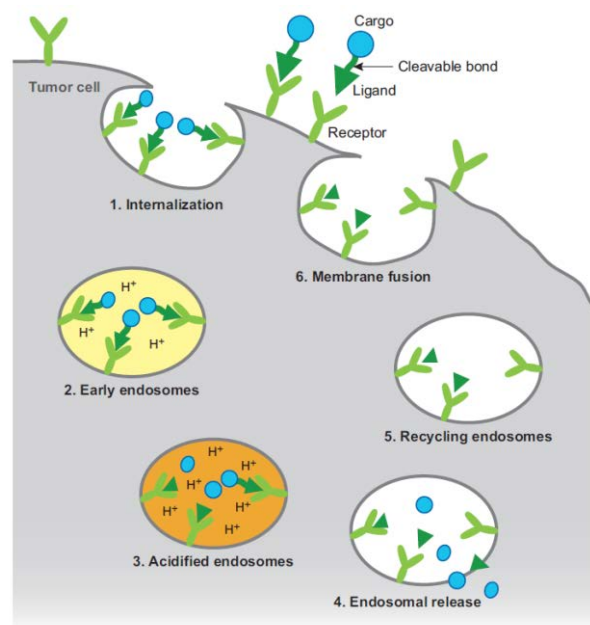


Figure 1.17 Internalisation of nanoconjugate into the cells by receptor-mediated endocytosis mechanism [72].

Trono's group [248] reported the pancreas cancer cell uptake of 5, 10, 20, 30, 40 and 50 nm AuNPs. Atomic absorption spectrometry (AAS) showed that the 20 nm particles were the particles preferentially taken up by pancreas cancer cells [248]. Conflicting published data on size-dependent cellular uptake can be attributed to several potential reasons include formation of clustered particles prior to interaction with cells or during adsorption on the cell membrane and various surface functionalisation of AuNPs [246].

The effects of AuNPs shape on intracellular uptake have also been investigated in many publications. For example, Schaeublin et al. [249] reported the differences in intracellular uptake of gold nanospheres (AuNSs) and gold nanorods (AuNRs) into a human keratinocyte cell line (HaCaT). Overall, AuNSs were more effectively taken up by the cells compared to AuNRs. Data from transmission electron microscopy (TEM) showed that AuNRs appeared as a single particle while AuNSs appeared as aggregated particles. It was concluded that the shape of AuNPs plays an important role in intracellular uptake and cellular response to introducing particles [246, 249]. Hutter et al. [250] investigated the intracellular uptake of nanospheres (AuNSs), nanorods (AuNRs) and nanosea-urchins gold coated with PEG or CTAB by

phagocytic microglia cells and by non-phagocytic neurons. The results showed that AuNRs were preferentially internalised by neurons while nanosea-urchins were most taken up by the microglia cells compared to other morphologies [250]. Recently Hinde et al. [251] investigated the intracellular uptake and translocation of differently shaped polymeric nanoparticles ranging from 5–100 nm in diameter and 20–500 nm in length. The nanoparticle geometries were micelles, vesicles, rods and worms with the same surface chemistries and loaded with equal amounts of doxorubicin. It was found that these polymeric nanoparticles with different shapes but the same surface chemistries transferred across the cellular barriers at different rates. The rods and worms shaped like polymeric nanoparticles entered the nucleus by passive diffusion and were able to deliver more doxorubicin into the nucleus than spherical nanoparticles as higher toxicity was induced when using the rods and worms shaped like drug carriers. It was concluded that delivering the drug, doxorubicin, inside the nucleus can be achieved with using suitable shapes [251]. Bio-distribution of AuNPs was first studied in the 1960s –1980s on rabbits [252] and rats [253]. After parenteral administration, it was realised that gold colloids were found in liver cells, excreted through bile and removed from the creature with faeces [246]. Furthermore, Sadauskas's group [254] studied the fate of AuNPs in the mice after intravenously injecting 2 and 40 nm particles. Results collected using electron microscopy showed that AuNPs accumulated in the macrophages of the liver (90 %) and spleen (10 %). They concluded that AuNPs internalised the cell by endocytosis, taken up mainly by Kupffer cells in the liver and lesser by macrophages in other sites [254]. In a following study, Sadauskas et al. [255] described the fate of 40 nm AuNPs injected intravenously in the mice. Most of these AuNPs localised in lysosomes of Kupffer cells one day after the injection, however, after 6 months only 20 % of the cells contained AuNPs [255]. Furthermore, Chithrani et al. [256] reported the exocytosis and removal of transferrin-coated AuNPs from cells. They found that 14 nm AuNPs were removed from the cells twice as fast as the 74 nm particles [256].

1.6.3 Intracellular tracking of fluorescently labelled gold nanoparticles using confocal laser scanning microscopy

Combining fluorescent markers with a molecule by physical or chemical interactions is known as fluorescent marker technology. Different substances such as amino acids,

environmental pollutants, drugs and molecules in-and-out side of cells and nucleotides can be monitored by using fluorescent probes. Moreover, diagnosis of diseases and detecting chemical processes in living creatures can be performed using fluorescent probes. Molecules that are labelled fluorescently possess pioneering features including easy and fast detection of certain targeted molecules, repetitive preparation techniques with non-radioactive and low doses providing high sensitivity and selectivity [257]. Fluorescent probes are used in medical and biological applications mainly to detect biomolecules. For example, they can be used to detect and identify RNA and DNA structures and to recognise the functional and active groups in proteins. In addition, analysing hormones, viral antigens, proteins and DNA hybridisations can be achieved using fluoroimmunoassay methods [257]. For biological labelling, either fluorescent dyes such as rhodamines, fluoresceins, naphthalimides and fluorenes are covalently attached to the molecule to be labelled through a functional group or through penetration of a fluorescent dye such as thiazole orange (TO), oxazole yellow (YO) and their dimmers (TOTO and YOYO) of cyanine dyes inside target species such as DNA structure by affinity and physical interactions [257]. On the other hand, conjugation of fluorescent probes with different molecules including ligand functionalised nanoparticles surfaces is an important application to track, image and investigate the nanoparticle fate inside the cells which helps to understand the interactions between those particles and cells thus improving their effectiveness for diagnosing and treating diseases. Attachment of dyes to functionalised AuNPs could facilitate tracking the gold particles in cells [174]. Cellular uptake of nanoparticles and efficacy of drug delivery can be detected using fluorescent conjugates. Imaging and quantification of AuNPs inside fixed or living cells can be accomplished using different approaches [258]. Moreover, different factors affect cell viability and internalisation of nanoparticles into human cells. These factors include metal type (such as inorganic metals, noble metals, metal oxide or semiconductor nanoparticles), particle shapes (such as spheres, rods, shells or diamonds), surface charge, surface structure and chemistry and the particle size [256, 258-260]. AuNPs can be detected by fluorescence either by attachment of a fluorescent probe to the AuNPs or through a fluorescent gold core [258, 261]. Several factors should be considered when using fluorescent molecules capped gold core including the distance between the fluorescent probe and the gold core, the diameter of AuNPs, transmission of fluorescent label energy which may prevent or enhance

the emissions of photons. In addition, more evidence (such as using other investigation techniques) should be provided when recording fluorescent signals as an indication of particle localisation to prove that the nanoconjugate is intact because the linkers or ligands can be detached from the nanoparticle surface during or even after cellular uptake by ligand exchange process or via proteolysis [258, 261-263]. Fu et al. [264] attached coumarin dye to the surface of AuNPs through a PEG-thiol ligand. It was found that the prepared conjugate was dramatically fluorescent. This can be attributed to the distance between the gold core and coumarin dye through using PEG-thiol spacer being large enough to avoid the fluorescence quenching effect of AuNPs [264, 265]. Moreover, these nanoparticles were nontoxic to MDA-MB-231 breast cancer cells according to cytotoxicity assay and the functionalised AuNPs were internalised by the tumour cells after one hour of incubation by non-specific endocytosis and they localised in the cytosol and perinuclear area [264].

Confocal laser scanning microscopy (CLSM) and other forms of microscopy are being used for fluorescence measurements [261, 266]. CLSM gives more information on a particle's location due to its ability to collect images of thin sections [261]. Shukla et al. [228] reported the evaluation of absorption of lysine and FITC modified AuNPs in RAW264.7 macrophage cells using different microscopy techniques such as atomic force microscopy (AFM), transmission electron microscopy (TEM) and confocal laser scanning microscopy (CLSM). The interactions between AuNPs and phagocytes were assessed and the biocompatibility of AuNPs was demonstrated by measuring the permeation and retention in the tissue without causing any damage to cell's functionalities. This conjugated system could be used in cancer diagnosis and therapy by combining cancer imaging and cancer-targeted drug delivery [125, 228, 258, 261].

1.7 Antibodies

1.7.1 Structure and function

Antibodies, also known as immunoglobulins (Igs), are glycoproteins with Y-shape, and nanosize generated by plasma cells and present in vertebrates. The immune system utilises plasma cells in recognition and neutralisation of pathogens such as

bacteria and viruses [267]. Figures 1.18 and 1.19 illustrate an antibody structure. The simple structure of immunoglobulin G molecule comprised of Y like-shape which has two identical heavy (H) and two identical light (L) chains bound by noncovalent interactions and disulfide bridges. The light chains are disulfide which is composed of a variable domain (VL) and constant domain (CL), connected to the heavy chains in C_L and C_H^1 sites, respectively while the heavy chains are disulfide which has a variable domain (VH) and three or four constant domains depending on the isotype, connected to each other in a hinge site. An antibody will have one type of the subunit of light chain (either lambda (λ) or kappa (κ) type) and one type of heavy chain assigned as γ , μ , α , ϵ or δ . γ and α chains divided into four domains (VH1, CH1, CH2 and CH3) and μ and ϵ chains divided into five domains. The type of heavy chain determines the type of immunoglobulin produced. Therefore, five different classes of antibodies are determined from their heavy chain and known as IgG, IgM, IgA, IgE or IgD. The IgG, IgE and IgD classes composed of the basic Ig monomeric structure that contains two light and two heavy chains. The IgA class can be found as a singlet, doublet or triplet of this basic Ig monomeric structure while IgM exists as pentameric structure. There are two identical domains used to identify an antigen (Fab fragment) and two identical domains with effector functions (Fc fragment) [268-270]. Antibodies are linked to antigens through their variable part and secreted by B lymphocytes of leukocytes with cooperation with other immune cells after activation occurred by antigens [268-272].

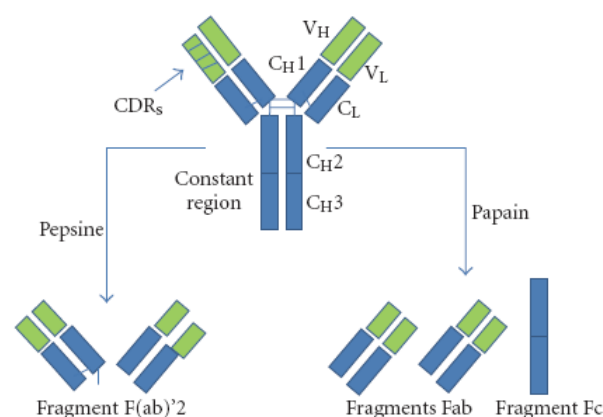


Figure 1.18 Ig molecule's structure having two heavy and two light chains bound by disulfide bridges [267].

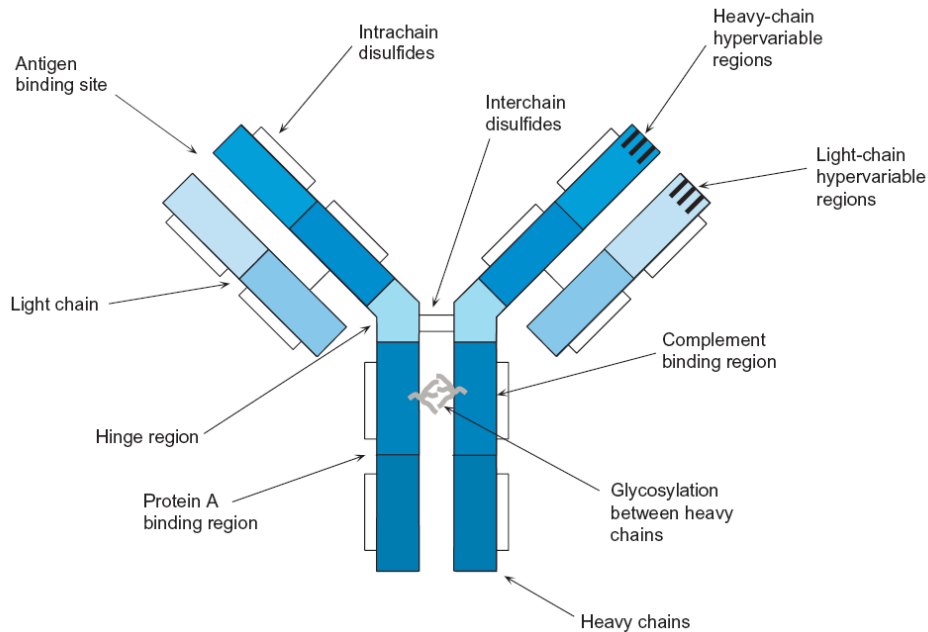


Figure 1.19 Illustration of structure of an immunoglobulin G (IgG) antibody molecule. Adapted from [270].

Antibodies have significant roles including their ability to neutralise and block pathogens and toxins, open the pores in the membrane of the pathogens or targeted cells by activating proteolytic cascades via IgM and IgG, opsonise and phagocytose pathogens via using antibodies, IgG, able to facilitate phagocytosis of pathogens by forming bonds with receptors of macrophages and dendritic cells, protect mucosal, and respond to parasites and allergies. Antibodies with the help of eosinophils contribute to removal of parasites [267]. In addition, antibodies can bind to different species such as oxins, drugs, fluorochromes or nanoparticles and they can be utilised in diagnostic and therapy of diseases [267]. The use of antibodies for human therapy is growing rapidly. So far, many antibodies are approved by the US Food and Drug Administration (FDA) and/or the European Medicines Agency (EMA) for tumour therapy and many are in phase I/II and III clinical trials (see [Table 1.2](#)) [273]. Antibodies can bind with over expressed antigens on the outer surface of all tumour cells and kill them [273].

1.7.2 Monoclonal antibodies (mAbs) in therapeutic applications

Engineering and purification of a laboratory-made antibodies produced by a single clone of cells to link specifically to a specific antigen are identified as monoclonal antibodies (mAbs) [274]. After approval of Rituximab, which is a humanized anti-CD20 monoclonal antibody, by the US Food and Drug Administration (FDA) as the first antibody for anticancer therapy, monoclonal antibodies (mAbs) have been used in hematology and oncology [268]. The disadvantages of mAbs in comparison to conventional chemotherapeutic agents include the fact that mAbs' ability to penetrate through tissues is limited, their molecular weights are relatively high and their distribution kinetics are slow. On the other hand, mAbs can be specifically directed to targeted specific antigens at tumour cells. Thus, the side effects can be reduced without harming healthy cells [275, 276]. Applications based on monoclonal antibodies are the fastest growing area of research in the pharmaceutical sector. Genetic engineering and immunological techniques engineering have been developed with promising potential to be used in different treatments. Several monoclonal antibodies have already been used as therapeutic agents by patients. In addition, various antibodies are still under clinical trials (Table 1.2) [268]. Monoclonal antibodies have shown significant achievement for both hematologic cancers and solid tumours in the last 20 years [275].

Table 1.2 Some monoclonal antibodies approved by FDA and/or EMEA for human therapy [277-280].

Product	Applications	Approval
Ramucirumab	Metastatic colorectal cancer	2015
Nivolumab	Squamous and non-squamous non-small cell lung cancer	2015
Pembrolizumab	Metastatic non-small cell lung cancer	2015
Daratumumab	Multiple myeloma	2015
Necitumumab	Squamous non-small cell lung cancer	2015
Elotuzumab	Multiple myeloma	2015
Cetuximab	Colon, head and neck cancers	2012
Inotuzumab ozogamicin	Acute lymphoblastic leukemia	In clinical phase III
Oportuzumab monatox	Bladder cancer	In clinical phase III
Margetuximab	Breast cancer	In clinical phase III
MM-302	Breast cancer	In clinical phase III

1.7.3 Antibodies targeting tumour antigens

The effectiveness of using mAb in cancer therapy depends on the nature of target antigen. Targeting tumour antigens by an appropriate antibody needs a complete analysis of tumour expression and normal tissue expression. The antigen should be plentiful and available constantly on the surface of tumours, it should be reachable, should be expressed homogeneously and a thorough understanding of the role of the antigen in tumour proliferation is important as well. In addition, minimum secretion of antigen is needed as secreted antigens may attach the desired antibody in the circulation leading to blocking the antibody from binding to the tumour surface [281]. It is important that the antigen and mAb conjugate penetrates slowly if the mechanism of action is the conjugation between mAb and receptors on the surface of tumour cells to activate or stop signalling or to activate antibody-dependent cell-mediated cytotoxicity (ADCC) or complement-dependent cytotoxicity (CDC). Thereby, the Fab region will be much more available to conjugate the mAb with surface receptors and to maximise Fc region to immune effector cells and complement proteins [275]. Better internalisation is preferred for antibodies or proteins that deliver toxins into the tumour cells and antibodies' action based on the downregulation of cell surface receptors [281].

1.7.4 Antibody conjugation

Immunoglobulins are significant for various applications in biological and clinical fields for diagnosis and treatment of diseases [270]. Antibodies conjugates can be used in targeted therapy for cancer and other diseases. Developing antibody conjugates for cancer treatment is currently one of the most common approaches used to investigate new drugs. Successful development of defined monoclonal antibody conjugates leads to specific delivery of a drug to diseased cells without harming normal cells [270]. Moreover, antibodies can be used in immunoassay or detection systems by conjugation and modification methods. For example, labelling antibody molecules with an enzyme, a fluorescent compound or biotin creates a detectable system can be then quantified or imaged [273]. Du and co-workers [282] developed a homogenous immunoassay using goat anti-human IgG antibody functionalised AuNPs using a light scattering method. This bioassay can be used in detecting

samples of human IgG in serum. This study suggested the promising possibility of using the bioassay in molecular biology and clinical diagnosis applications [282]. A system comprised of antibody conjugated nanoparticles can be applied for diagnosis and treatment. The key use of antibody conjugated nanoparticles in therapy is for designing a targeted drug delivery for tissue repair. While, the use of antibody conjugated nanoparticles in diagnosis has been reported for *in vivo* and *in vitro* applications, contrast agents for magnetic resonance imaging (MRI), enzyme immobilisation, immunoassays and cell sorting [267]. Different antibodies are commercially available. Some of them are bound to drugs (Mylortag®) and others to radioisotopes (i.e., ProstaScint®) and they are used in acute myeloid leukaemia and prostate cancer therapies, respectively. However, so far, antibodies conjugated to nanoparticles for therapeutic applications are still unavailable commercially although the main purposes of conjugating nanoparticles with antibodies are exploiting the fascinating properties of nanoparticles and combining them with the specificity and the selectivity abilities of antibodies of recognising antigens and promoting cells internalisation thus enhancing cells uptake and stability [267, 268].

1.7.5 Conjugation of antibodies to nanoparticles

Antibodies can be conjugated to nanoparticles through absorbance of the antibodies on nanoparticles via electrostatic interactions, covalent connection between the antibody and the surface of nanoparticles or through adapter ligands. When using adapter molecules in the conjugation process, streptavidin and biotin are involved in production of the complex [267]. The main advantage of using covalent attachment compared to physical adsorption is the binding is strong which can prevent displacement of the antibody in blood [267]. Unlike electrostatic coupling, covalent coupling provides more scope for designing novel conjugate systems based on NPs [283]. Ideal conjugation of antibody to nanoparticles can be obtained if the covalent linkage of the antibody occurred throughout the Fc (fragment: crystallisable) region whereas the Fab (fragment: antigen binding) region is positioned towards the medium to keep the antibody functional. Furthermore, to increase the chance of the antibody finding and binding to the desired antigen, the use of a spacer is suggested. Thus, such covalent linkage may improve the stability of antibody and control the accessible protein binding sites [267]. Varshney and co-workers [284] conjugated

biotin-labelled polyclonal goat anti-Escherichia coli antibodies to streptavidin-coated magnetic nanoparticles and then the conjugate was used in separation and quantification of Escherichia coli O157:H7 in ground beef samples [284]. Wartlick and co-workers [285] were first attached biotin-binding protein NeutrAvidin onto the surface of gelatine and human serum albumin nanoparticles followed by conjugating HER2 receptor specific antibody trastuzumab (Herceptin) to the surface of those nanoparticles in order to target HER2-overexpressing cells. It was found that the anti HER2 receptor with nanoparticles conjugate bonded and internalised HER2-overexpressing cells indicating the potential use of antibodies functionalised nanoparticles in targeted tumour and drug delivery systems [285]. Gelatin nanoparticles functionalised by anti-CD3 antibody on lymphocytic cells were prepared by Dinauer's group [286]. The NPs were internalised and bound to T-lymphocytic cells which express the TCR-receptor. The results indicate the promising potential of using this conjugate in targeted drug delivery [286]. Another study conducted by Pasqua's group [287] showed the synthesis of anti-E.coli antibody conjugated to carboxylic and alcoholic terminated AuNPs via N-(3-dimethylaminopropyl)-N'-ethylcarbodiimide hydrochloride (EDC) coupling reaction to detect E.coli pathogens. A successful binding of antibody-conjugated AuNPs to E. coli was observed after incubation in PBS at pH 7.4 [287]. Selvaraj and co-workers [288] investigated AuNPs as probes for detecting anticancer drug 5-fluorouracil (5FU) due to quenching ability of AuNPs against the fluorescent 5FU. The attachment of 5FU to AuNPs through complexation reactions was studied. In addition, antibacterial and antifungal activities of 5FU-AuNPs complex were evaluated by testing the microbial efficiency of the complex. The study concluded that AuNPs are excellent candidates as vehicles in drug delivery system [288].

1.7.5.1 Examples of antibodies conjugated nanoparticles applied in targeted drug delivery

Antibodies conjugated NPs for targeting drug delivery systems include:

1. Gupta et al. [289] reported the synthesis of monoclonal anticancer antibody 2C5 attached to PEGylated liposomes functionalised with doxorubicin for treatment of U-87 MG human brain tumours in an intracranial model in nude mice. The antibody-

conjugated liposomes provided valuable treatment control formulations with decrease in the tumour size [289].

2. Kou and co-workers [290] described the synthesis of paclitaxel-loaded poly (lactide-co-glycolide) (PLGA) nanoparticles coated with cationic SM5-1 single chain antibody (scFv) having a polylysine (SMFv-polylys) to investigate the cytotoxicity against human hepatocellular carcinoma cell lines (Ch-hep-3) *in vitro*. It was found that the PTX-loaded PLGA functionalised antibody (scFv) conjugate induced death in cancerous cells more effectively than PTX loaded PLGA nanoparticles suggesting the promising potential of antibodies conjugates to be used in target drug delivery [290].

3. Tyner et al. [291] functionalised the surface of inorganic nanoparticles comprised of magnesium–aluminium layered double hydroxides (LDHs) with disuccinimidyl carbonate (DSC) followed by loading of a huA33 antibody and a blood plasma protein (serum albumin). It was found that LDH-DSC-huA33 nanobiohybrids were 30 times more efficient against human A33 than that of LDH-DSC-albumin [291]. These studies indicate that antibodies can have significant role for drug delivery in cancer treatment.

An example of conjugation of antibody to AuNPs for labelling tumour stroma of surgically resected human pancreatic cancer tissue was reported by Eck et al. [292]. In this study, 15 nm AuNPs were stabilised by PEG using dithiol group anchored to the gold surface. Then, by using terminal carboxy group of PEG, the F19 monoclonal antibodies were attached to the PEGylated nanoparticles. By exploiting the advantage of optical scattering properties of AuNPs, visualisation of actual spatial distribution of a tumour and the stromal tissue has been achieved with dark field microscope [292].

1.8 Summary

Breast cancer is the most common cancer in women worldwide. While surgery and radiation therapy are still commonly used in breast cancer treatment, chemotherapy is often used as a treatment for many cancers, including breast cancer. Chemotherapy has potential risks including side-effects, and therefore treatment must be assessed on an individual basis. The main problem is finding the balance between delivering a high enough dose of the drug to kill the cancer cells without harming normal cells and thus causing adverse side effects to the patient. An emerging solution being investigated to overcome this problem is via the use of nanoparticles as vehicles, by conjugating them to an anticancer drug. The current study uses nanotechnology to investigate gold nanoparticles as delivery vehicles in one such investigation.

The utilisation of nanoparticles in targeted drug delivery systems (TDDs) has attracted significant attention due to the exclusive characteristics of nanoparticles which exist when combining with chemotherapeutic drugs. Gold nanoparticles exhibit unique physical, chemical and biological properties that can be exploited to improve pharmaceutical and clinical applications. Gold nanoparticles can be prepared easily with different controllable sizes and shapes, the surface can be functionalised with different biomolecules and ligands, have high stability in physiological environments and they possess excellent biocompatibility and non-cytotoxicity. In addition, due to the high surface to volume ratio of AuNPs, they can be applied to increase drug loading and this reduces the need for high doses.

Paclitaxel (PTX) is a chemotherapy agent. It is used to treat different types of cancer cells including breast cancer. However, PTX has several limitations including poor water solubility, lack of permeability into cells, low therapeutic index and non-specific release to the targeted cancerous cells causing severe side effects. These hurdles have limited its potential use in clinical applications. Therefore, developing a novel formulation is needed. Current research has focused on developing drug delivery system based on nanoparticles with biodegradable and non-toxic carriers to overcome the problems that exist in the commercially available anticancer drug.

The use of antibodies for human therapy is growing rapidly. Up to now, several antibodies have been approved by the US Food and Drug Administration (FDA) and/or the European Medicines Agency (EMA) for tumour therapy and many are in phase I/II clinical trials. Combining PTX as anticancer agent, AuNPs as nanocarriers and specific antibodies as active targeting ligands in one system as a nanobioconjugate can improve the effectiveness of the chemotherapy and reduce its side effects.

This thesis set out to make new cancer drug delivery systems based on gold nanoparticles. The drug was both non-covalently and covalently attached to the nanoparticles to explore if the type of attachment affected the efficiency of the delivery. The intracellular uptake of gold nanoparticles was investigated by loading different fluorescent dyes onto the surface of gold nanoparticles. The synthesised systems can be used to detect and track the fate of gold nanoparticles inside cells. Antibodies were loaded onto the gold nanoparticles-drug system to facilitate delivering and release of the drug at specific sites for cancer cells. These drug delivery systems were proposed as alternatives to conventional methods that use polyethylene glycol both as a linker and an antifouling agent. Its potential drawbacks have emerged as adverse side effects by the polymer itself or by its derivatives need to be considered.

Chapter 2. Experimental

2.1 Synopsis

This chapter covers the materials and pertinent experimental details used throughout this thesis. All relevant instrumentation techniques used are described herein.

2.2 Materials

This section gives details of all chemicals and reagents used to synthesise and functionalise gold nanoparticles (AuNPs) and various conjugates based on AuNPs in addition to conjugation of PTX with RB.

2.2.1 Chemicals and reagents

All chemicals and reagents were used as received without any further purification.

[Table 2.1](#) lists all chemicals used in this study.

Table 2.1 Chemicals and reagents.

Name and Purity	Supplier	Additional Information
Gold(III) chloride trihydrate, $\geq 99.9\%$	Sigma-Aldrich, Australia	Dissolved in Milli-Q water to desired concentration
Trisodium citrate dihydrate, 99 %	Ajax Finechem Pty Ltd, Australia	Dissolved in Milli-Q water to desired concentration
(\pm)- α -Lipoic acid, $\geq 99\%$	Sigma-Aldrich, Australia	Dissolved in ethanol to desired concentration
16-Mercaptohexadecanoic acid, 90 %	Sigma-Aldrich, Australia	Dissolved in ethanol to desired concentration
Ethanol, undenatured, 100 %	Chem-Supply Pty Ltd, Australia	Used as purchased
Ethanol, $\geq 99.5\%$ absolute	Sigma-Aldrich, Australia	Used as purchased
Paclitaxel, (PTX), $\geq 95\%$	Sigma-Aldrich, Australia	Dissolved in ethanol to desired concentration
Sodium hydroxide, $\geq 95\%$	Sigma-Aldrich, Australia	Dissolved in Milli-Q water to desired concentration
Tween [®] 20	Sigma-Aldrich, Australia	Used as purchased
N-(3-Dimethylaminopropyl)- N'-ethylcarbodiimide hydrochloride, 98 %	Sigma-Aldrich, Australia	Dissolved in Milli-Q water or ethanol to desired concentration
N-Hydroxysuccinimide, 98 %	Sigma-Aldrich, Australia	Dissolved in Milli-Q water or ethanol to desired concentration

2-(4-Amidinophenyl)-6-indolecarbamidine dihydrochloride (DAPI), $\geq 98\%$	Sigma-Aldrich, Australia	Dissolved in Milli-Q water or ethanol to desired concentration
Fluorescent Brightener 28	Sigma-Aldrich, Australia	Dissolved in Milli-Q water to desired concentration
1-Pyrenemethylamine hydrochloride, 95 %	Sigma-Aldrich, Australia	Dissolved in dimethyl sulfoxide to desired concentration
Rhodamine B, $\geq 95\%$	Sigma-Aldrich, Australia	Dissolved in EtOH or Milli-Q water to desired concentration
Dimethyl sulfoxide, anhydrous, $\geq 99.9\%$	Sigma-Aldrich, Australia	Used as purchased
Dimethyl sulfoxide-d ₆ , (DMSO-d ₆) 99.9 atom % D	Sigma-Aldrich, Australia	Used as purchased
Deuterium oxide (D ₂ O), 99.9 atom % D	Sigma-Aldrich, Australia	Used as purchased
Chloroform-d (CDCl ₃), 99.8 atom % D	Sigma-Aldrich, Australia	Used as purchased
EpCAM / CD326 Monoclonal Antibody	Thermo Fisher Scientific, Australia	Diluted in PBS to desired concentration
Anti-Human TARP Purified	Ebioscience, Australia	Diluted in PBS to desired concentration
Milli-Q water	Not Applicable	Milli-Q water with resistivity of 18.2 M Ω cm was used for all dilutions, aqueous solutions and rinsing.

2.3 Conjugation approaches

Three types of conjugation were utilised in the thesis.

1. Non-covalent binding. In this method the chemotherapy drug, paclitaxel, was mixed with thiol-AuNPs without any chemical reaction to obtain what was called PTX-thiol-AuNPs hybrid.

2. Covalent binding. In this method, the anticancer drug, PTX, with or without other molecules (a probe or antibodies) was covalently attached to thiol-AuNPs using EDC/NHS coupling reaction to synthesise the direct conjugates.

3. Covalent binding in reverse. In this method, the chemotherapy drug, PTX, (or other molecules i.e., a probe) was first covalently bonded to the carboxylic acid terminated alkanethiol (16-MHDA) to form ester bonds using EDC/NHS coupling. Then, the resulting conjugate was attached to AuNPs via chemisorption of thiols onto the AuNPs surface through an Au-S bond to form the reverse conjugate.

2.4 Non-covalent binding (hybrid preparation)

2.4.1 Synthesis of gold nanoparticles (AuNPs)

Gold nanoparticles were synthesised by sodium citrate reduction of HAuCl_4 as described by Turkevich et al. [293, 294] (see [Scheme 2.1](#)). A mechanism of this approach can be found in [Section 3.2](#) in [Chapter 3](#).

In all these experiments, prior to the synthesis, all glassware used was thoroughly cleaned in aqua regia (3 parts HCl , 1 part HNO_3), rinsed several times with Milli-Q water, sonicated for 10 minutes and oven-dried at $100\text{ }^\circ\text{C}$ to avoid undesirable nucleation and aggregation during AuNPs synthesis. Furthermore, as HAuCl_4 is corrosive, a glass or a plastic spatula was used to avoid its interactions with metal [295]. In a 250 mL conical flask, 100 mL of 1 mM HAuCl_4 solution (0.03938 g of HAuCl_4 in 100 mL Milli-Q water) was brought to the boil with vigorous stirring on a magnetic stirrer hotplate. Then, 10 mL of 38.8 mM trisodium citrate solution (0.11412 g of trisodium citrate in 10 mL Milli-Q water) was added rapidly. The original yellow solution was turned clear then dark blue, then finally to deep red-burgundy within a few minutes (see [Figure 2.1](#)). The reaction was completed within 15 minutes. The heat was then turned off and the solution was allowed to cool to room temperature with continued stirring. After the solution was cooled, the volume was adjusted to 100 mL with Milli-Q water. The resulting gold colloids were protected from light and stored at $4\text{ }^\circ\text{C}$ until required. The average diameter of AuNPs was approximately 17 ± 4 nm. The products were characterised by ultraviolet-visible spectroscopy (UV-Vis), transmission electron microscopy (TEM), dynamic light scattering (DLS), Fourier transform infrared spectroscopy (FT-IR) and nuclear magnetic resonance spectroscopy (^1H NMR) (see [Chapter 2](#), [Sections 2.9.1](#), [2.9.2](#), [2.9.3](#), [2.9.4](#) and [2.9.5](#)).

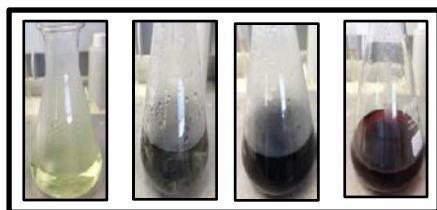
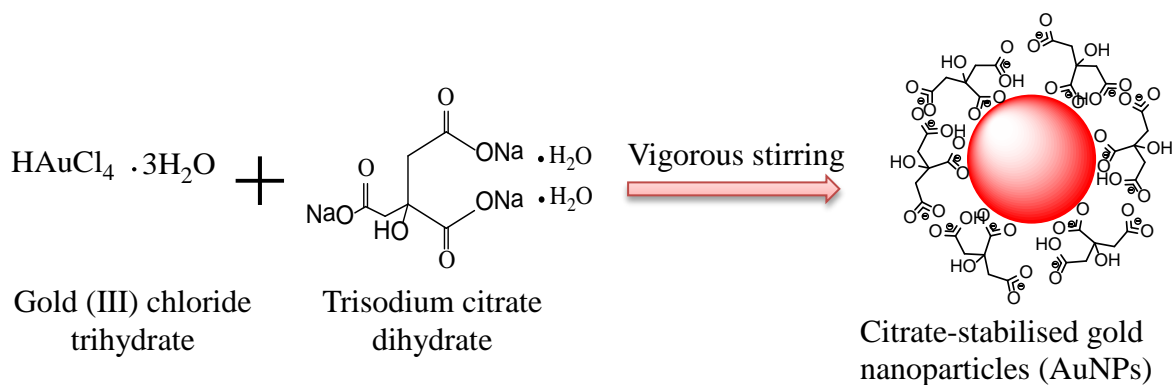


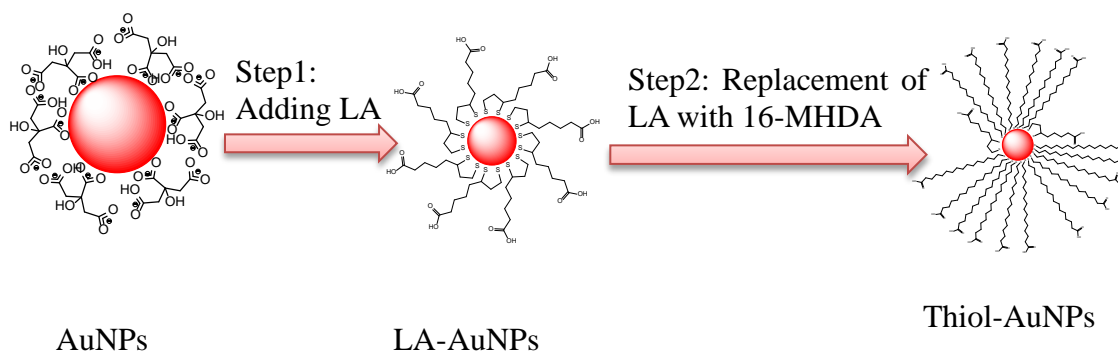
Figure 2.1 Optical properties of the colloidal gold prepared by the Turkevich's method as a function of time.



Scheme 2.1 Synthesis of citrate-stabilised gold nanoparticles (AuNPs).

2.4.2 Functionalisation of gold nanoparticles

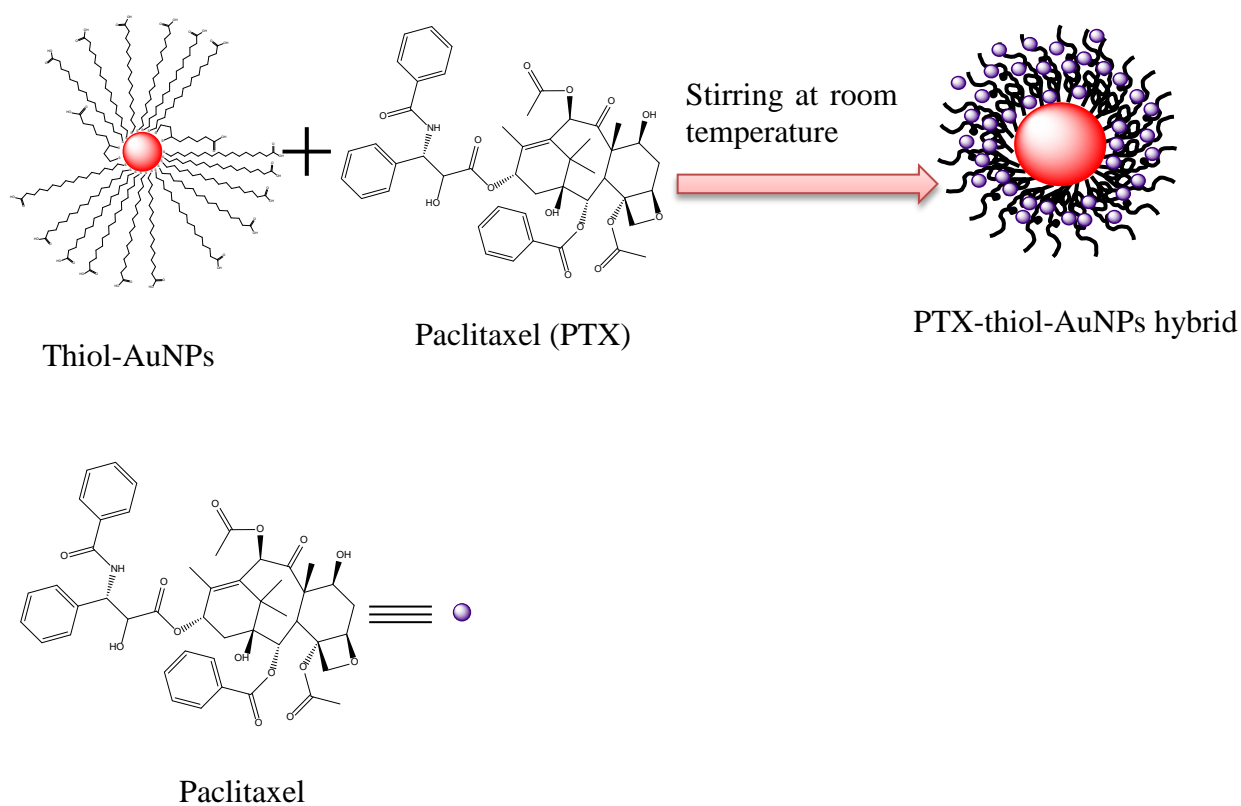
Gold nanoparticles were functionalised by a two-step approach based on the method described by Lin et al. (see [Scheme 2.2](#)) [296]. In a clean, sealed vial, a solution of sodium hydroxide (NaOH) (0.0007 g, 0.5 M) in Milli-Q water (40 μ L) was first added to as-prepared citrate-stabilised gold colloids (AuNPs) (4 mL) to adjust the pH due to the important role of using high basicity to reinforce and support static stabilisation of AuNPs [296]. Then, a solution of (\pm)- α -lipoic acid (LA) (0.0028 g) in ethanol (EtOH) (0.4 mL) was added to the mixture and the mixture was stirred gently for 18 h at room temperature. After that, a solution of 16-mercaptohexadecanoic acid (16-MHDA) (0.0028 g) in EtOH (0.4 mL) was added to the mixture with further stirring for 18 h at room temperature (see [Scheme 2.2](#)). From now on, this resulting product will be called “thiol-AuNPs”. The samples were centrifuged 5 times at 15700 g for 15 minutes to get rid of excess unbound thiols. The resultant product was protected from light and stored in a brown, sealed vial in the dark at 4 $^{\circ}$ C ready for further use and characterisation. This storage protocol was used for all particles prepared.



Scheme 2.2 Functionalisation of gold nanoparticles using two-step ligand exchange method.

2.4.3 Synthesis of PTX-thiol-AuNPs hybrid

In a clean, sealed vial, 3.5 mL of thiol-AuNPs were treated with 1.5 mL of paclitaxel (PTX) solution (3 mg PTX in 10 mL EtOH). The mixture was left stirring at room temperature for various lengths of time. After that, the samples were centrifuged at 15700 g for 15 minutes 5 times to remove unbound reagents. The synthesis of the hybrid is illustrated in [Scheme 2.3](#).



Scheme 2.3 Synthesis of PTX-thiol-AuNPs hybrid.

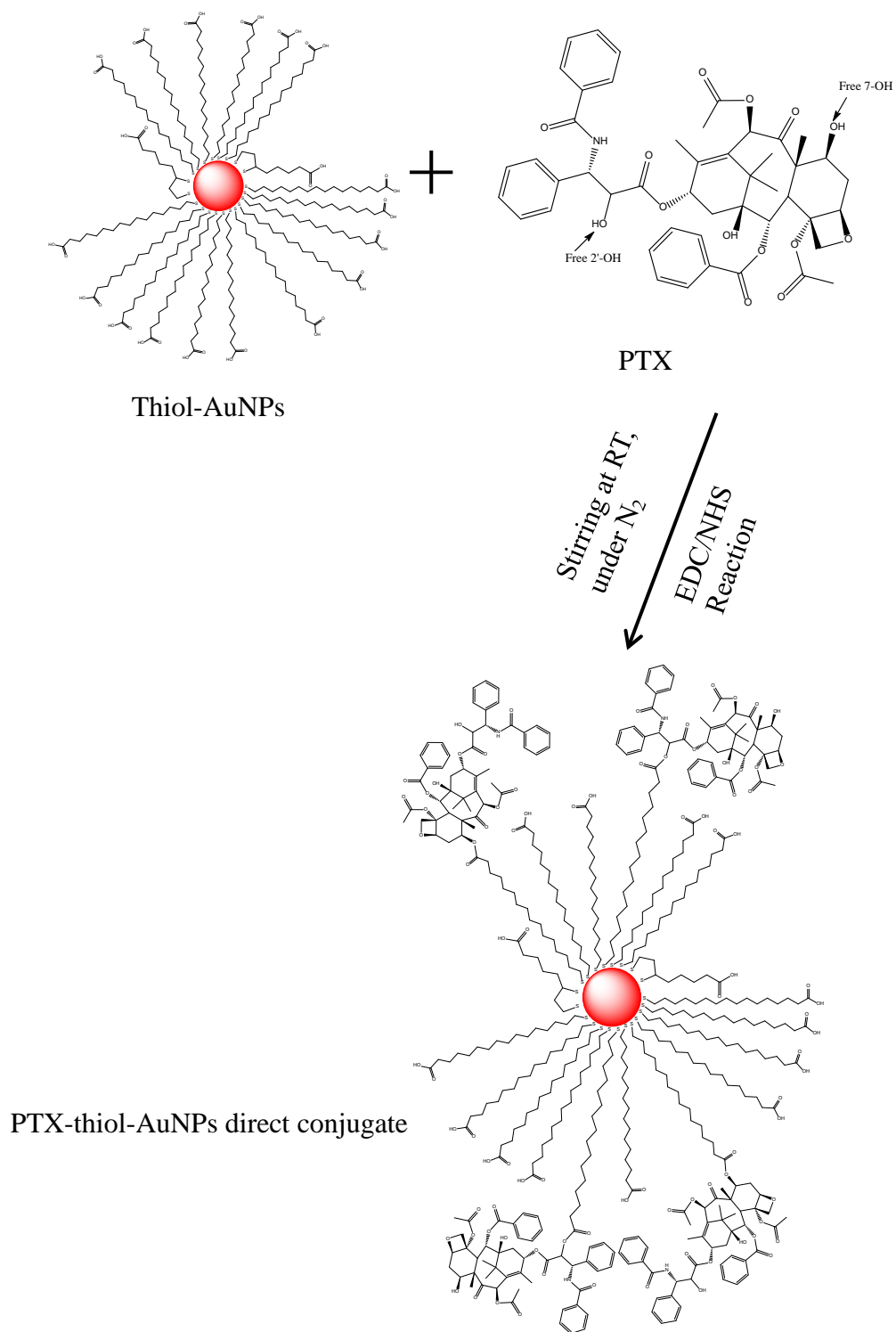
2.4.4 Preparation of phosphate buffered saline (PBS)

To prepare 10x dilution of PBS (0.15 M), 8 g of sodium chloride (NaCl), 0.2 g of potassium chloride (KCl), 1.44 g of sodium phosphate dibasic (Na₂HPO₄) and 0.24 g of potassium dihydrogen phosphate (KH₂PO₄) were dissolved in 900 mL of Milli-Q water and then made up to 1 litre. The PBS was adjusted to pH 7.4 using sodium hydroxide (NaOH) and hydrochloric acid (HCl) as required. Then, 100 mL PBS (0.015 M) was prepared by adding 10 mL from PBS stock to 90 mL Milli-Q water. PBS was stored at room temperature.

2.5 Covalent binding (direct conjugate preparation)

2.5.1 Synthesis of PTX-thiol-AuNPs direct conjugate using EDC/NHS coupling reaction

PTX-thiol-AuNPs direct conjugate was synthesised by EDC/NHS coupling using two carboxylic acid terminated alkanethiol ligands (see [Scheme 2.4](#)). Typically, the synthesised citrate-stabilised AuNPs colloid dispersions (see [Chapter 2, Section 2.4.1](#)) were first degassed with nitrogen (N_2) to avoid the oxidation of the alkanethiol acids then dispersed in phosphate buffered saline (PBS) pH 7.4 containing Tween 20 (1 mg mL^{-1}) for approximately 1 h and under N_2 . Tween 20 is used as a surfactant to stabilise the particles by physisorption onto the surface of AuNPs and prevent particle aggregation [158, 160]. After that, a solution of LA (0.0028 g of LA in 0.4 mL EtOH) was added to the mixture under nitrogen (N_2) at room temperature and stirred for 18 h followed by a solution of 16-MHDA (0.0028 g of 16-MHDA in 0.4 mL EtOH) with further stirring for 18 h at room temperature. Next, the chemotherapy drug, PTX, was prepared as a conjugate with the thiolated AuNPs (thiol-AuNPs) by introducing a solution of EDC (0.0015 g) and NHS (0.0023 g) simultaneously dissolved in EtOH (1 mL) and water (1 mL) (1:1) to the thiol functionalised AuNPs (4 mL) and the mixture was further stirred for 4 h. Then, PTX solution (0.3 mg of PTX in 1 mL of EtOH) was added to the mixture and stirred further overnight. Subsequently, the resulting sample was centrifuged at 15700 g for 15 minutes five times to get rid of unbound molecules (see [Scheme 2.4](#)). The products were then characterised.

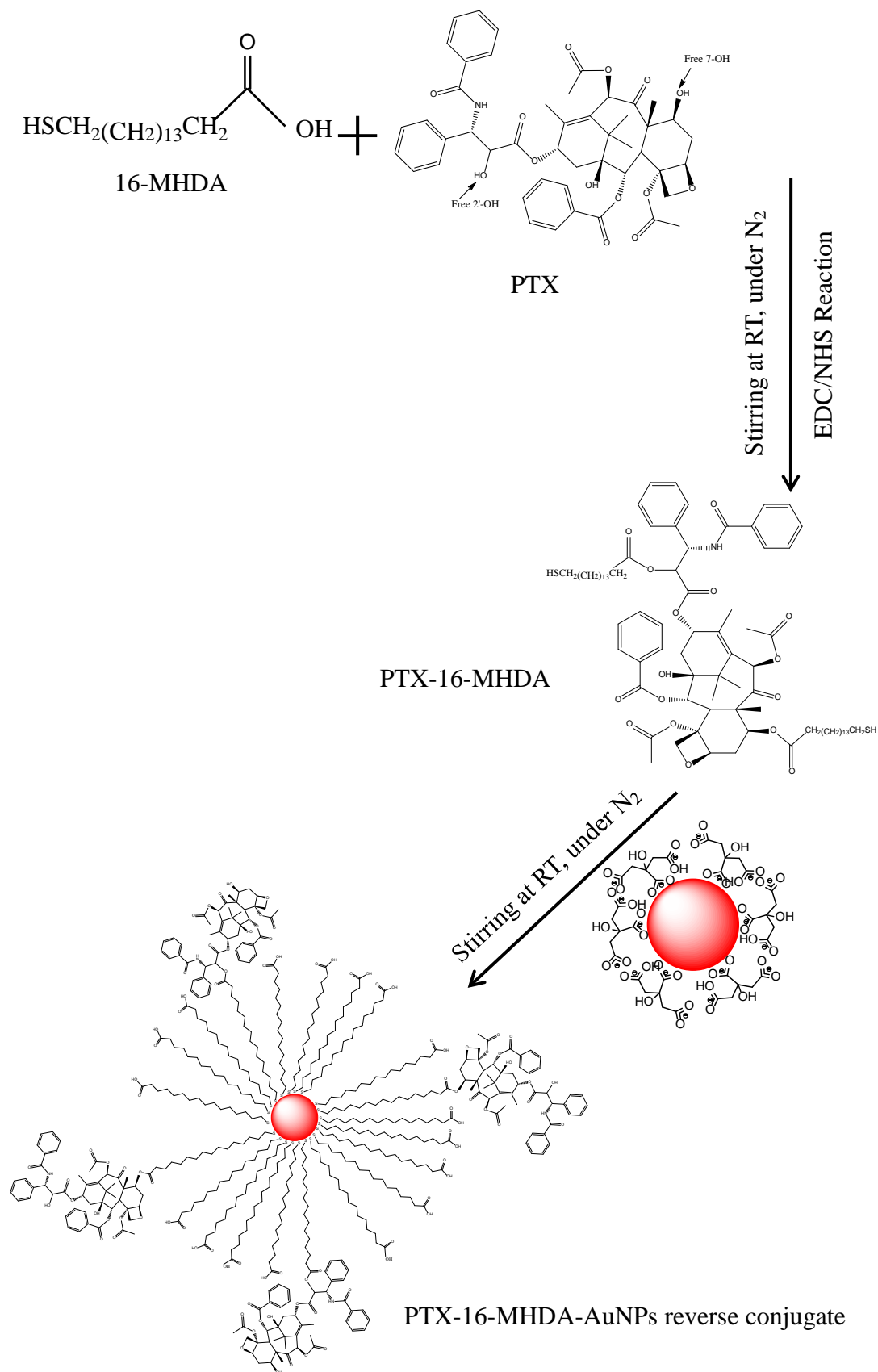


Scheme 2.4 Synthesis of PTX-thiol-AuNPs direct conjugate.

2.6 Covalent binding (reverse conjugate preparation)

2.6.1 Synthesis of PTX-16-MHDA-AuNPs (reverse conjugation method)

In this method, a solution of EDC (0.0015 g of EDC in 1 mL of EtOH) and NHS (0.0023 g of NHS in 1 mL of EtOH) was added to a solution of 16-MHDA (0.0028 g of 16-MHDA in 0.4 mL EtOH) and stirred under N₂ for 4 h. Then, a PTX solution (0.3 mg of PTX in 1 mL of EtOH) was added to the mixture and stirred for further 24 h. As synthesised AuNPs (4 mL) were dispersed in PBS buffer (1 mL) at pH 7.4 containing Tween 20 and stirred for approximately 1 h under N₂ environment. After that, the AuNPs mixture (4 mL) was added to the PTX-16-MHDA solution with further stirring overnight. Then, the resulting sample (PTX-16-MHDA-AuNPs reverse conjugate) was centrifuged at 15700 g for 15 minutes five times to get rid of unbound molecules (see [Scheme 2.5](#)). The samples were characterised by different techniques.



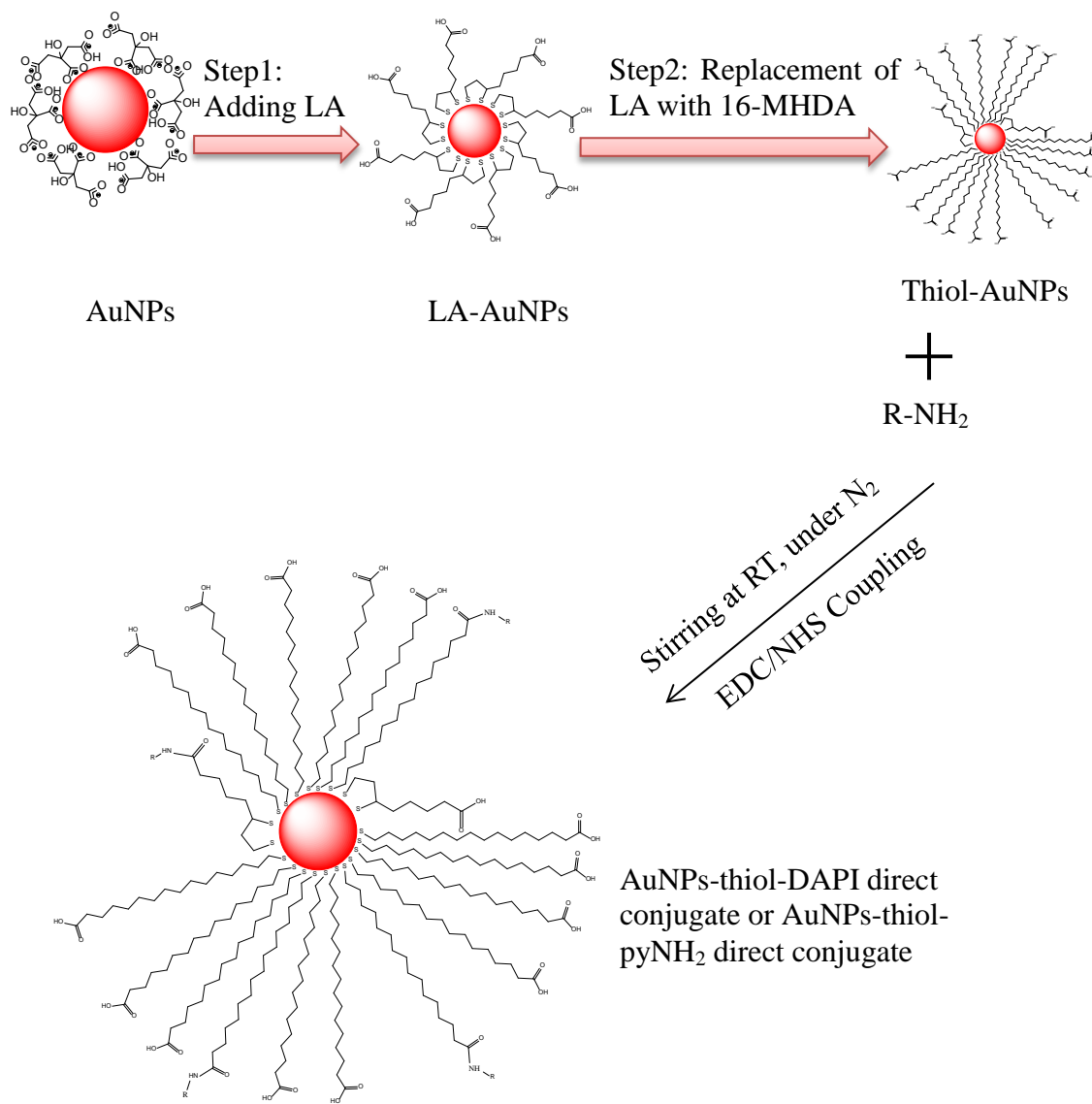
Scheme 2.5 PTX-16-MHDA-AuNPs reverse conjugate.

2.7 Preparation of fluorescently labelled AuNPs

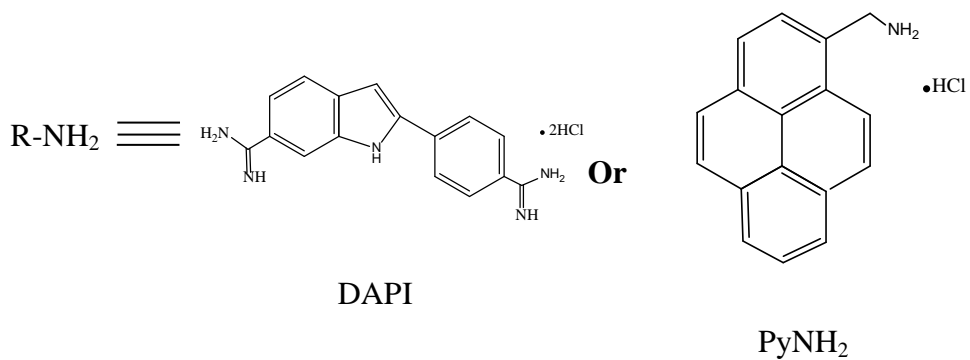
2.7.1 Using covalent attachment (direct conjugate preparation)

2.7.1.1 *Synthesis of AuNPs-thiol-DAPI direct conjugate*

Modifying the surface of thiol functionalised AuNPs with DAPI staining agent was performed using EDC/NHS coupling reaction. Typically, the synthesised citrate-stabilised gold nanoparticles (16 mL) were dispersed in phosphate buffered saline (PBS) pH 7.4 containing Tween 20 (4 mg mL⁻¹) for approximately 1 h, and under N₂. Then, a solution of LA (0.0112 g, 0.027 M) in 2 mL EtOH was added to the mixture and stirred for 18 h followed by a solution of 16-MHDA (0.0112 g, 0.0194 M) in 2 mL EtOH with further stirring for 18 h at room temperature. A solution of EDC (0.0126 g, 0.0109 M) and NHS (0.0184 g, 0.027 M) in 3 mL EtOH and 3 mL Milli-Q water (1:1) was added to as functionalised AuNPs and the mixture was further stirred for approximately 4 h. Then, a solution of 0.001 g of DAPI (0.0057 M) dissolved in 0.5 mL Milli-Q water was added and stirred overnight to obtain AuNPs-thiol-DAPI direct conjugate. Then, the resulting sample was centrifuged at 15700 g for 15 minutes five times, with fresh supernatant added after each centrifugation, to remove any unbound moieties (see [Scheme 2.6](#)). The product was characterised by fluorescence spectroscopy and confocal laser scanning microscopy (CLSM) (see [Chapter 2, Sections 2.9.6 and 2.9.7](#), respectively) in addition to other NP characterisation techniques.

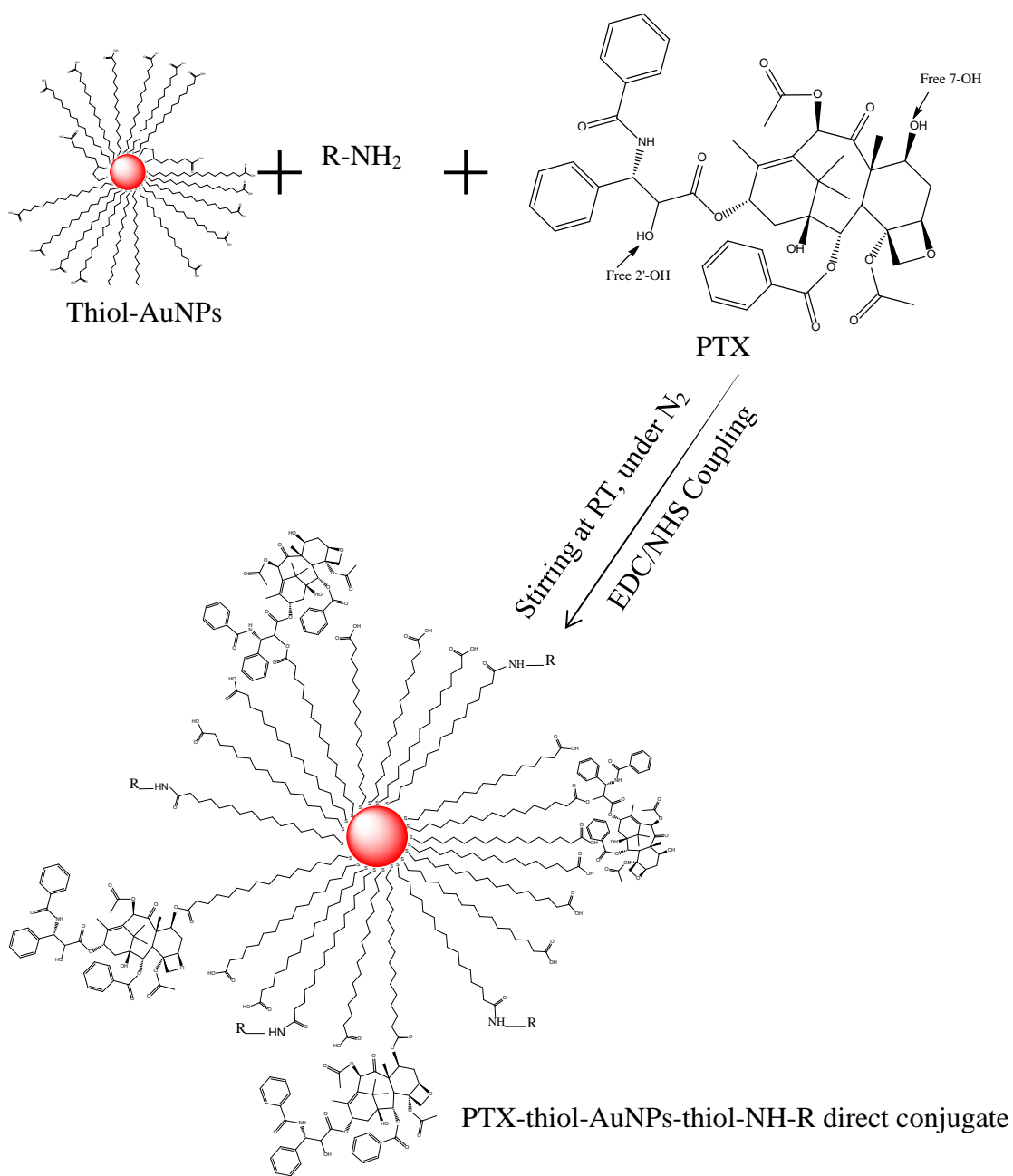


Scheme 2.6 Synthesis of RHN-thiol-AuNPs direct conjugate.



2.7.1.2 Synthesis of PTX-thiol-AuNPs-thiol-DAPI direct conjugate

Similarly, functionalising the surface of thiol modified AuNPs with DAPI staining and the anticancer drug, PTX simultaneously, was performed using EDC/NHS coupling reaction (see [Scheme 2.7](#)). Typically, after preparing thiol-AuNPs as described in [Section 2.7.1.1](#) in [Chapter 2](#), a solution of EDC and NHS, with same concentrations as in [Section 2.7.1.1](#) in [Chapter 2](#) and in EtOH and Milli-Q water (1:1) was added to thiol-AuNPs and the mixture was further stirred for approximately 4 h. Then, a solution of 0.001 g of DAPI (0.0057 M) dissolved in 0.5 mL Milli-Q water followed by a solution of PTX (0.003 g, 0.0035 M) dissolved in 1 mL EtOH added immediately. Then, the resulting sample was centrifuged at 15700 g for 15 minutes five times, with fresh supernatant added after each centrifugation, to remove any unbound moieties.



Scheme 2.7 Synthesis of PTX-thiol-AuNPs-thiol-NH-R direct conjugate by covalent coupling reaction.



2.7.1.3 Synthesis of AuNPs-thiol-pyNH₂ direct conjugate

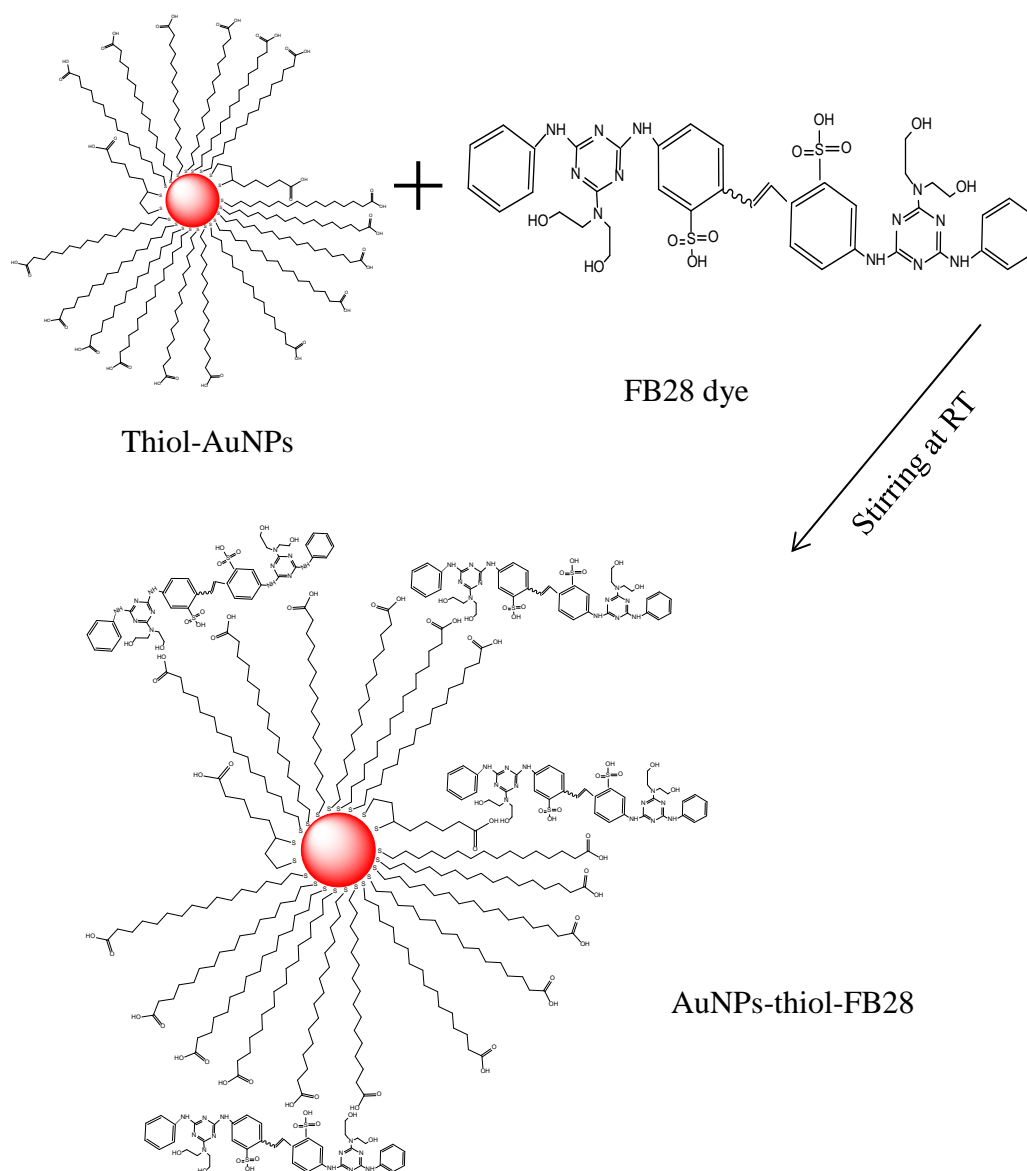
Likewise, conjugation thiolated AuNPs with pyNH₂ staining agent was accomplished using EDC/NHS chemistry. Typically, after activating the carboxylic ends of thiol-AuNPs using EDC/NHS mixture, a solution of 0.01 g of pyNH₂ (0.037 M) dissolved in 1 mL dimethyl sulfoxide (DMSO) added to the mixture and stirred overnight ([Scheme 2.6](#)).

2.7.1.4 Synthesis of PTX-thiol-AuNPs-thiol-pyNH₂ direct conjugate

Conjugation thiolated AuNPs with pyNH₂ staining agent and PTX simultaneously attached were made using EDC/NHS coupling reaction. Typically, after activating the carboxylic ends of thiol-AuNPs using EDC/NHS mixture, a solution of 0.01 g of pyNH₂ (0.037 M) dissolved in 1 mL DMSO followed by a solution of PTX (0.003 g, 0.0035 M) dissolved in 1 mL EtOH was added immediately to the mixture and stirred overnight (see [Scheme 2.7](#)).

2.7.1.5 Synthesis of AuNPs-thiol-FB28 hybrid

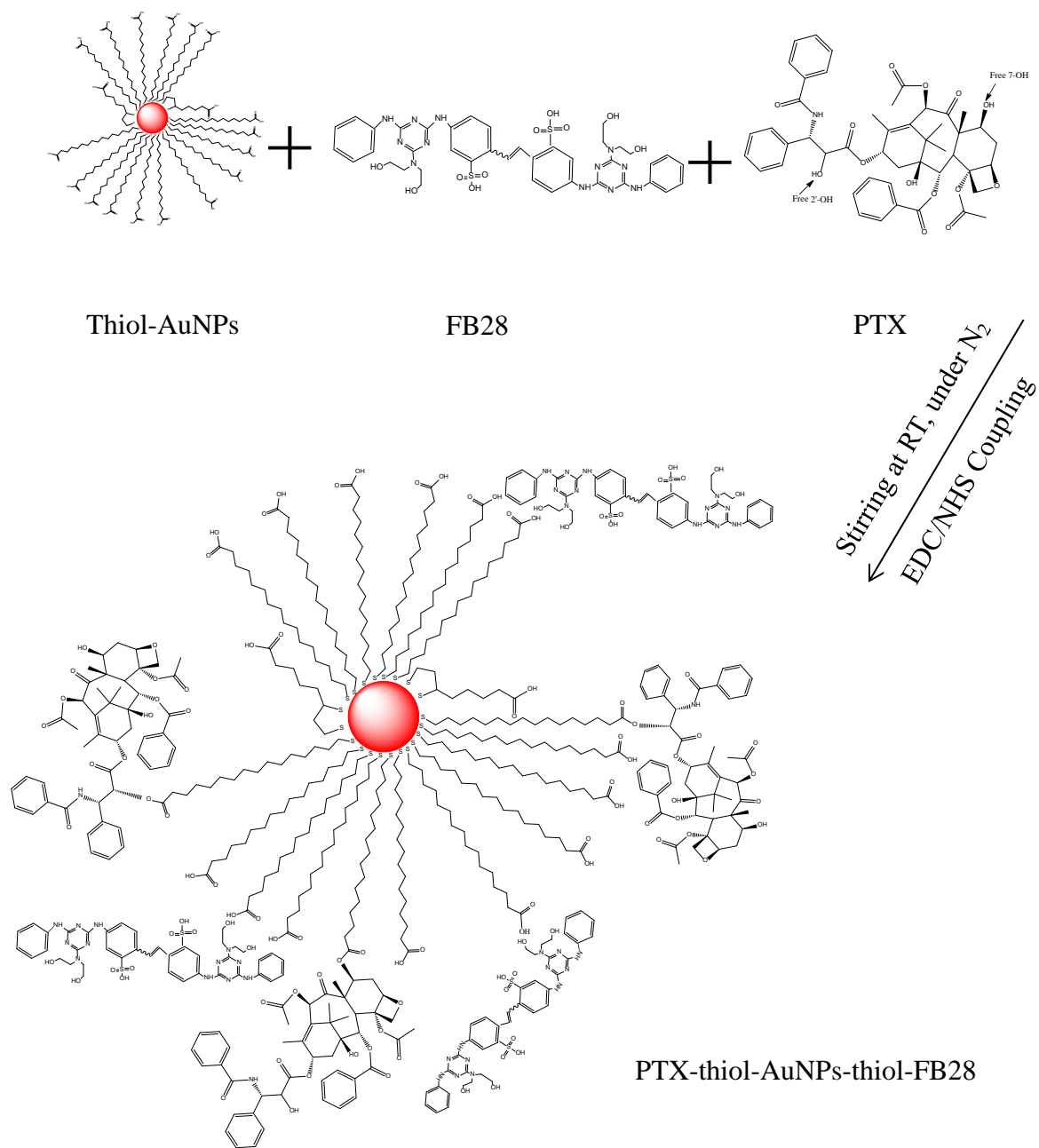
Immobilisation FB28 probe onto the surface of thiol functionalised AuNPs was carried out. A solution of 0.01 g of FB28 (0.0057 M) dissolved in 1 mL Milli-Q water was added to thiol-AuNPs and stirred overnight (Scheme 2.8).



Scheme 2.8 Synthesis of AuNPs-thiol-FB28 hybrid.

2.7.1.6 Synthesis of PTX-thiol-AuNPs-thiol-FB28 direct conjugate

Functionalisation of the surface of thiol-AuNPs with the FB28 probe and the chemotherapy drug, PTX, was performed as outlined for other labels. After activating the carboxylic ends of thiol-AuNPs using EDC/NHS mixture to conjugate PTX, a solution of 0.01 g of FB28 (0.0057 M) dissolved in 1 mL Milli-Q water followed by a solution of PTX (0.003 g, 0.0035 M) dissolved in 1 mL EtOH was added immediately ([Scheme 2.9](#)).

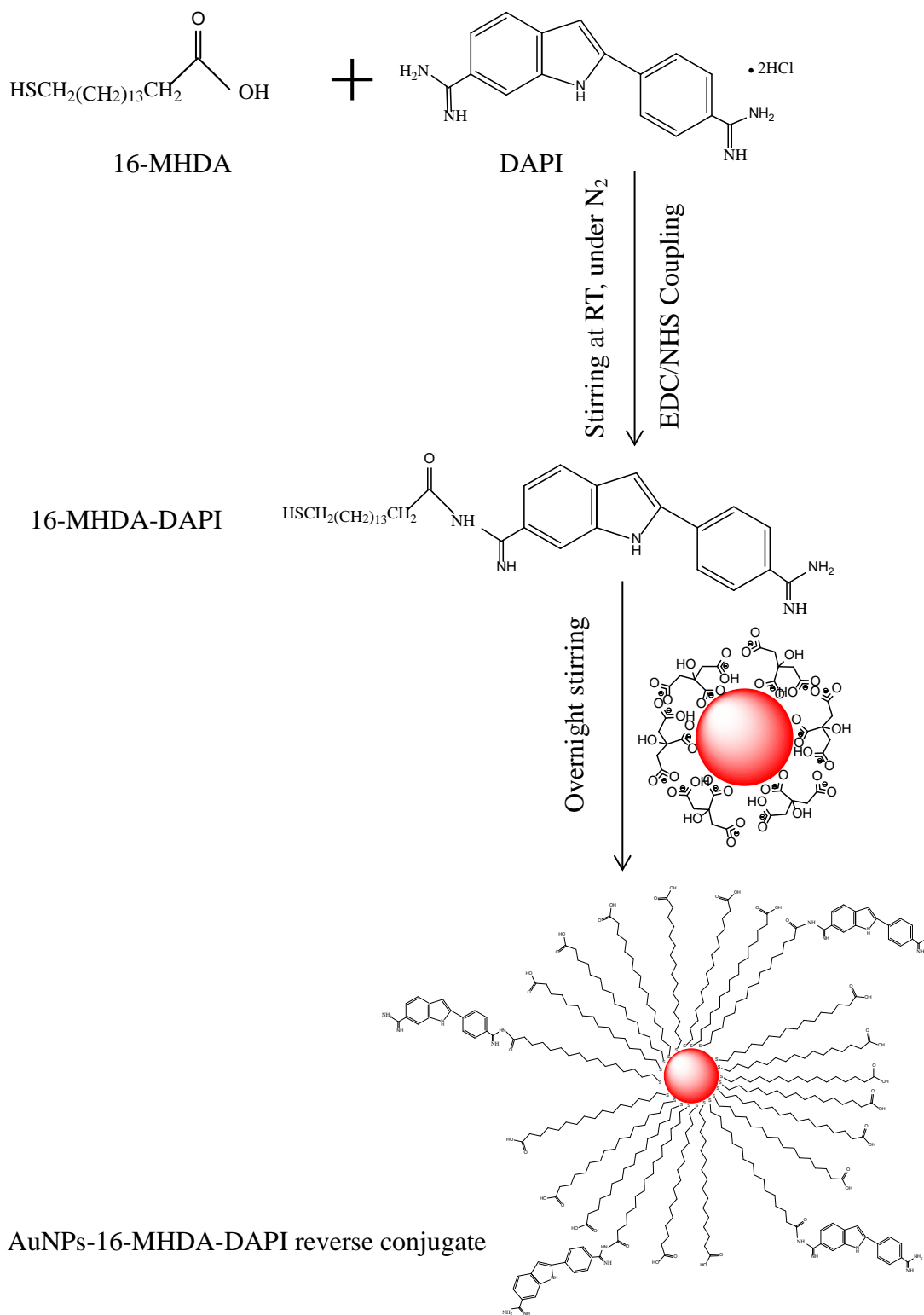


Scheme 2.9 Synthesis of PTX-thiol-AuNPs-thiol-FB28 direct conjugate.

2.7.2 Using covalent attachment (reverse conjugate preparation)

2.7.2.1 Synthesis of AuNPs-16-MHDA-DAPI reverse conjugate

Synthesis of AuNPs-16-MHDA-DAPI reverse conjugate was accomplished using EDC/NHS coupling reaction as well (see [Scheme 2.10](#)). In this method, a solution of EDC (0.018 g of EDC in 2 mL of EtOH) and NHS (0.0277 g of NHS in 2 mL of EtOH) was added to a solution of 16-MHDA (0.0168 g in 3 mL EtOH) and stirred under N₂ for 4 h. Then, DAPI solution (0.0015 g of DAPI in 0.5 mL of Milli-Q water, 0.009 M) was added to the mixture and stirred for further 24 h. As synthesised AuNPs (12 mL) were dispersed in PBS buffer at pH 7.4 containing Tween 20 and stirred for approximately 1 h under N₂. The 16-MHDA-DAPI solution was added rapidly to the AuNPs mixture with further stirring overnight. The resulting sample was centrifuged at 15700 g for 15 minutes five times to get rid of unbound molecules.

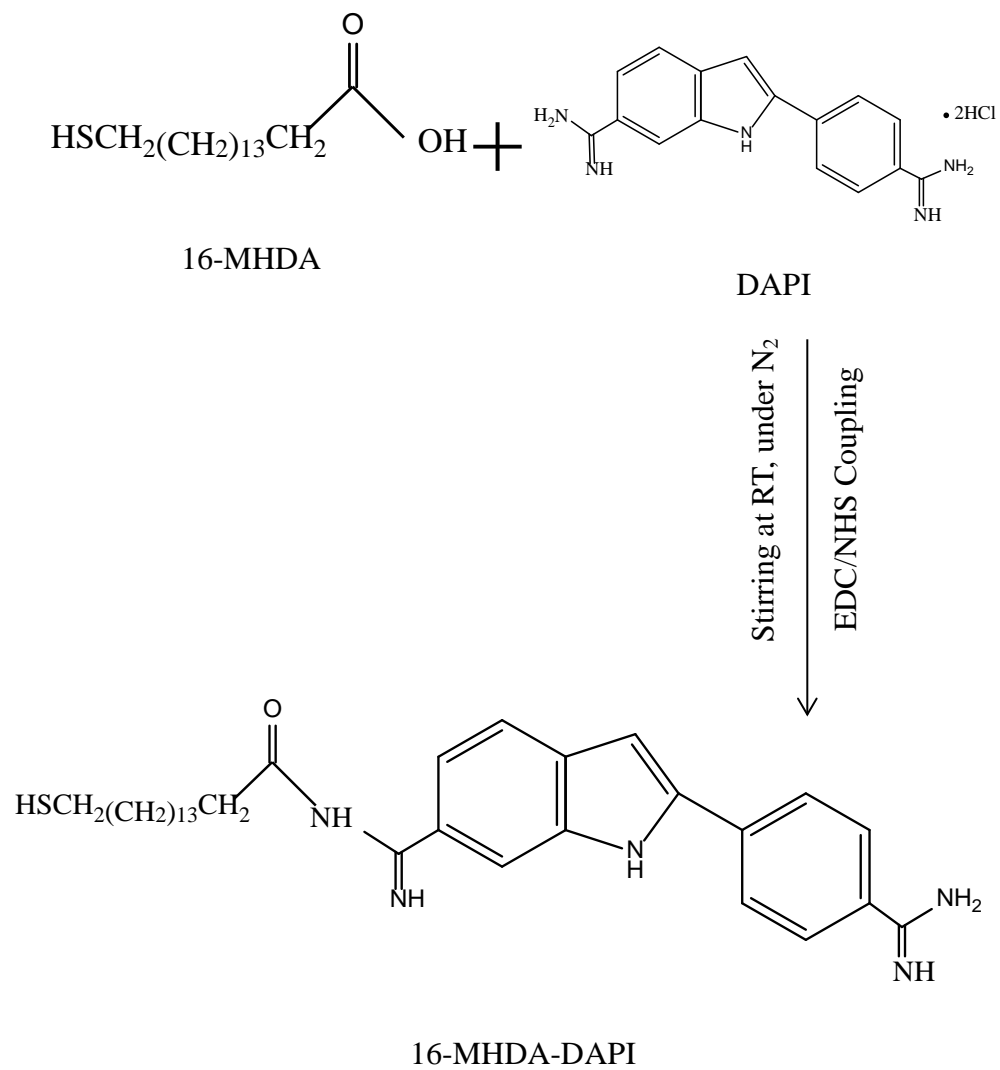


Scheme 2.10 Synthesis of AuNPs-16-MHDA-DAPI reverse conjugate.

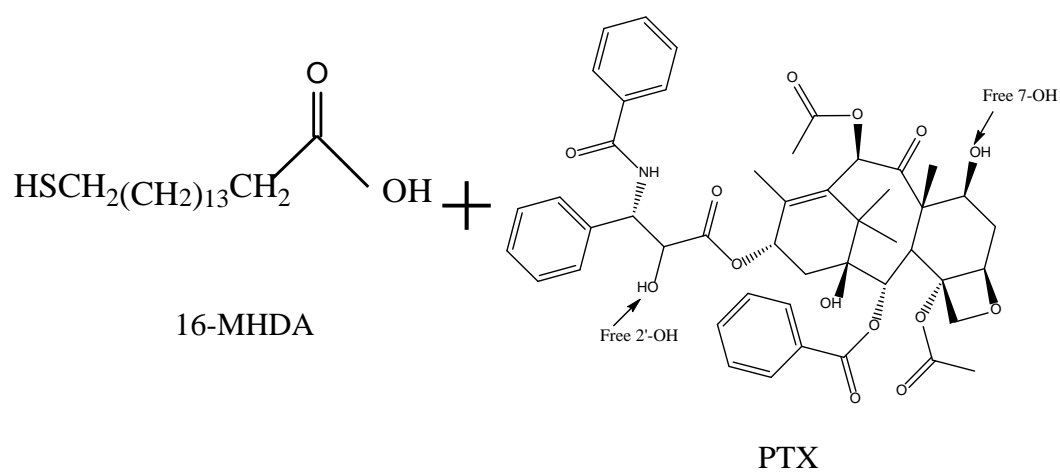
2.7.2.2 Synthesis of PTX-16-MHDA-AuNPs-16-MHDA-DAPI reverse conjugate

DAPI attached to 16-MHDA and PTX functionalised 16-MHDA conjugated all together onto AuNPs was performed using EDC/NHS chemistry and reverse method. In this method, a solution of EDC (0.018 g of EDC in 2 mL of EtOH) and NHS (0.0277 g of NHS in 2 mL of EtOH) was added to a solution of 16-MHDA (0.0168 g of 16-MHDA in 3 mL of EtOH) and stirred under N₂ for 4 h. Then, DAPI solution (0.0015 g of DAPI in 0.5 mL of Milli-Q water, 0.009 M) was added to the mixture and stirred for further 24 h. The same procedures were done with PTX. Typically, a solution of EDC (0.018 g) and NHS (0.0277 g) in EtOH was added to a solution of 16-MHDA (0.0168 g of 16-MHDA in 3 mL of EtOH) and stirred under N₂ for 4 h. Then, PTX solution (0.003 g of PTX in 1 mL of EtOH) was added to the mixture and stirred overnight. As synthesised AuNPs were dispersed in PBS buffer at pH 7.4 containing Tween 20 and stirred for approximately 1 h under N₂. 16-MHDA-DAPI solution and PTX-16-MHDA solution were added rapidly to the AuNPs mixture with further stirring overnight. The resulting sample was centrifuged to get rid of unbound molecules (see [Scheme 2.11](#)).

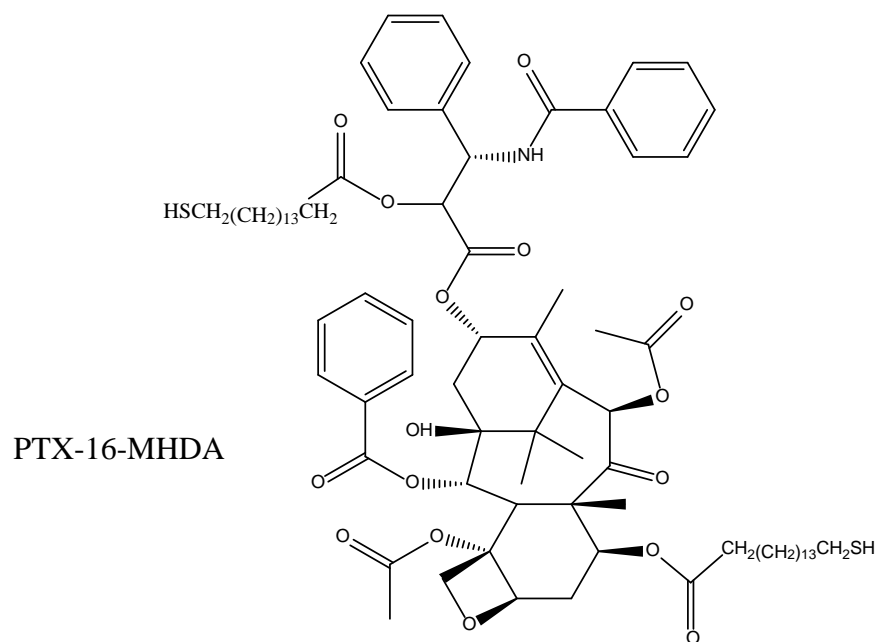
Step A: Synthesis of 16-MHDA-DAPI reverse conjugate



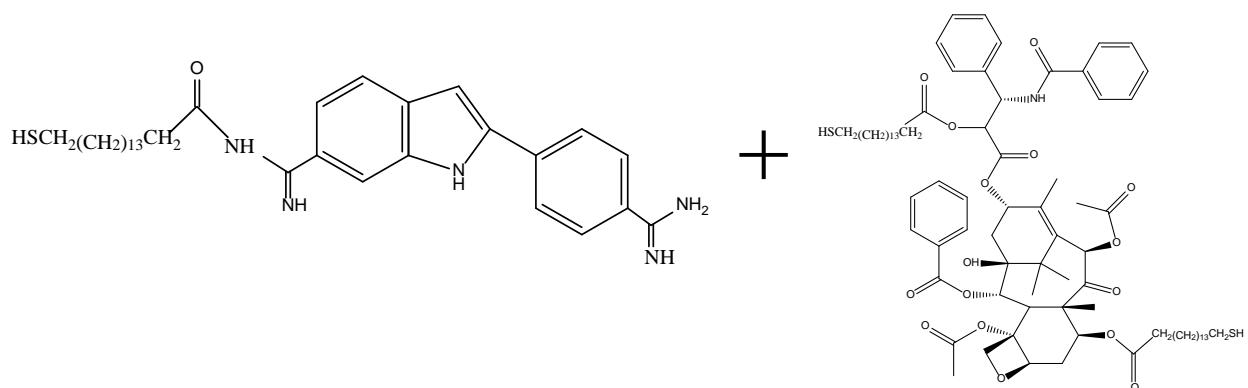
Step B: Synthesis of PTX-16-MHDA reverse conjugate



Stirring at RT, under N_2
EDC/NHS Coupling

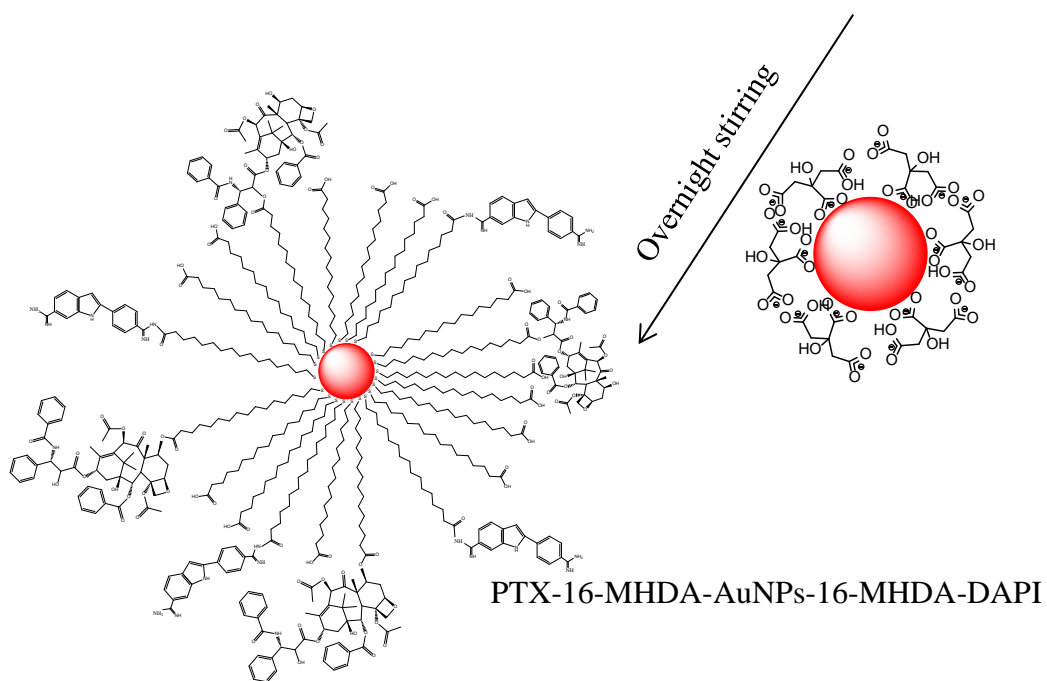


Step C: Synthesis of PTX-16-MHDA-AuNPs-16-MHDA-DAPI reverse conjugate



16-MHDA-DAPI

PTX-16-MHDA

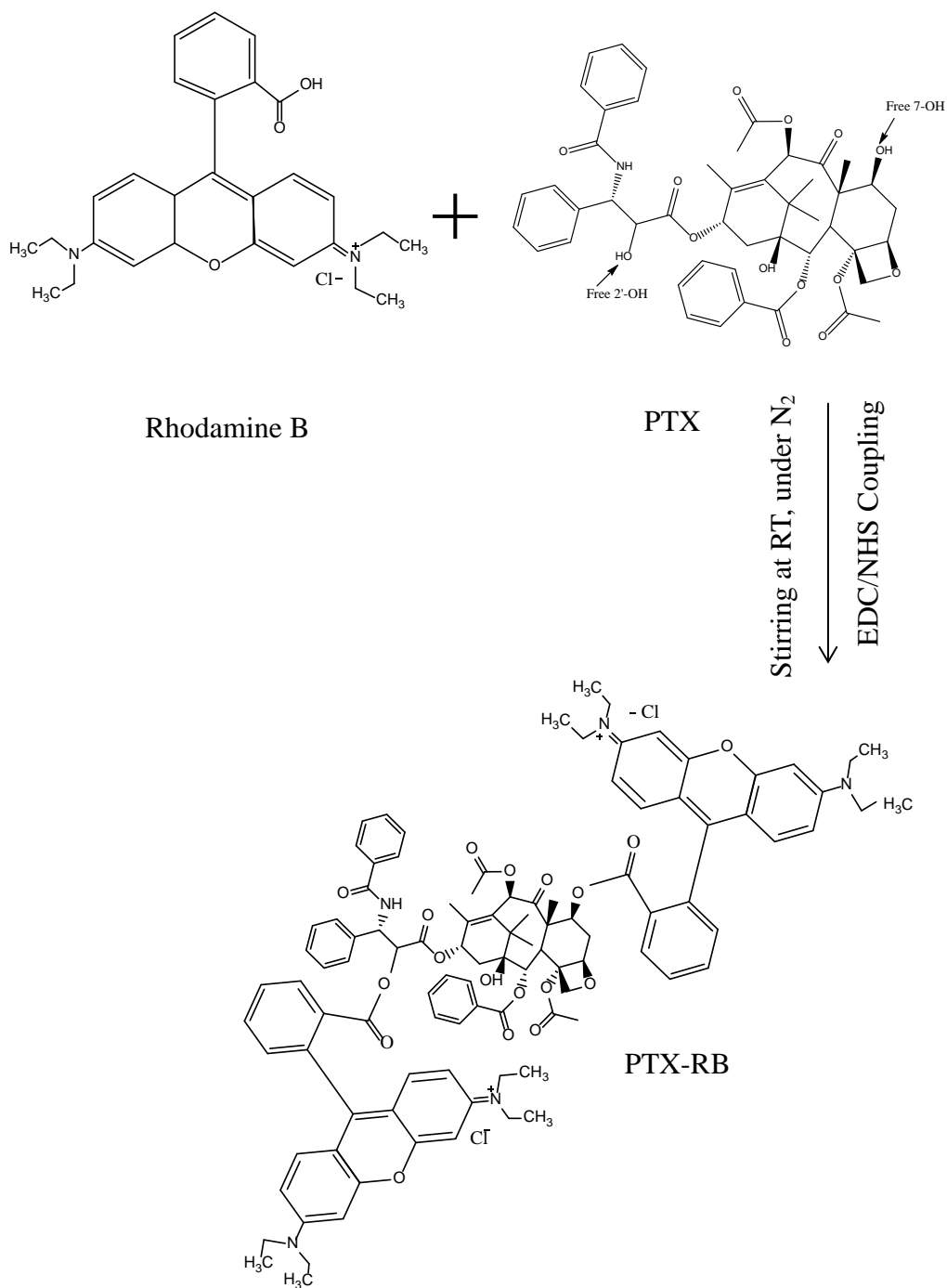


PTX-16-MHDA-AuNPs-16-MHDA-DAPI

Scheme 2.11 Synthesis of PTX-16-MHDA-AuNPs-16-MHDA-DAPI reverse conjugate.

2.7.3 Synthesis of rhodamine B attached paclitaxel

Rhodamine B (RB) conjugated paclitaxel (PTX-RB conjugate) was synthesised via EDC/NHS coupling reaction (see [Scheme 2.12](#)). The EDC promoted the dehydration reaction between the carboxylic group of RB and the hydroxyl groups of PTX (C₂-OH & C₇-OH). Typically, a solution of EDC (0.0045 g) and NHS (0.0069 g) dissolved in EtOH (5 mL) was added to RB solution (0.005 g of RB in 1 mL of EtOH) and the mixture was stirred for 4 h. Then a solution of PTX (0.003 g of PTX in 1 mL of EtOH) was added to the mixture and stirred overnight. The resulting conjugate was purified by removing the EDC/NHS moieties using CE dialysis tubing with molecular weight cut-off MWCO (0.5-1 KD) against PBS buffer (pH 7.4).

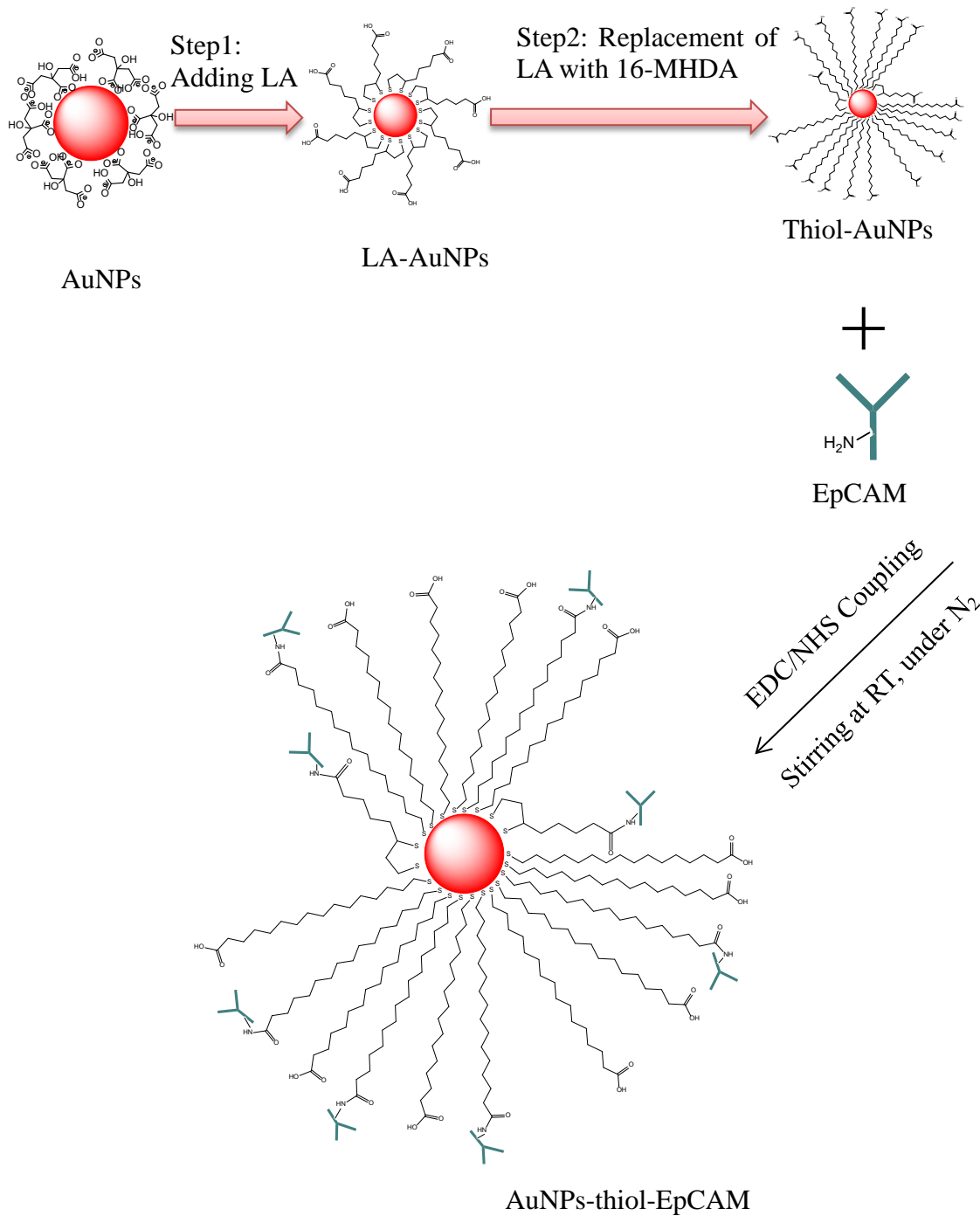


Scheme 2.12 Synthesis of PTX-RB conjugate.

2.8 Conjugation of antibodies

2.8.1 Synthesis of AuNPs-thiol-EpCAM direct conjugate

Attaching EpCAM antibodies to the surface of thiol-AuNPs was performed using EDC/NHS coupling reaction (see [Scheme 2.13](#)). Typically, AuNPs colloids (2 mL) were dispersed in PBS pH 7.4 containing Tween 20 (0.25 mg mL^{-1}) for approximately 1 h and under N_2 . The AuNPs were functionalised as normal and then, a solution of 30 μL of EpCAM diluted with 30 μL of PBS was added to the mixture and further stirred overnight. Then, the resulting sample was centrifuged at 15700 g for 15 minutes five times to remove any unbound moieties.

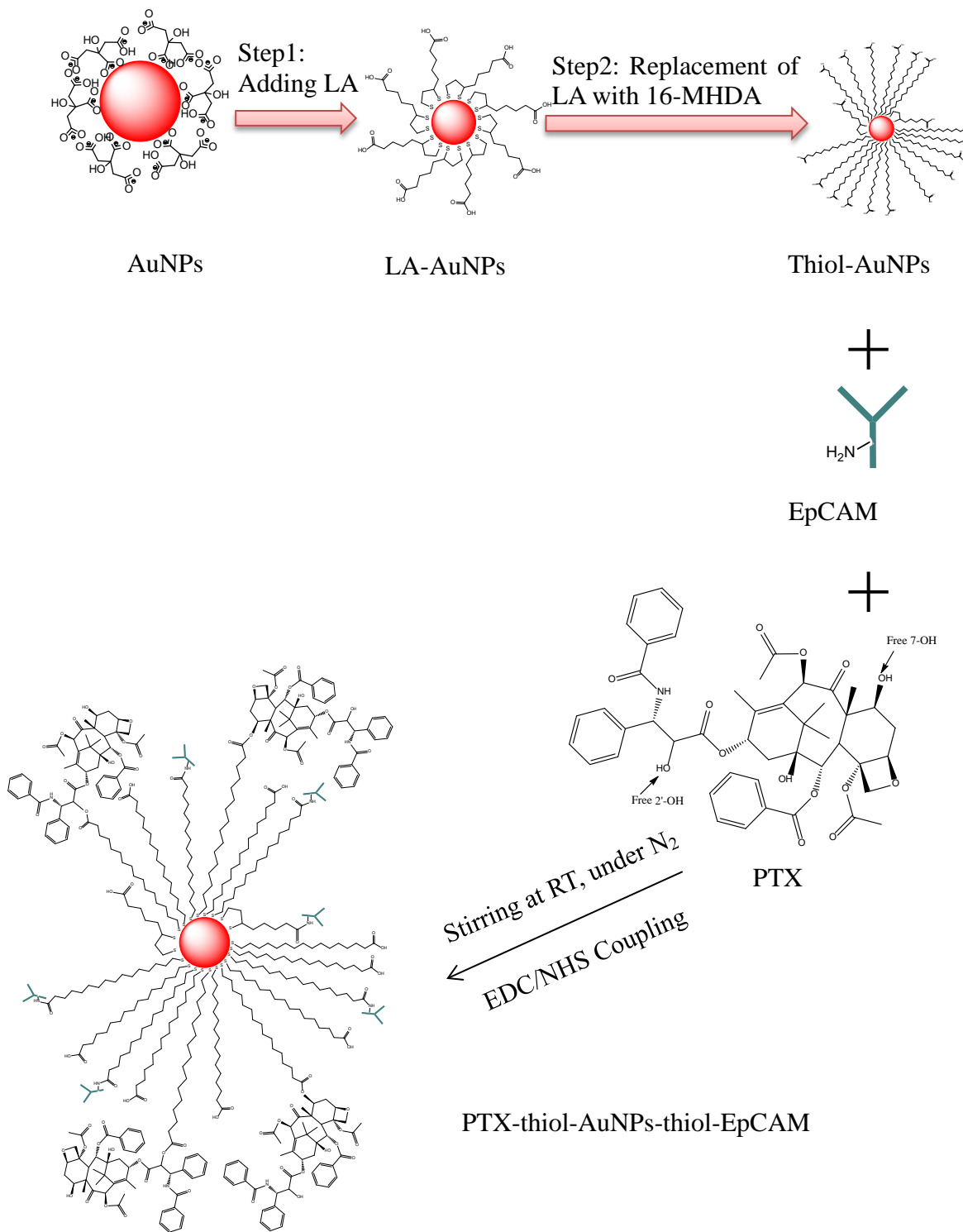


Scheme 2.13 Synthesis of AuNPs-thiol-EpCAM direct conjugate.

Synthesis of AuNPs-thiol-TARP direct conjugate is exactly equivalent.

2.8.2 Synthesis of PTX-thiol-AuNPs-thiol-EpCAM direct conjugate

Similarly, attaching EpCAM antibodies and PTX simultaneously to the surface of thiol-AuNPs was performed using EDC/NHS chemistry (see [Scheme 2.14](#)). Typically, after functionalising the surface of AuNPs with alkanethiol acids (see [Section 2.5.1 in Chapter 2](#)) and activating their carboxylic groups using EDC/NHS coupling, a solution of 30 μ L of EpCAM diluted with 30 μ L of PBS was added to the mixture followed by a solution of PTX (0.6 mg, 0.0007 M) dissolved in 1 mL EtOH was added immediately and further stirred overnight.



Scheme 2.14 Synthesis of PTX-thiol-AuNPs-thiol-EpCAM direct conjugate.

Synthesis of PTX-thiol-AuNPs-thiol-TARP direct conjugate is exactly equivalent.

2.8.3 Synthesis of AuNPs-thiol-TARP direct conjugate

Conjugation TARP antibodies to the surface of thiol-AuNPs was carried out in the same way as in case of attaching EpCAM antibodies. Typically, after activating the carboxylic groups terminated thiol-AuNPs (see [Section 2.5.1](#) in [Chapter 2](#)) via EDC/NHS coupling, a solution of 30 μL of TARP diluted with 30 μL of PBS was added to the mixture and further stirred overnight.

2.8.4 Synthesis of PTX-thiol-AuNPs-thiol-TARP direct conjugate

Similarly, attaching TARP antibodies and PTX simultaneously to the surface of thiol-AuNPs was performed using EDC/NHS chemistry. Typically, after activating the carboxylic groups terminated thiol-AuNPs (see [Section 2.5.1](#) in [Chapter 2](#)) via EDC/NHS coupling, a solution of 30 μL of TARP diluted with 30 μL of PBS was added to the mixture followed by a solution of PTX (0.6 mg, 0.0007 M) dissolved in 1 mL EtOH added immediately and further stirred overnight.

2.9 Characterisation techniques

Different techniques were used to characterise the as prepared AuNPs colloids, the functionalised AuNPs, the PTX-thiol-AuNPs hybrid, the PTX-thiol-AuNPs direct conjugate, the PTX-16-MHDA-AuNPs reverse conjugate, fluorescently labelled AuNPs samples (with DAPI, pyNH₂ or FB28 dyes), the PTX-RB conjugate and the antibodies (EpCAM or TARP) conjugated with thiol-AuNPs in the presence and in the absence of PTX. These techniques are described in the following sections.

2.9.1 Ultraviolet–Visible (UV-Vis) spectrophotometry

Ultraviolet–Visible (UV-Vis) spectrophotometry is used to measure the absorbance of a molecule at specific wavelengths when the electrons are excited by electromagnetic radiation [297]. Gold nanoparticles have strong absorbance in the visible region in the range between 510-550 nm [2]. The absorption of a molecule in a solution is determined by three main parameters which are molar extinction coefficient (ϵ), the concentration of the sample (c) and the path length (l), directed by Beer-Lambert law as shown in the following equation:

$$A = \epsilon l c \longrightarrow \text{Equation (1)}$$

Where A is the measured absorbance, ϵ is a wavelength-dependent absorptivity coefficient, l is the path length and c is the analyte concentration.

From this equation (1), the unknown concentrations can be calculated using an appropriate calibration curve [298].

2.9.1.1 Sample preparation

All NP samples were centrifuged at 15700 g for 15 minutes and washed with Milli-Q water. This procedure was repeated 5 times. Then, the nanoparticle pellets were redispersed in Milli-Q water. The highly concentrated samples were diluted by Milli-Q water to conform to any measurement technique limitations. The molar extension coefficient (ϵ) of AuNPs at 523 nm = $9.21 \times 10^8 \text{ M}^{-1} \text{ cm}^{-1}$ [299], ϵ of pyNH₂ at 344 nm = $22,000 \text{ M}^{-1} \text{ cm}^{-1}$ [300], ϵ of RB at 540 nm = $1.06 \times 10^5 \text{ L mol}^{-1} \text{ cm}^{-1}$ [301], ϵ of

FB28 at 350 nm = 4388 M⁻¹ cm⁻¹ [302, 303], ϵ of DAPI at 358 nm = 24,000 M⁻¹ cm⁻¹ [304] and ϵ of PTX at 228 nm = 29.8 mM⁻¹ cm⁻¹ [305].

2.9.1.2 Instrumentation and data acquisition

A dual-beam Varian Cary 50 (EST 70772) UV-Vis Spectrophotometer manufactured by Varian Inc., Melbourne, Australia was used for data acquisition. A quartz cuvette (2 mL, 10 mm path length) was used in all studies. The instrument was zeroed with Milli-Q water used as a background and the absorbance of the samples was determined.

2.9.2 Transmission electron microscopy (TEM)

In transmission electron microscopy (TEM), a beam of electrons focuses on and passes through a thin specimen which forms an image that can be magnified and displayed on a charge coupled device (CCD) camera or a more advanced direct detection device (DDD) camera system [306, 307].

2.9.2.1 Intracellular detection of AuNPs using transmission electron microscopy (TEM)

TEM is a commonly used technique for tracking and imaging metal nanoparticles due to the excellent contrast provided by high electron density of metallic nanoparticles. Therefore, conventional TEM devices are used to visualise nanoparticles bigger than 5 nm inside cells [258, 261]. Schaeublin et al. [249] used TEM to detect the intracellular uptake of gold nanomaterials. It was found that gold nanorods were accumulated in cytoplasmic vacuoles placed near the cell membrane [249]. Another study was reported by Chithrani et al. [247]. In this study, the intracellular uptake of various sized and shaped AuNPs were investigated using TEM. It was found that the AuNPs internalised inside cells and trapped in vesicles in the cytoplasm (see [Figure 2.2](#)) [247].

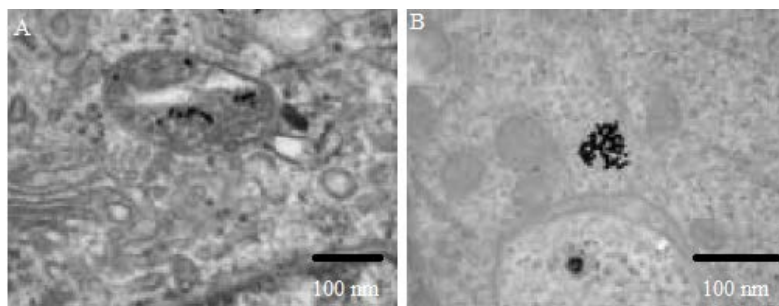


Figure 2.2 TEM images of gold nanoparticles trapped inside vesicles of a HeLa cell with sizes (A) 14 nm and (B) 30 nm. Adapted from [247] with some modifications.

2.9.2.2 Sample preparation

In all samples containing AuNPs without the cells, prior to imaging by TEM, a drop of the sample was air dried onto formvar and carbon coated 200 mesh copper grids. Preparation of T47D breast cancer cells treated with different samples based on AuNPs for TEM imaging was carried out. The cells were prepared in the School of Medical Science and Technology, Flinders University, South Australia, by collaboration with Assoc. Prof. Barbara Sanderson and a Masters student, Abeer Zaila.

The T47D cells were grown in a 75 cm² flask. 300 µL of AuNPs samples were added to 3 mL fresh medium. Then, 2 mL of the mixture was taken and added to cells. The cells were incubated in a humidified 37 °C with 5 % CO₂ incubator for 3-4 h. Then, they were washed by 2 mL of media. 1.5 mL Trypsin-EDTA was added onto the cells and incubated for 5-15 minutes. 5 mL of fresh media was added and mixed gently then transferred to 10 mL tube and centrifuged at 1000 rpm for 5 minutes. Afterward, the media was discarded and the cells fixed overnight in 500 µL of 4 % paraformaldehyde, 1.25 % glutaraldehyde in PBS and 4 % sucrose at pH 7.2. The next day, cells were washed buffer once every 5 minutes (PBS and 4 % sucrose). Later, post-fixative process was performed at Adelaide Microscopy. 2 % OsO₄ was added carefully to each vial and incubated for 45 minutes; dehydration using 70 % ethanol with one change was done followed by centrifuging the samples at 2000 rpm for 10 minutes; the cells were washed with 90 % ethanol and centrifuged twice 10

minutes each. Then, the cells were dehydrated using 100 % ethanol and centrifuged three times for 10 minutes each. The next step was resin infiltration using a 1:1 mixture of 100 % ethanol and epoxy resin for 1 h and 100 % resin for 1 h, then 100 % resin for another 1 h. The samples were centrifuged at 2000 rpm for 10 minutes. Cells were embedded overnight in fresh resin. Eventually, cells were polymerized in an oven at 70 °C for 24 h. Sections were cut on a Leica UC6 ultramicrotome using a diamond knife, stained with uranyl acetate and lead citrate and examined in a FEI Tecnai G2 Spirit transmission electron microscope.

2.9.2.3 Instrumentation and data acquisition

Transmission electron microscopy (TEM) characterisation was performed using a FEI Tecnai G2 Spirit transmission electron microscope with an accelerating voltage of 100 kV. Image J software was utilised to analyse TEM images.

2.9.3 Dynamic light scattering (DLS)

Dynamic light scattering is a quantitative technique which measures size distribution of small particles in suspension or solution media [308]. In this technique, the light is scattered in different directions when it hits particles smaller than its wavelength (smaller than 250 nm). Therefore, the Brownian motion of those particles can be observed [309].

2.9.3.1 Sample preparation

Prior to analysis, all the samples were diluted using Milli-Q water to appropriate concentrations.

2.9.3.2 Instrumentation and data acquisition

All measurements were taken on the particle analyser-Malvern HPPS manufacture by Malvern. Data was acquired with a scattering angle close to 180° at a temperature of 25 °C. Each measurement was run for 2 seconds and repeated three times per sample. All measurements were processed using the software supplied by the manufacturer which provided the mean hydrodynamic diameter. The measurements were carried out using a quartz cuvette (2 mL, 10 mm path length).

2.9.4 Fourier transform infrared (FT-IR) spectroscopy

FT-IR relies on measuring the energy of the vibrations of the molecular bonds [310]. It is used to determine the functional groups in a molecule and identify individual compounds in a mixture [311]. In addition, it can be used in combination with other spectroscopic systems such as ^1H NMR and ^{13}C NMR to identify unknown compounds [312]. In this work, FT-IR spectroscopy was used to probe the structure of the prepared compounds and particles.

2.9.4.1 Sample preparation

The samples were prepared using potassium bromide (KBr) discs. In these samples, approximately 0.02 g of KBr was ground and placed in the sample holder and used as a background. In order to prepare the sample discs, approximately 8 mg of the sample was ground with 0.02 g of KBr and placed in the sample holder to analyse the sample.

2.9.4.2 Instrumentation and data acquisition

A Perkin-Elmer Frontier FT-IR was used in order to analyse the samples. The spectra range was $500\text{-}4000\text{ cm}^{-1}$ or $500\text{-}4500\text{ cm}^{-1}$ in transmission mode at resolution of 2 cm^{-1} and 32 scans were averaged. Before the sample was scanned, a background scan of KBr disc was obtained. Data were collected using Spectrum version 10.4 software and exported into Microsoft Excel (2010) for re-plotting and analysing the resulting spectra.

2.9.5 Nuclear magnetic resonance spectroscopy (NMR)

Nuclear magnetic resonance spectroscopy (NMR) is used to determine the chemical structure of a compound by placing a molecule in a magnetic field to absorb the energy [313, 314]. Here, NMR spectroscopy was used to characterise the structure of molecules attached to AuNPs [315].

2.9.5.1 Sample preparation

Solutions of various conjugates based on AuNPs samples were centrifuged at 15700 g for 15 minutes and washed with Milli-Q water. This procedure was repeated five times and dried out so a thin film of each sample was obtained on the wall of a vial; then, it was dissolved in CDCl_3 or DMSO-d_6 (100 μL) and placed in a NMR tube. The AuNP sample was also centrifuged and washed as other samples but dissolved in D_2O (100 μL) and placed in a NMR tube. The free precursors (LA, 16-MHDA, PTX, DAPI, pyNH_2 , FB28 and RB) were dissolved in CDCl_3 or DMSO-d_6 (100 μL) and placed in a NMR tube. The chemical shifts (δ) for all samples were recorded in ppm and referenced to the solvent spectrum (7.26 ppm for CDCl_3 , 2.5 ppm for DMSO-d_6 and 4.8 ppm for D_2O).

2.9.5.2 Instrumentation and data acquisition

^1H NMR spectroscopy data were recorded on a 600 MHz-Bruker, NMR Spectrometer using TopSpin 3.2 NMR Software. The collected data were exported into Microsoft Excel (2010) for re-plotting and analysis the resulting spectra.

2.9.6 Fluorescence spectrophotometry

Fluorescence spectrophotometry is an analytical tool used to measure the intensity of photons emitted after an excited molecule first transfers from one of the different vibrational levels in the excited electronic state to the lowest vibrational level of that excited electronic state and then drops down to one of the different vibrational levels in the ground electronic state. This relaxation to the lower electronic state produces the photons. The emitted photons have different energies hence frequencies depending on which of the vibrational states in the ground electronic state are reached [316].

2.9.6.1 Sample preparation

All NP samples were centrifuged at 15700 g for 15 minutes and washed with Milli-Q water. This procedure was repeated 5 times. Then, the nanoparticle pellets redispersed in Milli-Q water or EtOH. The highly concentrated samples were diluted by Milli-Q water or EtOH to conform to any measurement technique limitations.

2.9.6.2 Instrumentation and data acquisition

A Varian Cary Eclipse Fluorescence Spectrophotometer was used to collect the excitation and emission spectra in the range between 200 and 600 nm. The measurements were carried out using a quartz cuvette (2 mL, 10 mm path length). For all the samples, a baseline correction was performed using Milli-Q water or EtOH.

It is worth mentioning the excitation and emission wavelengths of the fluorescent dyes used in this thesis.

λ_{ex} of DAPI = 358 nm [304], λ_{em} of DAPI = 457 nm [317].

λ_{ex} of pyNH₂ = 343 nm [318], λ_{em} of pyNH₂ = 378 nm [318].

λ_{ex} of FB28 = 343 nm, λ_{em} of FB28 = 435 nm [319]

λ_{ex} of RB = 540 nm [320], λ_{em} of RB = 567 nm [320].

2.9.7 Confocal laser scanning microscopy

Confocal laser scanning microscopy (CLSM) is an important technique used to image fluorescently labelled biological specimens due to the ability to obtain optical images with high resolution and depth selectivity [321].

CLSM is used to provide information about the fluorescent signal collected from fixed and immunofluorescently labelled samples in single, double, triple and multiple wavelength modes. Different fluorescent signals localised in the same part of the cell and three dimensional fluorescence distribution in the sample can be measured [322]. CLSM consists of a standard fluorescence microscope, multiple laser light sources, a monitor for display and software for collecting and analysing images [323]. A diagram of optical principle of CLSM is illustrated in [Figure 2.3](#).

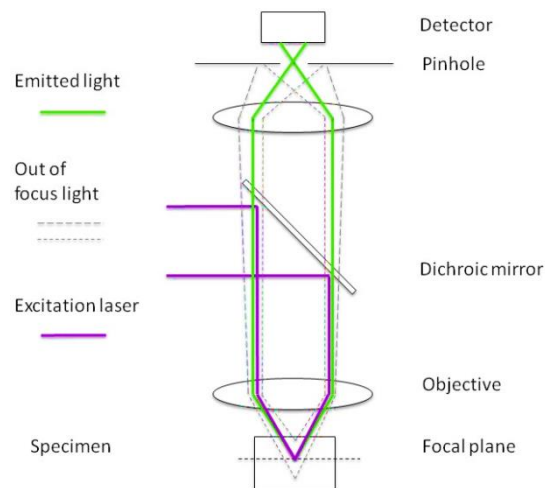


Figure 2.3 Simplified diagram illustrating the light path in a confocal laser scanning microscopy [323].

The sample is illuminated by a coherent laser beam, used to provide the excitation light, focused by objective lenses and scanned by mirrors across the specimen. The dye in the specimen fluoresces and emits light due to the interactions between the laser and the specimen. However, the same mirrors utilised to scan the exciting light from the laser are used to de-scan the emitted light allowing it to pass through those dichroic mirrors onto the pinhole. The pinhole aperture is located in the conjugate level with a scanning point on the sample. Thus, fluorescent signals from objects located above and below the focal plane are rejected. As a result, the out of focus signals are removed and only the signals originating from the in focus plane will be measured by a detector such as a photomultiplier (PMT) and assigning pseudocolors using a computer to provide the images [321, 324]. Therefore, images with enhanced contrast can be obtained by varying the scan speed of the laser when using this fundamental principle of CLSM in contrast to using conventional wide field optical systems [324, 325]. In addition, CLSM allows adjustment of the thickness of the optical parts in the specimen by changing the pinhole aperture's size. Also, three-dimensional images can be obtained by scanning and acquiring specific optical parts in the sample from certain depths [324].

2.9.7.1 Sample preparation

2.9.7.1.1 Preparation of AuNPs samples without cells

The as prepared AuNPs, thiol-AuNPs, PTX-thiol-AuNPs, AuNPs-thiol-DAPI, AuNPs-thiol-pyNH₂ and AuNPs-thiol-FB28 direct conjugates were first imaged by CLSM to investigate their appropriateness for microscopy experiments. Coverslips with thicknesses of 1.0-1.2 mm (Livingstone Premium Microscope Glass Slides) were immersed first in EtOH for 10 minutes and then, dried with nitrogen (N₂). After that, the AuNPs were diluted in Milli-Q water to reach the appropriate density for microscopy imaging. Approximately 20 µL of the dispersed AuNPs were added onto the coverslips and covered with another coverslip and mounted on a water lens of the confocal laser microscopy.

Confocal laser imaging was accomplished using the 405 nm diode laser for all the samples containing DAPI, pyNH₂ or FB28 dyes. Although the excitation wavelengths for the fluorescent dyes is less than 400 nm in ultraviolet region, the conjugates could be imaged using 405 nm excitation wavelength as the width of the excitation peaks for the probes provided enough absorption to excite the molecules using this laser wavelength (405 nm). The emitted fluorescence was detected by a photomultiplier tube (PMT). In RB, a 514 nm wavelength was used for excitation. The emitted fluorescence was detected by a photomultiplier tube (PMT 3) between 570 and 700 nm.

2.9.7.1.2 Preparation of T47D cells treated with different AuNPs samples

CLSM was used to investigate the T47D cell lines uptake of different samples listed in [Table 2.2](#) in addition to PTX-RB conjugate. After cell culture (refer to [Appendix C, Section C1.5.7](#) for preparation of T47D cells to CLSM imaging), T47D breast cancer cells were treated with 30 µL of fluorescently labelled AuNPs. For cells treated with RB alone or the PTX-RB conjugate, 15 µL of free RB and PTX-RB conjugate was mixed with 3 mL of fresh media, then 2 mL of this mixture was added to the cells for 1 h, 6 h and 24 h. Cell treated coverslips were washed twice with media then cells were harvested and placed carefully in a POC chamber (see [Figure](#)

2.4). 150 μ L of fresh media was added to the chamber after sealing and the cells were observed under fluorescence microscopy.

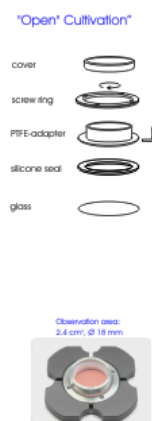


Figure 2.4 Method of placing coverslips POC chamber to observe live cells under inverted microscope [326].

Table 2.2 Exposure of T47D cells to various samples based on AuNPs.

AuNPs	AuNPs-thiol-DAPI direct conjugate	PTX-thiol-AuNPs-thiol-DAPI direct conjugate
Thiol-AuNPs	AuNPs-thiol-pyNH ₂ direct conjugate	PTX-thiol-AuNPs-thiol-pyNH ₂ direct conjugate
PTX-thiol-AuNPs direct conjugate	AuNPs-thiol-FB28 hybrid	PTX-thiol-AuNPs-thiol-FB28 direct conjugate
	AuNPs-16-MHDA-DAPI reverse conjugate	PTX-16-MHDA-AuNPs-16-MHDA-DAPI direct conjugate

2.9.7.2 Instrumentation and data acquisition

A Leica TCS SP5 scanning confocal microscope equipped with 405 nm, 488 nm and 561 nm diode lasers using LASAF software and with water immersion objective (Leica Biosystems, Australia) was used for particle and cell imaging. The single optical sections were recorded with average of 3 images using 63x magnification lenses. Optical sectioning was performed and 3D-images generated with pinhole size set at 1 array unit.

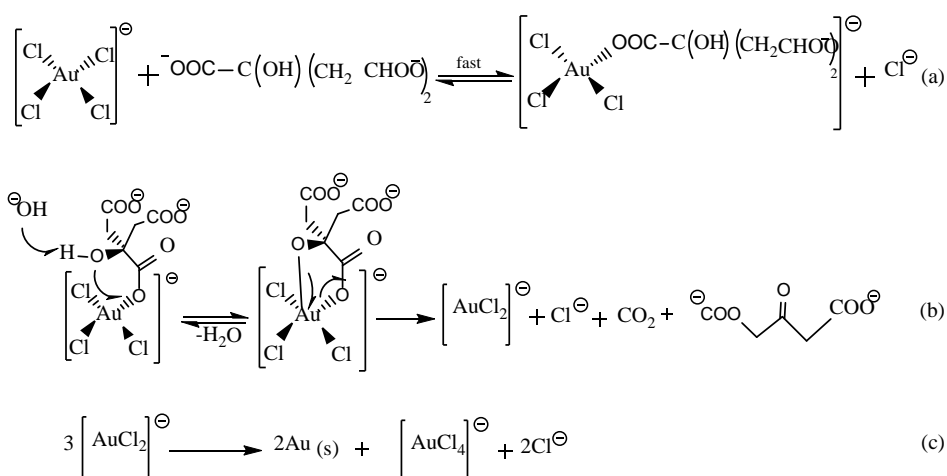
Chapter 3. Hybridisation of PTX with functionalised AuNPs

3.1 Introductory remarks

This chapter describes the synthesis mechanism and characterisation of AuNPs. It also outlines the functionalisation of their surface with carboxylic acid terminated alkanethiols using a two-step method described by Lin et al. [296] with some modifications to improve the stability of the designed system. Hybridisation of the particles with the breast anticancer drug, PTX, without chemical reactions provides a safe drug delivery system. This designed drug delivery system has not been reported previously. Most other research studies have used PEG as a linker between the AuNPs and PTX. However, this research project was focused on improving an efficient connection between the AuNPs and the chemotherapy by using –COOH terminated alkanethiol ligands to avoid the polymer complexity, its limitations which include hindering cellular uptake and endosomal escape [182] and health concerns (see [Section 1.5.5.1](#) in [Chapter 1](#) for more details about PEG drawbacks). Importantly, this loading method was by far the simplest and involved in fact no chemical linkages between the particle and the drug completely at odds with many complex chemical processes reported in the literature. This chapter describes results from the synthesis of PTX-thiol-AuNPs hybrid system and the cytotoxicity assessment of free PTX, thiol-AuNPs and PTX-thiol-AuNPs hybrid samples.

3.2 Description the synthesis of gold nanoparticles

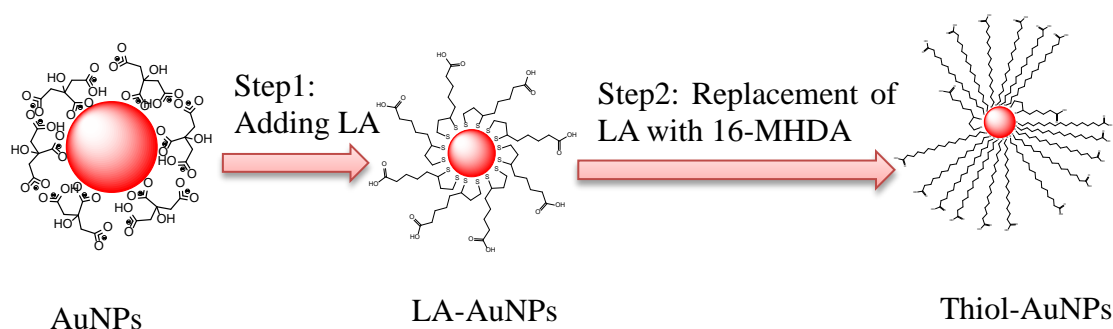
Monodispersed AuNPs were synthesised using trisodium citrate molecules. Citrate ions act simultaneously as reducing and stabilising agents for the nuclei of the AuNPs. The electrostatic repulsions between the negatively charged citrate ions cause the formation of stable AuNPs and prevent formation larger particles [327, 328]. Most of reactions and intermediate steps for synthesising AuNPs via citrate molecules are well known, however, some of the synthesis steps are still not completely understood [329, 330]. Generally, the synthesis of citrate-stabilised AuNPs involves three main steps. Firstly, (Au^{+3}) complexes are reduced to (Au^{+1}) by citrate anions. [Scheme 3.1.a](#) shows the ligand exchange with the citrate molecules to form a complex $[\text{AuCl}_3 (\text{C}_6\text{H}_5\text{O}_7)^{-2}]^-$. [Scheme 3.1.b](#) displays equilibrium reaction to obtain a closed ring, followed by a slow step including decarboxylation and reduction of (Au^{+3}). [Scheme 3.1.c](#) demonstrates the formation of Au (0) species by disproportionation reactions of multimolecular colloids, resulting from (Au^{+1}); with dicarboxy acetone molecules which exist in solution [331].



Scheme 3.1 The reduction of Au^{+3} species [331].

Moreover, lipoic acid-stabilised gold nanoparticles (LA-AuNPs) were synthesised as stated previously (see [Chapter 2, Section 2.4.2](#)). LA is a non-toxic natural product. It has been used as a food supplement. Its antioxidant and protective properties against

aging, diabetes mellitus and vascular and neurodegenerative diseases have been reported [332]. These advantages of LA make it a safe agent for clinical applications. [Scheme 3.2](#) shows the displacement of the citrate and chloride anions on the surface of AuNPs by disulfide groups after adding lipoic acid (LA) to the gold colloids made in the first step. It is known that LA possesses a carboxylate group and disulfide molecule S-S. Since sulfur atoms display strong affinity to gold at high pH, the negative charges of the stabilised AuNPs and disulfide bonds of LA create two sulfur-gold (S-Au) bonds. The formation of these new bonds delays the LA desorption kinetics, then allows the formation of a stable gold core by building up sufficient monolayers during the loss of electrostatic stability in the second step involving the exchange with 16-MHDA [296]. In addition, [Scheme 3.2](#) shows the second step where the particles are modified by ligand exchange reaction between the short chain of LA and the long chain ligands of 16-MHDA. The 16-MHDA binds to AuNPs by a single thiol bond and provides more stability to gold cores and lowers uncontrolled aggregation [333].



Scheme 3.2 Functionalisation of gold nanoparticles using two-step ligand exchange method.

After two-step functionalisation of AuNPs by thiol ligands, a solution of PTX, which has three hydroxyl groups and one amino group, was added to the mixture using conditions that would not see a chemical reaction occur. It was noticed that when centrifuging the PTX-thiol-AuNPs hybrid samples, the PTX settles at the bottom of the centrifuge tube close to the functionalised AuNPs. This can be attributed to van der Waals electrostatic interactions between the carboxylate groups of alkanethiol acids capped AuNPs and the hydroxyl groups and other functional groups of PTX

(see [Scheme 2.3](#) in [Chapter 2](#)). This means that several centrifugation steps are required for an effective separation of the AuNPs with bound PTX from the unbound PTX.

3.3 Characterisation of PTX-thiol-AuNPs hybrid

The results from the techniques used to characterise the products from the four steps, namely the as prepared AuNPs, LA functionalised AuNPs (LA-AuNPs), LA exchanged by 16-MHDA modified AuNPs (thiol-AuNPs) and LA exchanged by 16-MHDA modified AuNPs mixed with paclitaxel (PTX-thiol-AuNPs hybrid) are described in details in the following sections.

3.3.1 UV-Vis spectrophotometry characterisation and data analysis

UV-Vis spectrophotometry was used to investigate the absorbance maxima of the prepared AuNPs, the functionalised AuNPs through two steps and the PTX-thiol-AuNPs hybrid.

All UV-Vis data were collected after centrifuging and washing of the samples by Milli-Q water several times. Then, each sample was diluted in Milli-Q water (1:3 v/v) in UV-Vis cuvettes. The absorbance spectra were collected in the ultraviolet and visible regions between 200 and 800 nm.

Figure 3.1.a shows a UV-Vis spectrum of the citrate-stabilised AuNPs. The spectrum shows the characteristic absorbance for the surface plasmon resonance (SPR) band of AuNPs at approximately 523 nm. The absorbance wavelength of AuNPs (at 523 nm) is an indication of the formation of small particles (approximately 17 ± 4 nm in diameter) which was similar to that reported in the literature [334]. Figure 3.1.b displays the spectrum LA-AuNPs. A slight shift of the band to the red from 523 nm for colloidal AuNPs to 526 nm for LA-AuNPs sample is attributed to the attachment of LA onto the surface of AuNPs [296]. Figure 3.1.c demonstrates the spectrum of thiol-AuNPs. A slight shift of the surface plasmon resonance band from 526 nm for LA-AuNPs to 529 nm for thiol-AuNPs sample is assigned to the successful exchange between LA and 16-MHDA on the surface of AuNPs. In general, the size and shape of AuNPs affect the peak intensity and position of the surface plasmon absorption. Furthermore, when the size increases, the maximum absorbance is shifted to longer wavelengths. The results collected here are in agreement with other reports and they indicate no significant change in diameter occurred after surface functionalisation [194, 335]. Figure 3.1.d shows the absorption band of PTX alone at 228 nm [336] while Figure 3.1.e demonstrates the spectrum of PTX-thiol-AuNPs hybrid. A broad band for AuNPs and a band at approximately 230 nm assigned to PTX were observed. The existence of PTX related band with a slight shift to the red indicates the loading of PTX molecules onto the functionalised AuNPs surface.

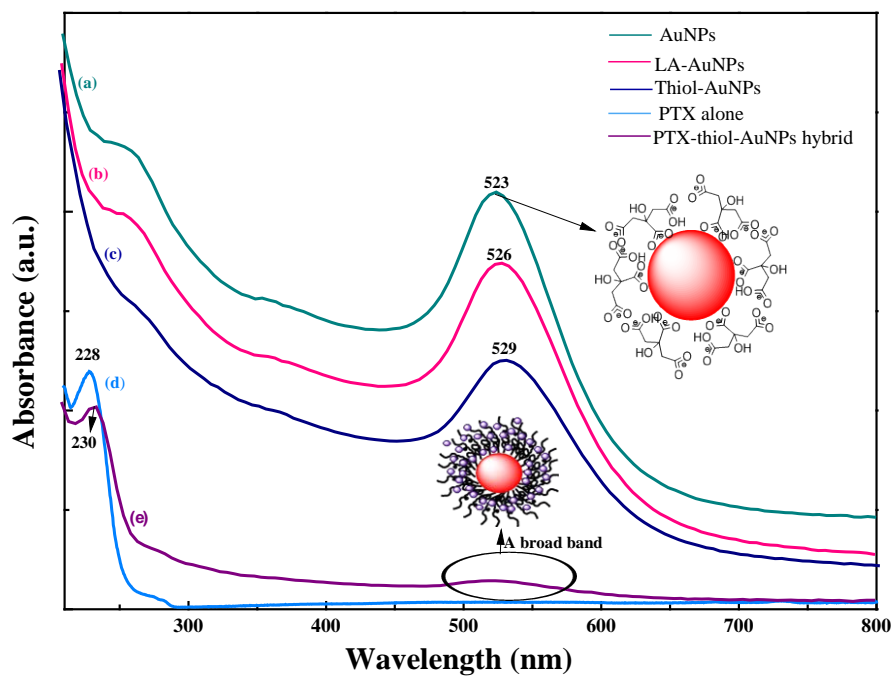


Figure 3.1 UV-Vis spectra of (a) colloidal AuNPs (b) LA-AuNPs (c) thiol-AuNPs (d) PTX alone and (e) PTX-thiol-AuNPs hybrid.

3.3.2 Analytical measurements of transmission electron microscopy (TEM)

Citrate-stabilised AuNPs, LA-AuNPs, thiol-AuNPs and PTX-thiol-AuNPs hybrid were characterised by transmission electron microscopy (TEM) to observe the core size of gold nanoparticles (see [Figure 3.2](#)). The particle size of a minimum of 150 particles of each type of the prepared samples was determined.

[Figure 3.2.a](#) shows the size distribution histogram of core AuNPs. The size distribution histogram shows a narrow size distribution of as prepared AuNPs. Dark spots of gold particles with size of approximately 17 ± 4 nm were recorded. The TEM image indicates the formation of particles with a spherical shape for most of the AuNPs with some triangular particles. These results suggest that the electrostatic stability due to the anionic charges of citrate molecules on the surface of AuNPs was high. [Figure 3.2.b](#) demonstrates the size distribution histogram of core AuNPs after functionalising its surface with LA. LA-AuNPs exhibited similar core size to AuNPs at or close to 17 nm. TEM images of thiol-AuNPs are displayed in [Figure 3.2.c](#). The average size of thiol-AuNPs was approximately 17.46 ± 4.8 nm with spherical particles. The results of TEM support the data obtained from DLS (see [Chapter 3, Section 3.3.3](#)). Paclitaxel was loaded onto the functionalised surface of AuNPs (thiol-AuNPs) by non-covalent interactions. [Figure 3.2.d](#) shows the TEM image and size distribution histogram of PTX-thiol-AuNPs hybrid. The dark particles were assigned to AuNPs whereas the shells may correspond to the loaded layer of thiol ligands and PTX. The average size of approximately 17.5 ± 4.8 nm was recorded.

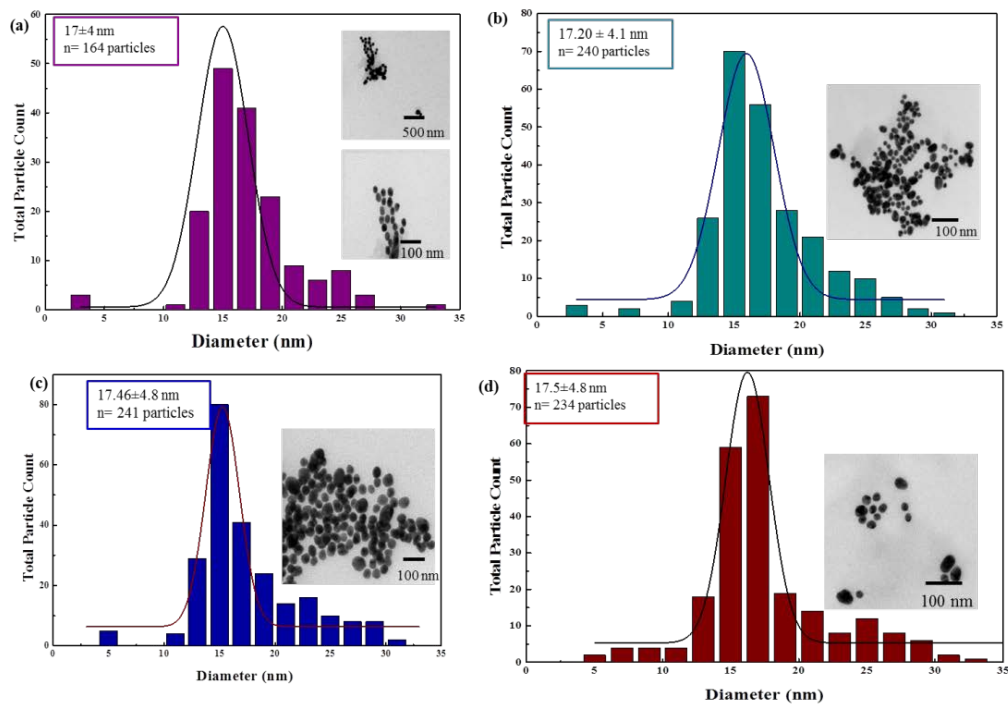


Figure 3.2 TEM images with size distribution histogram of (a) AuNPs (b) LA-AuNPs (c) thiol-AuNPs and (d) PTX-thiol-AuNPs hybrid.

3.3.3 Dynamic light scattering (DLS) measurement and analysis

Dynamic light scattering (DLS) was used to determine the size of the prepared colloidal AuNPs and then compare it with its counterparts after functionalisation and hybridisation. Each sample was diluted with water (1:4, v/v) and the size was characterised by this technique and compared to other techniques. In all data obtained via DLS, intensity distribution of particle size was recorded. In this situation, the measurement of particle size recorded will be significantly affected by the aggregation or larger particles present in the media as those larger particles can affect the distribution causing a larger average diameter for the particles [337]. [Figure 3.3.a](#) displays the intensity size distribution of the AuNPs of approximately 18.58 nm with a narrow size distribution. The polydispersity index, which is the ratio of particles of different size to the total number of particles, for the as prepared AuNPs value was small (0.238) indicating the presence of monodispersed AuNPs. This is in agreement with the size of AuNPs obtained using TEM analysis technique (17 ± 4 nm) indicating the mono-dispersity of AuNPs. After surface functionalisation of AuNPs with thiol ligands, the hydrodynamic size of the particles based on the intensity distribution factor increased (see [Figure 3.3.b](#) and [c](#)). The mean particles size of LA-AuNPs was found to be 21 nm with polydispersity index of 0.214. The particle size recorded by DLS was close to the size of LA-AuNPs measured by TEM (17.20 ± 4.1 nm) (see [Figure 3.3.b](#)). In the case of LA exchanged by 16-MHDA capped AuNPs sample the particle size was 24 nm with polydispersity index of 0.178 ([Figure 3.3.c](#)). To compare between the size values provided by TEM and DLS techniques, the approximate size recorded by TEM for thiol-AuNPs sample was (17.46 ± 4.8 nm), and this value is smaller than the value obtained from DLS (24 nm). This can be attributed to that DLS provides the hydrodynamic diameter of the particles in solution. Generally, both techniques (TEM and DLS) indicate formation of monodispersed colloidal AuNPs.

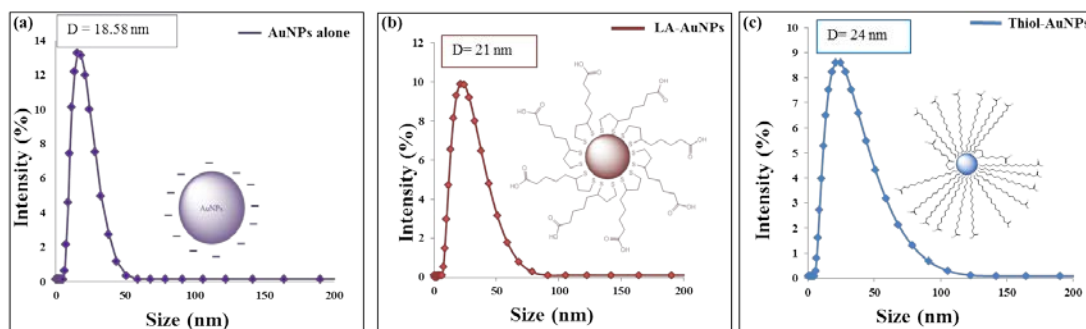


Figure 3.3 DLS measurements for (a) AuNPs colloids (b) LA-AuNPs and (c) thiol-AuNPs.

Lastly, different measurements at different mixing times were conducted for thiol-AuNPs mixed with PTX. The dispersion of the hybrid showed broad size distributions with increasing size. The intensity size distribution of PTX-thiol-AuNPs hybrid ranged between 68 nm and 71.27 nm. The size obtained is reasonable since the PTX were loaded to the functionalised surface (thiol-AuNPs) and this size was determined using DLS. DLS measures the hydrodynamic diameter of the sample in solution while the TEM technique provides the size in the absence of a solvent and the sample should be carefully dried [337]. In addition, this difference can be due to the fact that in TEM, the highly aggregated particles will not be counted; just the dispersed particles will determine the actual particle size while in DLS the larger particles will be measured and recorded and those larger particles dominate the intensity distribution histograms [338]. Moreover, the size measured by DLS is not only associated with the metallic core of the nanoparticles, as in case of using TEM to measure the particle size, but also all molecules or ligands (e.g., linkers and stabilisers) adsorbed on the surface of the nanoparticles influence on the particle size. Thus, the difference of particle size after adding the chemotherapy agent, PTX, could be attributed to the electrostatic interactions between the functionalised AuNPs and PTX molecules loaded on the gold surface and other molecules in the solution leading to self-assembly which would make the thickness surrounding the Au particles larger leading to an increase of the measured particle size [339]. Particle size

measurements based on AuNPs are shown in Table 3.1. The results from DLS analysis for PTX-thiol-AuNPs hybrid are represented in Table 3.2 and Figure 3.4.

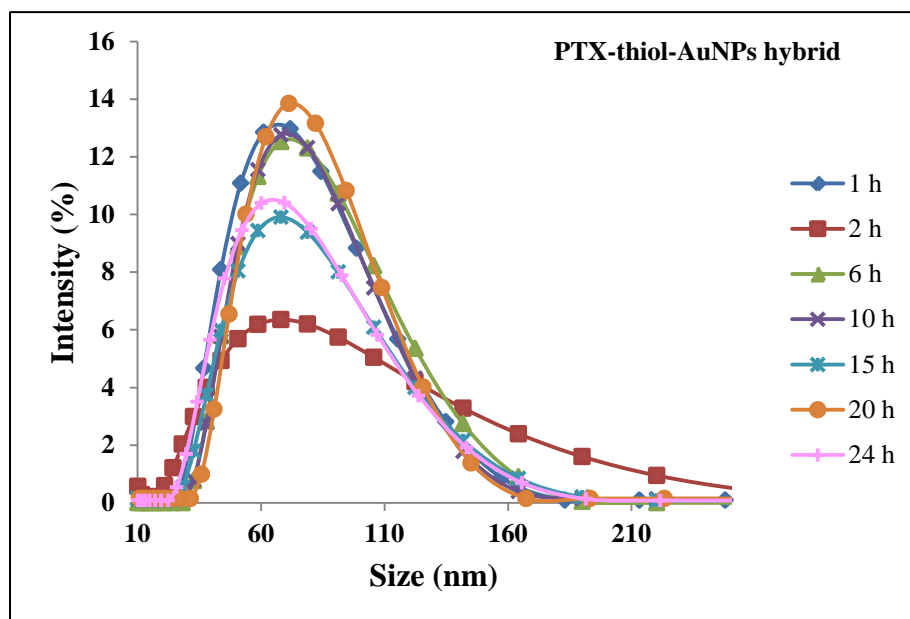


Figure 3.4 DLS measurements for PTX-thiol-AuNPs hybrid at different mixing times.

Table 3.1 Particle size measurements of AuNPs, LA-AuNPs, thiol-AuNPs and PTX-thiol-AuNPs hybrid using TEM and DLS analytical techniques.

Sample	Particle size (nm) using TEM	Particle size (nm) using DLS
AuNPs	17±4	18.58
LA-AuNPs	17.2±4.1	21
Thiol-AuNPs	17.46±4.8	24
PTX-thiol-AuNPs (1 h mixing)	17.5±4.8	71.27

Table 3.2 DLS measurements of PTX-thiol-AuNPs hybrid at different mixing times.

Mixing time (h)	z-average diameter (nm)	Size distribution by intensity (nm)	Intensity (%)	Width (nm)	Polydispersity index
1	30.83	71.27	82	27.45	0.492
2	29.89	68	66	51.28	0.752
6	28.45	68	80	26.44	0.543
10	48.93	68	82	25.66	0.404
15	32.31	68.06	68	28.43	0.697
20	28.31	71.2	87	33.03	0.760
24	40.44	69.5	77	22.08	0.482

3.3.4 FT-IR spectroscopy characterisation

Figure 3.5 shows FT-IR spectra for (a) trisodium citrate (b) AuNPs (c) LA alone (d) LA-AuNPs (e) 16-MHDA alone (f) thiol-AuNPs (g) PTX alone (h) PTX-thiol-AuNPs hybrid. The spectrum of trisodium citrate shows the common characteristic peaks observed in trisodium citrate sample [340]. The peaks at 3445 cm^{-1} and 3264 cm^{-1} are attributed to O-H stretching vibrations while the peaks at 2965 and 2920 cm^{-1} are assigned to asymmetric and symmetric stretching vibrations of methylene groups (CH_2), respectively. The peak at 1579 cm^{-1} is assigned to C=O asymmetric vibration. The band at 1392 cm^{-1} is attributed to C-H bending. The bands at 1273 , 1193 , 1154 , 1080 and 949 cm^{-1} are ascribed to C-O stretching vibrations [340] (see Figure 3.5.a). Figure 3.5.b shows the FT-IR spectrum of the citrate-stabilised AuNPs. A number of bands correlated with the citrate groups linked to the surface of AuNPs were observed. The spectrum of AuNPs shows their main characteristic peaks in agreement with the previously reported literature [341, 342]. The spectrum also shows the absorption band C=O stretching vibrations at 1660 cm^{-1} , a strong absorption band of C=O at 1579 cm^{-1} , the symmetric vibrations of COO^- at 1414 cm^{-1} , the stretching vibrations of C-O at 1020 cm^{-1} and the deformation of C-H at 650 cm^{-1} . Characteristic absorption peaks at approximately 3445 cm^{-1} and 3292 cm^{-1} are assigned to the presence of hydroxyl groups ($-\text{OH}$) of the citrate stabilised AuNPs. These observations indicate the successful formation of AuNPs.

LA was used to functionalise the surface of the prepared AuNPs. Figure 3.5.c shows FT-IR peaks of LA alone. The spectrum shows the main characteristic peaks observed in pristine LA sample [343, 344]. The absorption peaks at 2931 cm^{-1} and 2860 cm^{-1} are assigned to asymmetric and symmetric stretching vibrations of C-H, respectively. The band at 1693 cm^{-1} is ascribed to C=O of the carboxylic group. The band at 1465 cm^{-1} is attributed to CH_2 stretching while the peak at 1250 cm^{-1} is assigned to O-H stretching vibration of carboxylic group. In addition, the band at 931 cm^{-1} is assigned to O-H stretching vibrations and the band at 675 cm^{-1} is attributed to S-C. Disulfide stretching S-S bands usually can be seen in the region between 500 - 400 cm^{-1} [343, 344]. The main characteristic bands of pure LA were observed after capping LA onto AuNPs (see Figure 3.5.d). The resulting spectrum is compatible with the previously reported literature [296]. The splitting of the bands at 1644 and

1621 cm^{-1} due to C=O stretching vibrations imply the functionalisation of the surface of AuNPs with LA. This splitting may be due to the interactions between oxygen and the surface of AuNPs. The peak at 1410 cm^{-1} is due to symmetric stretching vibrations of COO^- [296]. A broad band between 3582 and 3108 cm^{-1} is due to hydroxyl groups from water molecules. Also, the stretching vibration of C-O at 1050 cm^{-1} and the deformation of C-H at 630 cm^{-1} were observed. Asymmetric and symmetric vibrations of methylene groups (CH_2) at 2925 and 2860 cm^{-1} are strongly visible in [Figure 3.5.d](#) and undetectable for citrate stabilised AuNPs in [Figure 3.5.b](#) indicating the successful attachment of LA onto AuNPs surface [296]. Lin et al. [296] also observed that the asymmetric and symmetric vibrations of methylene groups were strong in LA functionalised AuNPs while unnoticeable for citrate stabilised AuNPs [296].

The spectrum of pristine 16-MHDA shows the common characteristic bands observed for 16-MHDA [345] (see [Figure 3.5.e](#)). The peaks at 2915 cm^{-1} and at 2850 cm^{-1} are assigned to asymmetric and symmetric stretching vibrations of methylene groups (CH_2), respectively. The band at 1695 cm^{-1} is ascribed to C=O stretching vibrations of carboxylic group. The asymmetric and symmetric stretching vibrations of the O-C-O group were observed at 1469 cm^{-1} and 1428 cm^{-1} , respectively. A weak band at 2553 cm^{-1} is attributed to thiol group (S-H group) vibrations in 16-MHDA (see [Figure A.1](#) in [Appendix A](#)) and the band at 3033 cm^{-1} is attributed to O-H stretching vibration were observed [345]. In LA exchanged by 16-MHDA functionalised AuNPs (thiol-AuNPs), the characteristic absorption bands were observed and the spectrum is in agreement with other literature reported previously [346, 347] (see [Figure 3.5.f](#)). The absorption bands between ~ 3536 and 3230 cm^{-1} due to O-H stretching vibrations from water molecules were observed while the peaks at 2918 and 2849 cm^{-1} are attributed to asymmetric and symmetric stretching vibrations of methylene groups. The C=O stretching vibrations of the carboxylic group was observed at 1702 cm^{-1} [160]. The spectrum also shows asymmetric and symmetric stretching vibrations from O-C-O at 1640 and 1560 cm^{-1} [296], the C-H deformation of the alkyl group at 1404 cm^{-1} [346, 347], C-O stretching at 1020 cm^{-1} , C-S bending at 806 cm^{-1} and C-H bending at 646 cm^{-1} . The band at 2553 cm^{-1} assigned to S-H vibrations in free 16-MHDA disappeared after capping the 16-MHDA ligands to AuNPs indicating the successful attachment of 16-MHDA onto the AuNPs surface

(see [Figure A.1](#) in [Appendix A.1](#)) [345]. [Figure A.1.a](#) in [Appendix A.1](#) shows S-H band in free 16-MHDA while [Figure A.1.b](#) in [Appendix A.1](#) shows disappearance of this band after exchanging LA by 16-MHDA ligands.

The FT-IR spectrum of pristine PTX was also carried out. It shows the common characteristic bands observed in PTX [348, 349]. [Figure 3.5.g](#) shows the absorbance bands for pristine PTX. The peaks at 3514-3405 cm^{-1} are assigned to N-H and O-H stretching vibrations. The peaks at 2971 cm^{-1} and at 2891 cm^{-1} are attributed to asymmetric and symmetric stretching vibrations of methylene groups (CH_2), respectively. While the bands at 1735 and 1713 cm^{-1} are attributed to the carbonyl group (C=O) stretching vibrations from the ester groups. The C-N stretching vibrations are located at 1273 cm^{-1} and at 1247 cm^{-1} and the absorbance bands located at 1607, 1584, 1076, 943 and 705 cm^{-1} are ascribed to aromatic groups [348, 349]. The peak at 1645 cm^{-1} is due to the amide I. The FT-IR spectrum of PTX-thiol-AuNPs hybrid displays characteristic bands of both alkanethiol molecules and free PTX (see [Figure 3.5.h](#)). The absorption peaks at 2957 cm^{-1} and at 2893 cm^{-1} are due to asymmetric and symmetric stretching vibrations of methylene groups, respectively. The bands between 3681 and 3317 cm^{-1} are due to N-H stretching vibrations of PTX and O-H stretching vibrations which exist in the PTX structure, the peak at 3127 cm^{-1} is due to ($-\text{OH}$) groups from water molecules, the peak at 1640 cm^{-1} is attributed to the amide I of PTX while the band at 1720 cm^{-1} is attributed to the carbonyl group C=O stretching vibrations from the ester group. In addition, the peak situated at 1697 cm^{-1} is attributed to C=O stretching vibration of terminal carboxylic groups in alkanethiol acids [160] while the peaks at 1484 cm^{-1} and 654 cm^{-1} are due to C-H stretching and bending vibrations, respectively. The peak at 1090 cm^{-1} is assigned to C-O stretching vibrations. The band at 1410 cm^{-1} is assigned to symmetric stretching vibrations of COO^- [348, 349]. In addition, the absorption bands for PTX-thiol-AuNPs hybrid were broader than the bands for PTX and alkanethiol linkers indicating the successful loading of PTX onto the surface of AuNPs. The appearance of the main characteristic peak of PTX at 1720 cm^{-1} implies the successful loading of the chemotherapy agent, PTX, onto the functionalised AuNPs by hybridisation. These findings were in agreement with the results obtained by NMR as discussed in the next section.

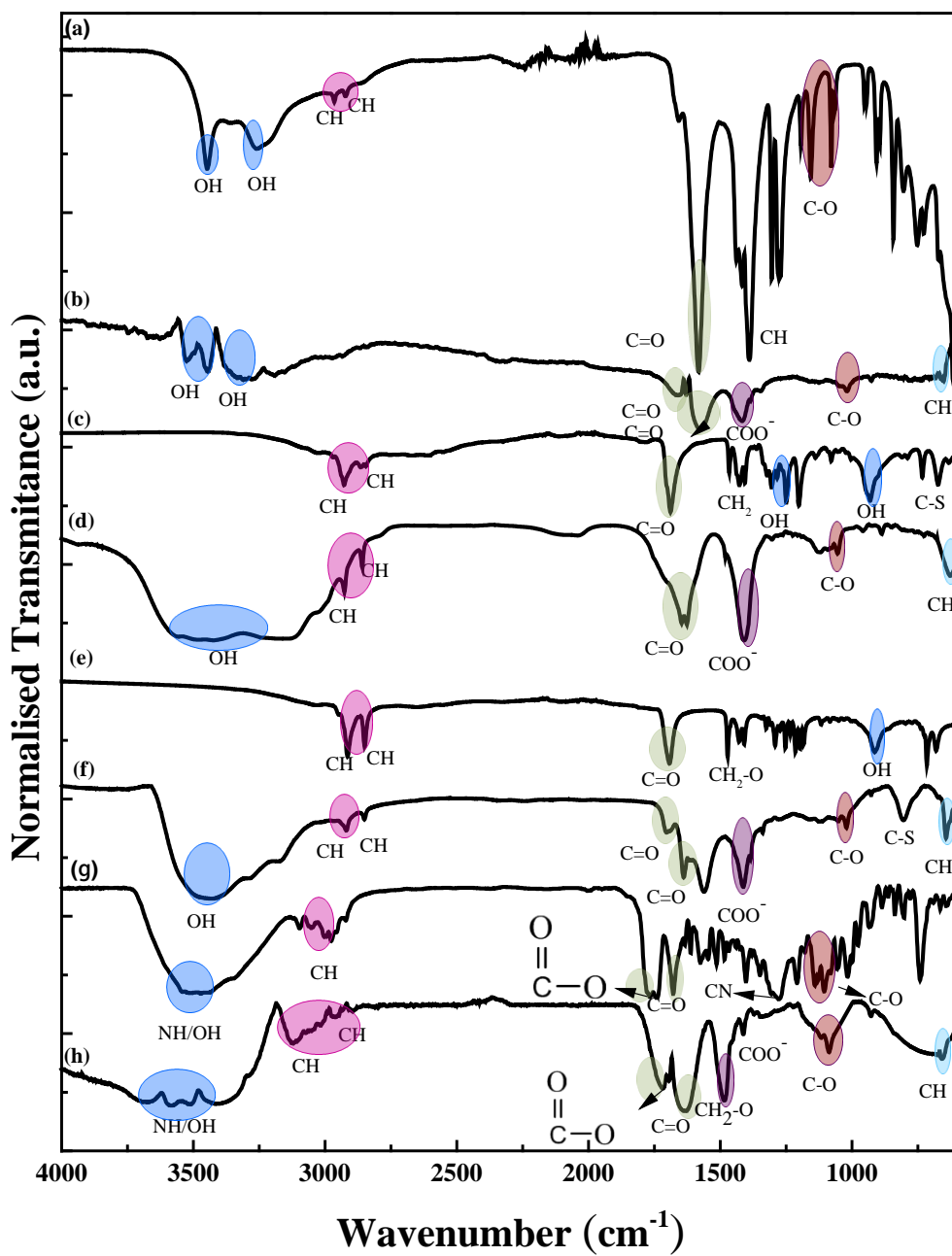


Figure 3.5 FT-IR spectra of (a) trisodium citrate (b) AuNPs colloids (c) LA alone (d) LA-AuNPs (e) 16-MHDA alone (f) thiol-AuNPs (g) PTX alone and (h) PTX-thiol-AuNPs hybrid.

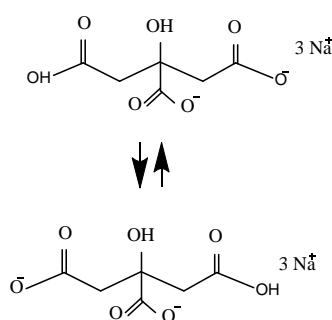
Table 3.3 FT-IR peak positions of trisodium citrate, AuNPs, pristine LA, LA-AuNPs, pristine 16-MHDA, thiol-AuNPs, pristine PTX and PTX-thiol-AuNPs hybrid.

Vibrational modes	O-H	C-H symmetric and asymmetric stretching	C=O stretching of esters	C=O stretching of carboxylic acid	C-O stretching	C-H bending
WN (cm ⁻¹)/ Trisodium citrate	3445, 3264	2965, 2920	1579	-	1273, 1193, 1154, 1080 and 949	1389
WN (cm ⁻¹)/ AuNPs alone	3445-3292	-	1660-1579	-	1020	650
WN (cm ⁻¹)/ Pristine LA	3021, 1250, 931	2931, 2860	-	1693	-	-
WN (cm ⁻¹)/ LA-AuNPs	3582 -3108	2925,2860	-	1644-1621 and the peak at ~1693 cm ⁻¹ not observed may due to peak overlap	1050	630
WN (cm ⁻¹)/ Pristine 16-MHDA	3033	2915, 2850	-	1695	-	-
WN (cm ⁻¹)/ Thiol-AuNPs	3536 -3230	2918, 2849	-	1640-1560 and 1702	1020	646
WN (cm ⁻¹)/ Pristine PTX	3514 - 3405	2971, 2891	1735-1713	-	-	-
WN (cm ⁻¹)/ PTX-thiol-AuNPs	3681-3317, 3127	2957, 2893	1720	1697-1640	1090	654

3.3.5 ^1H NMR spectroscopy characterisation of PTX-thiol-AuNPs hybrid

3.3.5.1 ^1H NMR spectroscopy characterisation of gold nanoparticles

^1H NMR was carried out on most of the novel nanoconjugates. D_2O was used as a solvent in the analysis of citrate stabilised AuNPs. [Figure 3.6](#) exhibits two doublet signals assigned to the protons of the two methylene groups $-\text{CH}_2$. One signal at $\delta = 2.49$ and 2.52 ppm and another one at $\delta = 2.58$ and 2.61 ppm. Those protons are diastereotopic meaning each signal couples only to itself. In addition, the shoulders in those signals can be attributed to the presence of complementary doublet peaks underneath those large signals [350]. It was noticed that one of the signals is larger than the other one. This can be attributed to a rapid exchange between these hydrogens in citrate molecules as shown in [Scheme 3.1](#):



Scheme 3.3 Rapid exchange between hydrogens in citrate molecules.

The spectra and the chemical shift of the citrate-stabilised gold colloids are shown in [Figure 3.6](#).

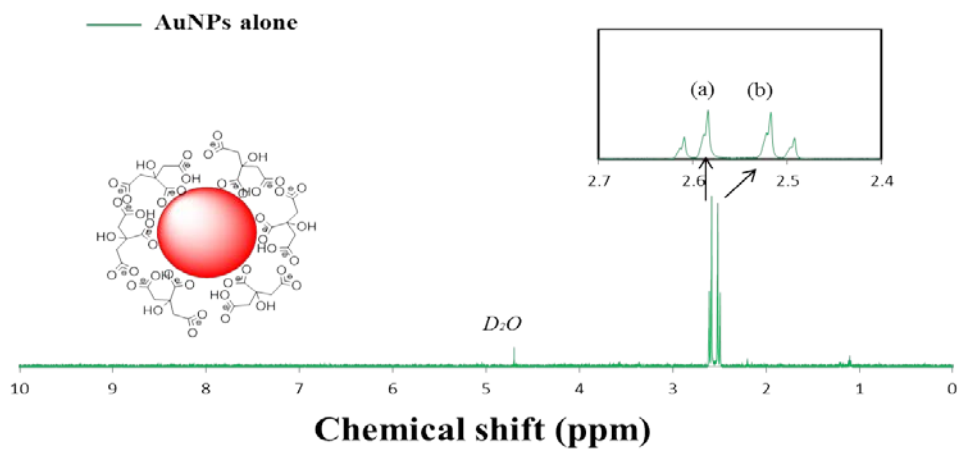


Figure 3.6 ^1H NMR spectra of AuNPs colloids.

3.3.5.2 ^1H NMR spectroscopy characterisation of LA attached AuNPs

Functionalisation the surface of AuNPs via LA ligands (LA-AuNPs) was confirmed by ^1H NMR spectroscopy. Compared to AuNPs alone, only peaks assigned to LA molecules were observed (see [Figure 3.7](#) and [Table 3.4](#)).

The signals ($\text{H}_{2\text{A}, 2\text{B}}$) which correspond to the methylene group next to the carboxylic acid ($-\text{COOH}$) appeared as a triplet at $\delta = 2.4$ ppm in both LA alone and LA-AuNPs samples without showing any chemical shifts. The H_6 proton was observed as multiple signals at $\delta = 3.57$ ppm in free LA. However, this proton was broadened in LA-AuNPs compared to that of free LA and it shifted slightly downfield at $\delta = 3.67$ ppm with $\Delta\delta = 0.1$ ppm. The reason for the spectral broadening is that methylene moieties close to thiolate/AuNPs are packed more densely than the methylene moieties further from the NPs, so they experience rapid spin relaxation from dipolar interactions and their spectra are broadened. On the other hand, the methylene groups further from the NPs possess free motion and spin relaxations, so they show narrower peaks as was observed in the protons of the methylene group close to carboxylic ($-\text{COOH}$) [351]. The $\text{H}_{8\text{A}, 8\text{B}}$ protons disappeared in the spectrum of LA-AuNPs (see [Figure 3.7](#)) because these protons on C_8 are close to the sulfur (S) atom and this finding is in agreement with a study conducted by Epple's group [352]. In their study, they prepared ultra-small silver-gold nanoparticles using sodium borohydride as a reducing agent and 11-mercaptoundecanoic acid (11-MUA) as a capping agent. It was noticed that, the α -methylene protons next to the thiol group disappeared after functionalising the nanoparticles with 11-MUA ligand [352]. Moreover, the peaks for H_4 appeared as multiplet shifted to higher field from $\delta = 1.5$ ppm in pure LA to $\delta = 0.9$ ppm in LA-AuNPs with $\Delta\delta = 0.6$ ppm. The H_3 peaks showed multiplet signals at $\delta = 1.7$ ppm in both LA alone and LA-AuNPs samples and no change in chemical shift was observed. The H_5 protons and $\text{H}_{7\text{A}}$ appeared as multiplet at $\delta = 1.92$ ppm in both LA alone and LA-AuNPs without a change in chemical shift. The shifting and broadening of some of the peaks in the spectrum for LA-AuNPs samples can be attributed to the attachment of LA onto the surface of AuNPs by the ligands exchange between the citrate molecules on AuNPs and sulfur atoms on LA which indicates the successful functionalisation the surface of AuNPs with LA ligands.

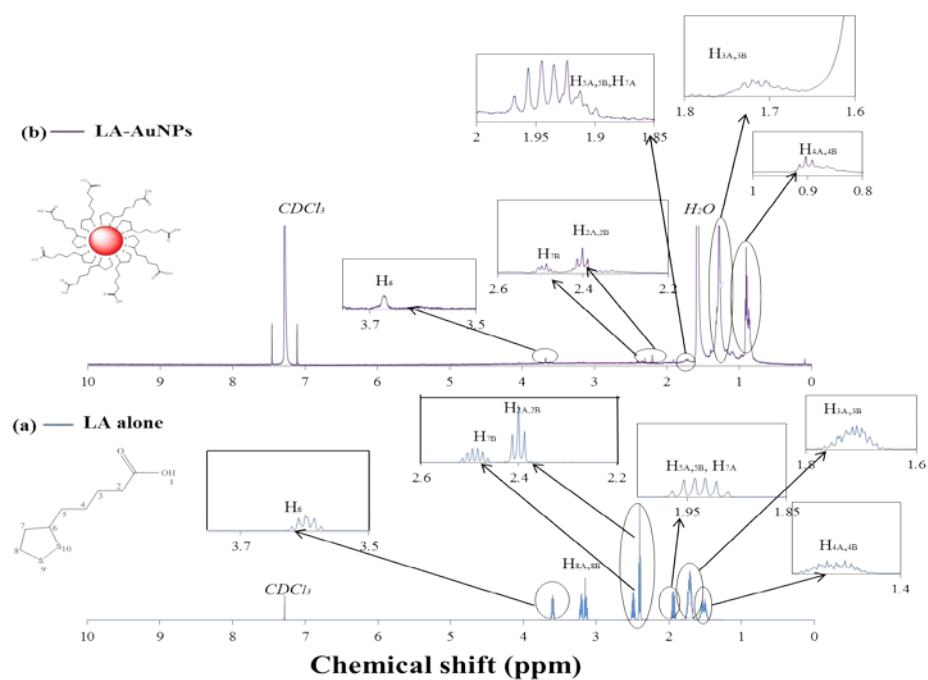


Figure 3.7 ^1H NMR spectra of (a) free LA molecules and (b) LA-AuNPs.

The chemical shift data for LA-AuNPs and free LA is shown in [Table 3.4](#).

Table 3.4 Chemical shifts (δ/ppm) of LA functionalised AuNPs and free LA.

Peak position	Peak assignment	δ (ppm) of free LA	δ (ppm) of LA-AuNPs	$\Delta\delta$ (ppm)
H ₁	O=C-OH	11.4 (undetectable)	11.4 (undetectable)	0
H _{2A,2B}	C-CH ₂	2.4	2.4	0
H _{3A,3B}	C-CH ₂	1.7	1.7	0
H _{4A,4B}	C-CH ₂	1.50	0.9	0.6
H _{5A,5B}	C-CH ₂	1.92	1.92	0
H ₆	S-CH ₂	3.57	3.67	0.1
H _{7A}	S-CH ₂ -CH ₂	1.92	1.92	0
H _{7B}	S-CH ₂ -CH ₂	2.46	2.46	0
H _{8A}	S-CH ₂	3.18	Disappeared	0
H _{8B}	S-CH ₂	3.12	Disappeared	0

3.3.5.3 ^1H NMR spectroscopy characterisation of thiol functionalised AuNPs

Figure 3.8 and Table 3.5 compare the ^1H NMR spectra for thiol-AuNPs and free 16-MHDA molecules. Badia and co-workers [353] found that the long chain alkanethiol modified the AuNPs surface is in a semicrystalline state [353]. Figure 3.8.a represents the ^1H NMR spectra of pristine 16-MHDA. Triplet peaks at $\delta = 2.7$ ppm are due to thiol proton (H_{17}) on sulfur atom, quartet peaks at $\delta = 2.54$ ppm are attributed to protons on C_{16} adjacent the sulfur atom, triplet spectra at $\delta = 2.37$ ppm are assigned to the protons on C_2 adjacent the carboxylic group. Also, multiplet peaks at $\delta = 1.64$ ppm and at 1.28 ppm correspond to the interior alkyl protons of 16-MHDA [352]. The proton on carbonyl carbon was undetectable.

In comparison to pure 16-MHDA, thiol-AuNPs showed the peaks corresponding to 16-MHDA (see Figure 3.8.b). The triplet peaks of thiol proton (H_{17}) on sulfur atom at $\delta = 2.7$ ppm disappeared after exposing 16-MHDA to the LA-AuNPs mixture. On the other hand, the triplet protons on C_2 at $\delta = 2.37$ ppm due to the protons close to the carbonyl group were still observed indicating that those protons are intact. The interior alkyl protons observed as multiplet at $\delta = 1.64$ ppm in 16-MHDA alone were slightly shifted upfield at $\delta = 1.59$ ppm with $\Delta\delta = 0.05$ ppm. Other peaks (the interior alkyl protons at $\delta = 1.28$ ppm, protons on C_2 at $\delta = 2.37$ ppm and those on C_{16} at $\delta = 2.54$ ppm) did not show any change in chemical shifts (see Figure 3.8.b). No signals assigned to LA were observed. This can be attributed to replacement of most of LA molecules with 16-MHDA and the gold surface was largely covered with the 16-MHDA ligands as expected.

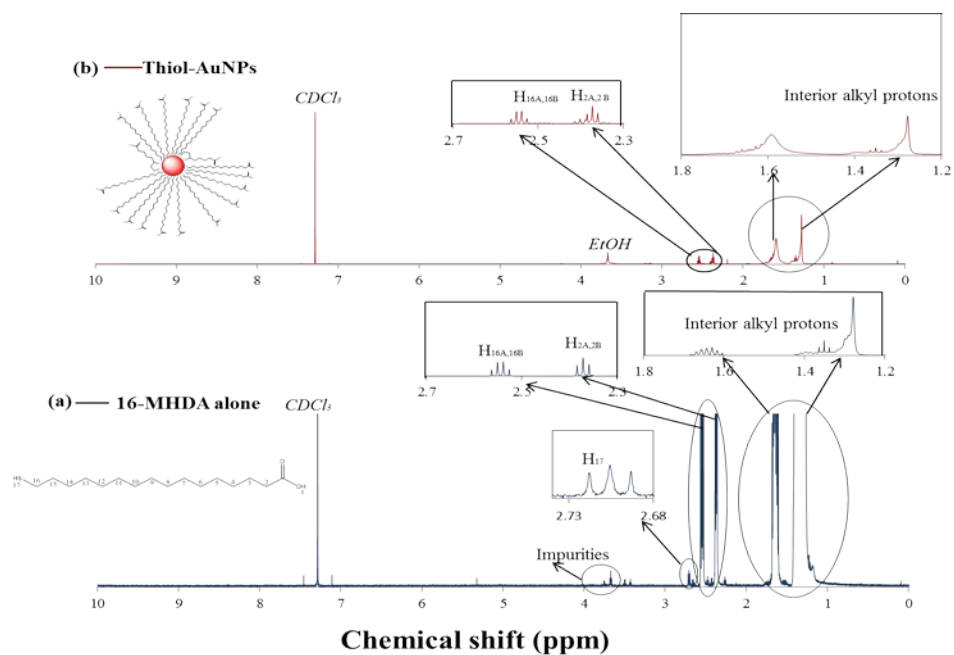


Figure 3.8 ^1H NMR spectra of (a) free 16-MHDA and (b) thiol-AuNPs.

Table 3.5 Chemical shifts (δ/ppm) of free 16-MHDA and thiol-AuNPs.

Peak position	Peak assignment	δ (ppm) of free 16-MHDA	δ (ppm) of thiol-AuNPs	$\Delta\delta$ (ppm)
H ₁	O=C-OH	10.8 (undetectable)	10.8(undetectable)	0
H _{2A,2B}	$\text{CH}_2 - \overset{\text{O}}{\parallel}{\text{C}}$	2.37	2.37	0
From H _{3A,3B} to H _{15A, 15B} (interior alkyl protons)	CH ₂ -CH ₂	1.28, 1.64	1.28, 1.59	0, 0.05
H _{16A, 16B}	HS-CH ₂	2.54	2.54	0
H ₁₇	S-H	2.7	Disappeared	0

3.3.5.4 ¹H NMR spectroscopy characterisation of PTX-thiol-AuNPs hybrid

¹H NMR spectrum of pure PTX [354, 355] is used as a reference for analysing the following data for PTX-thiol-AuNPs hybrid sample (see [Table 3.6](#)). Chloroform (CDCl₃) was chosen as a solvent for PTX alone and PTX-thiol-AuNPs hybrid samples because it possesses non-polar nature providing similar environment to the hydrophobic PTX [354]. Despite of the complexity of the PTX structure, its NMR signals can be easily assigned. The PTX signals are observed in the region between 1.0 and 8.5 ppm. Strong proton signals represent the methyl and acetate groups distributed in the region between 1.0 and 2.5 ppm. The majority of the protons in the taxane skeleton and the side-chain are located between 2.5 and 7.0 ppm. The proton signals in the aromatic structure caused by the C₂ benzoate, C₃' phenyl and C₃' benzamide groups are observed between 7.0 and 8.2 ppm [356] (proton integrations of PTX are shown in [Appendix A.2](#)). The ¹H NMR spectra generally show no significant differences in chemical shifts between PTX alone and PTX-thiol-AuNPs hybrid samples. However, slight shifts upfield for H₆ on C₆ and C₇-OH protons were observed (see [Table 3.6](#)). Moreover, importantly, the peaks for C₂'-OH and C₇-OH of PTX are still observed after mixing with thiol-AuNPs indicating no chemical reaction occurred between PTX and the thiol groups. Also, the other functional groups on PTX remained unchanged and the chemical shifts for most peaks did not show any changes after hybridisation (see [Table 3.6](#) and [Figure 3.9](#)). These results prove the physical interactions of van der Waals forces between PTX and the thiol-AuNPs ligands. The peaks related to the 16-MHDA and LA were difficult to detect. This may be due to the fact that the PTX molecules cover the surface of the functionalised AuNPs.

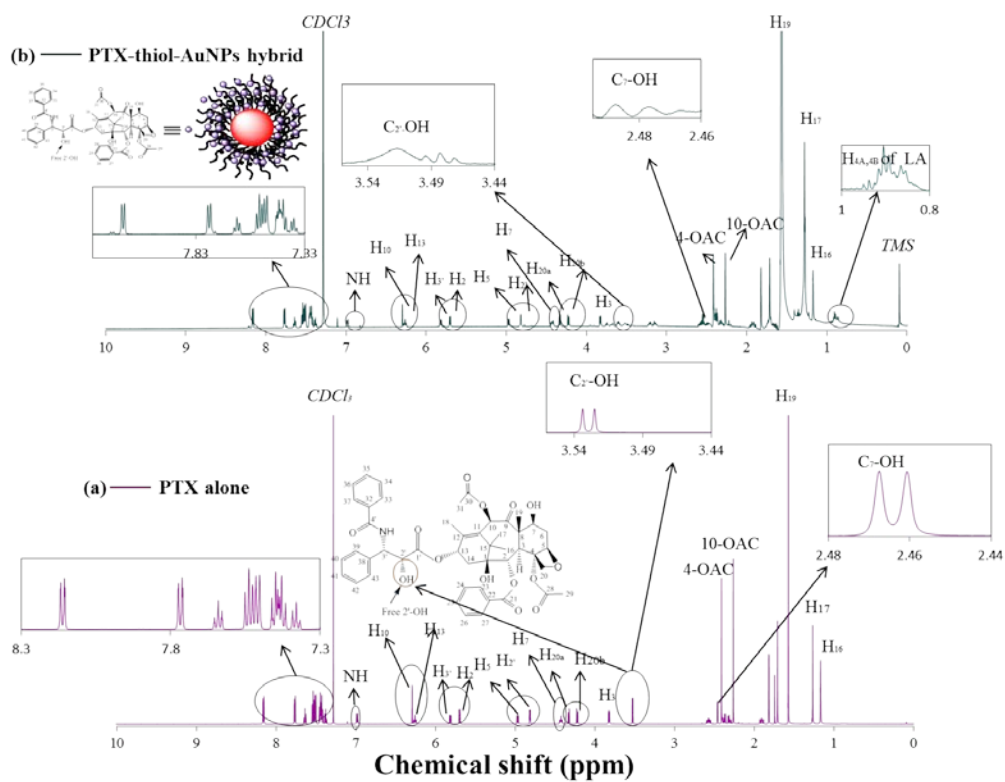


Figure 3.9 ^1H NMR spectra of (a) PTX alone and (b) PTX-thiol-AuNPs hybrid.

Table 3.6 Chemical shifts (δ /ppm) of PTX alone and PTX-thiol-AuNPs hybrid.

Peak position	δ (ppm) of free PTX	δ (ppm) of PTX-thiol-AuNPs hybrid	$\Delta\delta$ (ppm)
C ₁	4.41 (multiplet)	4.41 (multiplet)	0
C ₂	5.69 (doublet)	5.69 (doublet)	0
C ₃	3.81 (doublet)	3.81 (doublet)	0
C ₄ -OAC	2.38 (singlet)	2.38 (singlet)	0
C ₅	4.81 (two doublet signals)	4.81 (two doublet signals)	0
C ₆	2.57 (doublet), 1.91 (doublet)	3.1 (doublet), 1.92 (doublet)	0.53, 0.01
C ₇	4.43 (multiplet)	4.43 (multiplet)	0
C ₁₀	6.27 (singlet)	6.27 (singlet)	0
C ₁₃	6.24 (triplet)	6.24 (triplet)	0
C ₁₄	2.32 (doublet), 2.27(doublet)	2.32 (doublet), 2.27 (doublet)	0
C ₁₆	1.16 (singlet)	1.16 (singlet)	0
C ₁₇	1.26 (singlet)	1.26 (singlet)	0
C ₁₈	1.70 (singlet)	1.70 (singlet)	0
C ₁₉	1.76 (singlet)	1.76 (singlet)	0
C ₂₀	4.29 (doublet), 4.21 (doublet)	4.29 (doublet), 4.21 (doublet)	0
C _{23,27}	8.15 (two doublet signals)	8.15 (two doublet signals)	0
C _{24,26}	7.49 (multiplet)	7.49 (multiplet)	0
C ₂₅	7.64 (multiplet)	7.64 (multiplet)	0
10-OAC	2.41 (singlet)	2.41 (singlet)	0
C ₃₁	2.26 (multiplet)	2.26 (multiplet)	0
C _{33,37}	7.46 (multiplet)	7.46 (multiplet)	0
C _{34,36}	7.37 (multiplet)	7.37 (multiplet)	0
C ₃₅	7.33 (multiplet)	7.33(multiplet)	0
C _{39,43}	7.75 (multiplet)	7.75 (multiplet)	0
C _{40,42}	7.4 (multiplet)	7.4 (multiplet)	0
C ₄₁	7.47 (multiplet)	7.47 (multiplet)	0
C _{2'}	4.80 (quartet)	4.80 (quartet)	0
C _{3'}	5.80 (two doublet)	5.80 (two doublet)	0
C ₂ -OH	3.53 (doublet)	3.53 (doublet)	0
C ₁ -OH	1.80 (singlet)	1.80 (singlet)	0
C ₇ -OH	2.47 (two doublet)	2.49 (two doublet)	0.05
N-H	7.11(doublet)	7.11 (doublet)	0

3.3.6 Drug loading studies of PTX-thiol-AuNPs hybrid

The loading efficiency of anticancer PTX was investigated using UV-Vis spectrophotometry. Typically, seven samples of PTX-thiol-AuNPs hybrid at the same concentrations were incubated at room temperature for certain mixing times (see [Table 3.7](#) and [Figure 3.12](#)). For each sample, 3.5 mL of thiol-AuNPs were treated with 1.5 mL of PTX solution (3 mg PTX in 10 mL EtOH). The mixture was left stirring at room temperature for certain times (1 h, 2 h, 6 h, 10 h, 15 h, 20 h and 24 h). After that, the samples were resuspended in PBS (pH 7.4) and centrifuged at 15700 g for 15 minutes 5 times (see [Figure 3.10](#)). The pellets for each sample were redispersed in PBS (7.4). The NPs pellets were diluted and characterised by UV-Vis to measure the concentration of PTX loaded on the functionalised AuNPs and the concentration of AuNPs. The supernatant for each sample was gently dried to concentrate the PTX and other constituents. Then, the dried supernatant contents were redissolved in appropriate amounts of EtOH and characterised by UV-Vis spectrophotometry to measure the concentration of PTX (see [Figure 3.11](#)). This was then used to determine the mass of PTX in supernatant in order to be able to determine the total mass of PTX recovered from the NPs and supernatant and compare it with the initial amount of PTX used (0.45 mg) (see [Table 3.7](#) and see [Appendix A.3](#) for more details).

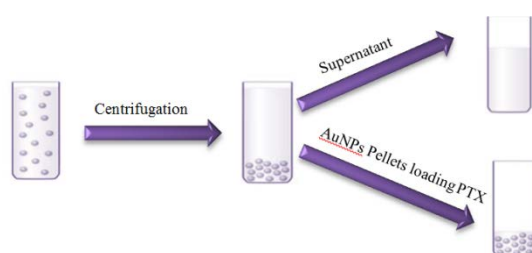


Figure 3.10 Experimental procedure for determining the composition of PTX-thiol-AuNPs hybrid after centrifugation.

To determine the number of PTX molecules in each AuNPs complex, the absorbance bands of PTX loaded to the thiol-AuNPs and free PTX in supernatant from the seven samples made with different mixing times were measured using UV-Vis

spectrophotometry. The absorbance peaks of PTX for different measurements were obtained by subtracting the normalised PTX-thiol-AuNPs hybrid spectra from the thiol-AuNPs spectra (Figure 3.11).

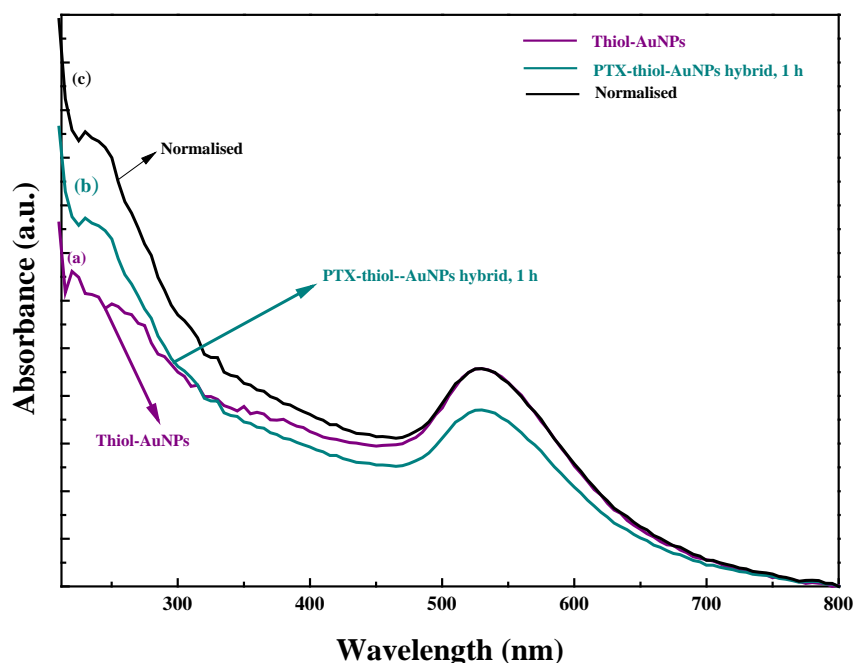


Figure 3.11 UV-Vis spectra of (a) thiol-AuNPs (b) PTX-thiol-AuNPs hybrid and (c) normalised spectrum.

The relationship between these absorbance values and the concentrations were obtained using Beer–Lambert law ($A = \epsilon \ell c$), where ϵ is the molar extinction coefficient of PTX = $29.8 \text{ mM}^{-1} \text{ cm}^{-1}$ [305], $\ell = 1 \text{ cm}$ while the molar extinction coefficient of AuNPs obtained from Sigma Aldrich = $9.21 \times 10^8 \text{ M}^{-1} \text{ cm}^{-1}$ [299]. Then, the number of moles of thiol-AuNPs was calculated from the known solution or suspension volumes of the samples. The results from these measurements for the experiments involving the production of hybrid PTX-thiol-AuNPs by mixing for different lengths of time are shown in Figure 3.13 and Table 3.7. The total amount of PTX observed in the supernatant after centrifugation plus that on the NPs was found to be constant for the different loading times and about equal to the total amount of PTX added during fabrication when the expected processing losses are considered (Figure 3.13).

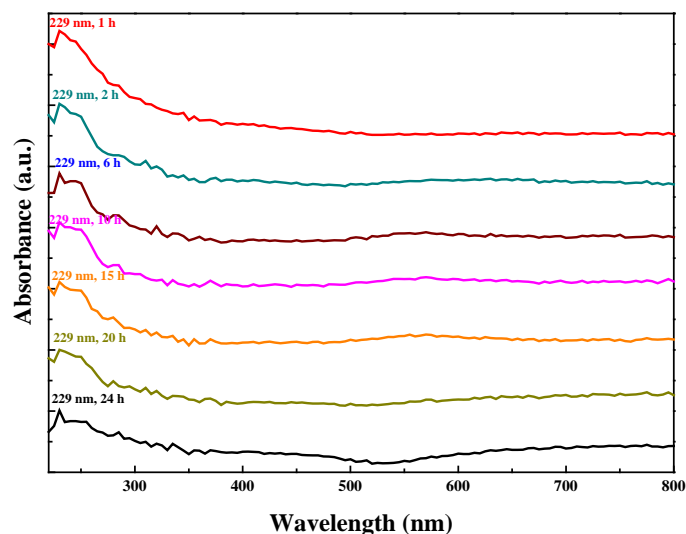


Figure 3.12 Subtracted UV-Vis spectra for PTX absorption on thiol-AuNPs at different times.

Table 3.7 Drug loading for PTX-thiol-AuNPs hybrid samples.

Mixing time (h)	Absorbance of PTX on functionalised surface of AuNPs (a.u.)	Conc. of PTX on thiol-AuNPs (μM)	Mass of PTX on thiol-AuNPs (mg)	Absorbance of PTX in supernatant (a.u.)	Conc. of PTX in supernatant (μM)	Mass of PTX in supernatant (mg)	Total mass of PTX (mg)
1	0.078	2.6	0.033	0.29	9.7	0.124	0.158
2	0.074	2.48	0.0317	0.47	15.8	0.202	0.234
6	0.070	2.3	0.0295	0.6	20	0.256	0.285
10	0.062	2.1	0.0267	0.65	21.8	0.279	0.306
15	0.061	2.05	0.026	0.66	22	0.282	0.308
20	0.05	1.879	0.0241	0.7	23.5	0.301	0.325
24	0.071	2.4	0.03	0.62	20.8	0.266	0.297

PTX-thiol-AuNPs hybrids were prepared by physically mixing thiol modified AuNPs (thiol-AuNPs) with PTX solution. For these nanoparticles there is no chemical connection between the PTX and the AuNPs. However, because of charge attractions and the hydrophobic nature of the long thiol chains and the drug molecule, PTX molecules interact with the functionalised AuNPs and stay associated with the nanoparticles. There is a relationship between the time the AuNP and PTX were mixed during the generation of the hybrid and the amount of PTX found to be

present in the hybrid (see Figure 3.13). The data acquired for various drug loaded on the thiol-AuNPs were plotted versus the data for free drug in the supernatant as a function with the time.

Figure 3.13 represents the loading amounts of PTX on the thiol-AuNPs (rhombus) and the free PTX in the supernatant (square). In general, the mass of PTX on thiol-AuNPs in the first 20 hours decreased as the mass of the drug in supernatant increased in the same duration. This meant that the highest loadings of drug could be obtained at the shorter times. With longer exposure times it is likely that the PTX may decompose in the aqueous environment leading to improved solubility of the decomposition products and lowering the amount of PTX attachment.

The hybrid used to treat the cells was from a mixing time of 1 h, which had a PTX loading of 0.033 mg (see Table 3.7).

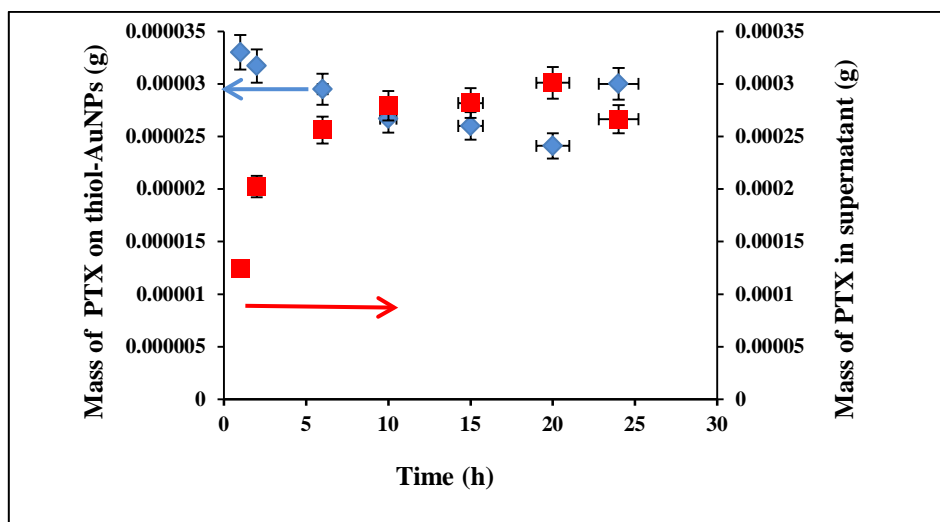


Figure 3.13 Loading curves for the hybrid AuNPs prepared using different interaction times between the AuNPs and PTX solution. The amount of PTX attached to the AuNPs is on the left axis (blue symbols) and the remaining free PTX (red symbols) is on the right axis.

The loading percentage of PTX on thiol-AuNPs was determined based on a method reported by Joshi et al. [357] using UV-Vis spectrophotometry. The absorption band of PTX, mixed with thiol-AuNPs for 1 h to synthesis PTX-thiol-AuNPs hybrid sample, was measured at 230 nm and the percentage of loading was assessed using the following equation:

$$\% \text{ loading} = A - \frac{B}{A} \times 100 = 0.6 - \frac{0.34}{0.6} \times 100 = 43 \%$$

Where A is the optical density (OD) of the total PTX added to thiol-AuNPs medium (see Figure 3.1 in Section 3.3.1, Chapter 3) and B is the OD of free PTX in the supernatant of PTX-thiol-AuNPs collected after centrifugation (Figure 3.12). The estimated loading percentage for PTX on thiol-AuNPs was 43 %.

3.3.7 Cytotoxicity assay for PTX-thiol-AuNPs hybrid

Experiments on breast cancer cell lines to investigate the *in vitro* effectiveness of the unique designed synthetic approach of PTX-thiol-AuNPs hybrid towards a novel delivery system were performed in the School of Medical Science and Technology, Flinders University, South Australia, by collaborating with Assoc.Prof. Barbara Sanderson and a PhD student, Daniela Figueroa. A detailed description of the experiments and results is in [Appendix C.1](#) and [C.2](#), respectively.

Briefly, a human ductal breast epithelial tumour cell line (T47D) was treated with a range of concentrations of thiol-AuNPs, PTX-thiol-AuNPs hybrid and the free PTX for different periods of time between 1 and 24 h of treatment to investigate the relative cell survival compared to untreated controls following the 3-(4,5-dimethylthiazol-2-yl)-2,5-diphenyltetrazolium bromide (MTT) procedure. [Figure 3.14](#) shows the T47D cell line relative survival versus the concentrations of thiol functionalised AuNPs (thiol-AuNPs) used for 24 h. It was noticed that no significant decrease in T47D cell line relative survival indicating no significant cytotoxicity was induced by any concentration tested of the thiol-AuNPs after a 24 hours treatment period.

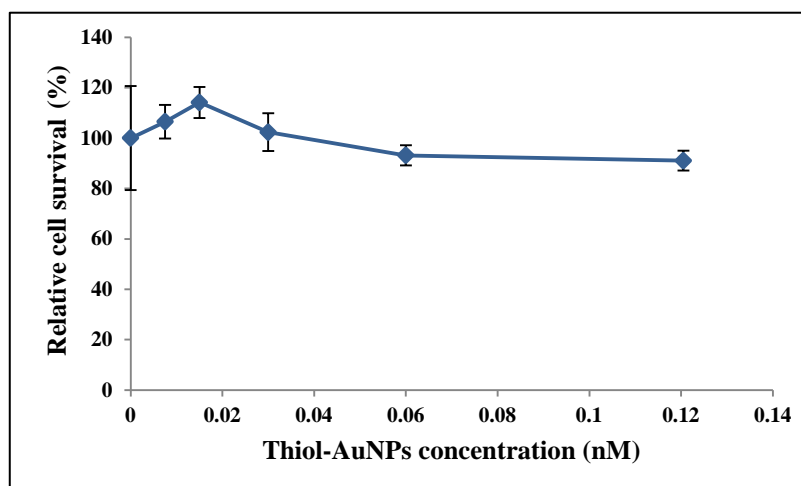


Figure 3.14 Response of T47D cells to 24 h treatment with functionalised AuNPs (thiol-AuNPs) determined using the MTT assay. Data shown as mean, n:3, *: $p \leq 0.05$.

On the other hand, data on the response of T47D cells to 24 h treatment with the hybrid PTX-thiol-AuNPs or PTX alone was compared and illustrated in Figure 3.15. The loading of PTX per PTX-thiol-AuNPs complex was calculated and converted to microgram per millimetre of PTX. The PTX concentration at the highest concentration treatment for each of the hybrid and the PTX solution varied (0.11 mg mL^{-1} for the PTX in hybrid PTX-thiol-AuNPs and 50 mg mL^{-1} for PTX alone). However, despite the difference in PTX concentration, there was no significant difference in relative survival (%) ($P < 0.05$) under all these treatment conditions (Figure 3.15). Therefore, there was no significant difference in cell killing ($P < 0.05$) by the highest dose of PTX alone when compared with that obtained using the hybrid though treatment with PTX alone required at least 1 order of magnitude higher concentration of PTX when compared with that required when the hybrid is involved. Additionally, when combining the anticancer PTX with AuNPs in the same construct, the PTX solubility is improved and its permeability into the cells is enhanced. The data shows a significant reduction of relative cell survival in T47D cancer cells treated with either PTX alone or PTX-thiol-AuNPs hybrid indicating high cytotoxicity was induced. However, a much greater reduction in the relative cell survival was observed for the cells treated with the hybrid. The results reveal the effectiveness of combining PTX with AuNPs through van der Waals forces at killing T47D breast cancer cells.

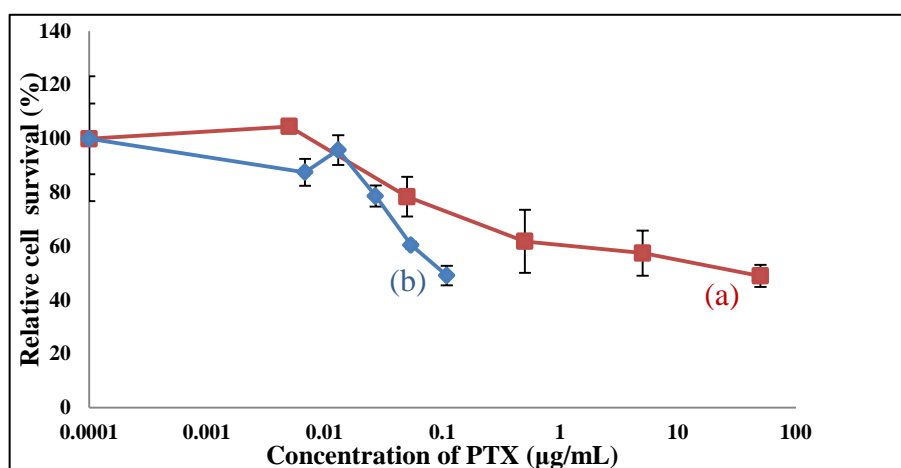


Figure 3.15 Response of T47D cells to 24 h treatment with (a) PTX and (b) PTX-thiol-AuNPs hybrid. Data shown as mean, $n=3$, *: $p \leq 0.05$.

3.4 Concluding remarks

This chapter investigated the synthesis mechanism of AuNPs, the surface modification with carboxylic acids terminated alkanethiols and the design of a novel AuNPs based drug delivery system by physical mixing of PTX with the thiol-AuNPs. The prepared AuNPs based samples were characterised using UV-Vis spectrophotometry, DLS, TEM, FT-IR and NMR to confirm AuNPs production, the surface functionalisation with carboxylic acids terminated alkanethiols, the hybrid PTX-thiol-AuNPs production as well.

The stability of the engineered system PTX-thiol-AuNPs hybrid was investigated using UV-Vis spectrophotometry and it was noticed that there is a relationship between the time the AuNPs and PTX were mixed during the generation of the hybrid and the amount of PTX found to be present in the hybrid.

The response of T47D breast cancer cells treated with the thiol-AuNPs, free PTX and PTX-thiol-AuNPs hybrid was assessed. It was found that thiol-AuNPs were nontoxic at the concentrations tested indicating their potential use as safe system in drug delivery or other biological applications. However, PTX-thiol-AuNPs hybrid was more effective than PTX alone at killing cancer cells indicating that the method of loading the nanoparticle can have a significant effect on ultimate activity with the most effective nanoparticle requiring a 1000 times less active drug to induce the same cell mortality. The results of this study could impact on the current direction of development of novel cancer drugs, as the combination of a drug with AuNPs offers a potential solution to lower the adverse side effects produced by many drugs available in the market by lower the amount of active drug required in the therapy.

Chapter 4. Chemical conjugation of PTX to functionalised AuNPs

4.1 Introductory remarks

This chapter describes the covalent conjugation of the chemotherapy agent, PTX, with the thiolated AuNPs using two methods. In the first method, the surface of AuNPs was first functionalised using a two-step approach described by Lin et al. [296] and detailed in [Chapter 3, Section 3.2](#); followed by attachment of PTX onto the surface of AuNPs by forming ester bonds between the (C₂-OH) and (C₇-OH) groups on PTX and (-COOH) groups on carboxylic acids terminated alkanethiols modified the surface of AuNPs using EDC/NHS chemistry. The conjugate formed was called PTX-thiol-AuNPs direct conjugate. The advantages of using EDC/NHS coupling compared to other crosslinking agents is that no additional chemical moieties are required [358] and the excess reagents and any by-products can be easily removed by dialysis or gel-filtration.

In the second method, the PTX was first covalently connected to 16-MHDA molecules through formation of ester bonds between the (C₂-OH) and (C₇-OH) groups on PTX and (-COOH) groups on 16-MHDA using EDC/NHS coupling. After that, AuNPs were added to the reaction mixture and the thiol groups on the end of 16-MHDA were chemisorbed onto the surface of AuNPs and formed Au-S strong bonds while the (-COOH) ends of 16-MHDA were already attached to (C₂-OH) and (C₇-OH) groups of PTX. This conjugate was called PTX-16-MHDA-AuNPs reverse conjugate.

The purpose of using different binding approaches to make the PTX loaded AuNPs is to investigate which approach leads to the most effective killing of breast cancerous cells. The long-term goal of this area of research is to mitigate the side effects of PTX by specifically delivering the drug in a dose-effective way to malignant cells without damaging healthy cells.

The analytical results from the synthesis of these two conjugates and the cytotoxicity assessment of these conjugates were presented herein.

4.2 Description of covalent conjugation between paclitaxel and gold nanoparticles

4.2.1 Description the synthesis of PTX-thiol-AuNPs direct conjugate

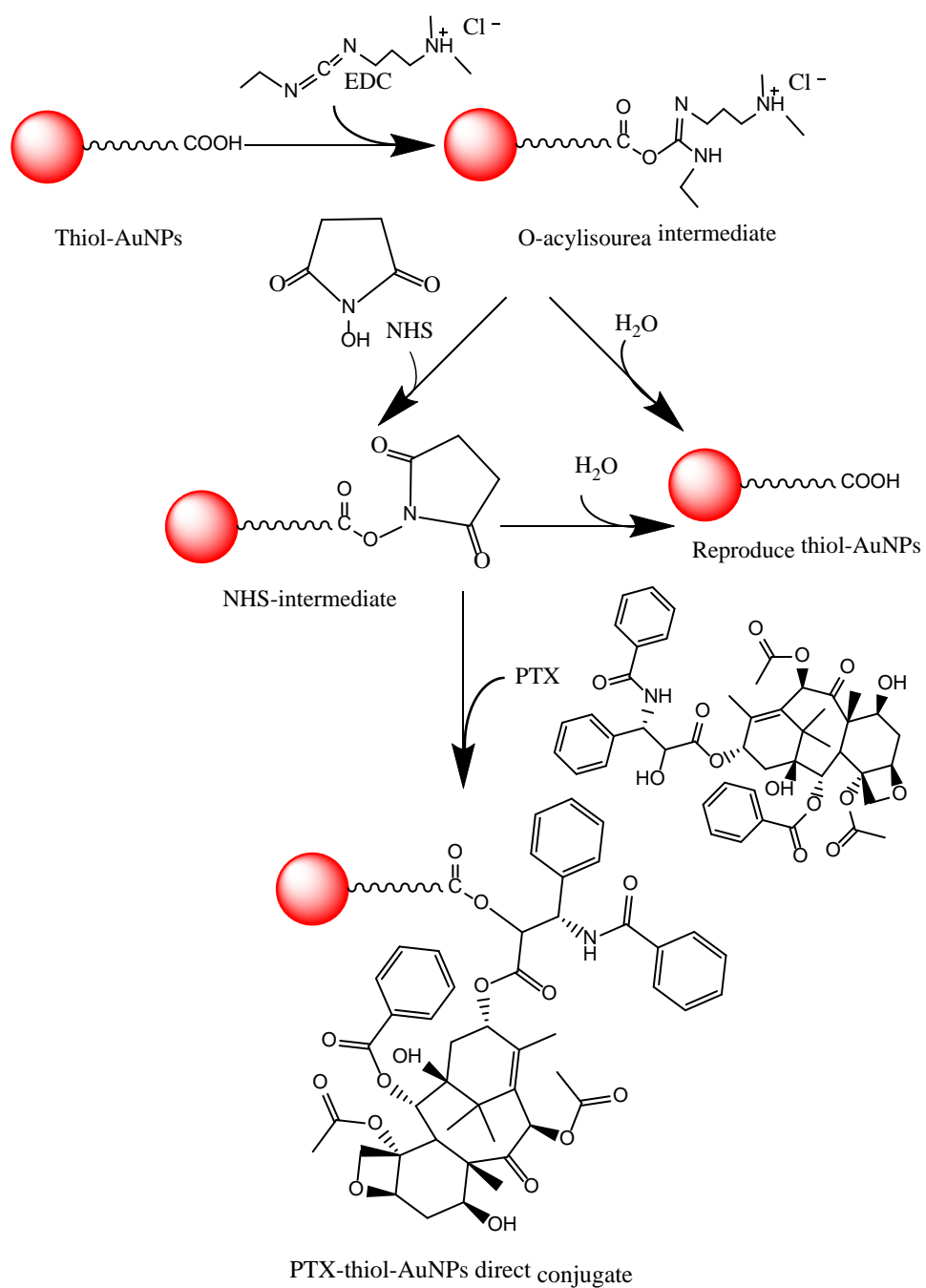
For the synthesis of PTX conjugated to thiol functionalised AuNPs (PTX-thiol-AuNPs direct conjugate), the synthesis of AuNPs followed by functionalisation their surfaces was required (refer to [Section 2.4.1](#) and [2.5.1](#) in [Chapter 2](#) for the full synthesis methods). Previous studies involving PEGlated AuNPs as delivery vehicles have used the 2' and 7 positions on the PTX molecule for the attachment [43, 193, 194, 359, 360]. There are other approaches available for chemical modification of the drug molecule and indeed other approaches which explore ways to facilitate association of the PTX with the AuNPs would be valuable. The work reported here uses a two-step functionalisation of carboxylic acid terminated alkanethiols in the presence of Tween 20 as a surfactant due to its ability to provide more stability to the functionalised AuNPs when adding EDC/NHS solution compared to the use of NaOH solution. The conjugation of PTX onto the thiolated AuNPs through ester bonds between the hydroxyl groups on the position (C₂-OH) and (C₇-OH) in PTX molecule and carboxylic ends on alkanethiols functionalised gold surface using crosslinking water soluble agents (N-(3-dimethylaminopropyl)- N'-ethylcarbodiimide hydrochloride, EDC) with (N-hydroxysuccinimide, NHS) was carried out. Although EDC/NHS are usually used as cross linking agents to form amide bonds between activated carboxyl ends and amine groups [361], in this study the EDC/NHS reaction was used to form ester bonds (see [Scheme 2.4](#) in [Chapter 2, Section 2.5.1](#)) which has been demonstrated previously [358, 362]. Everaerts et al. [358] reported a successful crosslinking of a reconstituted dermal bovine collagen (RDBC) material using EDC/NHS coupling [358].

In our study, the ester bonds were successfully formed and confirmed via ¹H NMR.

4.2.1.1 The function of EDC/NHS coupling reaction

EDC is a water soluble carbodiimide used to activate the formation of amide or ester bonds between carboxyl and amino or hydroxyl groups, respectively.

In this study, EDC was used to promote the formation of ester bonds between the carboxylic group located at the end of alkanethiol ligands (LA and 16-MHDA) and the hydroxyl groups situated at (C₂-OH) and (C₇-OH) of PTX. EDC reacts with carboxylic acid group and activates it to form an active O-acylisourea intermediate. This O-acylisourea can be easily substituted by a nucleophile (i.e., a primary amine or hydroxyl group) to form amide or ester bonds, respectively. However, the O-acylisourea intermediate is unstable in aqueous media and causes intermediate hydrolysis leading to production of N-unsubstituted urea and other by-products. In addition, the O-acylisourea intermediate must be used immediately after dissolving in water. Therefore, N-hydroxysuccinimide (NHS) is usually coupled with EDC to improve the stability and the efficiency in the reaction media by forming much more stable NHS esters (comparing to the O-acylisourea intermediate) with carboxylates which can then react with free groups, (in this case free OH on C₂ and C₇ of PTX molecule) to form ester bonds [363, 364] (see [Scheme 4.1](#)).

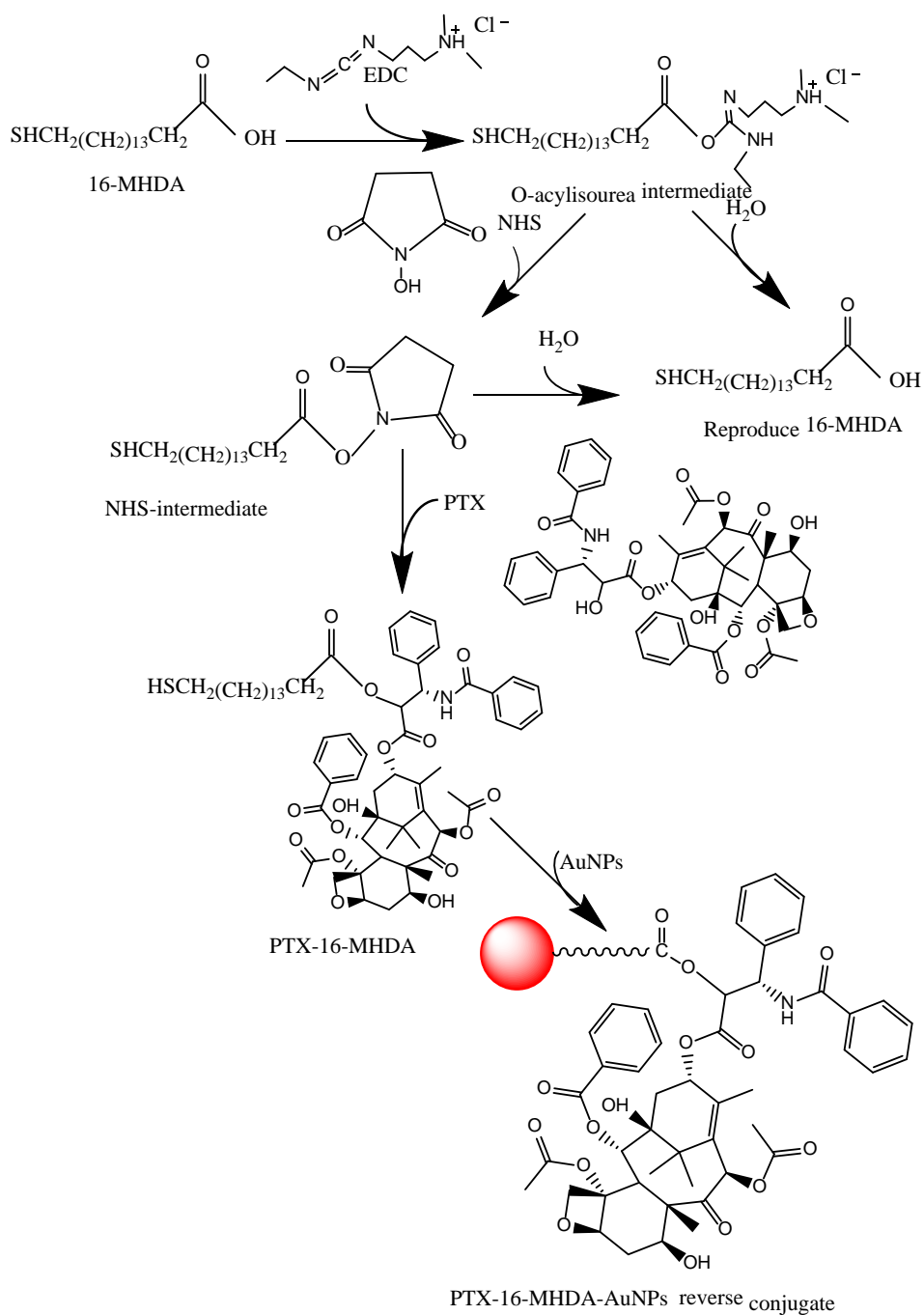


Scheme 4.1 Schematic illustration of esterification process between the thiol-AuNPs and the anticancer PTX using EDC/NHS coupling reaction. An equivalent scheme can be drawn for the C₇ position of PTX.

4.2.2 Description the synthesis of PTX-16-MHDA-AuNPs reverse conjugate

In this synthesis method, one ligand containing a thiol group at one end and a carboxylic group at the other end was used as a linker to attach the biomolecule PTX onto the surface of AuNPs. Typically, the carboxyl group terminated alkanethiol (16-MHDA) was first attached to PTX by dehydration (taking out water molecules) of carboxylic end and free hydroxyl on 16-MHDA and PTX molecules, respectively using EDC/NHS coupling reaction, so ester bonds were developed (see [Scheme 4.2](#)). Then, after adding AuNPs to the mixture, the sulfur atoms on 16-MHDA chemisorbed onto the surface of AuNPs by developing Au-S bonds and displacement with citrate and chloride anions on the AuNPs due to the strong affinity of thiols to AuNPs (see [Scheme 2.5](#) in [Chapter 2, Section 2.6.1](#) for the full synthesis method) [296].

4.2.2.1 The function of EDC/NHS coupling reaction



Scheme 4.2 Schematic illustration of esterification process between PTX and 16-MHDA using EDC/NHS coupling reaction; followed by adding AuNPs to form PTX-16-MHDA-AuNPs reverse conjugate. An equivalent scheme can be drawn for the C₇ position of PTX.

4.3 Characterisation techniques

4.3.1 Characterisation of PTX-thiol-AuNPs direct conjugate

4.3.1.1 UV-Vis analysis of PTX-thiol-AuNPs direct conjugate

UV-Vis spectrophotometry was utilised to observe the maxima absorbance bands for AuNPs before and after functionalisation with carboxylic acids terminated alkanethiol ligands followed by conjugation with the chemotherapy, PTX. [Figure 4.1.a](#) shows the distinctive absorption band of AuNPs at 523 nm before surface modification. [Figure 4.1.b](#) shows a red shift of the band from 523 nm to 526 nm after modification the AuNPs with LA ligands. [Figure 4.1.c](#) shows further shift to red after adding 16-MHDA molecules. [Figure 4.1.d](#) represents PTX-thiol-AuNPs direct conjugate. The signal of PTX at 228-230 nm was undetectable due to the low amount of PTX attached to the conjugate. In addition, a broad peak at 534 nm for thiol-AuNPs was detected. The red shift of the band from 529 nm in [Figure 4.1.c](#) to 534 nm in [Figure 4.1.d](#) is an indication of the successful conjugation between PTX and the thiol-AuNPs.

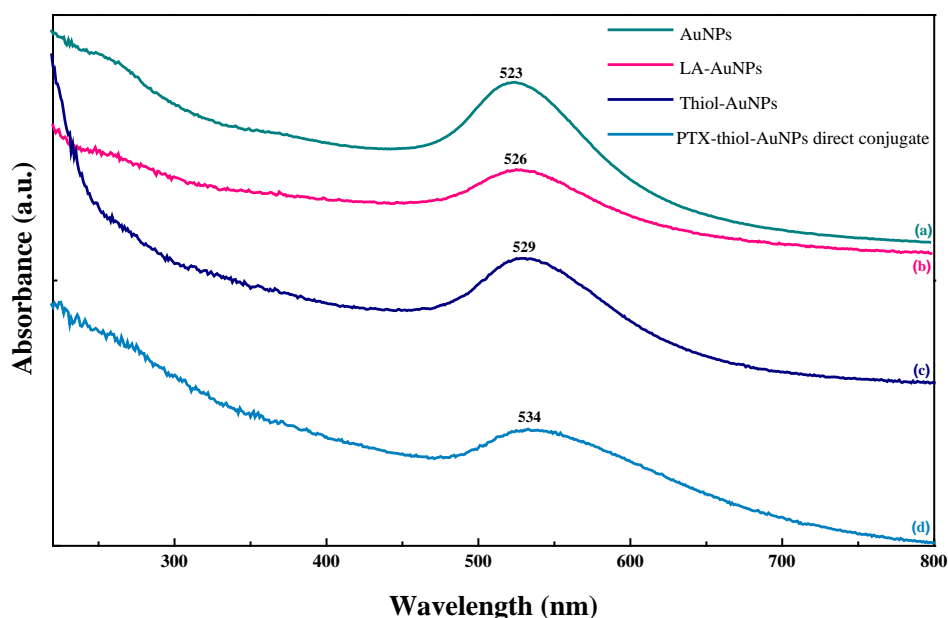


Figure 4.1 UV-Vis spectra of (a) AuNPs (b) LA-AuNPs (c) thiol-AuNPs and (d) PTX-thiol-AuNPs direct conjugate.

4.3.1.2 TEM analysis of PTX-thiol-AuNPs direct conjugate

The direct conjugate (PTX-thiol-AuNPs) was characterised by transmission electron microscopy (TEM) to confirm the integrity of monodispersed gold nanoparticles. Figure 4.2 shows a typical TEM image of the conjugate. The size distribution histogram shows a relatively narrow size distribution of PTX-thiol-AuNPs direct conjugate. Dark spots of AuNPs with size of approximately 17.13 ± 4.1 nm were observed. The TEM image indicates the formation of spherical shape of most AuNPs with some irregular particles.

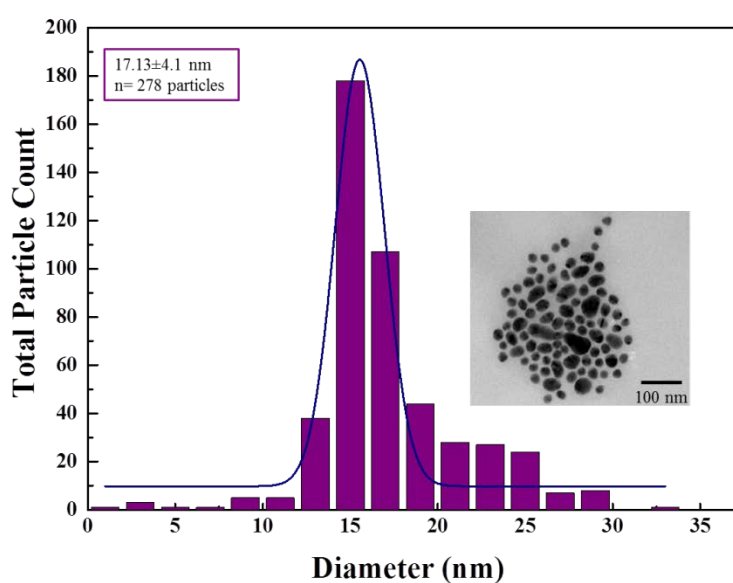


Figure 4.2 TEM image with size distribution histogram of PTX-thiol-AuNPs direct conjugate.

4.3.1.3 Dynamic light scattering (DLS) of PTX-thiol-AuNPs direct conjugate

In Chapter 3, Section 3.3.3, dynamic light scattering (DLS) was used to determine the particle size of the prepared colloidal AuNPs then compare it with its counterparts after functionalisation (see Chapter 3, Section 3.3.3 for data analysis of AuNPs alone and the functionalised particles). In this Chapter, likewise, DLS was utilised to observe the particle size for PTX-thiol-AuNPs direct conjugate. The sample was diluted with water (1:4, v/v) and the size was characterised by this technique besides other techniques. The mean particle size of PTX-thiol-AuNPs direct conjugate was 53 nm with polydispersity index of 0.524 (see Figure 4.3). The value of polydispersity index was small indicating the formation of monodispersed AuNPs.

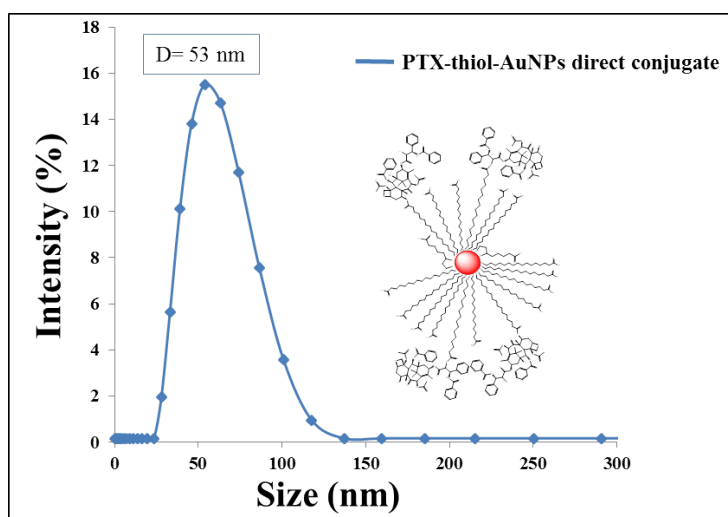


Figure 4.3 DLS size distribution (intensity graph) of PTX-thiol-AuNPs direct conjugate.

4.3.1.4 FT-IR analysis of PTX-thiol-AuNPs direct conjugate

Figure 4.4 and Table 4.1 shows the FT-IR spectra of PTX-thiol-AuNPs direct conjugate. Figure 4.4.a represents the LA functionalised AuNPs, Figure 4.4.b shows the bands for LA exchanged by 16-MHDA attached AuNPs (thiol-AuNPs) while Figure 4.4.c exhibits the spectra for PTX conjugated to the thiolated AuNPs (PTX-thiol-AuNPs direct conjugate). The FT-IR analysis for LA-AuNPs and thiol-AuNPs spectra was detailed in Chapter 3, Sections 3.3.4 and Table 3.3). Figure 4.4.a shows a broad absorption band between 3582 and 3108 cm^{-1} is due to hydroxyl groups stretching vibrations in the carboxylic acid terminated alkanethiols and from water residues. Likewise, the absorption signal of O-H stretching vibrations resulted from carboxylic groups terminated alkanethiols and from water molecules at approximately the same region (between 3536 and 3230 cm^{-1}) was observed after replacement of LA with 16-MHDA (Figure 4.4.b). Similarly, the same absorption band corresponding to the hydroxyl (-OH) stretching vibrations in combination with secondary amino group (-NH) stretching vibrations existed after conjugation of the chemotherapy agent, PTX, with the thiol-AuNPs at the region between 3580-3232 cm^{-1} (Figure 4.4.c). An absorption band of the spectrum of LA-AuNPs, thiol-AuNPs and then in PTX-thiol-AuNPs direct conjugate located at around the region of 1640 cm^{-1} assigned to C=O stretching vibrations (in samples containing LA and/or 16-MHDA) and/or amide I (in case of PTX containing sample) [296] was observed. Similarly, the presence of the absorption peak at $\sim 1100 \text{ cm}^{-1}$ is attributed to C-O stretching vibrations of all the samples. Importantly, the bands at 1702 cm^{-1} in LA-AuNPs and at 1698 cm^{-1} in thiol-AuNPs spectra are attributed to C=O stretching vibrations of carboxylic group while the band at 1735 cm^{-1} in the spectrum of PTX-thiol-AuNPs direct conjugate is due to the formation of ester group [43]. The results indicate the formation of ester bond between PTX and carboxylic acids ends of alkanethiols.

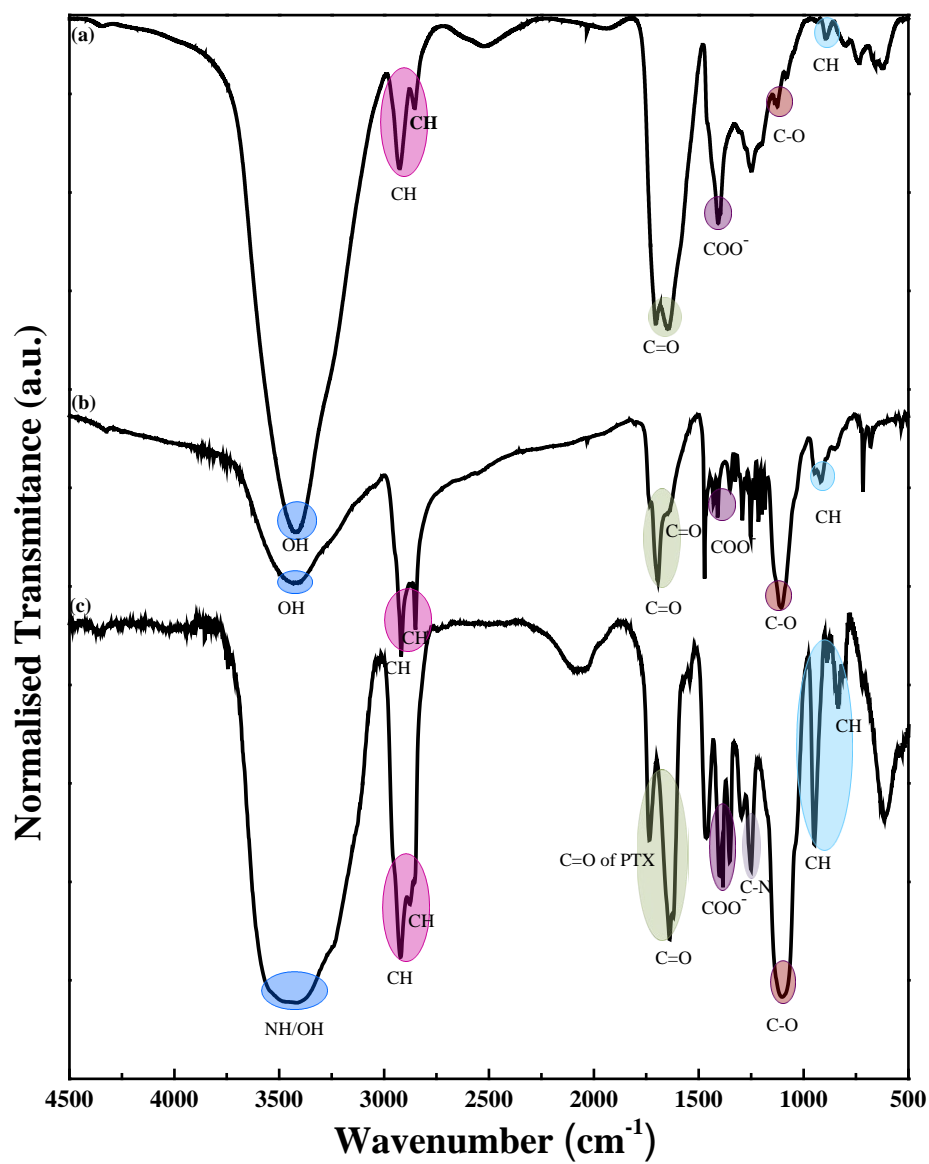


Figure 4.4 FT-IR spectra of (a) LA-AuNPs (b) thiol-AuNPs and (c) PTX-thiol-AuNPs direct conjugate.

Table 4.1 FT-IR peak positions of LA-AuNPs, thiol-AuNPs and PTX-thiol-AuNPs direct conjugate.

Vibrational modes	WN (cm ⁻¹)/ LA-AuNPs	WN (cm ⁻¹)/ thiol-AuNPs	WN (cm ⁻¹)/ PTX-thiol-AuNPs
O-H and/or NH	3582-3108	3536-3230	3580-3232
C-H asymmetric and symmetric stretching	2917- 2849	2917- 2849	2921, 2873, 2849
C=O stretching of esters	-	-	1735
C=O stretching of carboxylic acid	1702, 1640, 1402	1998, 1640, 1402	1640
Aromatic groups	-	-	1465
C-O stretching	1100	1100	1100
C-N stretching	-	-	1250
C-H in-plane deformation	894	914	948, 832

4.3.1.5 ¹H NMR spectroscopy characterisation of PTX-thiol-AuNPs direct conjugate

Figure 4.5 shows the ¹H NMR spectra for (a) LA-AuNPs (b) thiol-AuNPs and (c) PTX-thiol-AuNPs direct conjugate. The LA-AuNPs and thiol-AuNPs spectra were observed by ¹H NMR spectroscopy (refer to Chapter 3, Sections 3.3.5.2 and 3.3.5.3 for the detailed spectra). Both NaOH and Tween 20 were used to adjust the pH and provide more stability to the AuNPs in the surrounding environment. It was noticed that there was no difference when using NaOH or Tween 20 in the two-step functionalisation particles (adding LA in the first step then followed by adding 16-MHDA in the second step). However, when adding EDC/NHS in the presence of NaOH the particles agglomerated and the red-burgundy was turned to blue whereas in case of using Tween 20 the colour continued red-burgundy indicating the stability of the particles was higher. Figure 4.5.a and Table 4.2 display the chemical shifts of LA in LA-AuNPs sample after washing up the Tween 20 and centrifuging the sample several times.

Table 4.2 ¹H NMR data (δ /ppm) for pristine LA and LA-AuNPs in CDCl₃.

Peak position	Peak assignment	δ (ppm) of pure LA	δ (ppm) of LA-AuNPs	$\Delta\delta$ (ppm)
H ₁	O=C-OH	11.4 (undetectable)	11.4 (undetectable)	-
H _{2A,2B}	C-CH ₂	2.4	2.35	0.05
H _{3A,3B}	C-CH ₂	1.7	1.68	0.02
H _{4A,4B}	C-CH ₂	1.50	1.28	0.22
H _{5A,5B}	C-CH ₂	1.92	1.90	0.02
H _{6A,6B}	S-CH ₂	3.57	3.66	0.09
H _{7A}	S-CH ₂ -CH ₂	1.92	1.9	0.02
H _{7B}	S-CH ₂ -CH ₂	2.46	2.43	0.03
H _{8A}	S-CH ₂	3.18	Disappeared	-
H _{8B}	S-CH ₂	3.12	Disappeared	-

Figure 4.5.b and Table 4.3 show the ¹H NMR spectra of thiol-AuNPs. Some peaks assigned to LA and others appointed to 16-MHDA moieties were observed. The interior alkyl protons of 16-MHDA were observed as multiplet at $\delta = 1.28$ and 1.59 ppm with slightly change in some of the protons chemical shifts. The triplet (H₂) of 16-MHDA at $\delta = 2.37$ ppm due to the protons close to the carbonyl group were still observed indicating that those protons are intact. The triplet peaks (H₁₇) of 16-MHDA on sulfur atom at $\delta = 2.7$ ppm disappeared after exposing 16-MHDA to the LA-

AuNPs mixture. The quartet peaks at $\delta = 2.54$ ppm are attributed to protons (H_{16}) adjacent the sulfur atom and show no chemical shift after functionalisation the AuNPs surface. No significant chemical shift was observed after functionalising the surface of AuNPs using a two-step method when using Tween 20 as a surfactant compared to when stabilising the particles using NaOH.

Table 4.3 Chemical shifts (δ /ppm) for thiol-AuNPs and free 16-MHDA.

Peak position	Peak assignment	δ (ppm) of free 16-MHDA	δ (ppm) of thiol-AuNPs	$\Delta\delta$ (ppm)
H ₁	O=C-OH	10.8 (undetectable)	10.8 (undetectable)	0
H _{2A,2B}	$\begin{array}{c} \text{O} \\ \parallel \\ \text{CH}_2 - \text{C} \end{array}$	2.37	2.37	0
From H _{3A,3B} to H _{15A,15B} (interior alkyl protons)	CH ₂ -CH ₂	1.28, 1.64	1.28, 1.59	0, 0.05
H _{16A,16B}	HS-CH ₂	2.54	2.54	0
H ₁₇	S-H	2.7	Disappeared	0

Figure 4.5.c shows the ¹H NMR spectra of PTX-thiol-AuNPs direct conjugate. After attaching PTX to thiol-AuNPs using EDC/NHS coupling, the proton signals at C₂-OH and C₇-OH disappeared indicating the successful formation of ester bonds between the hydroxyl groups at C₂-OH and C₇-OH of PTX and the carboxylic ends on alkanethiol acids (16-MHDA and LA) on AuNPs surface. This is discussed in more detail later in Chapter 4 in Section 4.3.2.4. The other functional groups on PTX remained unchanged. In addition, some peaks relevant to LA and others related to 16-MHDA appeared. The ¹H NMR spectra generally showed slight chemical shift changes between PTX alone and PTX-thiol-AuNPs direct conjugate samples after covalent binding. The peaks in the first part of the spectra (0-4 ppm) generally overlapped with other signals from LA and 16-MHDA molecules and it was difficult to identify each signal individually. It was noticed that C₁₉ upfield shifted from $\delta = 1.76$ ppm to $\delta = 2.72$ ppm with $\Delta\delta = 0.96$ ppm and 10-OAC upfield shifted from $\delta = 2.27$ ppm to $\delta = 2.265$ ppm with $\Delta\delta = 0.005$ ppm. However, the peaks in the region between 5 and 10 ppm in PTX-thiol-AuNPs conjugate's sample were easily identified and assigned to PTX molecule and they did not show any chemical shifts except for

C₁₀ shifted from $\delta = 6.27$ ppm to $\delta = 6.29$ ppm with $\Delta\delta = 0.02$ ppm (see [Figure 4.5](#) and [Table 4.4](#)).

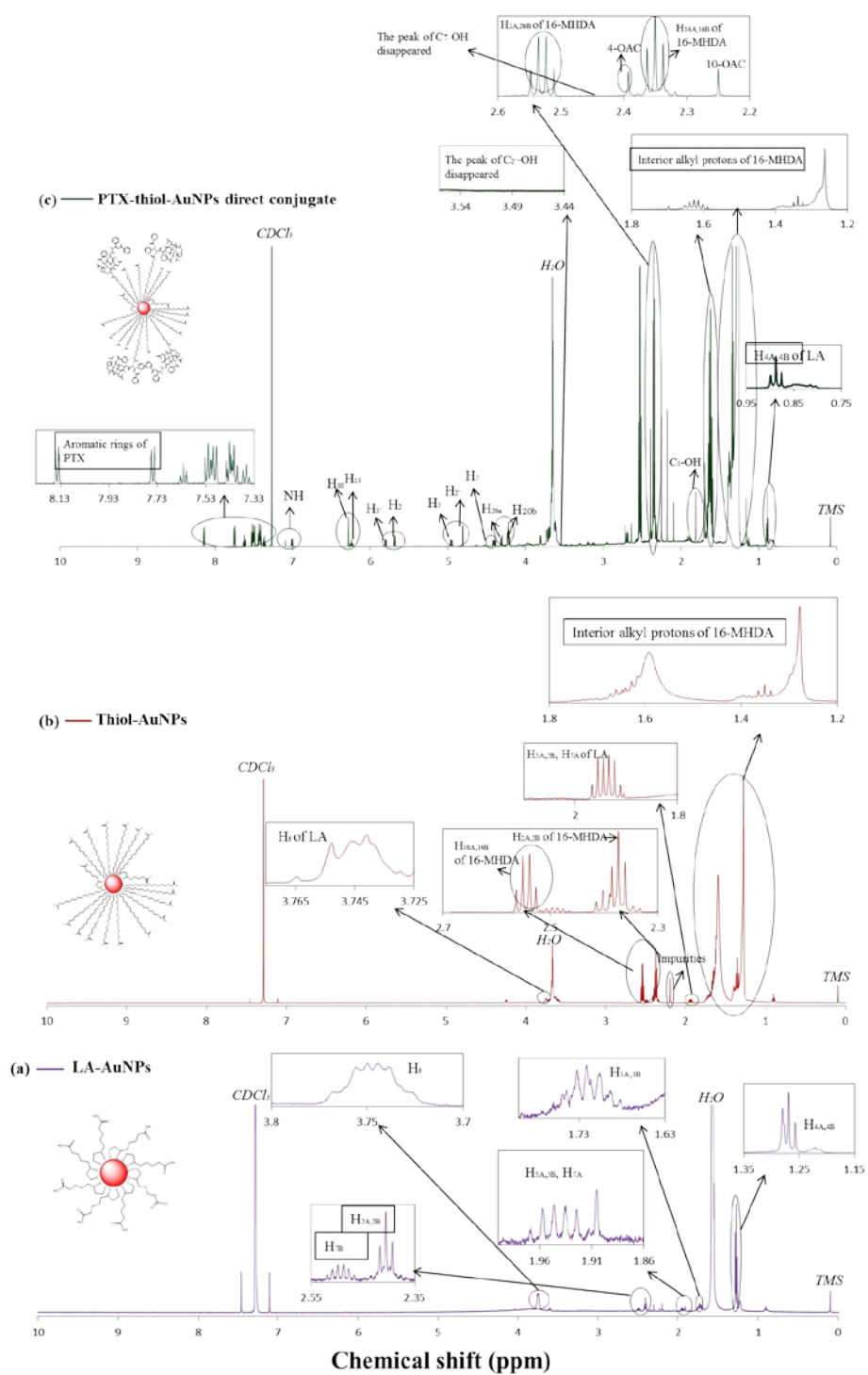


Figure 4.5 ^1H NMR spectra of (a) LA-AuNPs (b) thiol-AuNPs and (c) PTX-thiol-AuNPs direct conjugate.

Table 4.4 ¹H NMR chemical shifts (δ /ppm) for the protons of free PTX and PTX-thiol-AuNPs direct conjugate.

Peak position	δ (ppm) of free PTX	δ (ppm) of PTX-thiol-AuNPs	$\Delta\delta$ (ppm)
C ₁	4.41 (multiplet)	4.41	0
C ₂	5.69 (doublet)	5.7 (doublet)	0.01
C ₃	3.81(doublet)	Overlapped with other signals	-
C ₄ -OAC	2.41 (singlet)	2.41 (singlet)	0
C ₅	4.81(two doublet signals)	4.81	-
C ₆	2.57 (doublet), 1.91 (doublet)	Overlapped with other signals	-
C ₇	4.43 (multiplet)	4.43	-
C ₁₀	6.27(singlet)	6.29 (singlet)	0.02
C ₁₃	6.24 (triplet)	6.24 (triplet)	0
C ₁₄	2.32 (doublet), 2.27 (doublet)	Overlapped with other signals	-
C ₁₆	1.16 (singlet)	Overlapped with other signals	-
C ₁₇	1.26 (singlet)	Overlapped with other signals	-
C ₁₈	1.70 (singlet)	Overlapped with other signals	-
C ₁₉	1.76 (singlet)	2.72 (singlet)	0.96
C ₂₀	4.29 (doublet), 4.21 (doublet)	4.29 (doublet), 4.21 (doublet)	0
C _{23,27}	8.15 (two doublet signals)	8.15 (two doublet signals)	0
C _{24,26}	7.49 (multiplet)	7.49 (multiplet)	0
C ₂₅	7.64 (multiplet)	7.64 (multiplet)	0
10-OAC	2.27 (singlet)	2.265 (singlet)	0.005
C ₃₁	2.26 (multiplet)	Overlapped with other signals	-
C _{33,37}	7.46 (multiplet)	7.46 (multiplet)	0
C _{34,36}	7.37 (multiplet)	7.37 (multiplet)	0
C ₃₅	7.33 (multiplet)	7.33 (multiplet)	0
C _{39,43}	7.75 (multiplet)	7.75 (multiplet)	0
C _{40,42}	7.4 (multiplet)	7.4 (multiplet)	0
C ₄₁	7.47 (multiplet)	7.47 (multiplet)	0
C _{2'}	4.80 (quartet)	4.80 (quartet)	0
C _{3'}	5.80 (two doublet)	5.80 (two doublet)	0
C ₂ -OH	3.53 (doublet)	Disappeared	-
C ₁ -OH	1.80 (singlet)	1.80 (singlet)	0
C ₇ -OH	2.47 (two doublet)	Disappeared	-
N-H	7.11 (doublet)	7.11 (doublet)	0

4.3.1.6 Preparation of PTX-thiol-AuNPs direct conjugate for drug loading studies

The loading efficiency of anticancer PTX was investigated using UV-Vis spectrophotometry. Typically, eleven samples of PTX-thiol-AuNPs direct conjugate at the same concentrations were incubated at room temperature for certain mixing times (see [Figure 4.6](#) and [Table 4.5](#)). For each sample, 3.5 mL of thiol-AuNPs were treated with 1 mL of PTX solution (3 mg PTX in 10 mL EtOH). The mixture was left stirring at room temperature for certain times (1 h, 2 h, 6 h, 10 h, 15 h, 20 h, 24 h, 48 h, 72 h, 96 h and 120 h). After that, the samples were resuspended in PBS (pH 7.4) and centrifuged at 15700 g for 15 minutes 5 times. The pellets for each sample were redispersed in PBS (7.4). The NPs pellets were diluted and characterised by UV-Vis to measure the concentration of PTX loaded on the functionalised AuNPs and the concentration of AuNPs. However, the signals for PTX were undetectable in the conjugate samples due to low amount of PTX attached to the conjugates. On the other hand, the supernatant for each sample was gently dried to concentrate the PTX and other constituents. Then, the dried supernatant contents were redissolved in appropriate amounts of EtOH and characterised by UV-Vis spectrophotometry to measure the concentration of PTX. This was then used to determine the mass of PTX in supernatant in order to be able to determine the mass of PTX loaded to the functionalised AuNPs by subtracting the obtained mass of PTX in supernatant from the initial amount of PTX used (0.3 mg) (see [Table 4.5](#)). The relationship between these absorbance values and the concentrations were obtained using Beer–Lambert law ($A = \epsilon \ell c$), where ϵ is the molar extinction coefficient of PTX = $29.8 \text{ mM}^{-1} \text{ cm}^{-1}$ [305], $\ell = 1 \text{ cm}$ while the molar extinction coefficient of AuNPs obtained from Sigma Aldrich = $9.21 \times 10^8 \text{ M}^{-1} \text{ cm}^{-1}$ [299]. The initial amount of PTX used minus the total amount of PTX observed in the supernatant after centrifugation were used to give an approximate value of the loaded amount of PTX on the thiol-AuNPs ([Figure 4.6](#) and [Table 4.5](#)).

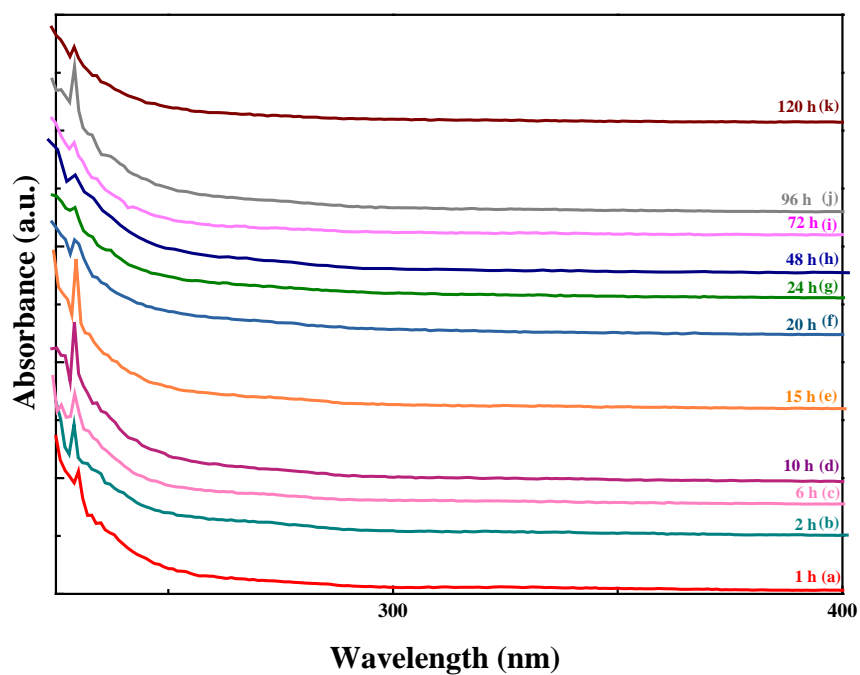


Figure 4.6 UV-Vis spectra for PTX in supernatant of PTX-thiol-AuNPs direct conjugate samples at different times.

Figure 4.7 represents the free PTX in the supernatant (rhombus). In general, the mass of PTX in the supernatant slightly decreased in the first 24 h. With longer conjugation times the concentration of the free PTX in supernatant become constant.

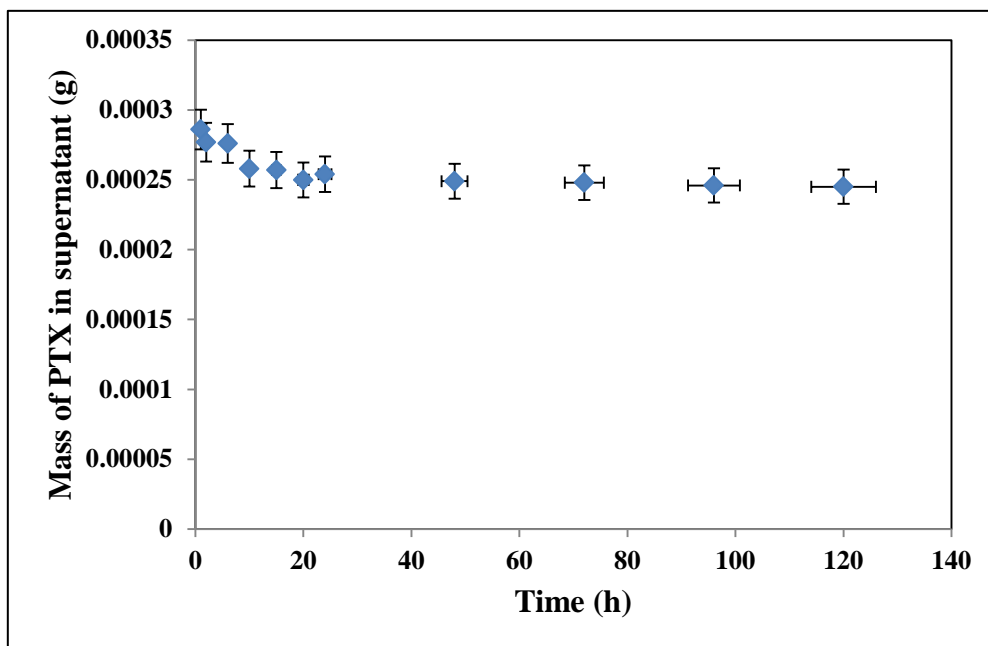


Figure 4.7 The amount of PTX left in the supernatant.

Table 4.5 Drug loading of PTX-thiol-AuNPs direct conjugate samples.

Mixing time (h)	Absorbance of PTX in supernatant (a.u.)	Concentration of PTX in supernatant (μM)	Mass of PTX in supernatant (mg)	Mass of PTX on thiol-AuNPs (mg)	Total mass of PTX (mg)
1	2.08	69.8	0.298	0.002	0.3
2	1.93	64.8	0.277	0.023	0.3
6	1.928	64.69	0.276	0.024	0.3
10	2.817	94.5	0.258	0.042	0.3
15	1.7	57	0.257	0.043	0.3
20	2.64	88.6	0.25	0.05	0.3
24	1.61	54	0.254	0.046	0.3
48	1.74	58.4	0.249	0.051	0.3
72	1.63	54.7	0.248	0.052	0.3
96	2.53	84.9	0.246	0.054	0.3
120	1.33	44.6	0.245	0.055	0.3

4.3.1.7 Cytotoxicity assay for PTX-thiol-AuNPs direct conjugate

Experiments on breast cancer cell lines to investigate the *in vitro* effectiveness of the designed synthetic approach of PTX-thiol-AuNPs direct conjugate towards a novel delivery system were performed. A detailed description of the experiments and results is in [Appendix C](#). T47D cells were treated with PTX-thiol-AuNPs direct conjugate for 24 h. Five different concentrations were prepared for the experiment in serial dilutions starting with 0.109 nM. As shown in [Figure 4.8](#). After exposing the cells to the conjugate, it was noticed that at a concentration of 0.054 and 0.109 nM, the viability of the cells were significantly decreased in comparison to the untreated control ($p \leq 0.05$). The results indicate the potential use of the anticancer agent, PTX, and gold nanoparticles conjugate for drug delivery in breast cancer treatment.

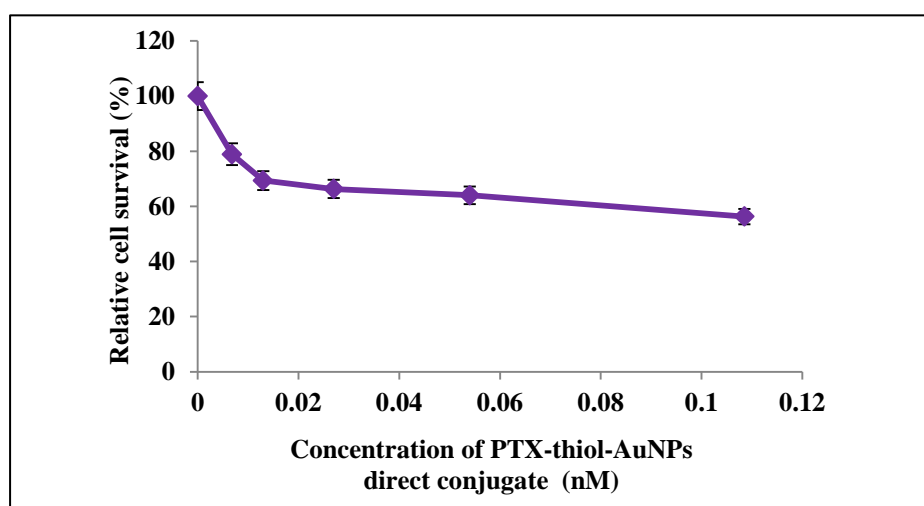


Figure 4.8 Response of T47D cells to treatment with PTX-thiol-AuNPs direct conjugate using MTT assay. Shown in concentration of PTX conjugated thiol-AuNPs (nM) versus relative survival (%) compared to the untreated control. Data shown as mean, n:3, *: $p \leq 0.05$.

4.3.1.8 Comparison of cytotoxicity for PTX-thiol-AuNPs direct conjugate at different pHs

Experiments on T47D breast cancer cell lines to examine the cytotoxicity of PTX loaded nanoparticles *in vitro* at different pHs and assess the possibility of using PTX loaded AuNPs to target cancerous cells were performed in the School of Medical Science and Technology, Flinders University, South Australia, by collaborating with Assoc. Prof. Barbara Sanderson and a Masters student, Nur Hikmatul Auliya. A description of the experiments is in [Appendix C](#). The PTX-thiol-AuNPs direct conjugate was prepared at seven different concentrations, starting with a dose 0.05513 nM prepared at two different pH values (pH 7.4 & 6.5, where acetic acid was used to adjust the pH). T47D cells were treated with the conjugate at two different pHs (pH 7.4 & 6.5) for 24 h ([Figure 4.9](#)). At physiological pH (7.4) ([Figure 4.9.a](#)), at the highest dose 0.05513 nM of PTX-thiol-AuNPs conjugate showed a significant decrease of cell viability in the cell line down to only ~60 % compared to untreated sample ($p \leq 0.05$), while other lower concentrations showed no significant toxicity to cell line at level $p \leq 0.05$. The two sets of data for pH 7.4 ([Figure 4.8](#) and [Figure 4.9.a](#)) are very consistent. [Figure 4.9.b](#) shows the starting dose of 0.00027 nM had a different impact at pH 6.5 than that in pH 7.4. At the lower pH, concentration of AuNP measured reduced cell viabilities of T47D significantly ($p \leq 0.05$). At concentrations of 0.00276 nM has decreased cell line by ~60 % and a 10 fold increase of that concentration reduced cell viability to only 28 %. Viability decreased to a mean of 7 % at the highest concentration (0.05513 nM). The PTX-thiol-AuNPs direct conjugate showed a significant difference ($p \leq 0.05$) in cytotoxicity between the two different pHs at concentrations tested. Relative viabilities at 0.05513 nM was ~60 % at pH 7.4 while at pH 6.5 only ~7 %. The cytotoxicity of PTX alone was performed at pH 7.4 and 6.5 by our group and other groups [229, 365]. It was revealed that PTX alone inhibits T47D breast cancer cells at physiological pH down to 50 % at dose of 59 μ M [229]. However, a significant decrease of cytotoxicity of paclitaxel was observed at pH 6.5 which leads to tumour drug resistant in murine EMT6 and in human MGH-U1 cells [365]. Given the pH around cancer tumours is typically lower than physiological pH [366], the attachment of the PTX to the nanoparticle is an important step to improve the efficiency of the drug compared to the drug alone and points to potential strategies for targeted treatments.

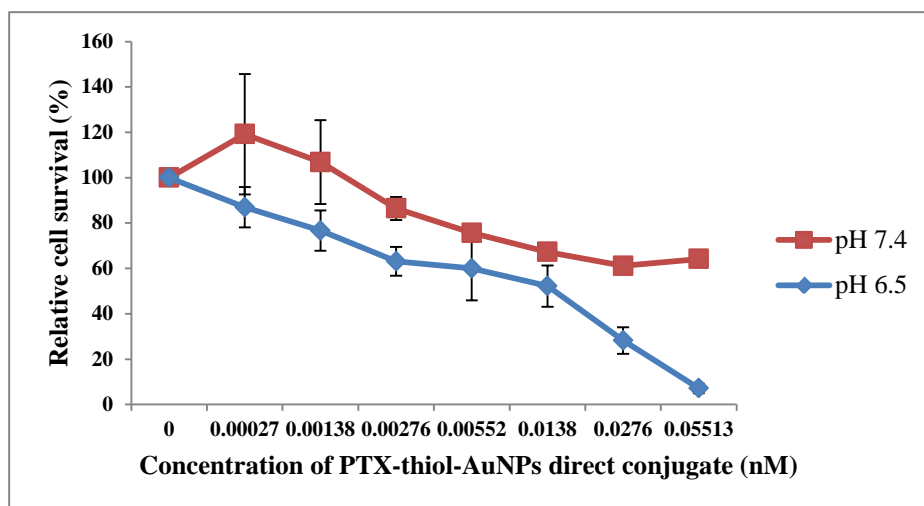


Figure 4.9 Response of T47D cell line to treatment with PTX-thiol-AuNPs direct conjugate at (a) pH 7.4 and (b) pH 6.5 using MTT assay. Shown in concentration of PTX in direct conjugate (nM) versus relative survival (%) compared to untreated control. Data shown as mean, n:3, *: $p \leq 0.05$.

4.3.2 Characterisation of PTX-16-MHDA-AuNPs reverse conjugate

4.3.2.1 UV-Vis analysis of PTX-16-MHDA-AuNPs reverse conjugate

UV-Vis spectrophotometry was utilised to observe the maxima absorbance bands for NHS attached 16-MHDA (NHS-16-MHDA) step (intermediate step) followed by observing the PTX absorption band after binding with 16-MHDA (PTX-16-MHDA) step. The absorbance bands of AuNPs and PTX after conjugation of PTX to AuNPs (PTX-16-MHDA-AuNPs reverse conjugate) step were also measured.

Figure 4.10.a shows a UV-Vis spectrum of 16-MHDA modified NHS (16-MHDA-NHS). The spectrum shows the characteristic absorbance band for NHS at 260 nm (no purification process was accomplished for this step) [367]. Figure 4.10.b displays the spectrum of 16-MHDA functionalised PTX (PTX-16-MHDA). The PTX absorbance band at 230 nm was obviously observed. In addition, a broad band with slight shifting to the red assigned to NHS molecules was observed. The reason for the existence of NHS band in this step is the fact that the reaction mixture contains EDC/NHS molecules beside PTX and 16-MHDA and no purification process was applied in this step to remove the EDC/NHS molecules. Figure 4.10.c represents the attachment between AuNPs and PTX-16-MHDA. In this step, after conjugation of the PTX to AuNPs by chemisorption of thiols from 16-MHDA molecules attached to PTX, the particles were centrifuged 5 times to get rid of unbound moieties and then UV-Vis spectra were collected. The band for PTX at 230 nm was undetectable due to low amount of PTX attached to the surface of AuNPs. However, a broad band at approximately 533 nm for AuNPs was noticed. The broad band of AuNPs after exposure to PTX-16-MHDA gives an indication that the attachment between the AuNPs and the 16-MHDA molecules functionalised PTX was accomplished.

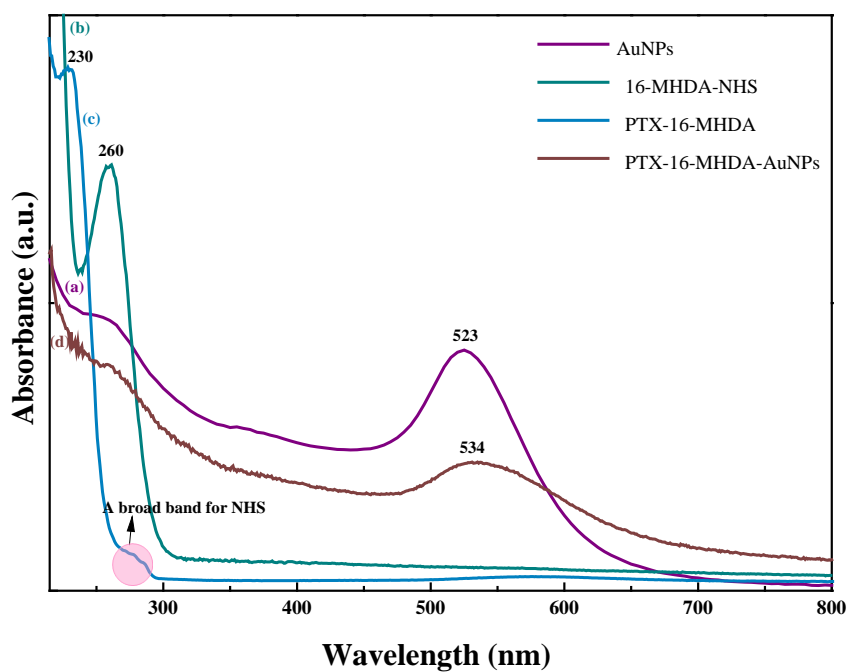


Figure 4.10 UV-Vis spectra of (a) AuNPs (b) 16-MHDA-NHS (c) PTX-16-MHDA and (d) PTX-16-MHDA-AuNPs reverse conjugate.

4.3.2.2 Dynamic light scattering (DLS) of PTX-16-MHDA-AuNPs reverse conjugate

DLS was used to determine the particle size of PTX-16-MHDA-AuNPs reverse conjugate. The sample was diluted with water (1:4, v/v) and the size was characterised by this technique besides other techniques. The mean particle size of PTX-16-MHDA-AuNPs reverse conjugate was 50 nm with polydispersity index of 0.64 (see Figure 4.11). The value of polydispersity index was slightly small indicating the formation of monodispersed AuNPs.

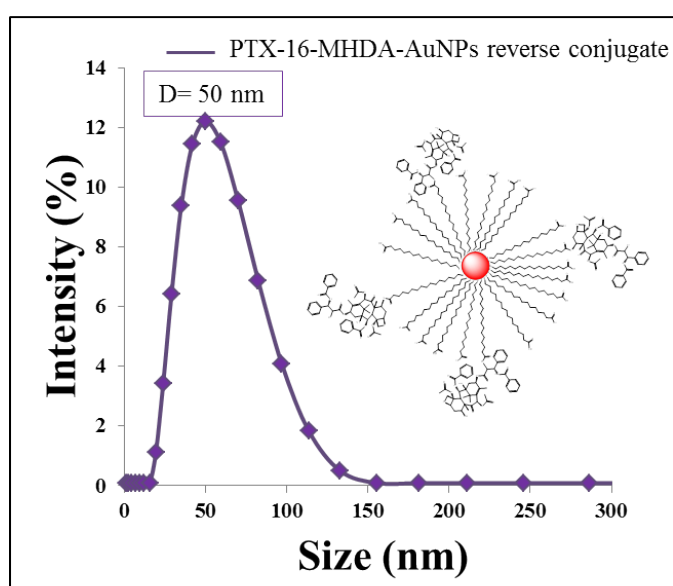


Figure 4.11 DLS measurement for PTX-16-MHDA-AuNPs reverse conjugate.

4.3.2.3 FT-IR analysis of PTX-16-MHDA-AuNPs reverse conjugate

Figure 4.12.a shows FT-IR spectra of 16-MHDA attached NHS. No purification process was carried out for this step. The peak at 1742 cm^{-1} is assigned to succinimidyl carbonyl group, the peak at 1705 cm^{-1} represents the existence of the carbonyl groups of terminal carboxylic acid while the bands at 2923 and 2849 cm^{-1} are attributed to the stretching vibrations of CH_2 groups [32]. In addition, the bands at 1637 cm^{-1} and 1610 cm^{-1} are assigned to $\text{C}=\text{O}$ stretching vibration. The peak at 1560 cm^{-1} is due to the secondary amide $\text{C}=\text{O}$ vibrational stretches [33]. The peak at 1402 cm^{-1} is due to symmetric stretching vibrations of COO^- . The peak at 1250 cm^{-1} is due to $\text{C}-\text{N}$ stretching vibration, at 1171 cm^{-1} and 1096 cm^{-1} are attributed to $\text{C}-\text{O}$ vibrations and at 617 is due to $\text{C}=\text{C}-\text{C}$ bending of the pyrimidine ring of Xanthine [43, 160, 368]. The spectrum in Figure 4.12.b shows PTX attached to 16-MHDA. No purification process was accomplished for this functionalisation step as well. The peaks at 2918 cm^{-1} and 2849 cm^{-1} are assigned to methylene groups stretching vibrations. The band at 1721 cm^{-1} is due to carbonyl group $\text{C}=\text{O}$ stretching vibrations from the ester group as observed previously while the peak at 1650 cm^{-1} is allocated to the amide I of PTX or to $\text{C}=\text{O}$ stretching vibration of 16-MHDA [36]. The peaks at 3555 cm^{-1} and 3276 cm^{-1} are due to NH and OH stretching vibrations. The peak at 2972 cm^{-1} is assigned to aromatic $\text{C}-\text{H}$ stretch [43, 160, 368]. Figure 4.12.c shows the PTX-16-MHDA-AuNPs reverse conjugate after centrifugation. The peaks at 2918 , 2873 and 2849 cm^{-1} are assigned to CH stretching vibrations. The band at 1735 cm^{-1} is due to carbonyl group $\text{C}=\text{O}$ stretching vibrations from the ester group. The band at 1640 cm^{-1} is assigned to $\text{C}=\text{O}$ stretching vibrations of 16-MHDA or amide I of PTX while the peak at 1465 cm^{-1} is assigned to aromatic groups in PTX. The bands at $3590-3088\text{ cm}^{-1}$ are due to $\text{N}-\text{H}/\text{O}-\text{H}$ stretching vibrations, at 1100 cm^{-1} is due to $\text{C}-\text{O}$ stretching vibrations, at 1250 cm^{-1} is assigned to $\text{C}-\text{N}$ stretching vibrations. The band at 1402 cm^{-1} is attributed to a symmetric stretching vibration of COO^- . The bands at 948 cm^{-1} and at 832 cm^{-1} are due to $\text{C}-\text{H}$ in plane deformation [43, 160, 368].

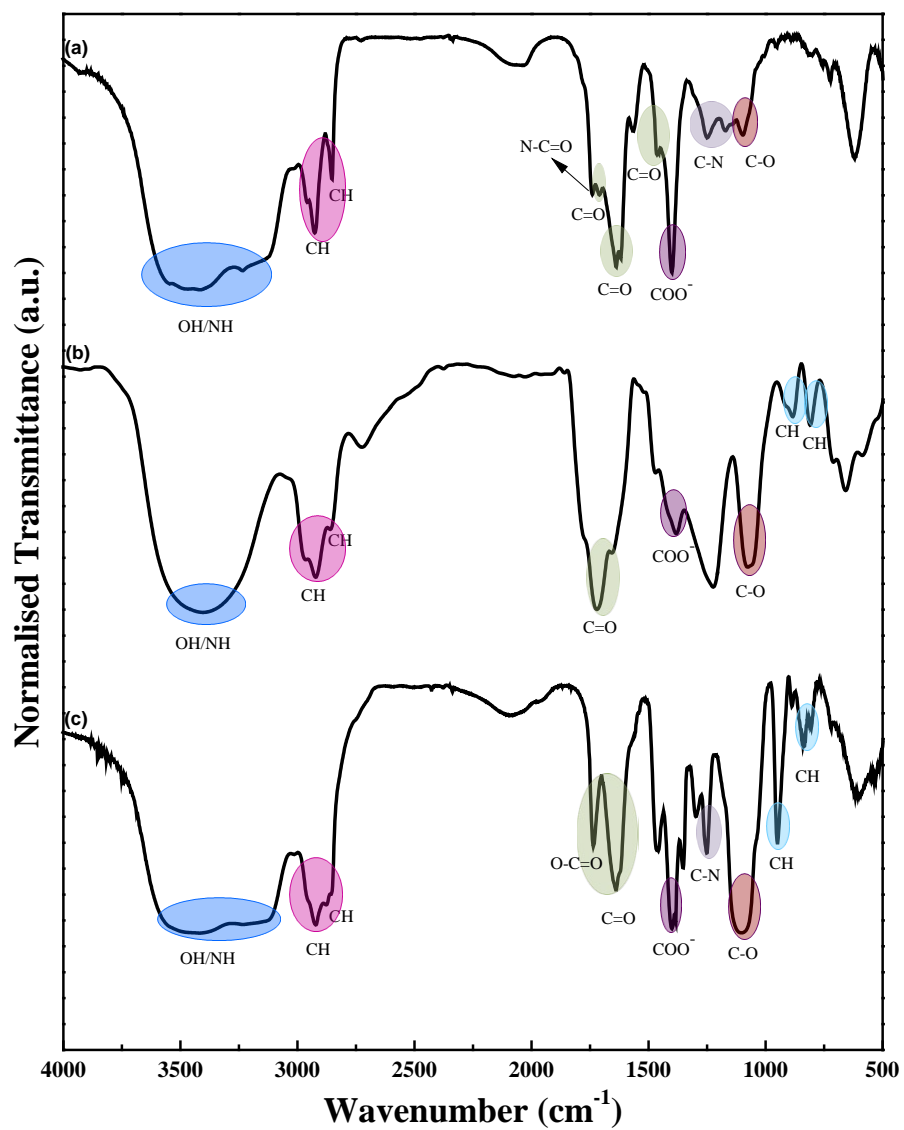


Figure 4.12 FT-IR spectra of (a) 16-MHDA-NHS (b) PTX-16-MHDA and (c) PTX-16-MHDA-AuNPs reverse conjugate.

4.3.2.4 ¹H NMR spectroscopy characterisation of PTX-16-MHDA-AuNPs reverse conjugate

Since the steps before adding AuNPs for preparing the reverse conjugate were non-purified and contain EDC/NHS with 16-MHDA and or PTX, the NMR spectra were not collected. However, the resulting PTX-16-MHDA-AuNPs reverse conjugate after centrifugation steps was analysed using ¹H NMR spectroscopy and compared with free PTX. It was found that after attaching PTX-16-MHDA molecules to AuNPs, all the main characteristic peaks corresponding to PTX and 16-MHDA were observed (see the detailed spectral for free 16-MHDA and PTX in [Chapter 3, Sections 3.3.5.3](#) and [3.3.5.4](#), respectively). As expected, the signals of 16-MHDA were observed in PTX-16-MHDA-AuNPs reverse conjugate. Some peaks assigned to PTX overlapped with other peaks of 16-MHDA in the region between 1 and 4 ppm making some PTX peaks difficult to see. Overall, it was observed that there were no significant chemical shift changes of the signals assigned to PTX after conjugation. However, several important changes were seen in the ¹H NMR spectrum. Successful conjugation via formation of an ester bond between 16-MHDA and carbon 2' in the PTX molecule is evidenced by two factors. Firstly, the absence of the hydroxyl proton resonance (3.57 ppm, [Figure 4.13](#)) and secondly the collapse of the C₂' proton resonance (4.83 ppm) from a doublet of doublets (J= 2.6, 5.0 Hz) before conjugation, due to coupling with both hydroxyl proton on carbon 2' and the proton on C₃', to a single doublet (J=2.6 Hz) due to the coupling only to the C₃' proton (see [Figure 4.13](#)). A selective 1D NMR COSY experiment (see [Appendix B.1.A](#)) tuned to the C₂' proton resonance confirmed a single coupling and a lack of a peak for the hydroxyl proton on carbon 2', further confirming the loss of this hydroxyl proton as a result of conjugation. In a similar manner, conjugation at C₇ in the PTX molecule can also be inferred from two pieces of evidence. Firstly, the absence of the hydroxyl proton resonance (2.46 ppm) on carbon 7 and secondly the collapse of the complex multiplet signal for C₇ proton before conjugation to a doublet of doublets. Specifically, before conjugation the C₇ proton was coupled to the C₇ hydroxyl proton in combination with the diastereotopic C₆ protons yielding a complex multiplet. After conjugation coupling only to the diastereotopic C₆ protons yields a doublet of doublets (J = 6.7, 10.9 Hz). Further, a selective 1D NMR COSY experiment (see [Appendix B.1.B](#)) tuned to the C₇ proton resonance confirmed couplings to just the two protons on C₆ and no peak

for the hydroxyl proton on carbon 7, further confirming the loss of this hydroxyl proton as a result of conjugation.

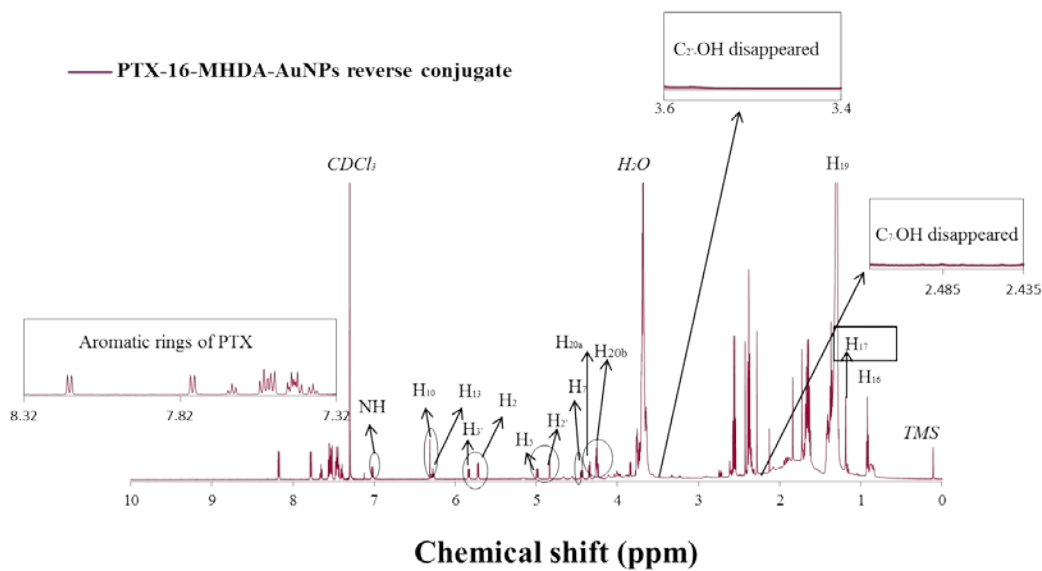


Figure 4.13 ¹H NMR spectra of PTX-16MHDA-AuNPs reverse conjugate.

4.3.2.5 Cytotoxicity assay for PTX-16-MHDA-AuNPs reverse conjugate

Experiments on T47D breast cancer cell lines to investigate the *in vitro* effectiveness of the designed PTX-16-MHDA-AuNPs reverse conjugate towards an efficient delivery system were carried out. A detailed description of the experiments is in [Appendix C](#). T47D cells were treated with PTX-16-MHDA-AuNPs reverse conjugate for 24 h. Five different concentrations were prepared for the experiment in serial dilutions starting with 0.109 nM. As shown in [Figure 4.14](#). No significant cytotoxicity was observed on the cells treated with reverse conjugate at any concentration tested for the 24 hours treatment period ($p < 0.05$). This is likely due to the fact that the reverse method is not as effective at loading the AuNP with PTX as the other conjugate methods.

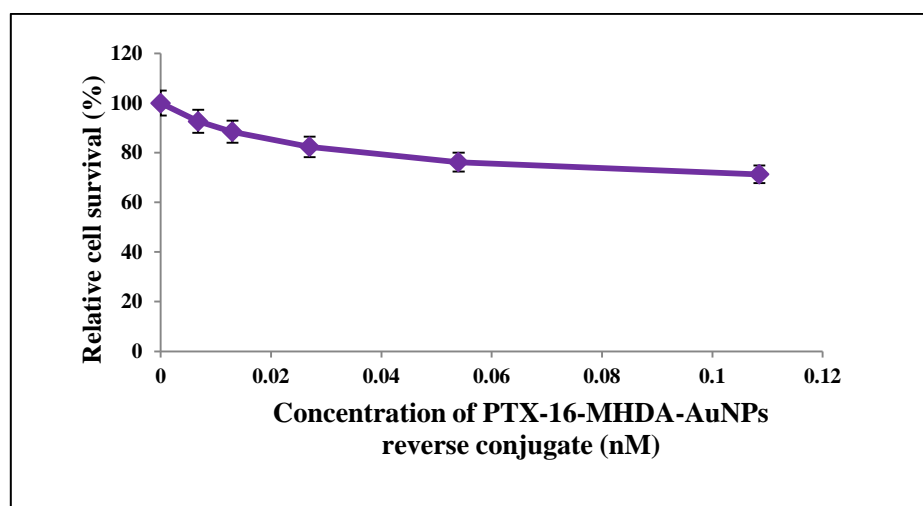


Figure 4.14 Response of T47D cells to treatment with PTX-16-MHDA-AuNPs reverse conjugate using MTT assay. Data shown as mean, n:3, *: $p \leq 0.05$.

4.3.2.6 Comparison of cytotoxicity for PTX-16-MHDA-AuNPs reverse conjugate at different pHs

Breast cancer cell lines (T47D) were treated with seven different concentrations of PTX-16-MHDA-AuNPs reverse conjugate at two different pHs (pH 7.4 & 6.5) for 24 h to examine the cytotoxicity of PTX *in vitro* at different pHs and assess the possibility of using the reverse conjugate to target cancerous cells. Figure 4.15 shows a significant decrease in the number of T47D cells compared to untreated control at $p \leq 0.05$ at each concentration tested at both pH values (7.5 & 6.5). At the first three low concentrations (0.0083, 0.0414 & 0.829 nM), the survival rate percentage reached ~60 % at pH 6.5 (Figure 4.15.b) and ~70 % at pH 7.4 (Figure 4.15.a). These cell viabilities at pH 7.4 are similar to those observed in the previous experiments (Figure 4.14). There was a gap of 10 % cell viability at different pHs. At higher concentrations (0.1658 to 1.658 nM) the number of viable cells reduced significantly. Starting from 0.1658 to 1.658 nM, the cell viability went from ~60 % to only ~8 % and ~70 % to only ~16 % at pH 6.5 and 7.4, respectively. In general, the tendency of cytotoxicity of the reverse conjugate was similar for both pHs, even though cell viability of T47D at pH 6.5 (blue line) was lower than that pH 7.4 (the difference is ~10 %). The higher concentration of AuNP leads to a significant cancer cell killing. Even at the higher nanoparticle concentrations, the concentration of PTX would be considerably lower than that currently used in the clinic pointing to the possibility of reducing side effects considerably by using a nanoparticle based delivery system.

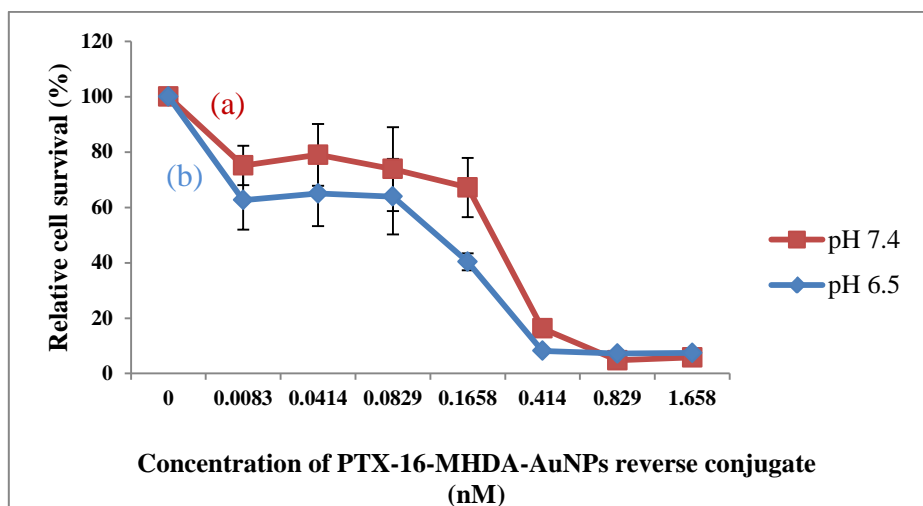


Figure 4.15 Comparison of response of T47D cell line to treatment with PTX-16-MHDA-AuNPs reverse conjugate at (a) pH 7.4 and (b) pH 6.5 using MTT assay. Shown in concentration of PTX in reverse conjugate (nM) versus relative survival (%) compared to untreated control. Data shown as mean, n:3, *: $p \leq 0.05$.

4.4 Concluding remarks

This chapter considered two covalent conjugation options for modification of AuNPs with the breast cancer chemotherapy agent, PTX. The prepared direct conjugate (PTX-thiol-AuNPs) and reverse conjugate (PTX-16-MHDA-AuNPs) samples were characterised using UV-Vis spectrophotometry, DLS, TEM, FT-IR and NMR to confirm the successful conjugations. The drug loading efficiency of PTX-thiol-AuNPs direct conjugate was evaluated. The response of T47D breast cancer cells to 24 h *in vitro* treatment with different concentrations of free PTX, PTX-thiol-AuNPs direct conjugate and PTX-16-MHDA-AuNPs reverse conjugate to 24 h was examined. Significant reduction in cell cancer viability was observed when T47D cancerous cells were treated with PTX-thiol-AuNPs direct conjugate indicating high cytotoxicity was induced. In PTX-thiol-AuNPs direct conjugate, the cell killing was much higher than the cells treated with PTX alone. On the other hand, the reduction of cell relative survival was not significant in case of cells treated with PTX-16-MHDA-AuNPs reverse conjugate compared to PTX alone or PTX-thiol-AuNPs direct conjugate. This is probably due to the fact that the reverse method is not as effective at loading the AuNP with PTX as the other conjugate methods. For the reverse case, the species self-assembling onto the nanoparticle is much bulkier with the PTX already attached. This will limit both the diffusion rate of the species and their ability to assemble in a highly packed fashion on the surface. Both these factors will decrease the loading of the drug on the surface. The response of T47D cancer cells to 24 h *in vitro* treatment with different concentrations of PTX-thiol-AuNPs direct conjugate and PTX-16-MHDA-AuNPs reverse conjugate to 24 h at two different pHs (7.5 & 6.5) was tested. In case of T47D cells treated with PTX-thiol-AuNPs direct conjugate, significant reduction of cell viability at different pHs was observed. However, the decrease of cell viability was higher at pH 6.5 than at pH 7.4. In case of T47D cells exposed to PTX-16-MHDA-AuNPs reverse conjugate, also significant reduction of relative cell survival was observed. However, no significant difference of cell viability reduction was observed at different pHs, although the cell viability was significantly reduced at the lower pH (6.5).

Chapter 5. Characterisation of conjugates based on fluorescent agents

5.1 Introductory remarks

This chapter aimed to investigate the effectiveness of AuNPs as nanocarriers by detection of their intracellular uptake with a view to understanding the targeting and treatment of the cancer cells. For this purpose, multifunctional gold nanoparticles that have different functionalities in one construct were designed. Conjugation of a fluorescent dye, which acts as a marker to detect the permeation and cellular uptake of AuNPs using confocal laser scanning microscopy (CLSM), and an anticancer drug onto the functionalised AuNPs provides a drug delivery system that can be tracked and used efficiently for treating unhealthy cells.

DAPI, 2-(4-amidinophenyl)-6-indolecarbamide dihydrochloride, 4',6-diamidino-2-phenylindole dihydrochloride, is a fluorescent dye commonly used for staining DNA molecules by producing a stable complex with a stronger fluorescent signal than DAPI alone [369, 370]. The binding of DAPI onto DNA occurs because the nitrogen in the indole in DAPI structure develops a bifurcated hydrogen bond with A-T regions in DNA [369]. DAPI can be used for other life science applications. For example, Rudershausen et al. [362] reported the covalent attachment of the fluorescent dye, DAPI, dichlorotriazinyl derivative, DTAF or rhodamine B onto the surface of the superparamagnetic dextran nanoparticles [362]. In their study, they used bifunctional carboxylic acid as a spacer to link the fluorescent dye via one of its amino groups to hydroxyl groups of the dextran nanoparticles. Since dextran has many functionalities (-OH), biomolecules, such as antibodies or proteins, can be covalently bound to the already fluorescently labelled dextran which can be used as a nanocarrier system [362]. DAPI can be used for staining both living and fixed cells [371]. In this study, DAPI has been attached to thiol-AuNPs and used as probe to investigate the cellular uptake of AuNPs in living cells and to study DAPI behaviour when it is part of a AuNPs conjugate and compare the behaviour with free DAPI.

This chapter also investigated the intracellular uptake of AuNPs using another fluorescent dye called 1-pyrenemethylamine hydrochloride, pyNH₂. PyNH₂ is a positively charged molecule with one functional group (-NH₂) and it has been used in different biomedical applications. For example, Yang et al. [372] used pyNH₂ to prepare functionalised graphene oxide (GO) by conjugation of polyethylene glycol (PEG) and folic acid (FA), followed by loading of human telomerase reverse transcriptase (hTERT) small interfering RNA (siRNA) with an assistance of 1-pyrenemethylamine hydrochloride (pyNH₂) through π - π stacking onto the surface of GO. This system was designed for tumour targeting delivery of siRNA. It was found that after loading pyNH₂, the PEG functionalised GO was non-toxic [372]. This finding does suggest that fluorescent pyNH₂ could be used as a probe for AuNPs *in vitro* detection inside the cell system. Another study conducted by Lodeiro et al. [373] has shown the synthesis of new pyNH₂ derivatives by binding of two pyNH₂ units to the carbonyl precursor 2,6-bis(2-formylphenoxy)methyl) pyridine. In this study, two biscromophoric sensors and one monocromophoric system based on pyrene emission have been synthesised to be used for selective fluorescence sensing applications [373].

In addition, this chapter investigated the intracellular uptake of AuNPs using fluorescent brightener 28 (FB28) as a probe. Fluorescent brighteners, among them fluorescent brightener 28, are colourless dyes of the Calcofluor White M2R group. They are soluble in water and used to provide brightness and whiteness to paper and textile products and are included in laundry detergents to keep washed items looking bright and white [374, 375]. In biological applications, they are utilised to stain cell walls of plants and fungi [376]. Darken [376] was the first to report the biological application of Calcofluor White M2R in terms of its usage for observing fungi and bacteria cell walls [376]. Since this work, the fluorescent dye has been utilised to visualise cell walls of various sorts of fungi, bacteria, algae and plants [303, 377, 378]. For example, Davey et al. [375] described the potential use of fluorescent brighteners as stains for flow cytometric analysis of different types of microorganisms and spores [375]. Fluorescent brighteners absorb UV light and emit blue fluorescence [375].

The main purpose of using different fluorescent dyes was to investigate the appropriate dye for biological use and determine which gives the strongest signals. DAPI and pyNH₂ have been chosen as staining agents due to having functional groups (-NH₂) that can be linked to carboxylic ends of alkanethiols on the surface of AuNPs using EDC/NHS coupling reaction. Another reason for choosing DAPI and pyNH₂ is to compare the behaviour of positively charged molecules (DAPI or pyNH₂) before and after conjugation to AuNPs surface to their negatively charged counterparts (FB28). In addition, FB28, which shows non-covalent binding to the nanoparticle, was used as a probe to examine its effectiveness as a staining agent and compare it with dyes covalently bound to AuNPs.

In current study, DAPI, pyNH₂ or FB28 were used as markers to detect the intracellular uptake of AuNPs. After functionalisation of AuNPs using the two-step conjugation methods, a carboxylic acid terminal end on AuNPs surface was obtained. An EDC/NHS coupling reaction was used to crosslink the fluorescent dye, DAPI (or pyNH₂), and the anticancer drug, PTX, simultaneously to the AuNPs. Amino groups (-NH₂) of DAPI (or pyNH₂) and hydroxyl groups at C₂' and C₇ positions of PTX with carboxyl groups of 16-MHDA or LA, used as linkers and stabilisers, amide and ester bonds were formed via using EDC/NHS chemistry. FB28 was immobilised onto the surface of functionalised AuNPs by van der Waals interactions. An EDC/NHS coupling reaction was used to crosslink the anticancer drug, PTX, to the AuNPs through attachment of C₂' and C₇ hydroxyl groups of PTX with carboxyl groups of 16-MHDA or LA to form ester bonds via using EDC/NHS chemistry.

Lastly, this chapter focused on tracking the intracellular uptake of PTX molecules using rhodamine B as a staining fluorescent dye. In general, rhodamine dyes are fluorophores that show good photostability and photophysical properties allowing use in different applications [379] including their use as laser dyes [380], as fluorescent probes to characterise the surface of polymer nanoparticles [381], for tracking of polymer-bioconjugates [382] and imaging in living cells [383]. As an example of using rhodamine dyes in biological applications, Jaworska et al. [384] investigated the cellular uptake of rhodamine 6G (R6G) alone and R6G conjugated to AuNPs by live cells via using fluorescence confocal laser scanning microscopy (CLSM) and surface-enhanced Raman scattering (SERS) [384]. The results suggested

internalisation and distribution of AuNPs conjugated with R6G inside cells mediated by an endocytosis mechanism [384].

RB fluorescent dye was also used to detect the anticancer agent, PTX, inside live cells by crosslinking RB to the anticancer, PTX. An EDC/NHS coupling reaction was used to crosslink the RB dye to the anticancer drug, PTX. C₂' and C₇ hydroxyl groups of PTX with carboxyl groups of RB, ester bonds were formed via using EDC/NHS chemistry.

This chapter studies the characterisation of different conjugates based on fluorescent dyes to obtain various conjugates using UV-Vis spectrophotometry, fluorescence spectroscopy, TEM, DLS, FT-IR and NMR spectroscopies. The cytotoxicity assays of these conjugates based on fluorescent agents were also investigated.

5.2 Characterisation of fluorescently labelled AuNPs

5.2.1 UV-Vis analysis of fluorescently labelled AuNPs

UV-Vis spectrophotometry was used to characterise different preparation steps of fluorescently labelled AuNPs. [Table 5.1](#) displays the various conjugates characterised by UV-Vis and other characterisation techniques during conjugation steps.

UV-Vis spectrophotometry of these various conjugates is provided in [Figure 5.1](#). In each case, the expected absorption peaks of the various dyes were observed both in the free molecules and after attachment to the nanoparticles [372, 385-392]. Attachment to the particle generally leads to a slight red shift of the absorption peaks suggesting the molecules had been attached to the AuNPs. The observation of fluorescence after attachment confirms the molecules are far enough from AuNP due to the presence of chains of carboxylic acids terminated alkanethiols (16-MHDA and LA used as linkers) to suppress any quenching due to the nanoparticles. The SPR absorption peak of the AuNPs was red-shifted and became broad (between 526 and 627 nm) after conjugation of the dyes onto the thiol-AuNPs. This finding, the red shift of AuNPs, is in agreement with a study conducted by Ou et al. [387]. In their study, carbon nanotube (CNT)-gold nanoparticle composites in aqueous solution using pyNH₂ as an interlinker were synthesised. They found that after functionalisation AuNPs, the absorbance bands of pyNH₂ decreased and the SPR absorption peak of AuNPs were shifted to red region from 508 to 556 nm due to interparticle plasmon coupling phenomenon [387]. In current study, the shift of the SPR peak further supports the attachment to the functionalised AuNPs. In the conjugates containing PTX, a peak at 228-230 nm would be expected but due to low amount of the anticancer drug, PTX, attached to the prepared conjugates and the presence of highly absorbing dye molecules which will dominate the signal, the PTX signal could not be observed.

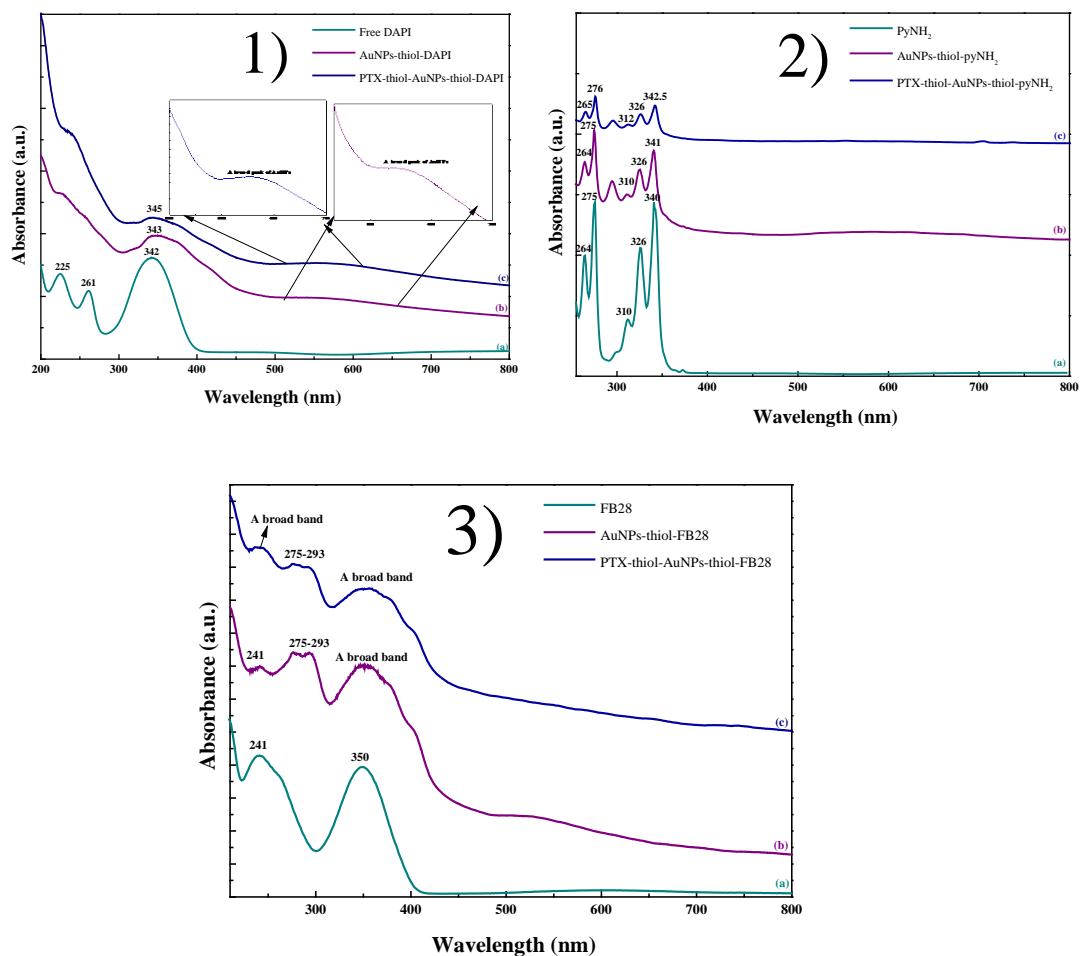


Figure 5.1 UV-Vis spectra of various fluorescent containing nanoparticles or their precursors. 1) DAPI 2) pyNH₂ and 3) FB28.

Table 5.1 Various fluorescent containing nanoparticles characterised by different techniques at different conjugation steps.

Step 1	Step 2	Step 3
Free DAPI	AuNPs-thiol-DAPI direct conjugate	PTX-thiol-AuNPs-thiol-DAPI direct conjugate
Free pyNH ₂	AuNPs-thiol-pyNH ₂ direct conjugate	PTX-thiol-AuNPs-thiol-pyNH ₂ direct conjugate
Free FB28	AuNPs-thiol-FB28 hybrid	PTX-thiol-AuNPs-thiol-FB28 direct conjugate

5.2.2 Fluorescence spectroscopy analysis of fluorescently labelled AuNPs

Fluorescence spectroscopy was used to characterise different preparation steps of fluorescently labelled AuNPs. Table 5.1 displays the various conjugates characterised by fluorescence spectroscopy during conjugation steps. In all samples analysed using fluorescence spectroscopy, a blank of Milli-Q water or EtOH was run initially. Each sample was diluted with Milli-Q water or EtOH (1:4, v/v). Fluorescence spectra of these various conjugates are provided in Figures 5.2, 5.3 and 5.4. In each case, the expected excitation and emission peaks of the various dyes were observed both in the free molecules and after attachment to the nanoparticles. The functionalised AuNPs (thiol-AuNPs) alone have no fluorescence emission bands.

Figure 5.2.A illustrates the fluorescence excitation and emission spectra of free DAPI dissolved in EtOH. An intense and significant excitation peak of DAPI appeared at 358 nm [304] along with small peak observed at 258 nm [369]. The broad fluorescence emission band of DAPI was observed at 460 nm [317] using an excitation wavelength of 358 nm. Figure 5.3.A illustrates the fluorescence excitation and emission spectra of free pyNH₂ dissolved in EtOH. An intense excitation peak assigned to pyNH₂ observed at 342 nm along with smaller peaks observed at 326 and 276 nm [393]. An intense fluorescence emission band of free pyNH₂ using an excitation wavelength of 342 nm was observed at 376 nm in addition to two other weaker bands at 394 and 416 nm [318, 394]. Figure 5.4.A illustrates the fluorescence excitation and emission spectra of free FB28 dissolved in Milli-Q water. An intense excitation peak assigned to FB28 observed at 343-353 nm. The excitation spectrum of free FB28 was recorded at an emission wavelength of 435 nm. An intense fluorescence emission band of free FB28 was observed at 435 nm when using an excitation wavelength of 343 nm [319]. After conjugation the staining agents DAPI or pyNH₂ to AuNPs containing samples, the excitation and emission bands were shifted slightly to the red (Figures 5.2.B and C and 5.3.B and C) and broader emission bands were observed in case of attachment of PTX molecules (see Figures 5.2.C and 5.3.C). These results are in agreement with a study reported by Basu et al. [389]. They synthesised AuNPs in toluene using two-phases (water-toluene) in the presence of sodium borohydride as a reducing agent and a series of cationic

surfactants. The fluorescent dye 1-methylaminopyrene (MAP) was used for the surface functionalisation of the AuNPs. The emission bands at $\lambda_{\text{ex}} = 328$ nm were observed at 377, 397 and 417 nm [389]. In this study, after attachment of pyNH₂ to thiol-AuNPs the emission band shifted to 377 nm. Observing the broad peak after the attachment of the fluorescent agents (DAPI or pyNH₂) and PTX molecules simultaneously to functionalised AuNPs and the peak shifting to longer wavelength indicate the attachment of the staining agents to thiol-AuNPs and PTX-thiol-AuNPs direct conjugates. However, after loading FB28 to AuNPs containing conjugates (AuNPs-thiol-FB28 hybrid and PTX-thiol-AuNPs-thiol-FB28 direct conjugate), no shifts of excitation and emission wavelengths were observed (Figure 5.4.B and C). In addition, the fluorescence intensity was decreased after loading FB28 to thiol-AuNPs. These results are in agreement with the findings reported by Albani et.al. [302]. They found that after attaching of Calcofluor to asialylated acid glycoprotein, no position change of emission maximum of the fluorophore was noticed and the fluorescence intensity decreased [302]. Fluorescent dyes, except FB28, covalently conjugated to thiol-AuNPs showed a red shift in excitation and emission positions. It can be concluded that no chemical reaction occurred between the functional groups of FB28 and carboxylic acids terminated alkanethiols.

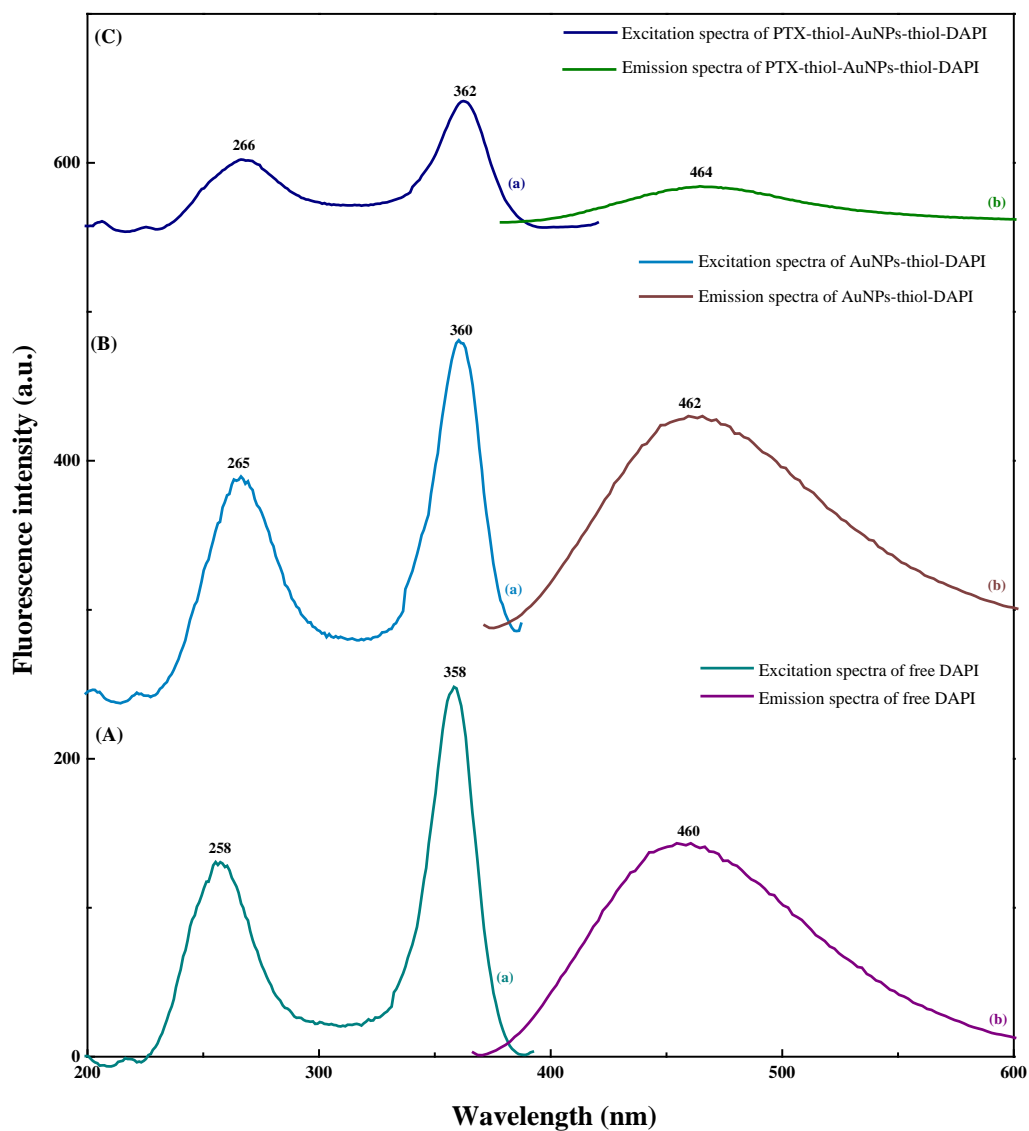


Figure 5.2 Fluorescence (a) excitation and (b) emission spectra of (A) free DAPI (B) AuNPs-thiol-DAPI direct conjugate and (C) PTX-thiol-AuNPs-thiol-DAPI direct conjugate. The excitation spectrum was recorded at an emission wavelength of 460 nm. The emission spectrum was recorded using an excitation wavelength of 358 nm.

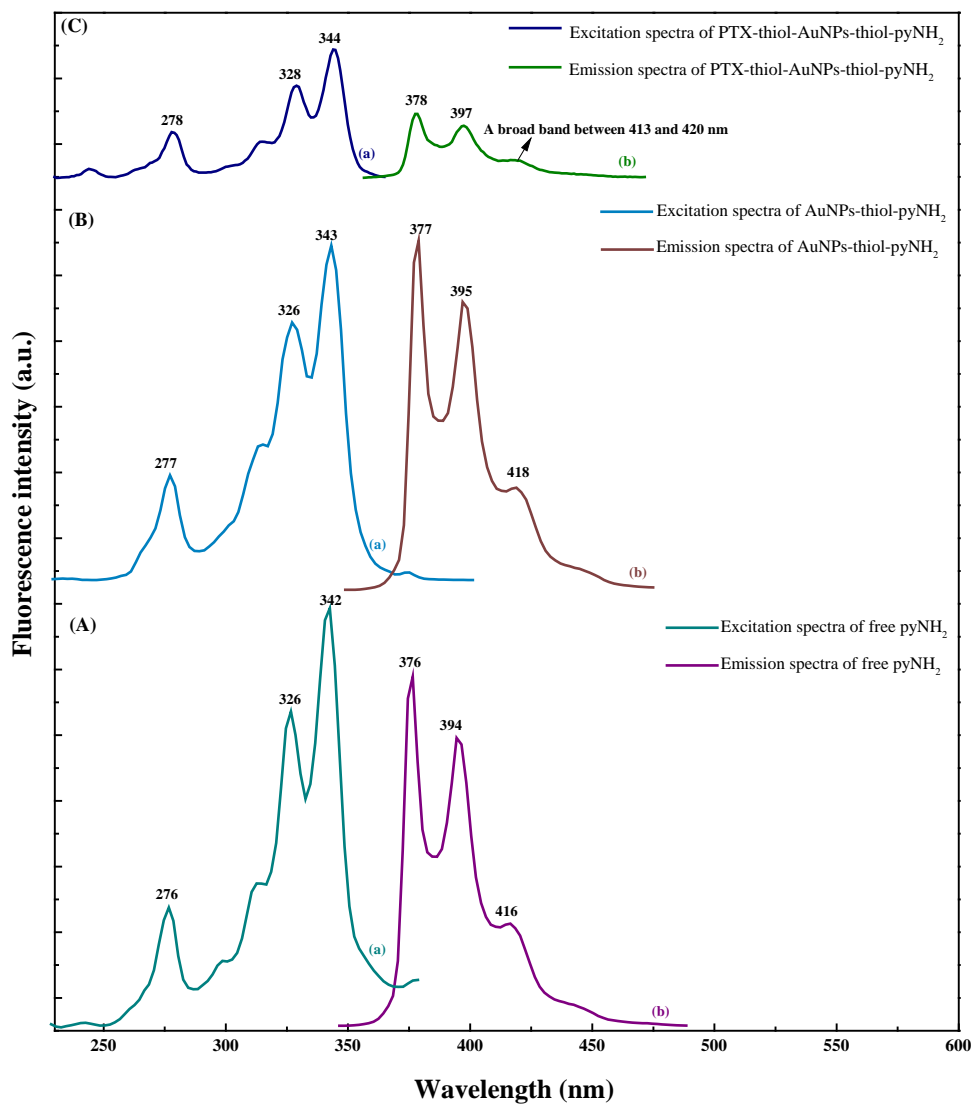


Figure 5.3 Fluorescence (a) excitation and (b) emission spectra of (A) free pyNH₂ (B) AuNPs-thiol-pyNH₂ direct conjugate and (C) PTX-thiol-AuNPs-thiol-pyNH₂ direct conjugate. The excitation spectrum was recorded at an emission wavelength of 376 nm. The emission spectrum was recorded using an excitation wavelength of 342 nm.

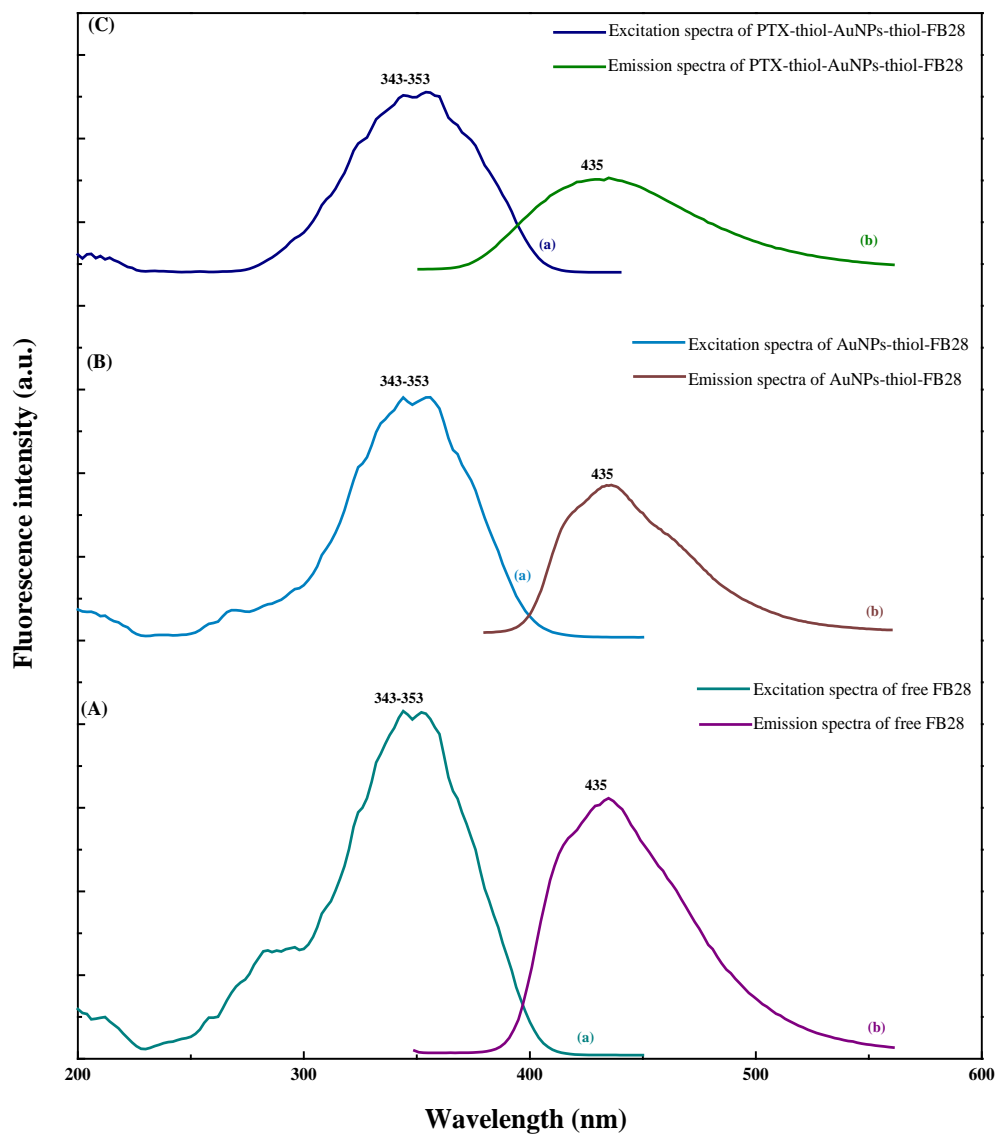


Figure 5.4 Fluorescence (a) excitation and (b) emission spectra of (A) free FB28 (B) AuNPs-thiol-FB28 hybrid and (C) PTX-thiol-AuNPs-thiol-FB28 direct conjugate. The excitation spectrum was recorded at an emission wavelength of 435 nm. The emission spectrum was recorded using an excitation wavelength of 343 nm.

5.2.3 TEM measurements of fluorescently labelled AuNPs

PTX-thiol-AuNPs-thiol-DAPI and PTX-thiol-AuNPs-thiol-pyNH₂ conjugates were characterised by transmission electron microscopy (TEM) to confirm the integrity of monodispersed gold nanoparticles. Figure 5.5 shows typical TEM images of the conjugates. The size distribution histogram shows a narrow size distribution of both conjugates. Dark spots of AuNPs were observed. The increase of particle size in these two conjugates compared to the as-prepared AuNPs suggests a slight potential aggregation of these particles. The TEM images indicate the formation of spherical shape of most AuNPs with some irregular particles.

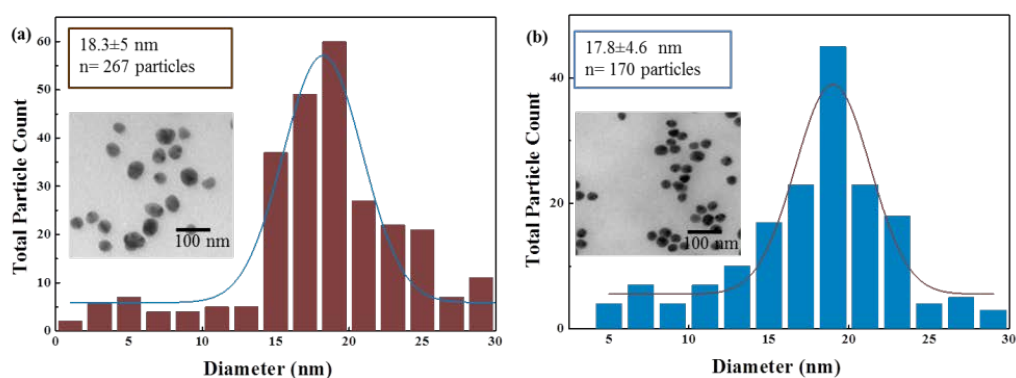


Figure 5.5 TEM images with size distribution histogram of (a) PTX-thiol-AuNPs-thiol-DAPI and (b) PTX-thiol-AuNPs-thiol-pyNH₂ direct conjugates.

5.2.4 Dynamic light scattering (DLS) analysis of fluorescently labelled AuNPs

Dynamic light scattering (DLS) was used to determine the size of the various fluorescently labelled AuNPs conjugates (see Table 5.2). Each sample was diluted with Milli-Q water (1:4, v/v) and the size was determined. In each case, an increase of the size after loading the PTX to the fluorescently labelled AuNPs was observed (see Figure 5.6). Narrow polydispersity indexes were recorded for all fluorescently labelled AuNPs conjugates indicating the formation of monodispersed nanoparticles. (see Table 5.2).

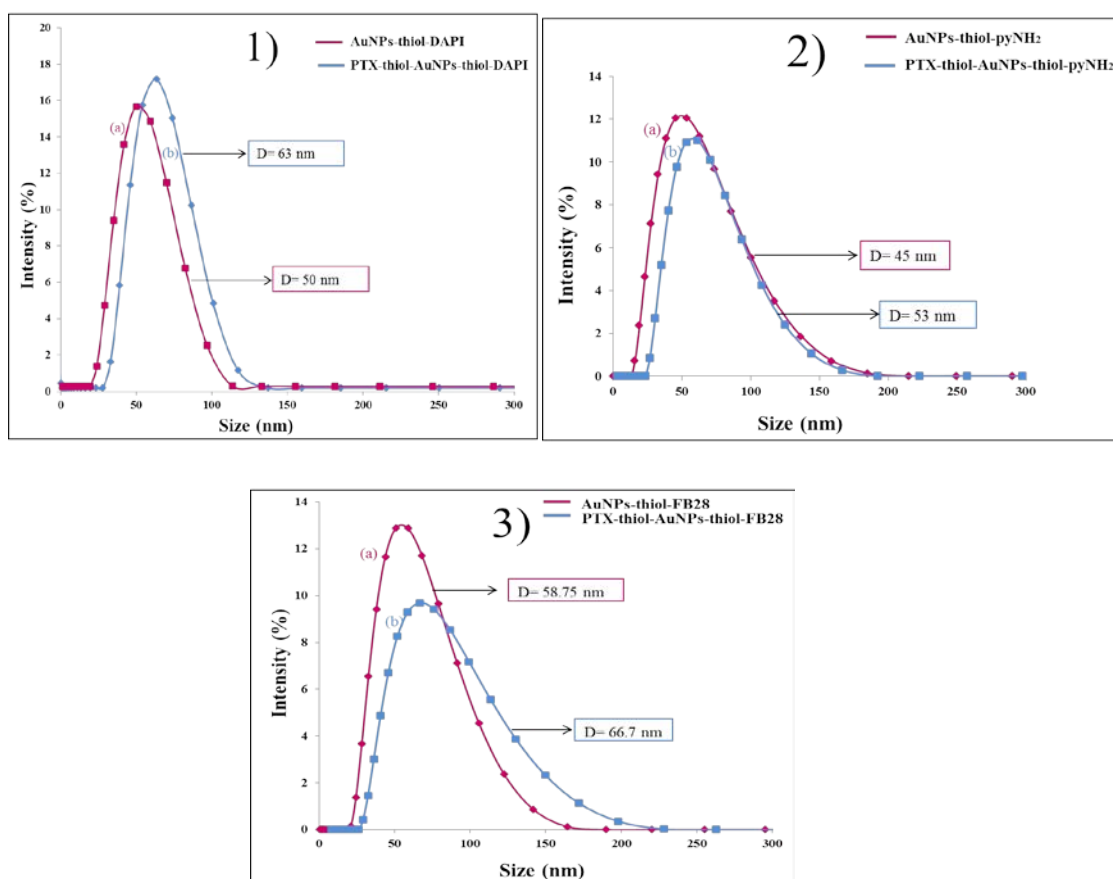


Figure 5.6 DLS measurements of various fluorescent containing nanoparticles. 1) DAPI 2) pyNH₂ and 3) FB28.

Table 5.2 DLS measurements of various fluorescent containing nanoparticles.

Sample	Size distribution by intensity (nm)	Polydispersity index
AuNPs-thiol-DAPI direct conjugate	50	0.394
PTX-thiol-AuNPs-thiol-DAPI direct conjugate	63	0.371
AuNPs-thiol-pyNH ₂ direct conjugate	45	0.196
PTX-thiol-AuNPs-thiol-pyNH ₂ direct conjugate	53	0.280
AuNPs-thiol-FB28 hybrid	58.75	0.356
PTX-thiol-AuNPs-thiol-FB28 direct conjugate	66.7	0.371

5.2.5 FT-IR spectroscopy characterisation of fluorescently labelled AuNPs

FT-IR analysis of different AuNPs samples containing a fluorescent stain (DAPI, pyNH₂ or FB28) was carried out. The FT-IR analysis of LA-AuNPs, thiol-AuNPs and PTX-thiol-AuNPs conjugates was detailed in Sections 3.3.4 and 4.3.1.4 in Chapters 3 and 4, respectively.

Figure 5.7 and Table 5.3 show FT-IR spectra of (a) DAPI alone (b) AuNPs-thiol-DAPI direct conjugate and (c) PTX-thiol-AuNPs-thiol-DAPI direct conjugate. Figure 5.8 and Table 5.4 show the FT-IR spectra of (a) pyNH₂ alone (b) AuNPs-thiol-pyNH₂ direct conjugate and (c) PTX-thiol-AuNPs-thiol-pyNH₂ direct conjugate. While Figure 5.9 and Table 5.5 show the absorbance bands for (a) FB28 alone, (b) AuNPs-thiol-FB28 hybrid and (c) PTX-thiol-AuNPs-thiol-FB28 direct conjugate.

Figure 5.7.a shows the characteristic peaks of free DAPI sample. The spectrum of DAPI alone shows the common characteristic peaks observed in DAPI [395, 396]. An absorption band in the 3387-3344 cm⁻¹ range corresponds to the presence of OH groups from absorbed water and the primary and secondary N-H groups that also absorb in this range [397]. Asymmetric CH₃ stretching at ~2975 cm⁻¹, the band assigned to C=N stretching at ~1672 cm⁻¹ were observed. Also, peaks at ~1610 and 1540 cm⁻¹ can be attributed to amide I and amide II, respectively while the stretching vibrations for aromatic structures appeared at ~1505, 1480 and 1461 cm⁻¹. C-N stretching vibrations were observed at 1329, 1252, 1090 and 1050 cm⁻¹ and CH deformation bands occurred at 880, 850 and 814 cm⁻¹ [395, 396].

Figure 5.8.a shows FT-IR spectrum of free pyNH₂. The spectrum of pyNH₂ alone shows the main characteristic peaks observed in pyNH₂ [396, 398]. An absorbance band at ~3420 cm⁻¹ assigned to NH stretch, the asymmetric and symmetric CH₂ stretching at ~2949 and 2887 cm⁻¹, respectively were observed. C-C aromatic ring stretching vibrations at ~1604, 1590, 1480, 1467 and 1513 cm⁻¹, the CH₂ bending at ~1460 cm⁻¹, symmetric C-H deformation vibrations at ~1374 cm⁻¹, C-N stretching vibrations at ~1328, 1248 and 1090 cm⁻¹ were observed [396, 398].

The FT-IR spectrum of FB28 alone is illustrated in [Figure 5.9.a](#). The FT-IR spectrum of FB28 alone shows the main characteristic peaks observed in fluorescent brightener [399]. A broad band at $\sim 3525\text{-}3282\text{ cm}^{-1}$ is attributed to O–H and N–H stretching vibrations. The peaks at ~ 1613 , 1592 , 1538 and 1504 cm^{-1} are assigned to C=C and C=N stretching vibrations in the aromatic rings, respectively [400, 401]. The peak at $\sim 1418\text{ cm}^{-1}$ is assigned to C–H deformation of the alkyl group whereas the peak at 1362 cm^{-1} is due to OH bending. The absorbance bands at ~ 1309 and 1223 cm^{-1} are assigned to C–N stretching in the aromatic rings. The band at $\sim 1176\text{ cm}^{-1}$ is due to O=S=O asymmetric stretching vibrations in SO₃H groups [402]. The band at $\sim 1048\text{ cm}^{-1}$ is due to –SO₃ symmetric stretching vibrations. The peaks at ~ 1081 and 1022 cm^{-1} are due to C–O–C deformation whereas the peaks at ~ 830 and 758 cm^{-1} are assigned to aromatic =C–H out of plane deformation vibrations [401].

[Figures 5.7.b](#), [5.8.b](#) and [5.9.b](#) and [Tables 5.3](#), [5.4](#) and [5.5](#) show the main characteristic peaks of fluorescent dyes (DAPI, pyNH₂ or FB28) after loading to thiol-AuNPs. The observations from FT-IR indicate the presence of the fluorescent molecules on the thiolated AuNPs. Some characteristic peaks assigned to carboxylic terminated alkanethiols were observed as well. Importantly, the asymmetric and symmetric C–H stretching of the alkyl groups at ~ 2917 and 2849 cm^{-1} , respectively were observed. In pyNH₂ conjugated to thiol-AuNPs, a new peak at $\sim 1722\text{ cm}^{-1}$ assigned to C=O stretching vibration indicating the conjugation of –NH of pyNH₂ with the carbonyl group of carboxylic terminated alkanethiol acids was observed [153, 374, 381]. However, in case of DAPI conjugated to thiol-AuNPs, the FT-IR spectra were complex in the region between 1640 and 1736 cm^{-1} . Thus, it was difficult to observe the new peak allocated to C=O stretching vibration as an indication of the conjugation of –NH of DAPI with –COOH of alkanethiols.

In AuNPs-thiol-FB28 conjugate, no peaks assigned to the formation of ester bonds between –OH groups of FB28 molecules and –COOH groups of carboxylic ends of alkanethiols were obtained (see [Figure 5.9.b](#)), indicating no covalent reaction occurred. The loading of FB28 onto thiol-AuNPs surface can be ascribed to the van der Waals electrostatic interactions between FB28 and carboxylic acids terminated alkanethiols. Other peaks either can be assigned to the staining agents or to carboxylic acids terminal alkanethiols or AuNPs overlapped. Likewise,

unsurprisingly, the samples of thiol-AuNPs containing any of the fluorescent agents and the anticancer, PTX, simultaneously show very complex FT-IR spectra with many overlapping bands. Some common characteristic of the bands are attributed to the present of PTX molecules and others assigned to the staining agent moieties (see [Figures 5.7.c](#), [5.8.c](#) and [5.9.c](#) and [Tables 5.3](#), [5.4](#) and [5.5](#)). Importantly, as shown in [Chapter 4](#) in [Section 4.3.1.4](#), the peak at 1736 cm^{-1} is assigned to the carbonyl group C=O stretching vibrations from the ester group and it is one of main characteristic bands of PTX in addition to a signal at $\sim 1247\text{ cm}^{-1}$ which is due to C-N stretching vibration of PTX were observed in all cases. However, other bands overlapped significantly and were difficult to observe. Therefore, other analytical techniques were utilised.

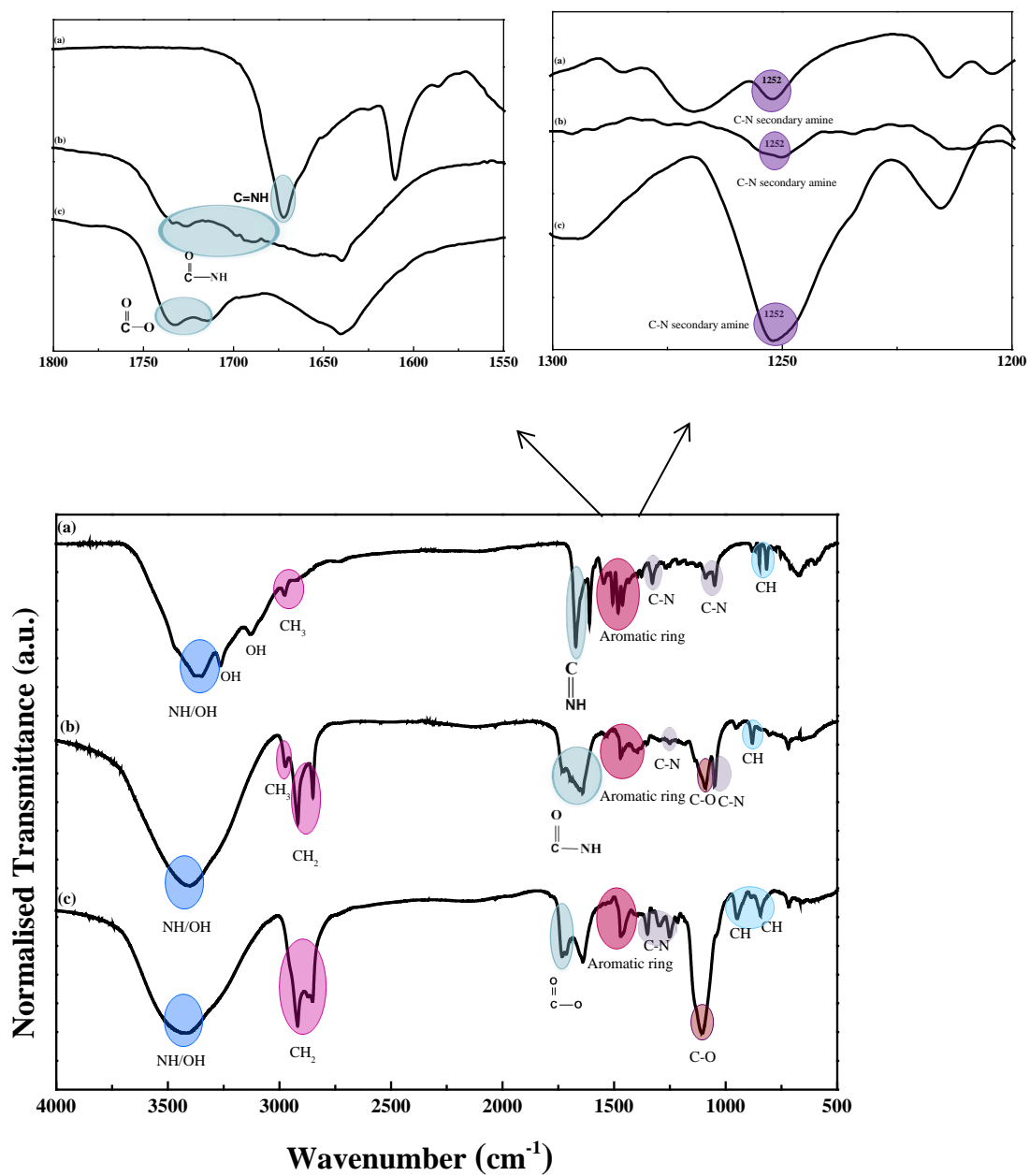


Figure 5.7 FT-IR spectra of (a) DAPI alone (b) AuNPs-thiol-DAPI direct conjugate and (c) PTX-thiol-AuNPs-thiol-DAPI direct conjugate.

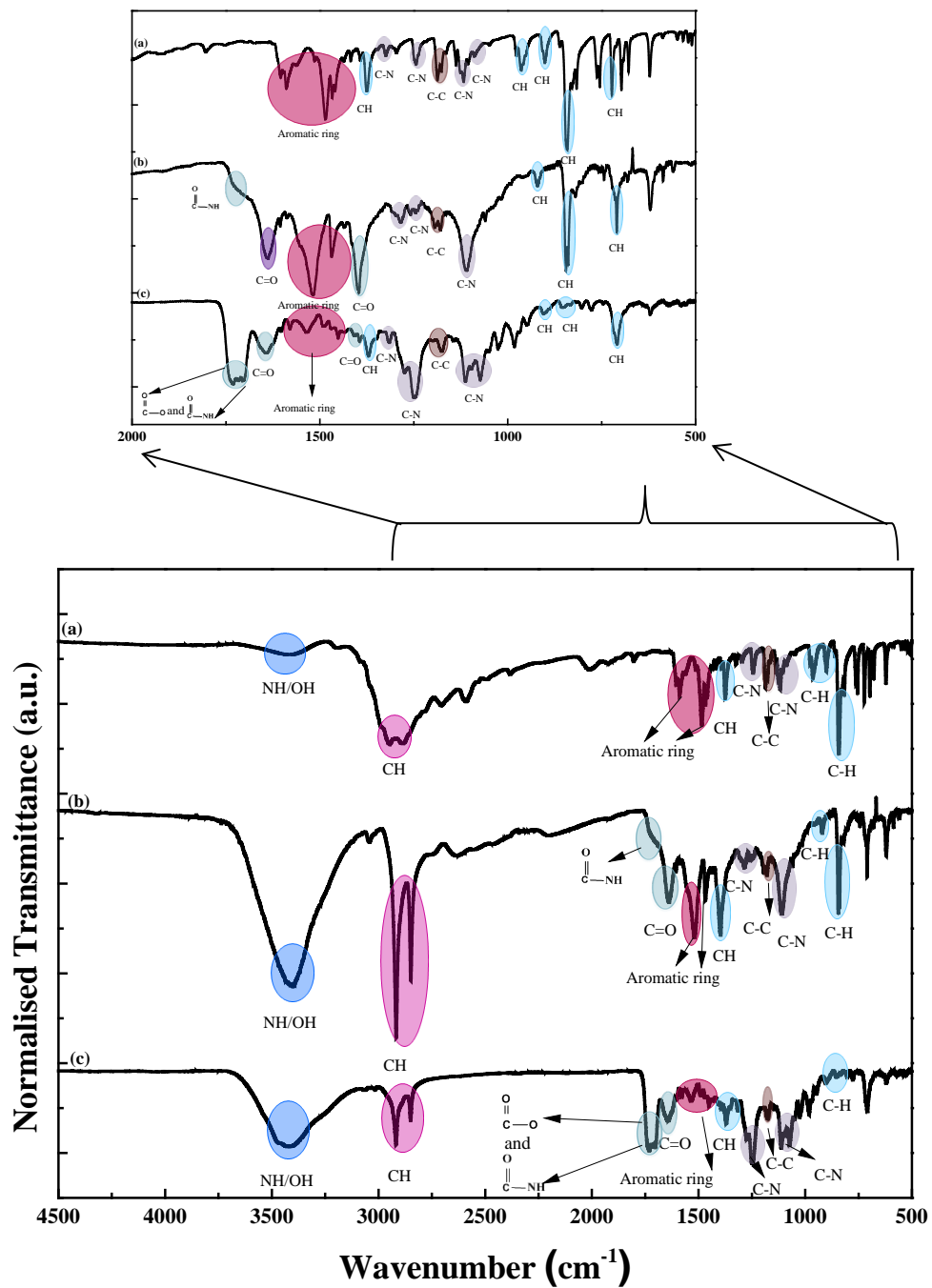


Figure 5.8 FT-IR spectra of (a) pyNH_2 alone (b) AuNPs-thiol- pyNH_2 direct conjugate and (c) PTX-thiol-AuNPs-thiol- pyNH_2 direct conjugate.

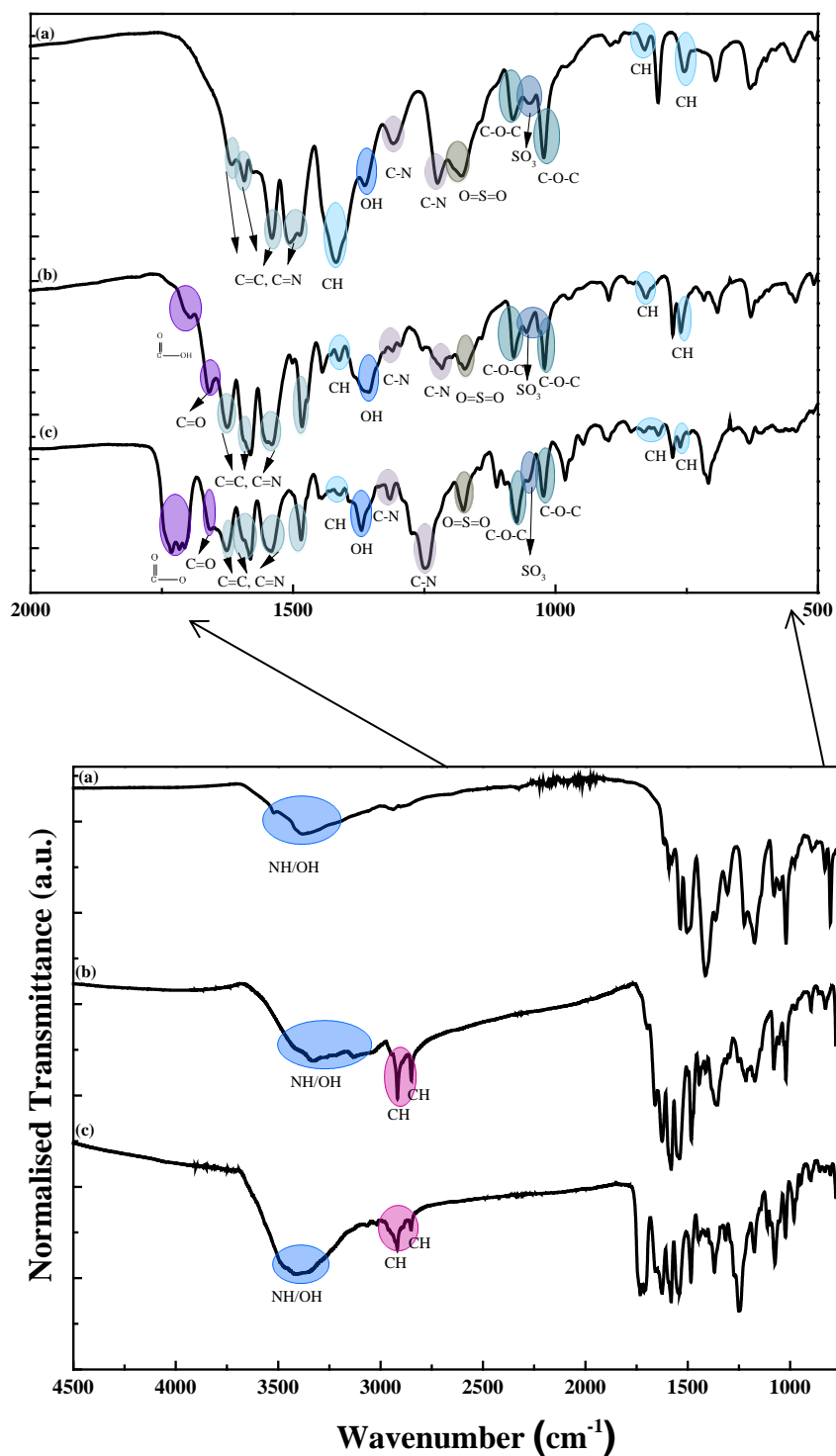


Figure 5.9 FT-IR spectra of (a) free FB28 (b) AuNPs-thiol-FB28 hybrid and (c) PTX-thiol-AuNPs-thiol-FB28 direct conjugate.

Table 5.3 FT-IR peak positions of DAPI alone, AuNPs-thiol-DAPI direct conjugate and PTX-thiol-AuNPs-thiol-DAPI direct conjugate.

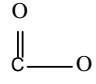
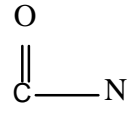
Vibrational modes	WN (cm ⁻¹)/ DAPI alone	WN (cm ⁻¹)/ AuNPs-thiol-DAPI	WN (cm ⁻¹)/ PTX-thiol-AuNPs-thiol-DAPI
NH/OH stretching	3387-3344, 3126, 3258	3365-3460	3365-3500
Asymmetric and symmetric C-H stretching, respectively	2975	2975, 2917, 2850	2917, 2850
C=N	1672	Overlapped	Overlapped
Ester bond 	-	-	1715- 1736
Amide bond 	-	1722	Overlapped with other peaks appeared between 1717 and 1736
C=C-C aromatic ring stretching vibrations	1505, 1479, 1461	1475	1475
C-N stretching vibration	1329, 1252, 1090, 1050	1247, 1050	1333, 1248
C-O stretching vibration	-	1093	1100
C-H bending	880, 850, 814	880	948, 840

Table 5.4 FT-IR peak positions of pyNH₂ alone, AuNPs-thiol-pyNH₂ direct conjugate and PTX-thiol-AuNPs-thiol-pyNH₂ direct conjugate.

Vibrational modes	WN (cm ⁻¹)/ PyNH ₂ alone	WN (cm ⁻¹)/ AuNPs-thiol-pyNH ₂	WN (cm ⁻¹)/ PTX-thiol-AuNPs-thiol-pyNH ₂
NH/OH stretching	3420	3420	3378-3470
Asymmetric and symmetric C-H stretching, respectively.	2949, 2887	2917, 2850	2917, 2850
Ester bond $\begin{array}{c} \text{O} \\ \parallel \\ \text{C} - \text{O} \end{array}$	-	-	1715- 1736
Amide bond $\begin{array}{c} \text{O} \\ \parallel \\ \text{C} - \text{N} \end{array}$	-	1727	Overlapped with other peaks appeared between 1717 and 1736 1643
C=O stretching	-	1640	1640
C=C-C aromatic ring stretching vibrations	1604, 1590, 1480, 1467, 1513	1536, 1467	1580, 1485, 1536, 1452
C-N stretching vibration	1320, 1244, 1175, 1114, 1090	1317, 1244, 1196, 1175, 1114	1317, 1248, 1175, 1114, 1094, 1024
C-H bending	1374	Undetectable	1370
C-C stretching	1176	1176	1176
C-O stretch	-	1285, 1110	1275, 1074
C-H out of plane and in-plane vibrations	967, 900, 722, 840, 815, 761	920, 845, 836, 743, 710, 620	980, 776, 708, 904, 850, 803, 948

Table 5.5 FT-IR peak positions of FB28 alone, AuNPs-thiol-FB28 hybrid and PTX-thiol-AuNPs-thiol-FB28 direct conjugate.

Vibrational modes	WN (cm ⁻¹)/ FB28 alone	WN (cm ⁻¹)/ AuNPs-thiol-FB28	WN (cm ⁻¹)/ PTX-thiol-AuNPs-thiol-FB28
NH/OH stretching	3520-3231	3427-3133	3490-3285
Asymmetric and symmetric C-H stretching, respectively.	-	2917, 2849	2917, 2849
Ester bond $\begin{array}{c} \text{O} \\ \parallel \\ \text{C} \text{---} \text{O} \end{array}$	-	-	1715- 1736
C=O stretching of carboxylic acid	-	1698	1704
C=O stretching	-	1660	1660
C=C and C=N aromatic ring stretching vibrations	1619, 1592, 1538, 1504	1624, 1592, 1538	1624,1592, 1538
OH bending	1362	1362	1365
C-N stretching vibration of aromatic ring	1309, 1223	1309, 1223	1309, 1247
C-H bending	1418	1418	1418
O=S=O asymmetric stretching vibrations	1176	1176	1176
C-O-C deformation	1081, 1022	1081, 1022	1081, 1022
=C-H aromatic out of plane deformation	830, 758	830, 758	830, 758

5.2.6 ^1H NMR spectroscopy characterisation of fluorescently labelled AuNPs

^1H NMR spectroscopy characterisation of each free staining agent and after conjugation with AuNPs was carried out (see Table 5.1). DMSO- d_6 was used as a solvent due to the fact that DMSO- d_6 was appropriate in the following steps of conjugation a dye and/or PTX with thiol-AuNPs. Figure 5.13.a and Table 5.6 show the ^1H NMR spectrum of free DAPI. The chemical shifts for DAPI alone (Figure 5.10) ranging between 7.0 and 10 ppm were observed with 6 distinctive signals (doublet, $\text{H}_{2', 6', 7}$), (triplet, $\text{H}_{3', 5'}$), (doublet, H_4), (two doublet, H_5), (singlet, H_3) and (singlet, NH indole) [403]. DAPI resonances $\text{H}_{3'}$, $\text{H}_{5'}$, $\text{H}_{2'}$, and $\text{H}_{6'}$ of the phenyl ring were not resolved and overlapped with H_7 . These protons were labelled $\text{H}_{3', 5'}$ and $\text{H}_{2', 6', 7}$ and their chemical shifts were observed at $\delta = 7.98$ ppm and 8.2 ppm, respectively. On the other hand, the resonances for the protons on indole ring (H_3 , H_4 , H_5 and NH) were observed at chemical shifts $\delta = 7.32$, 7.79, 7.47 and 9.2 ppm, respectively [403, 404].

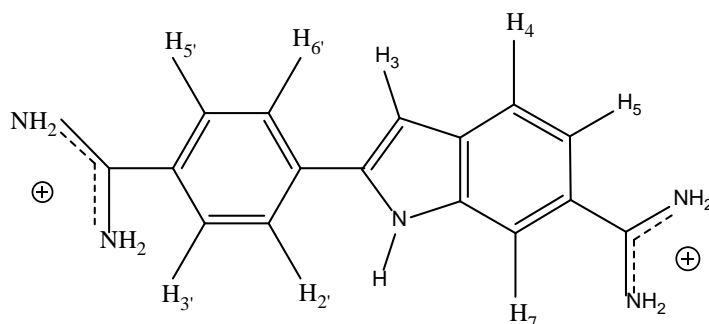


Figure 5.10 Chemical structure and proton numbering of DAPI alone.

Figure 5.14.a shows the ^1H NMR spectrum of free pyNH $_2$ (Figure 5.11). The chemical shifts are presented in Table 5.7. In pure pyNH $_2$ sample, 4 different types of protons were observed: 4.82 (singlet, H_j), 8.12 (multiplet, $\text{H}_{d,e,f,g}$), 8.35 (multiplet, $\text{H}_{b,c}$) and 8.47 (doublet, H_a) [405]. However, the protons of $-\text{NH}_2$ were undetectable (see Figure 5.14.a and Table 5.7).

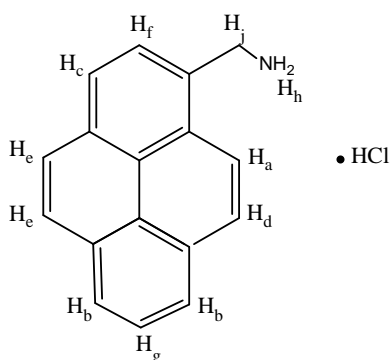


Figure 5.11 Chemical structure of pyNH₂.

Figure 5.15.a and Table 5.8 show the ¹H NMR spectrum of free FB28 (Figure 5.12). The chemical shifts for FB28 alone were observed with 9 distinctive signals (doublet, 7.5), (doublet, 7.75), (triplet, 6.86), (triplet, 7.18), (singlet, 8), (singlet, 8.97), (singlet, 9.16), (singlet, 3.66) and (singlet, 3.58). The doublets may originate from cis-trans isomerism structures [406].

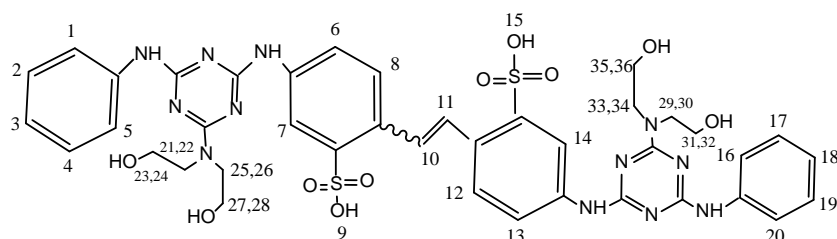


Figure 5.12 Chemical structure and proton numbering of FB28.

It was noticed that the singlet signal of -NH₂ for both DAPI alone and pyNH₂ alone samples and the signal of -OH in FB28 alone were not observable. Generally, the protons of amine, amide and hydroxyl groups appear as broad peaks and have a chemical shift between 1 and 5 ppm. However, labile nitrogen and/or oxygen connected with protons show rapid exchange with the solvent making the protons difficult to observe by NMR spectroscopy. In addition, probable detection of these protons attached N or O atoms needs special environment of low temperature, pH and buffer concentration causing resonating of protons over a wide range of chemical

shifts [407]. These reasons may contribute to the difficulty in observing the -NH_2 protons for free DAPI and pyNH_2 molecules and -OH proton for FB28 alone. Although NH_2 protons were not observable using ^1H NMR spectroscopy, it was assumed that covalent binding occurred between NH_2 group on DAPI or pyNH_2 and -COOH groups on thiol-AuNPs as the chemical conditions (EDC/NHS chemistry) have been used previously in this research project and shown a successful attachment between $\text{C}_{2'}$ -OH and C_{7} -OH of PTX and the carboxylic ends of thiol-AuNPs confirmed by ^1H NMR spectra. In addition, Rudershausen et al. [362] reported a successful covalent attachment of fluorescent dye, DAPI onto the surface of the superparamagnetic dextran nanoparticles through bifunctional carboxylic acid used as spacer to link the fluorescent dye via one of its amino groups to hydroxyl groups of the dextran nanoparticles by using carbodiimide activation [362]. However, as observed before, no signal assigned to the protons of the exchangeable amino group in case of DAPI and pyNH_2 and hydroxyl group in FB28 was observed (see [Figures 5.13.a](#), [5.14.a](#) and [5.15.a](#)).

After attaching DAPI or pyNH_2 to the functionalised AuNPs, all the peaks assigned to these staining agents were slightly upfield shifted (see [Figures 5.13.b](#) and [5.14.b](#) and [Tables 5.6](#) and [5.7](#)) whereas after loading FB28 to the functionalised surface of AuNPs all peaks in aromatic region were shifted to downfield except for $\text{H}_{8,12}$, $\text{H}_{10,11}$ and $\text{H}_{6,13}$. The $\text{H}_{8,12}$ and $\text{H}_{10,11}$ were slightly shifted to upfield and $\text{H}_{6,13}$ did not change its position. The $\text{H}_{21,22,25,26,29,30,33,34}$ and $\text{H}_{23,24,27,28,31,32,35,36}$ did not show any position changes ([Figure 5.15.b](#) and [Table 5.8](#)). In case of conjugation DAPI to thiol-AuNPs, the $\text{H}_{2', 6', 7}$ peak was the most shifted due to nuclear overhauser effects (NOE), which are the transmissions of spin polarization from one nuclear spin to another nuclear spin via cross-relaxation, of NH_2 protons only with the unresolved proton $\text{H}_{2', 6', 7}$ [404]. In addition, some peaks appeared wider than that in free DAPI indicating the successful conjugation of DAPI onto the functionalised AuNPs. However, the proton of indole nitrogen in AuNPs-thiol-DAPI sample disappeared after binding to the surface of functionalised AuNPs. This can be attributed to the low concentration of DAPI molecules in the prepared sample (AuNPs-thiol-DAPI direct conjugate) compared to its concentration in free DAPI sample [408] as well as the broad nature of the peak which will make it difficult to observe at low concentrations. A study conducted by Trotta et al. [408] reported a similar result. They characterised DAPI

bound to a DNA oligomer (d(CGATCG))₂ using ¹H NMR spectroscopy. They found that when increasing the concentration of DAPI, the imino proton spectra of DAPI·(d(CGATCG))₂ complexes appeared more intense. In case of conjugation pyNH₂ to thiol-AuNPs, a large upfield chemical shift was recorded to H_j from pyNH₂ molecule. The resonance shift for H_j was from $\delta = 4.81$ ppm in free pyNH₂ to $\delta = 4.49$ ppm in AuNPs-thiol-pyNH₂ conjugate with $\Delta\delta = 0.32$ ppm. This shift can be ascribed to the fact that H_j is adjacent to amino group (–NH₂) where the attachment occurred. In FB28 loaded thiol-AuNPs, the largest shift to downfield was recorded for aromatic –NH and –SO₃H of FB28 (see [Figure 5.15.b](#) and [Table 5.8](#)).

In all AuNPs samples containing a fluorescent agent, most of the peaks in the chemical shift region between 0 and 4 ppm can be assigned to LA and 16-MHDA functionalised the AuNPs surface (see [Figures 5.13.b](#), [5.14.b](#) and [5.15.b](#)) (the detailed ¹H NMR for LA and 16-MHDA can be found in [Chapter 3](#), [Sections 3.3.5.2](#) and [3.3.5.3](#), respectively). Some peaks were unobservable due to the solvent (water and DMSO-d₆) peaks whereas some other peaks are impurities from the solvent. On the other hand, the resonance of H₁₇ on sulfur atom disappeared after replacement of 16-MHDA with LA indicating the successful exchange.

[Figures 5.13.c](#), [5.14.c](#) and [5.15.c](#) and [Tables 5.6](#), [5.7](#) and [5.8](#) demonstrate ¹H NMR spectra of the fluorescent agents and the chemotherapeutic, PTX, loaded simultaneously to the functionalised AuNPs. The main observations in these conjugates are:

1. Some peaks assigned to PTX overlapped with other peaks for DAPI or FB28 staining agents in the region between 7 and 10 ppm making those peaks difficult to see. No peaks assigned to PTX overlapped with peaks for pyNH₂ in the same region making those peaks easy to see.
2. Large chemical shifts to downfield was recorded to H_{2', 6', 7} from DAPI molecule. The resonance shift for H_{2', 6', 7} was from $\delta = 8.2$ ppm in DAPI alone to $\delta = 9$ ppm in PTX-thiol-AuNPs-thiol-DAPI conjugate giving $\Delta\delta = 0.8$ ppm. Also, upfield shifting was observed for H_{3', 5'} from DAPI molecules. The shift for H_{3', 5'} was from $\delta = 7.98$ ppm in DAPI alone to $\delta = 7.63$ ppm in PTX-thiol-AuNPs-thiol-DAPI conjugate with

$\Delta\delta = 0.35$ ppm. This can be assigned to the effects of formation new bonds between DAPI and the thiol-AuNPs and between PTX and the thiol-AuNPs as well. A large upfield chemical shift was recorded for H_j from pyNH₂ molecule. The resonance shift for H_j was from $\delta = 4.81$ ppm in free pyNH₂ to $\delta = 4.73$ ppm in PTX-thiol-AuNPs-thiol-pyNH₂ direct conjugate with $\Delta\delta = 0.08$ ppm. The reason of this shift can be ascribed to the fact that H_j is adjacent to amino group ($-NH_2$) where the attachment occurred. Some signals assigned to FB28 were upfield shifted ($H_{7,14}$, $H_{10,11}$) while other downfield shifted ($H_{21,22,25,26,29,30,33,34}$, $H_{23,24,27,28,31,32,35,36}$ and $H_{3,18}$) in PTX-thiol-AuNPs-thiol-FB28 conjugate.

3. Importantly, the peaks assigned to the resonance of C_7 -OH and C_2 -OH observed at $\delta = 2.47$ and 3.53 ppm, respectively in free PTX disappeared after conjugation of PTX with thiol-AuNPs. When expanding the spectra no peaks were recorded in the region between 2.4-2.5 ppm (for C_7 -OH) and 3.50-3.60 ppm (for C_2 -OH) indicating the successful formation of ester bonds.

4. The peaks in the region between 0 and 4 ppm assigned to the presence of PTX, 16-MHDA and LA molecules overlapped making those peaks difficult to see. However, the peaks in the region between 4 ppm and 7 ppm allocated to PTX molecules were observed (refer to [Chapter 4, Section 4.3.1.5](#) for more details).

5. The purpose of using ¹H NMR with FB28 containing samples was to further investigate if there was a covalent binding between $-OH$ groups on FB28 and $-COOH$ ends from alkanethiol acids and to confirm the loading of FB28 molecules onto the AuNPs surface.

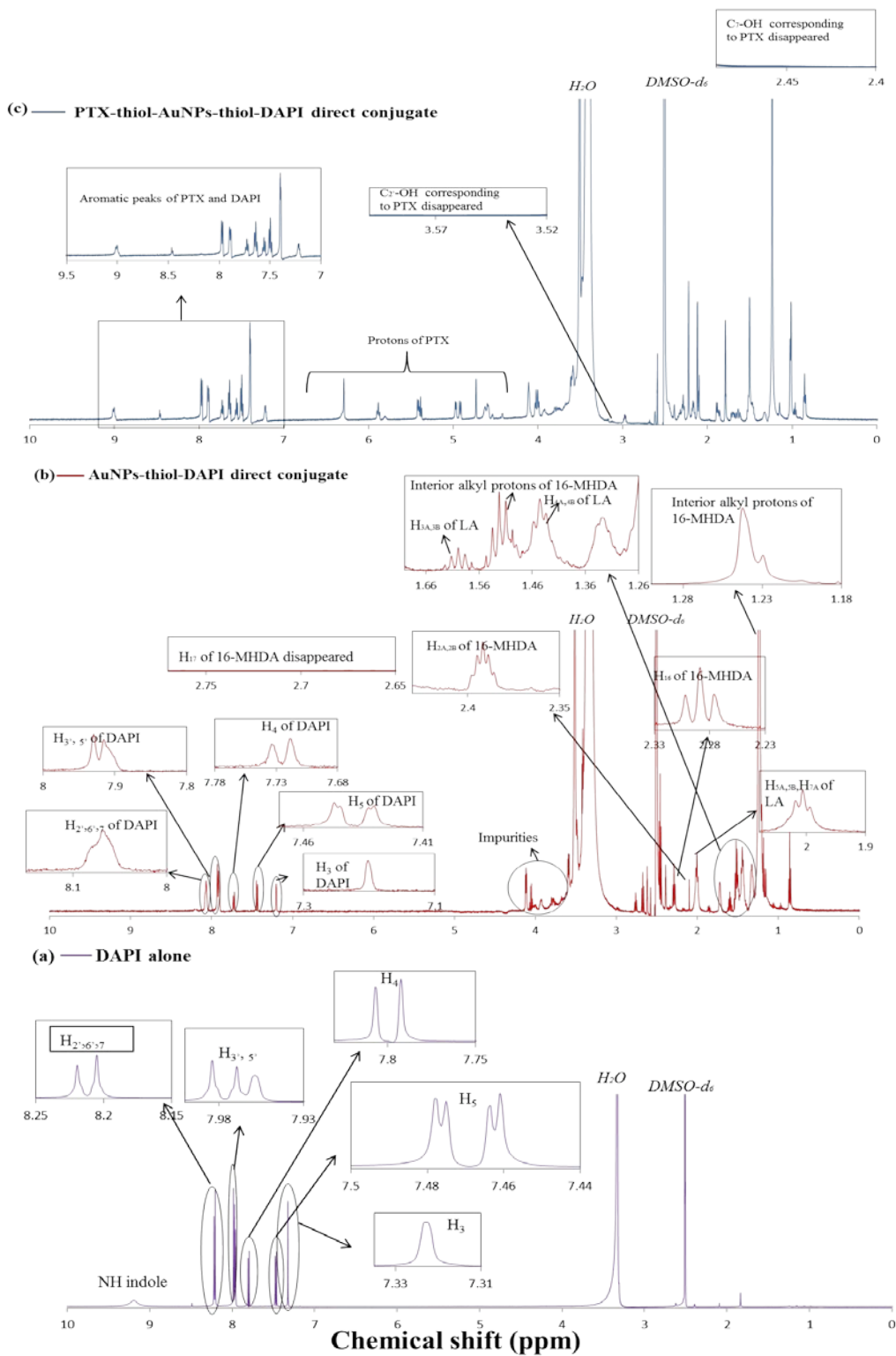


Figure 5.13 ^1H NMR spectra of (a) DAPI alone (b) AuNPs-thiol-DAPI direct conjugate and (c) PTX-thiol-AuNPs-thiol-DAPI direct conjugate.

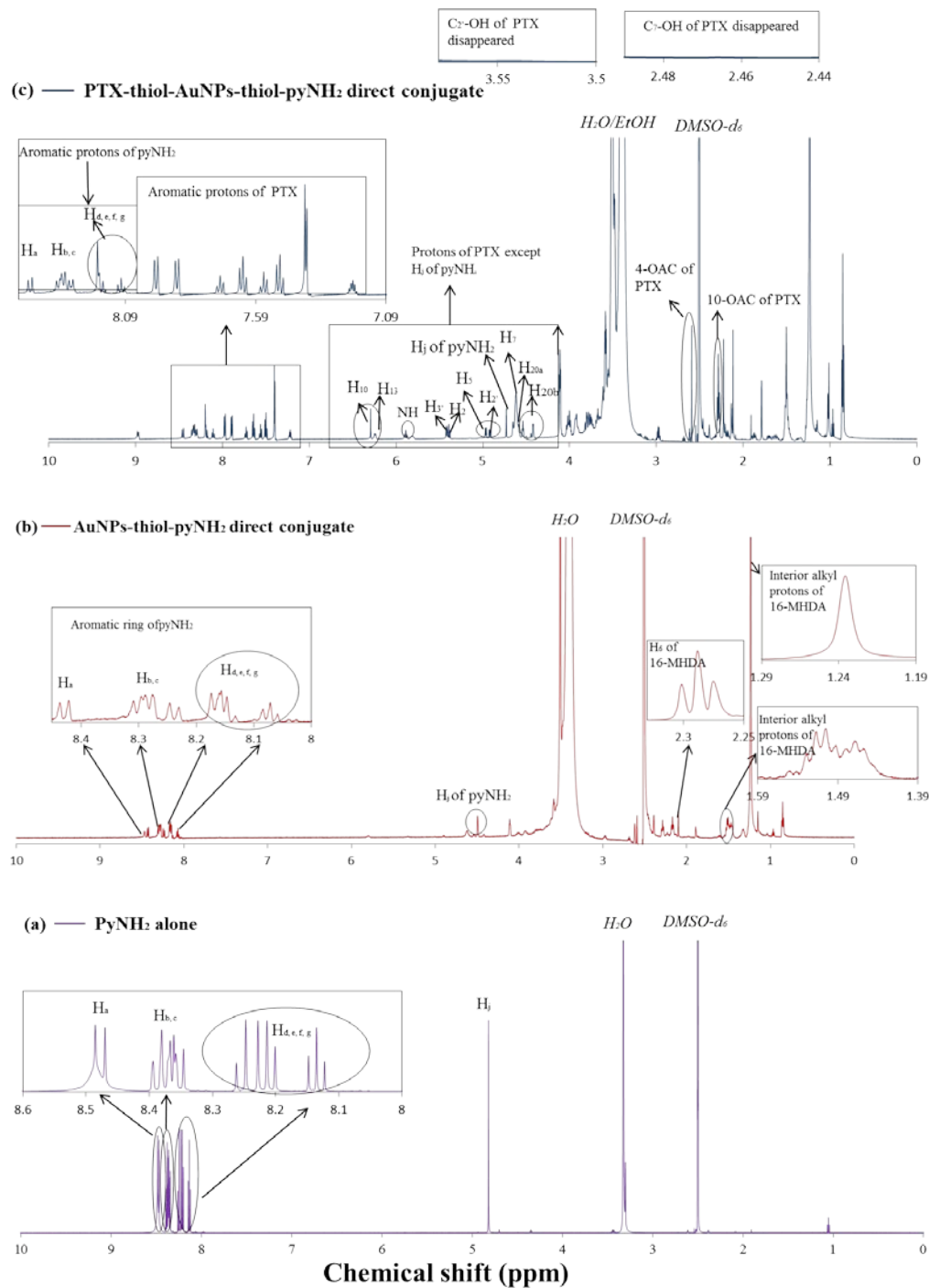


Figure 5.14 ¹H NMR spectra of (a) pyNH₂ alone (b) AuNPs-thiol-pyNH₂ direct conjugate and (c) PTX-thiol-AuNPs-thiol-pyNH₂ direct conjugate.

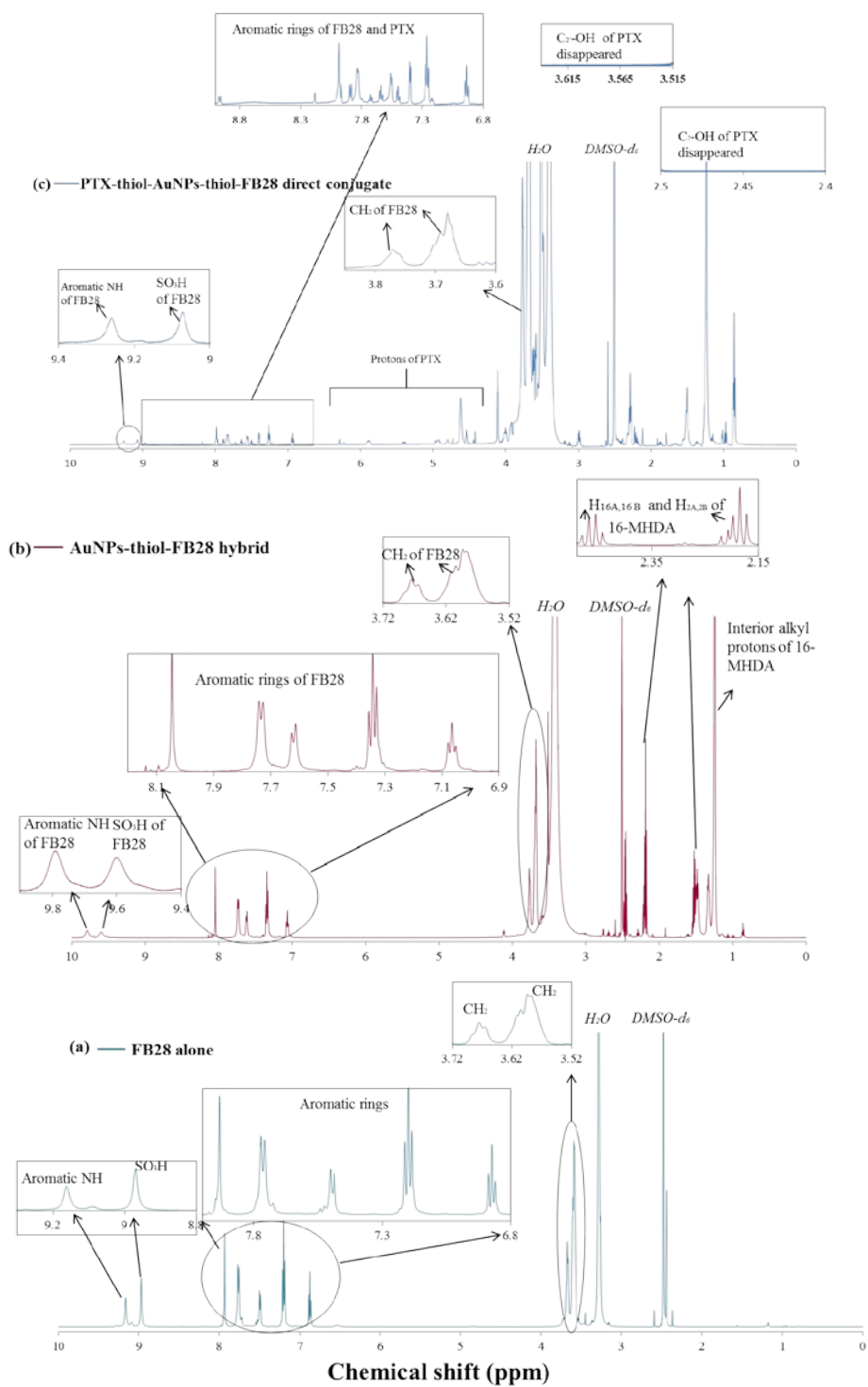


Figure 5.15 ^1H NMR spectra of (a) FB28 alone (b) AuNPs-thiol-FB28 hybrid and (c) PTX-thiol-AuNPs-thiol-FB28 direct conjugate.

Table 5.6 Chemical shifts (δ /ppm) for DAPI alone, AuNPs-thiol-DAPI direct conjugate and PTX-thiol-AuNPs-thiol-DAPI direct conjugate.

Peak position of free DAPI	δ (ppm) of free DAPI	δ (ppm) of AuNPs-thiol-DAPI	$\Delta\delta$ (ppm) of AuNPs-thiol-DAPI and free DAPI	δ (ppm) of PTX-thiol-AuNPs-thiol-DAPI	$\Delta\delta$ (ppm) of PTX-thiol-AuNPs-thiol-DAPI and free DAPI
H _{2',6',7'}	8.2	8.065	0.135	9	0.8
H _{3',5'}	7.98	7.93	0.05	7.63	0.35
H ₄	7.79	7.72	0.07	Overlapped with PTX peaks	-
H ₅	7.47	7.43	0.04	Overlapped with PTX peaks	-
H ₃	7.32	7.2	0.12	Overlapped with PTX peaks	-
NH indole	9.2	Not observed	-	Not observed	-
NH ₂	Not observed	Not observed	-	Not observed	-

Table 5.7 Chemical shifts (δ /ppm) for free pyNH₂, AuNPs-thiol-pyNH₂ direct conjugate and PTX-thiol-AuNPs-thiol-pyNH₂ direct conjugate.

Peak position of free pyNH ₂	δ (ppm) of free pyNH ₂	δ (ppm) of AuNPs-thiol-pyNH ₂	$\Delta\delta$ (ppm) of AuNPs-thiol-pyNH ₂ and free pyNH ₂	δ (ppm) of PTX-thiol-AuNPs-thiol-pyNH ₂	$\Delta\delta$ (ppm) of PTX-thiol-AuNPs-thiol-pyNH ₂ and free pyNH ₂
H _a	8.47	8.42	0.05	8.45	0.02
H _{b,c}	8.35	8.23	0.12	8.29	0.06
H _{d,e,f,g}	8.12	8.06	0.06	8.08	0.04
H _j	4.81	4.49	0.32	4.73	0.08
H _h	Undetectable	-	-	-	-

Table 5.8 Chemical shifts (δ /ppm) for free FB28, AuNPs-thiol-FB28 hybrid and PTX-thiol-AuNPs-thiol-FB28 direct conjugate

Peak position of free FB28	δ (ppm) of free FB28	δ (ppm) AuNPs-thiol-FB28	$\Delta\delta$ (ppm) of AuNPs-thiol-FB28 and free FB28	δ (ppm) of PTX-thiol-AuNPs-thiol-FB28	$\Delta\delta$ (ppm) of PTX-thiol-AuNPs-thiol-FB28 and free FB28
H _{7,14}	9.16	9.79	0.63	9.05	0.11
H _{10,11}	8.97	9.6	0.63	9.3	0.33
H _{6,13}	8	8	0	8	0
H _{8,12}	7.75	7.73	0.02	Overlapped with PTX aromatic peaks	-
H _{1,5,16,20}	7.5	7.61	0.11	Overlapped with PTX aromatic peaks	-
H _{2,4,17,19}	7.18	7.32	0.14	Overlapped with PTX aromatic peaks	-
H _{3,18}	6.86	7.05	0.19	6.92	0.06
H _{21,22,25,26,29,30,33,34}	3.66	3.66	0	3.75	0.09
H _{23,24,27,28,31,32,35,36}	3.58	3.58	0	3.68	0.1

5.2.7 Cytotoxicity evaluation of fluorescently labelled AuNPs

Cytotoxicity assessment on T47D breast cancer cell lines treated with different concentrations of various staining agents containing gold nanoparticles to examine their safety and suitability to trace the intracellular uptake of AuNPs by T47D cells was carried out. A description of the experiments and results is in [Appendix C](#). Briefly, T47D cells were treated with a variety of concentrations of AuNPs-thiol-DAPI, AuNPs-thiol-pyNH₂ direct conjugates and AuNPs-thiol-FB28 hybrid for 24 h of treatment to investigate the relative cell survival and compare that to untreated controls following the crystal violet assay procedure.

As synthesised AuNPs and thiol-AuNPs were considered safe to T47D cell lines as the cell relative survival was continuously above 80 %, indicating no significant cytotoxicity was induced by any concentrations tested of the AuNPs and thiol-AuNPs after 24 hours treatment period.

[Figure 5.16](#) shows response of T47D cell line to 24 h treatment with AuNPs-thiol-DAPI, AuNPs-thiol-pyNH₂ direct conjugates or AuNPs-thiol-FB28 hybrid. The data for cells treated with DAPI or FB28 containing samples shows no significant reduction of relative cell survival indicating no cytotoxicity. Likewise, the data for cells treated with AuNPs-thiol-pyNH₂ direct conjugate shows no significant decrease of relative cell survival in cell lines treated with the concentrations between 3.7×10^{-6} and 3.7×10^{-4} mM of the conjugate. The results reveal the suitability of AuNPs-thiol-DAPI direct conjugate and AuNPs-thiol-FB28 hybrid at any concentration tested to detect the cellular uptake and localisation of AuNPs and suggesting use of these conjugates will be possible in other medical applications. However, the AuNPs-thiol-pyNH₂ direct conjugate can be considered a safe product for intracellular applications when using very low concentrations. It is worth mentioning that when a treatments' relative survival is higher than 100 % it just means that there are more alive cells in these wells than in the control ones, which potentially means that the cells are proliferating.

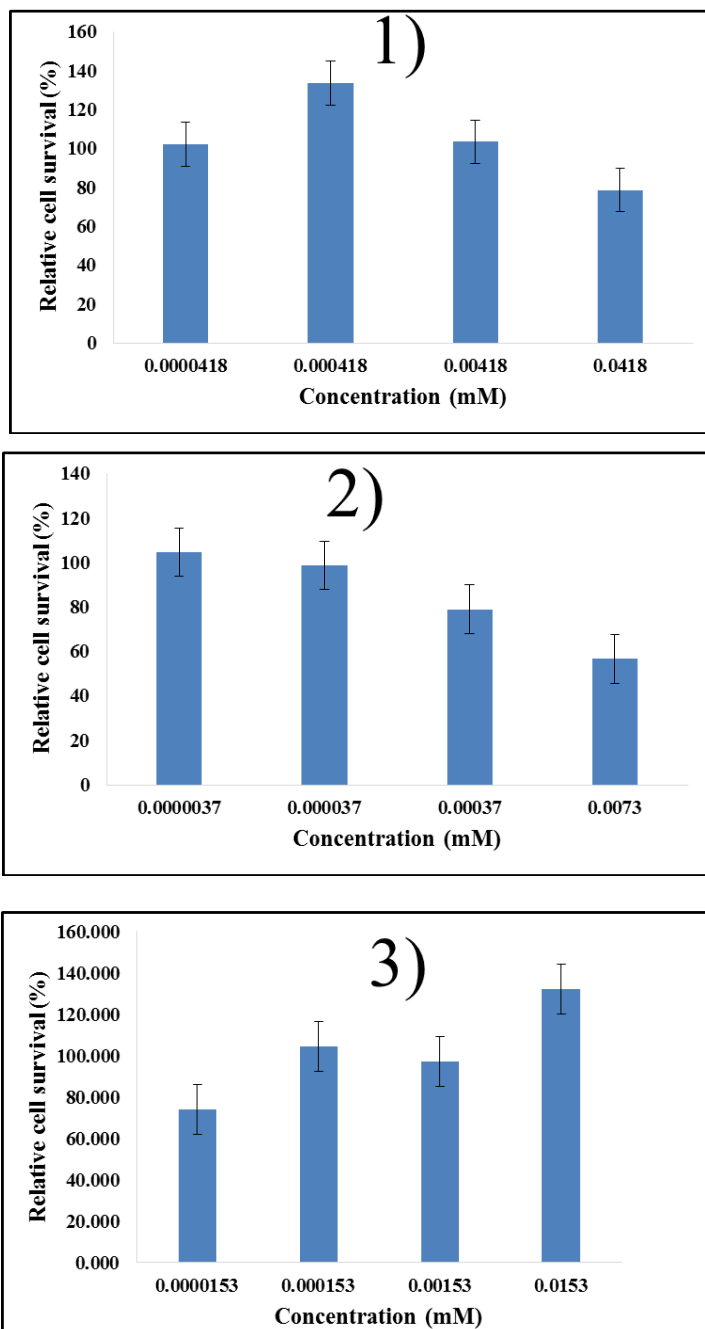


Figure 5.16 Cytotoxicity analysis of various fluorescent containing nanoparticles. 1) AuNPs-thiol-DAPI direct conjugate 2) AuNPs-thiol-pyNH₂ direct conjugate and 3) AuNPs-thiol-FB28 hybrid in T47D human breast cancer cells. Results were tested by One-way ANOVA and statistical significance showing * at P<0.05.

5.3 Characterisation of PTX-16-MHDA-AuNPs-16-MHDA-DAPI reverse conjugate

5.3.1 UV-Vis analysis of PTX-16-MHDA-AuNPs-16-MHDA-DAPI reverse conjugate

The UV-Vis absorbance bands of free PTX and free DAPI were detailed in [Chapter 3, Section 3.3.1](#) and [Chapter 5, Section 5.2.1](#) respectively. Briefly, the main absorbance band of free DAPI appeared at 342 nm and two weaker bands showed at 261 and 225 nm. The absorbance band of free PTX was observed at 228 nm. [Figure 5.17.a](#) shows a UV-Vis spectrum for 16-MHDA functionalised DAPI. A strong absorbance peak at 344 nm assigned to DAPI was observed with a slight shift to the red compared to free DAPI. A small band at 258 nm may assign to DAPI or to NHS was observed and no purification process was applied in this step. This shift can be attributed to the formation of amide bond between ($-\text{NH}_2$) groups of DAPI and ($-\text{COOH}$) groups of carboxylic acid terminated alkanethiols. [Figure 5.17.b](#) displays the spectrum for 16-MHDA attached PTX. The PTX absorbance band at 229 nm [8] was obviously observed. In addition, a broad band with slight shifting to the red assigned to NHS molecules was observed as no purification was applied in this step. [Figure 5.17.c](#) shows the absorbance bands of 16-MHDA-DAPI and PTX-16-MHDA conjugated AuNPs simultaneously (PTX-16-MHDA-AuNPs-16-MHDA-DAPI reverse conjugate) where purification was applied through centrifugation of the sample 5 times. The main distinctive and broad absorption peak assigned to DAPI was observed at 349 nm with longer wavelength compared to 16-MHDA-DAPI conjugate (344 nm). A broad band due to the presence of AuNPs was obtained between 528 and 585 nm. However, the PTX absorption band was not observed in the reverse conjugate due to the low amount of PTX attached to the conjugate.

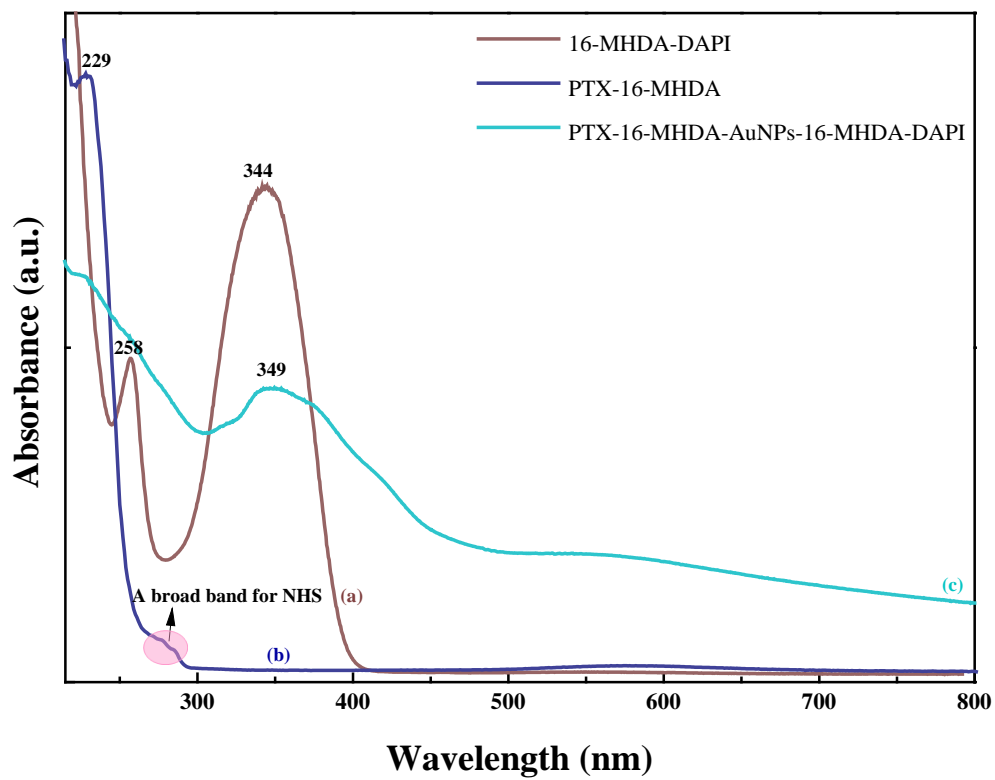


Figure 5.17 UV-Vis spectra of (a) 16-MHDA-DAPI (b) PTX-16-MHDA and (c) PTX-16-MHDA-AuNPs-16-MHDA-DAPI reverse conjugate.

5.3.2 Fluorescence spectroscopy analysis of PTX-16-MHDA-AuNPs-16-MHDA-DAPI reverse conjugate

The fluorescence excitation and emission spectra of free DAPI dissolved in EtOH was detailed in [Section 5.2.2](#) in [Chapter 5](#). [Figure 5.18.A](#) shows the excitation and emission peaks for 16-MHDA functionalised DAPI dissolved in EtOH where the sample was not purified. An intense and significant excitation peak of DAPI appeared at 359 nm along with small and split peak observed at 250-258 nm. The fluorescence emission band of DAPI was observed at 461 nm with excitation wavelength of 358 nm. [Figure 5.18.B](#) shows the excitation and emission peaks of PTX-16-MHDA-AuNPs-16-MHDA-DAPI reverse conjugate where the sample was centrifuged several times to remove unbound molecules. An intense fluorescence excitation spectrum for DAPI was observed at 360 nm along with a smaller peak at 263 nm. The emission spectrum of DAPI in the reverse conjugate was also red shifted to 462 nm. These observations indicate the attachment of DAPI and PTX onto the surface of AuNPs and formation new bonds.

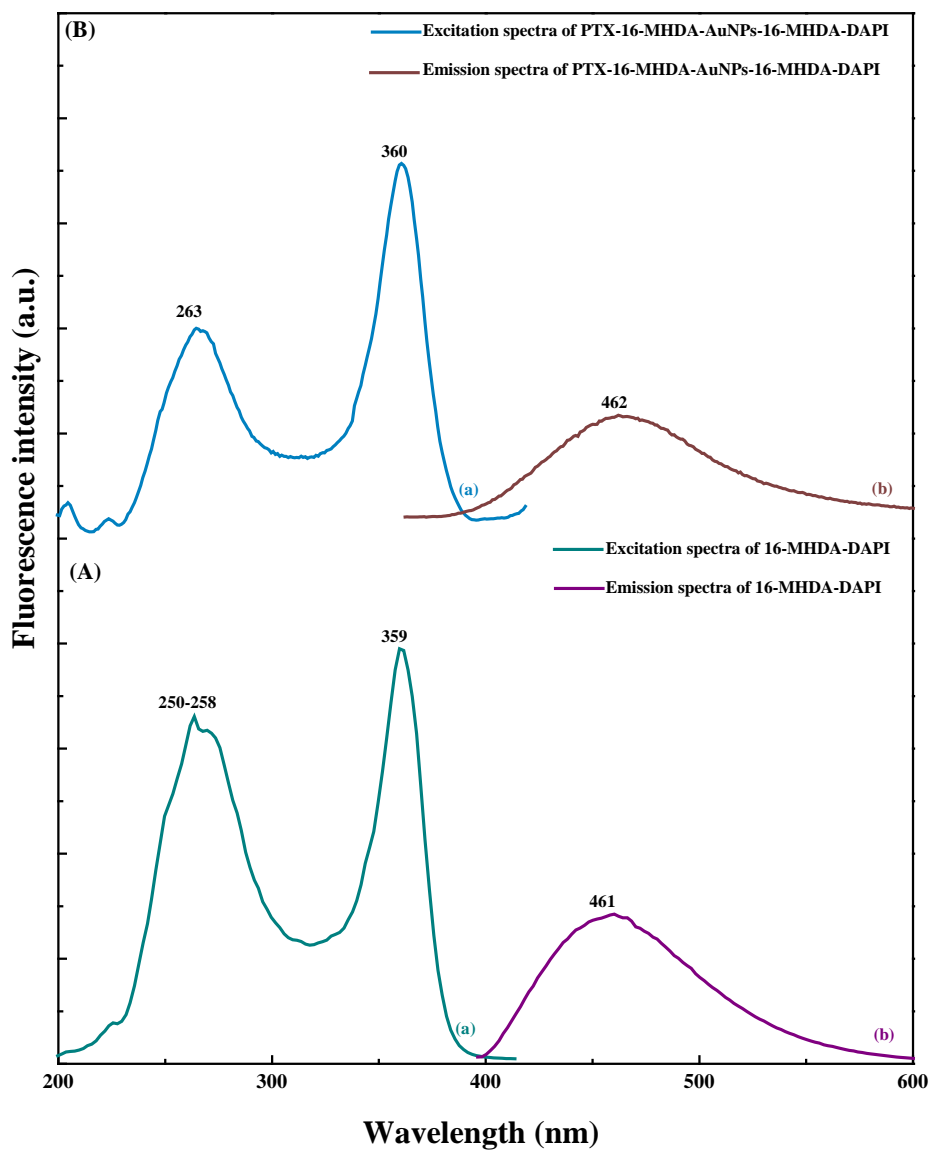


Figure 5.18 Fluorescence (a) excitation and (b) emission spectra of (A) 16-MHDA-DAPI reverse conjugate and (B) PTX-16-MHDA-AuNPs-16-MHDA-DAPI reverse conjugate. The excitation spectrum was recorded at an emission wavelength of 460 nm. The emission spectrum was recorded using an excitation wavelength of 358 nm.

5.3.3 Dynamic light scattering (DLS) analysis of PTX-16-MHDA-AuNPs-16-MHDA-DAPI reverse conjugate

Dynamic light scattering (DLS) was used to determine the size of the AuNPs-16-MHDA-DAPI then compare it with the PTX-16-MHDA-AuNPs-16-MHDA-DAPI reverse conjugate. Figure 5.19.a shows the particle size of AuNPs-16-MHDA-DAPI reverse conjugate. The particle size from the intensity size distribution was 35 nm with a relatively narrow polydispersity index of 0.136. Figure 5.19.b displays the size distribution of PTX-16-MHDA-AuNPs-16-MHDA-DAPI reverse conjugate. An increase of the size from 35 nm to 48 nm was observed after attaching PTX and DAPI dye at the same time to the AuNPs. This increase is due to the presence of PTX molecules on AuNPs leading to increased aggregation as the PTX will lower the number of charged groups on the surface. A narrow polydispersity index of 0.343 was recorded for PTX-16-MHDA-AuNPs-16-MHDA-DAPI reverse conjugate indicating the formation of monodispersed nanoparticles.

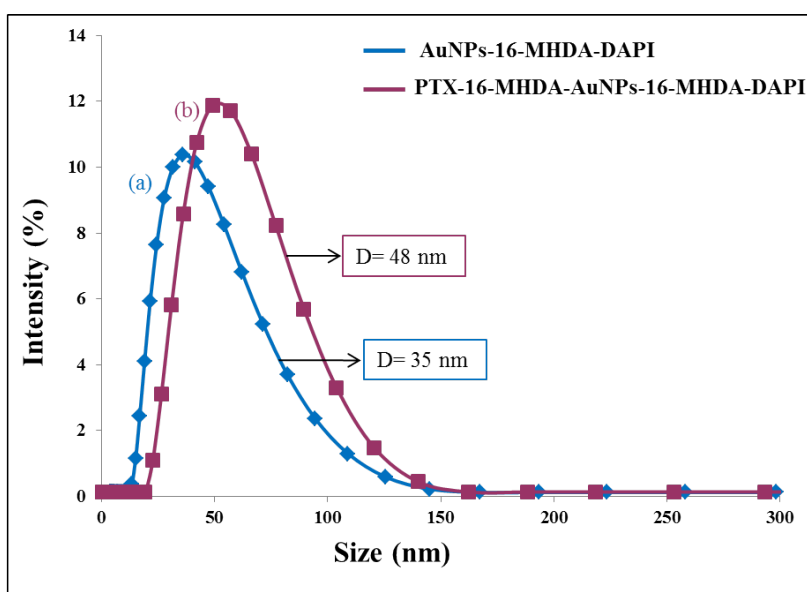


Figure 5.19 DLS measurements for (a) AuNPs-16-MHDA-DAPI and (b) PTX-16-MHDA-AuNPs-16-MHDA-DAPI reverse conjugates.

5.3.4 FT-IR spectroscopy characterisation of PTX-16-MHDA-AuNPs-16-MHDA-DAPI reverse conjugate

The steps before adding AuNPs for preparing the reverse conjugate were non-purified and contain EDC/NHS, unbound 16-MHDA, residual of dissociated PTX or unreacted DAPI. Therefore, FT-IR spectrum was recorded just in the last step after adding AuNPs and purifying the reacted mixture by repeated centrifugation. The resulting spectrum was compared to free PTX and free DAPI which were detailed in [Sections 3.3.4 and 5.2.5](#), [Chapters 3 and 5](#), respectively. [Figure 5.20](#) and [Table 5.9](#) show FT-IR spectra for PTX-16-MHDA-AuNPs-16-MHDA-DAPI reverse conjugate. The main characteristic peaks of free DAPI and free PTX were observed after conjugating 16-MHDA-DAPI and PTX-16-MHDA molecules onto the surface of AuNPs indicating the presence of PTX and DAPI molecules in the resulting reverse conjugate. Some distinctive bands assigned to 16-MHDA were also observed. The asymmetric and symmetric stretching of CH₂ in 16-MHDA molecules at ~2917 and 2849 cm⁻¹, respectively were observed. The peak at 1735 cm⁻¹ is allocated to the carbonyl group C=O stretching vibrations from the ester group of PTX. This band is one of major characteristic bands of PTX. However, some peaks either allocated to DAPI, PTX or to 16-MHDA overlapped due to the presence of these bands in the same vibrational regions (see [Figure 5.20](#) and [Table 5.9](#)).

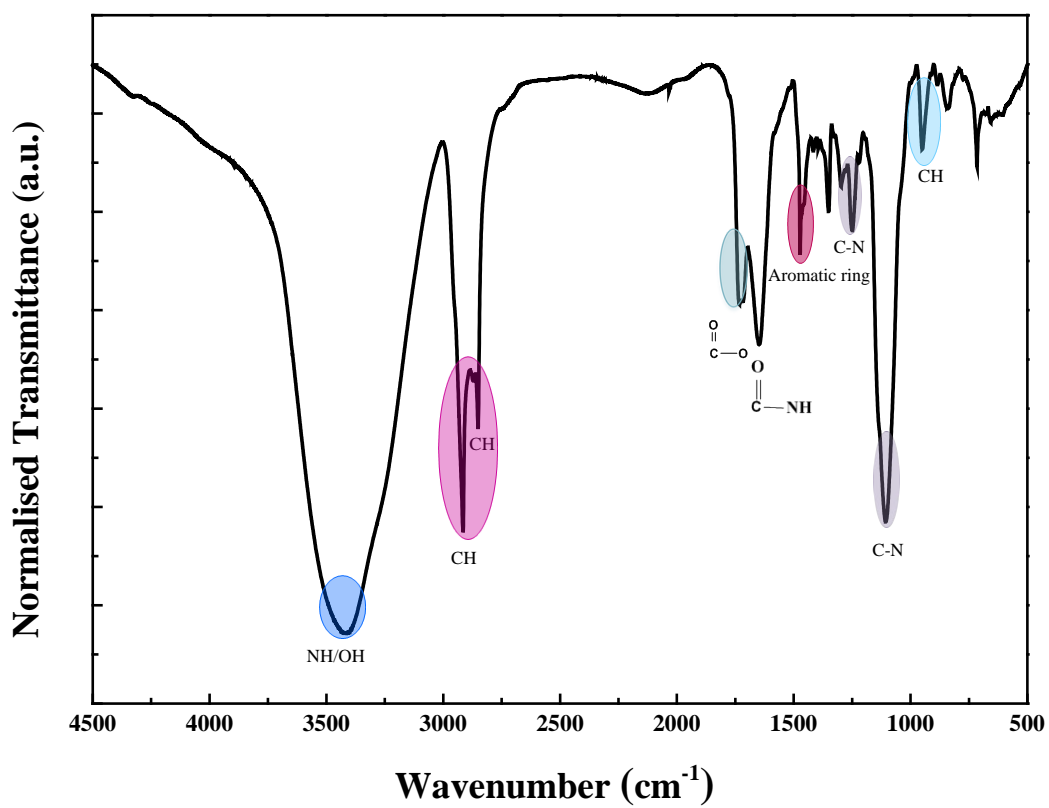


Figure 5.20 FT-IR spectrum of PTX-16-MHDA-AuNPs-16-MHDA-DAPI reverse conjugate.

Table 5.9 FT-IR peak positions of DAPI alone, free PTX and PTX-16-MHDA-AuNPs-16-MHDA-DAPI reverse conjugate.

Vibrational modes	WN (cm ⁻¹)/ free DAPI	WN (cm ⁻¹)/ free PTX	WN (cm ⁻¹)/ PTX-16-MHDA-AuNPs-16-MHDA-DAPI reverse conjugate
O-H and/or NH	3387-3344, 3126, 3258	3514-3405	3432-3403
Asymmetric and symmetric CH stretching	2975	2971, 2891	2917, 2849
C=N stretching vibration	1672	-	Overlapped with other bands in the same region
C=O stretching of esters	-	1735-1713	1735-1713
Amide I	1612	1647	1649
Aromatic groups	1505, 1479 and 1461	1607, 1584,	1472
C-N stretching	1329, 1252, 1090 and 1050	1273-1250, 1100	1250, 1100
C-H in-plane deformation	880, 850 and 814	943, 705	948, 840

5.3.5 ^1H NMR analysis of PTX-16-MHDA-AuNPs-16-MHDA-DAPI reverse conjugate

^1H NMR spectra were collected after synthesis and purification of PTX-16-MHDA-AuNPs-16-MHDA-DAPI reverse conjugate. However, the ^1H NMR spectra for non-purified steps, where EDC/NHS agents; unbound 16-MHDA; DAPI and/ or PTX are present, were not recorded due to the fact that it is difficult to distinguish between these molecules and the bound moieties. [Figure 5.21](#) shows the signals of PTX-16-MHDA-AuNPs-16-MHDA-DAPI reverse conjugate after centrifugation (see the detailed spectral for free 16-MHDA, free PTX and DAPI alone in [Chapters 3 and 5, Sections 3.3.5.3, 3.3.5.4 and 5.2.6](#), respectively). Most observations regarding to ^1H NMR signals for PTX-16-MHDA-AuNPs-16-MHDA-DAPI reverse conjugate are similar to PTX-thiol-AuNPs-thiol-DAPI conjugate (refer to [Chapter 5, Section 5.2.6](#)). In the region between 1 and 4 ppm, some peaks of PTX overlapped with the 16-MHDA peaks. The peaks which appeared in the area between 4.2 and 7 ppm were assigned to PTX molecules. The peaks in the region between 7 and 10 ppm are allocated to aromatic rings of DAPI and PTX molecules. Generally, no significant chemical shifts were observed. Some peaks allocated to PTX overlapped with other peaks for DAPI in the region between 7 and 10 ppm making those peaks difficult to see. The hydroxyl protons resonance on carbon C_2 ($\delta = 3.53$ ppm) and C_7 ($\delta = 2.47$ ppm) of the PTX molecule disappeared after conjugation which indicates the successful formation of ester bonds between 16-MHDA and PTX molecules.

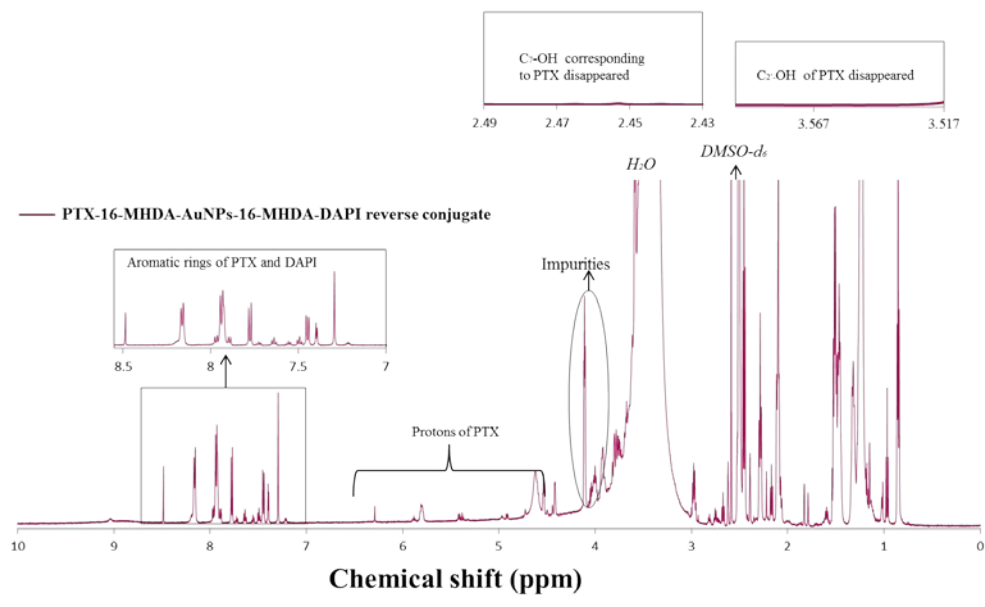


Figure 5.21 ¹H NMR spectra of PTX-16-MHDA-AuNPs-16-MHDA-DAPI reverse conjugate.

5.3.6 Cytotoxicity assessment of AuNPs-16-MHDA-DAPI reverse conjugate

Response of T47D cell line to 24 h treatment with the AuNPs-16-MHDA-DAPI reverse conjugate was examined and illustrated in Figure 5.22. The results show no decrease in relative survival in cells treated with the reverse conjugate at concentrations between 3.96×10^{-4} and 3.96×10^{-8} mM. However, significant decrease in relative cell survival up to ~ 50 % was observed at higher concentrations (0.0396 mM). The results reveal that the reverse conjugate containing DAPI agent can be toxic at high concentrations.

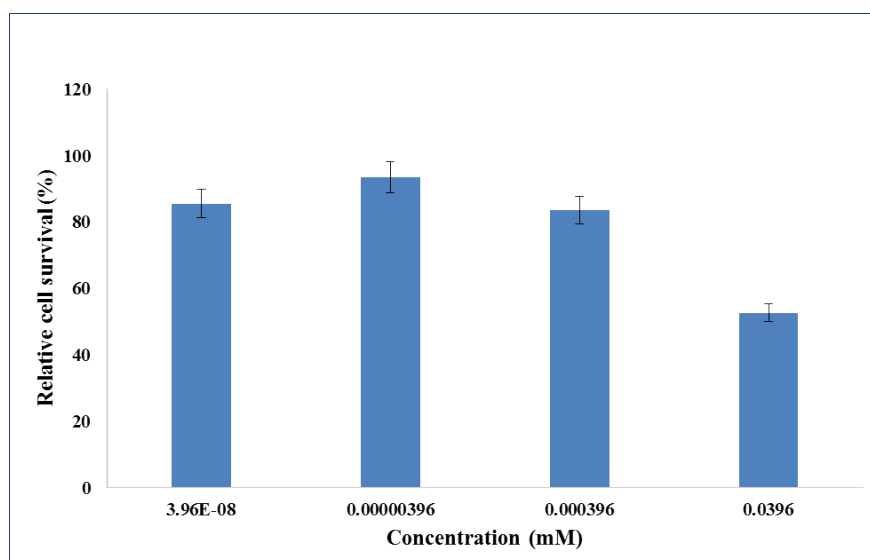


Figure 5.22 Cytotoxicity analysis of AuNPs-16-MHDA-DAPI reverse conjugate in T47D human breast cancer cells. Results were tested by One-way ANOVA and statistical significance showing * at $P < 0.05$.

5.4 Characterisation of paclitaxel conjugated to rhodamine B (PTX-RB conjugate)

5.4.1 UV-Vis analysis of PTX-RB conjugate

Figure 5.23.a shows the absorbance band of free PTX at 228 nm while Figure 5.23.b shows the major absorption peak of pure RB dissolved in EtOH at 551 nm [320]. Figure 5.23.c displays the coupling of RB with PTX. A slight shift of the RB band to red region from 551 nm for free RB to 553 nm for PTX-RB conjugate was observed.

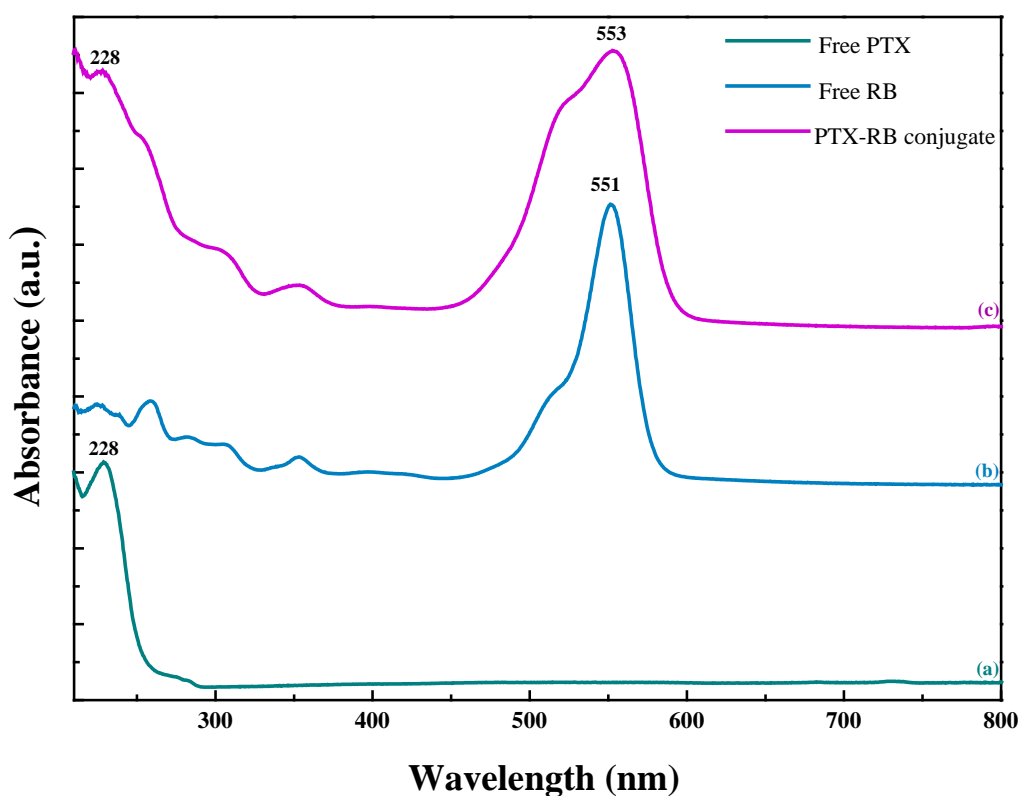


Figure 5.23 UV-Vis spectra of (a) free PTX (b) free RB and (c) PTX-RB conjugate.

To determine the number of PTX molecules attached to RB, the absorbance bands of free RB and PTX-RB conjugate were measured using UV-Vis spectrophotometry. The absorbance peak of PTX was obtained by subtracting PTX-RB spectra from free RB spectra (Figure 5.24). The data were collected between the absorption wavelength

400 nm and 200 nm. The background calculations for the samples displayed the concentrations acquired based on Beer-Lambert Law ($A = \epsilon l c$, where ϵ of PTX = $29.8 \text{ mM}^{-1} \text{ cm}^{-1}$, $l = 1 \text{ cm}$, while the absorbance was calculated by plotting vertical and horizontal lines as shown in Figure 5.24 and calculating the absorption value ($A = 0.1 \text{ a.u.}$). Then, the concentration of PTX was determined as following:

$$C = A/\epsilon$$

$$C = 0.1/ 29.8 \text{ mM}^{-1} \text{ cm}^{-1}$$

$$C = 3.35 \times 10^{-3} \text{ mM} = 3.35 \times 10^{-6} \text{ M.}$$

The concentration of RB in PTX-RB sample was calculated using Beer-Lambert Law as well ($A = \epsilon l c$, where ϵ of RB = $1.06 \times 10^5 \text{ L mol}^{-1} \text{ cm}^{-1}$ [409], $l = 1 \text{ cm}$ and the absorption value was measured using UV-Vis ($A = 1.7 \text{ a.u.}$). Thereby, the RB concentration = $1.6 \times 10^{-6} \text{ M}$. The concentrations for RB ($1.6 \times 10^{-6} \text{ M}$) and PTX ($3.35 \times 10^{-6} \text{ M}$) molecules in the conjugate sample were close to each other.

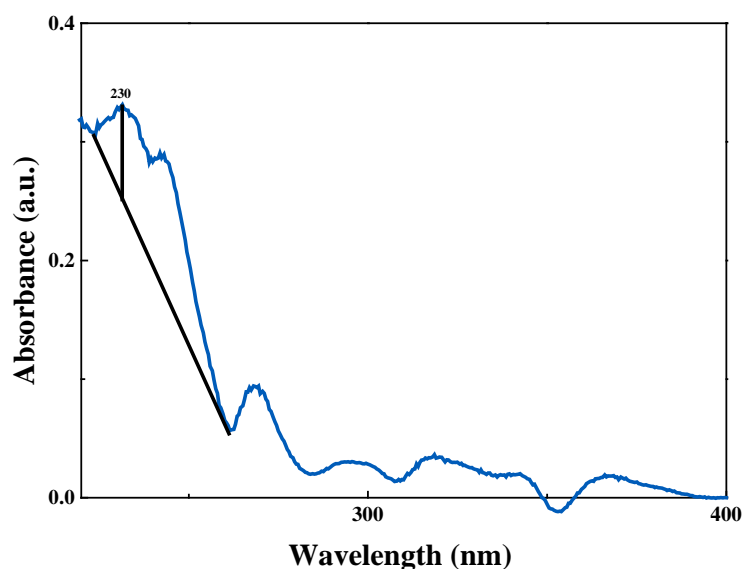


Figure 5.24 Spectrum after subtracting PTX-RB spectra from free RB spectra.

5.4.2 Fluorescence spectroscopy analysis of PTX-RB conjugate

In all samples analysed using fluorescence spectroscopy an EtOH blank was run initially. [Figure 5.25.A](#) illustrates the fluorescence excitation and emission spectra of pristine RB dissolved in EtOH. An intense excitation peak of RB appeared at 540 nm [320, 410, 411]. The excitation spectrum of RB was recorded using an emission wavelength of 567 nm. The fluorescence emission band of RB was observed at 567 nm [320]. The emission spectrum of RB was recorded at an excitation wavelength of 540 nm. [Figure 5.25.B](#) shows the fluorescence excitation and emission spectra of PTX-RB conjugate. The excitation band of RB was shifted to the red (from 540 nm to 550 nm) in the conjugate. This shift can be attributed to the formation of new ester bonds between carboxylic group on RB and hydroxyl groups (C₂-OH and C₇-OH) on PTX. The excitation spectrum of RB in PTX-RB conjugate was recorded at an emission wavelength of 567 nm. The emission peak of PTX-RB conjugate using an excitation wavelength of 540 nm was observed with a red shift compared to free RB. The emission peak of PTX-RB conjugate was shifted from 567 nm in free RB to 577 nm in PTX-RB conjugate. This shift indicates the successful conjugation of PTX with RB molecules.

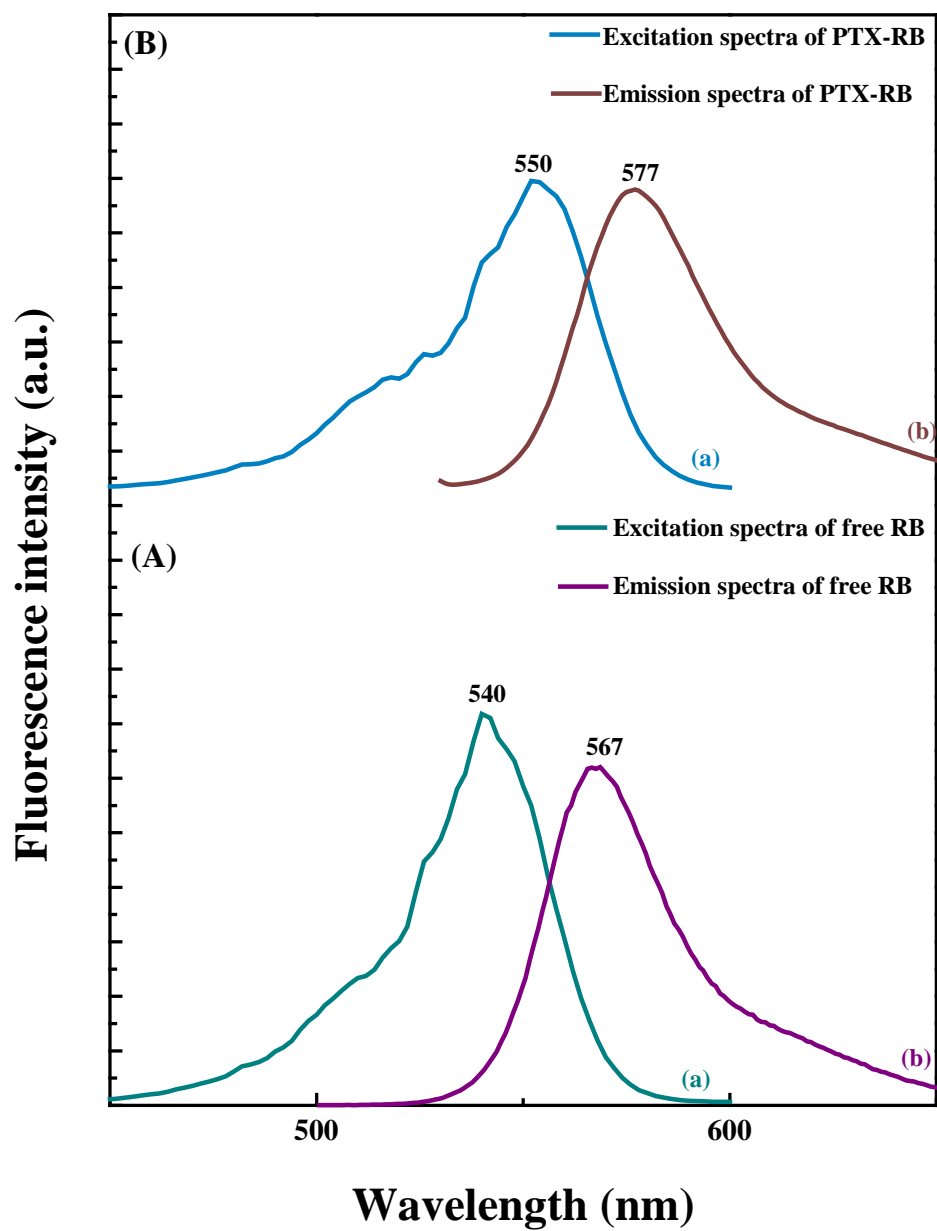


Figure 5.25 Fluorescence (a) excitation and (b) emission spectra of (A) free RB and (B) PTX-RB conjugate. The excitation spectrum was recorded at an emission wavelength of 567 nm. The emission spectrum was recorded using an excitation wavelength of 540 nm.

5.4.3 FT-IR spectroscopy characterisation of PTX-RB conjugate

Figure 5.26 shows the FT-IR spectra of pristine RB and RB attached PTX. In Figure 5.26.a, the spectrum of pristine RB shows bands at 1712 cm^{-1} attributed to the carboxyl group monitored as C=O stretching vibrations while the bands at 1245 and 1051 cm^{-1} are due to C-O stretching vibrations. The peak at 1647 cm^{-1} is due to C-N stretching vibrations, at 1590 , 1529 , 1468 and 1338 cm^{-1} are assigned to aromatic structure vibrations. The bands at 1555 and 1530 cm^{-1} are due to heterocycle vibrations while the band at 1340 cm^{-1} is due to C-aryl vibrations [412]. A band at 2974 cm^{-1} and a weak signal at 2928 cm^{-1} are attributed to methylene groups ($-\text{CH}_2$ and $\text{C}-\text{CH}_3$) stretching vibrations, respectively. The band at 3403 cm^{-1} is due to OH stretching vibrations while the band at 1414 cm^{-1} is due to symmetric stretching vibrations of COO^- . The band at 1134 cm^{-1} is due to aromatic C-H in plane bending vibrations. A weak band at 820 cm^{-1} is assigned to out of plane bending vibration while the band at 682 cm^{-1} is due to C-C wagging vibrations [412-414]. The band at 1183 cm^{-1} is allocated to C-N bond stretching vibration [412]. As expected, PTX-RB conjugate has a very complex FT-IR spectrum with many overlapping peaks. However, a distinct peak assigned to PTX was observed at 1728 cm^{-1} which indicates the formation of ester bands (see Figure 5.26 and Table 5.10).

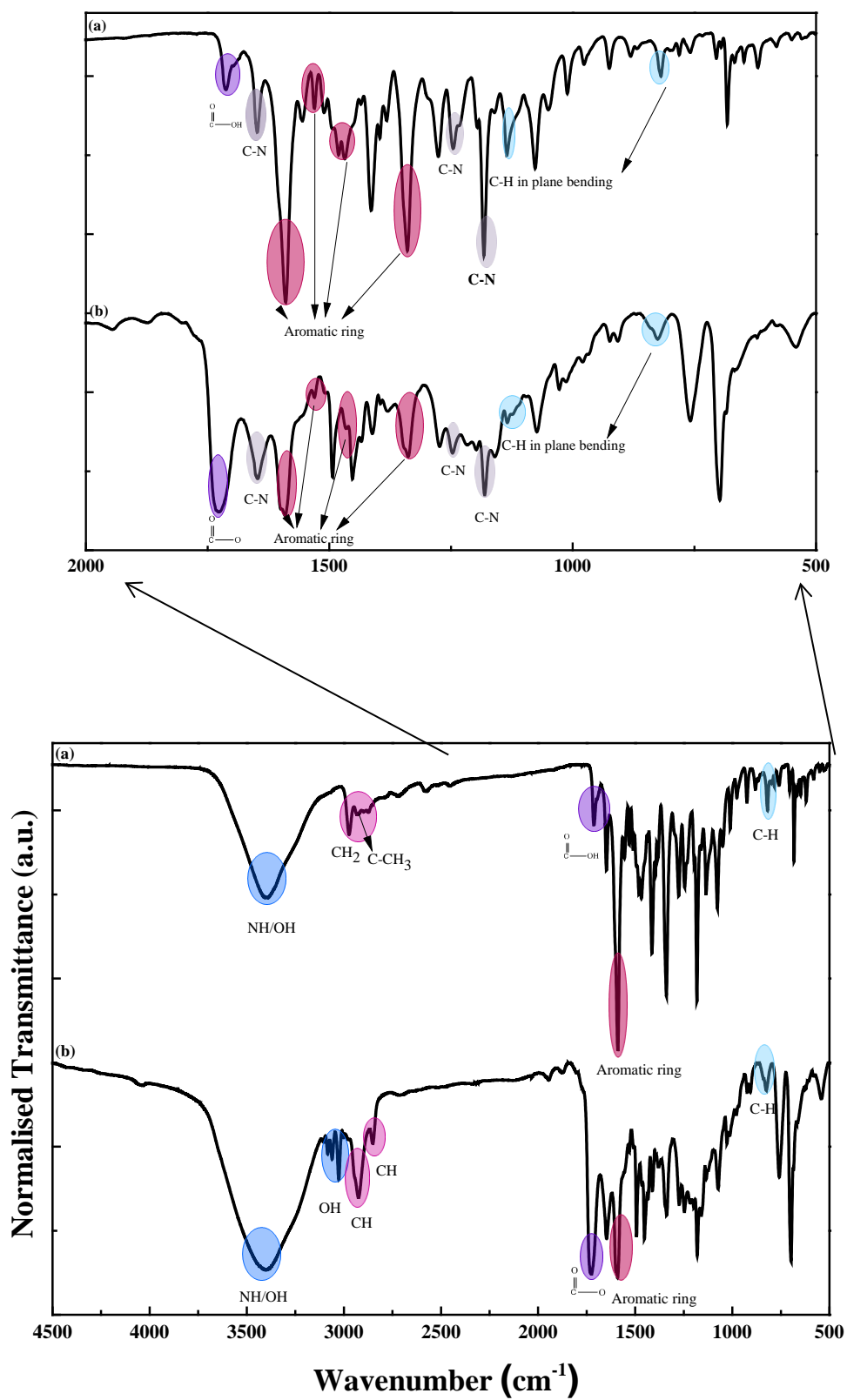


Figure 5.26 FT-IR spectra of (a) RB alone and (b) PTX-RB conjugate.

Table 5.10 FT-IR peak positions of RB alone and PTX-RB conjugate.

Vibrational modes	WN (cm ⁻¹)/ RB alone	WN (cm ⁻¹)/ PTX-RB
OH/NH	3403	3403
CH ₂ stretching	2974	It was hidden by OH from water molecules.
Asymmetric and symmetric C-H stretching, respectively.	2928	2925, 2849
Carbonyl bond of $\begin{array}{c} \text{O} \\ \parallel \\ \text{C}-\text{OH} \end{array}$	1712	-
Ester bond $\begin{array}{c} \text{O} \\ \parallel \\ \text{C}-\text{O} \end{array}$	-	1728
C=C-C aromatic ring stretching vibrations	1590, 1529, 1468 and 1338	1590, 1529, 1468 and 1338
C-N stretching vibration	1647, 1245 and 1183	1647, 1247 and 1183
Aromatic C-H in plane bending vibration	1134	1134
C-H out of plane and in-plane vibrations	820	824

5.4.4 ^1H NMR spectroscopy characterisation of PTX-RB conjugate

Paclitaxel attached rhodamine B was synthesised by reacting RB with PTX using EDC/NHS coupling (see [Section 2.7.3, Chapter 2](#) for the full synthesis details). ^1H NMR characterisations were performed using DMSO-d_6 as a solvent. [Figure 5.28.a](#) shows the ^1H NMR spectra of pristine RB. The characteristic signals of pristine RB ([Figure 5.27](#)) were observed. The chemical shifts are displayed in [Table 5.11](#). Several different types of protons for RB were observed: 8.24 (doublet, H_a), 7.88 (triplet, H_b), 7.83 (triplet, H_c), 7.48 (doublet, H_d), 7.094 (doublet, H_e), 7.023 (doublet, H_f), 6.97 (singlet, H_g), 3.65 (quartet, H_h) and 1.21 (triplet, H_i).

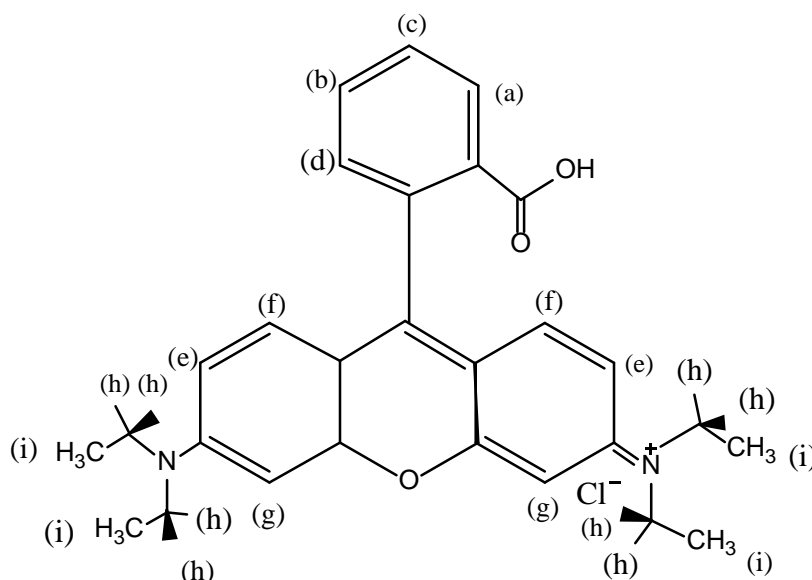


Figure 5.27 Chemical structure of rhodamine B.

The ^1H NMR spectrum of free PTX was detailed in [Chapter 3, Section 3.3.5.4](#).

[Figure 5.28.b](#) displays the ^1H NMR spectra of PTX conjugated to RB and the chemical shifts are provided in [Table 5.11](#). The peaks of free RB were observed in the PTX-RB ^1H NMR spectrum and other peaks assigned to PTX were also observed. Importantly, the $\text{C}_2\text{-OH}$ and $\text{C}_7\text{-OH}$ peaks of PTX disappeared in PTX-RB conjugate spectrum indicating the attachment between RB and PTX. In addition, slight shifts to downfield of RB after conjugation with PTX were noticed for some peaks in the

aromatic region. The most affected peak was H_a due to its closeness to carboxyl group where the attachment occurred. The peak of H_a shifted from 8.22 ppm to 8.96 ppm with $\Delta\delta = 0.74$ ppm is further evidence of the conjugation between PTX and RB molecules. However, some RB's peaks (H_d , H_e , H_f and H_g) overlapped with the peaks of PTX in the aromatic area.

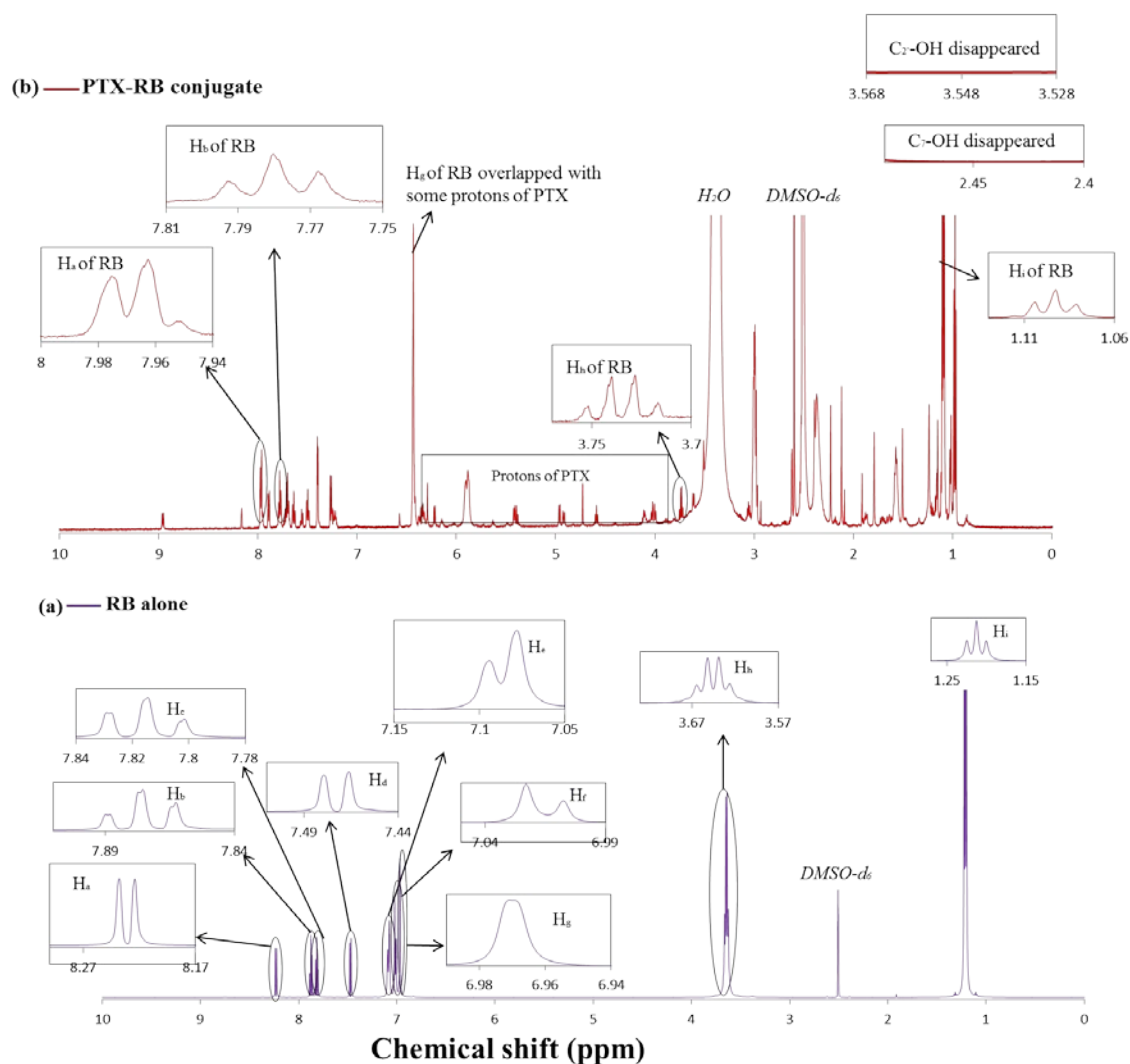


Figure 5.28 ^1H NMR spectra of (a) free RB and (b) PTX-RB conjugate.

Table 5.11 ¹H NMR chemical shifts (δ / ppm) for RB alone and PTX-RB conjugate.

Peak position of free RB	δ (ppm) free RB	δ (ppm) PTX-RB	$\Delta\delta$ (ppm)
H _a	8.22	7.96	0.26
H _b	7.85	7.78	0.07
H _c	7.8	Overlapped	-
H _d	7.47	Overlapped	-
H _e	7.07	Overlapped	-
H _f	7.02	Overlapped	-
H _g	6.97	6.43	0.54
H _h	3.65	3.72	0.07
H _i	1.19	1.08	0.11

5.4.5 Cytotoxicity evaluation of free RB

Response of T47D cell line to 24 h treatment with the free RB was examined and illustrated in Figure 5.29. The results show no decrease in relative survival in cells treated with free RB indicating no cytotoxicity was induced by any concentration tested. The results reveal that RB is nontoxic and safe for intracellular applications. The cytotoxicity of PTX-RB conjugate has not assessed due to the fact that a concentration of 59 μM of free PTX killed 50 % of cells in 24 hours (see Figure 3.15 in Chapter 3, Section 3.3.7). However, the concentration of PTX in the prepared conjugate (PTX-RB) was 3.35 μM (refer to Section 5.4.1 in Chapter 5) which after the 100 fold dilution required for cell viability experiments would likely not reduce the number of viable cancer cells a great deal (less than 10 %). Therefore, the cytotoxicity assay was not carried out for this conjugate.

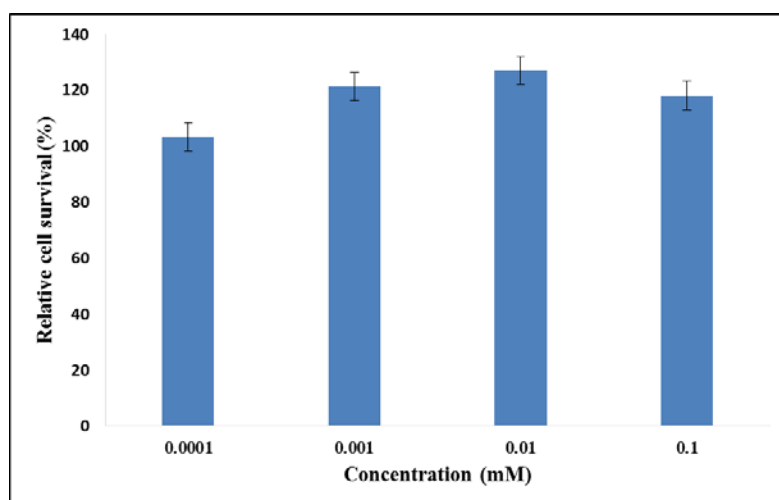


Figure 5.29 Cytotoxicity analysis of free RB in T47D human breast cancer cells. Results were tested by One-way ANOVA and statistical significance showing * at $P < 0.05$.

5.5 Concluding remarks

This chapter focused on characterisation of various fluorescent dyes (DAPI, pyNH₂ and FB28) based on AuNPs samples with or without the anticancer agent, PTX, using different characterisation techniques. In addition, the attachment of the chemotherapeutic, PTX, to RB was also characterised using different characterisation techniques. The response of T47D breast cancer cells to 24 h *in vitro* treatment with different concentrations of AuNPs-thiol-DAPI direct conjugate, AuNPs-thiol-pyNH₂ direct conjugate, AuNPs-thiol-FB28 hybrid, AuNPs-16-MHDA-DAPI reverse conjugate and free RB was examined. It was found that AuNPs-thiol-DAPI direct conjugate and AuNPs-thiol-FB28 hybrid were nontoxic at any concentration tested to investigate the cellular uptake and localisation of AuNPs and suggesting use of these conjugates will be possible in other medical applications. The AuNPs-thiol-pyNH₂ direct conjugate and AuNPs-16-MHDA-DAPI reverse conjugate can be considered safe products for intracellular applications when using very low concentrations. Free RB was nontoxic at any concentration tested, suggesting the potential use of RB in biomedical applications.

Chapter 6. Intracellular uptake of gold nanoparticles

6.1 Introductory remarks

The potential use of gold nanoparticles in biomedical applications requires understanding of the interactions between the target tissues or cells and the particles. Research has focused on the influence of nanoparticle size, shape and surface functionalisation with different molecules on interactions between those particles and cells [415]. Conjugation of fluorescent probes with different molecules including ligand functionalised nanoparticles surfaces is an important application to track, image and investigate the nanoparticles' fate and cellular uptake inside cells which helps to understand the interactions between those particles and cells thus improving their applications for diagnosis and treatment of diseases.

In this chapter, confocal laser scanning microscopy (CLSM) was used as an analytical technique to investigate the intracellular delivery, cellular uptake and localisation of AuNPs in different samples and at different incubation times. CLSM and other forms of microscopy are widely used for fluorescence measurements [261, 266]. CLSM provides more information on a particle's location due to its ability to collect images of thin sections [261]. Shukla et al. [228] reported the evaluation of absorption of lysine and FITC modified AuNPs in RAW264.7 macrophage cells using laser confocal scanning microscopy [228]. The interactions between AuNPs and phagocytes were assessed and the biocompatibility of AuNPs was demonstrated by measuring the permeation and retention in the tissue without causing any damage to cells' functionalities. This conjugated system could be used in cancer diagnosis and therapy by combining cancer imaging and cancer-targeted drug delivery [125, 228, 261, 416].

In the present study, $\sim 17\pm 4$ nm AuNPs are used to investigate a potential effect on T47D breast cancer cells, the internalisation, cellular uptake and distribution of fluorescently labelled AuNPs based conjugates with different fluorescent dyes

(DAPI, pyNH₂ and FB28, refer to [Chapter 2, Sections 2.7.1](#) and [2.7.2](#) for full synthesis) using CLSM and TEM techniques. AuNPs are an ideal system for studying their influences on human cells due to their properties (refer to [Chapter 1, Section 1.5.2](#) for more details about AuNPs properties). *In vitro* studies have already shown that AuNPs with core sizes of 10-20 nm are taken up by T47D cancerous cells [417]. AuNPs were shown to be trapped in vesicles inside the cytoplasm [418]. Hence, internalisation and cellular uptake of AuNPs are mediated by an endocytosis mechanism [419].

6.2 Cellular uptake of AuNPs by T47D breast cancer cells

AuNPs show potential use as drug delivery vehicles because the as-prepared AuNPs and thiolated AuNPs were not toxic to human T47D cells as the relative survival of the cells was continuously above 80 % (refer to [Chapter 3, Section 3.3.7](#)) indicating no cytotoxicity was induced at the concentrations tested. T47D cell lines were treated with various types of AuNPs (see [Table 6.1](#)). AuNPs samples were tagged with three types of fluorescent stains, DAPI, pyNH₂ and FB28, to make the particles useful for fluorescence imaging. The treated cells were studied with CLSM to investigate the internalisation and localisation of AuNPs inside the cells. A detailed description of the experiments is in [Appendix C](#). Briefly, 6-well plates were prepared and coverslips were placed then seeded with 0.3×10^5 cells mL⁻¹ concentration of cell suspension. Plates were incubated for 24 h at a humidified 37 °C with 5 % CO₂. Cells were treated with AuNPs samples. The following day, cells were harvested from plates to a POC chamber. Then, 150 µL of fresh media was added and fluorescence was measured. Fluorescently labelled AuNPs show fluorescence signals obviously whereas unlabelled AuNPs did not show fluorescence in cells. TEM was used to confirm the localisation of AuNPs inside the malignant cells.

Table 6.1 Exposure of T47D cells to various samples based on AuNPs.

AuNPs	AuNPs-thiol-DAPI direct conjugate	PTX-thiol-AuNPs-thiol-DAPI direct conjugate
Thiol-AuNPs	AuNPs-thiol-pyNH ₂ direct conjugate	PTX-thiol-AuNPs-thiol-pyNH ₂ direct conjugate
PTX-thiol-AuNPs direct conjugate	AuNPs-thiol-FB28 hybrid	PTX-thiol-AuNPs-thiol-FB28 direct conjugate
	AuNPs-16-MHDA-DAPI reverse conjugate	PTX-16-MHDA-AuNPs-16-MHDA-DAPI reverse conjugate

6.2.1 CLSM analysis of AuNPs used as negative controls

Three types of AuNPs (as prepared AuNPs, thiol-AuNPs and PTX-thiol-AuNPs direct conjugate) were first imaged by CLSM to investigate their appropriateness for microscopy experiments. CLSM shows images of these three types of AuNPs in the absence of cells. No fluorescence was observed for any of these three samples in or outside cells (see Figure 6.1.a, b and c).

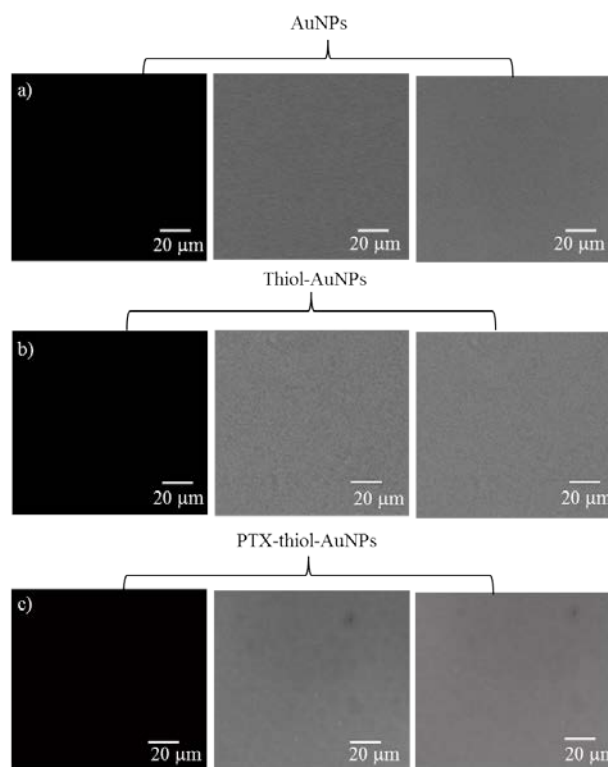


Figure 6.1 Confocal fluorescence (left) ($\lambda_{\text{ex}} = 405 \text{ nm}$, $\lambda_{\text{em}} = 478\text{-}700 \text{ nm}$), bright field (middle) and overlaid (right) images of (a) AuNPs (b) thiol-AuNPs and (c) PTX-thiol-AuNPs direct conjugate. All images recorded at room temperature.

Images for T47D living cells in the absence of fluorescent dyes (T47D living cells alone, T47D living cells treated with AuNPs, thiol-AuNPs or with PTX-thiol-AuNPs direct conjugate) were collected using CLSM (Figure 6.2) to make sure that they do not show any fluorescence and are suitable for fluorescence microscopy. No fluorescence was detected along the spectra for any of these cells. The observations indicate the suitability of AuNPs and their conjugates and T47D cells for imaging by CLSM.

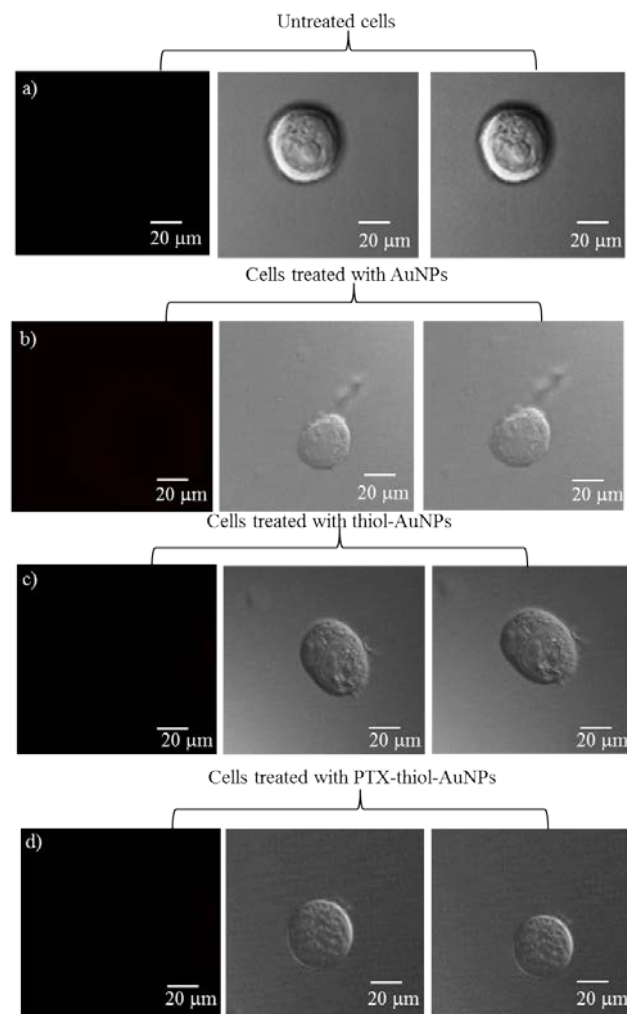


Figure 6.2 Fluorescence (left) ($\lambda_{\text{ex}} = 405 \text{ nm}$ $\lambda_{\text{em}} = 478\text{-}700 \text{ nm}$), bright field (middle) and overlaid (right) images of T47D human breast cancer cells (a) untreated cells (b) treated with AuNPs (c) treated with thiol-AuNPs and (d) treated with PTX-thiol-AuNPs direct conjugate.

6.2.2 CLSM analysis of fluorescently labelled AuNPs

Fluorescence images of AuNPs tagged three different dyes (DAPI, pyNH₂ and FB28) in the absence and in the presence of the anticancer drug, PTX and in the absence of cells were obtained as shown in Figure 6.3. Basically, all the images show fluorescence after adding a fluorescent dye to prepare various conjugates (see Table 6.2). Various sizes of the fluorescent dots in several hundred nanometers in diameter were obtained indicating the nanoparticles emitted fluorescence. Some of these spots were small and others were larger indicating aggregation of the particles. Image 6.3.c shows clearly clusters of fluorescently labelled AuNPs due to the aggregation of the particles. Importantly, no big leakage of any of the fluorescent dyes was observed indicating formation of stable conjugates. No differences in fluorescence in the absence or presence of PTX were found.

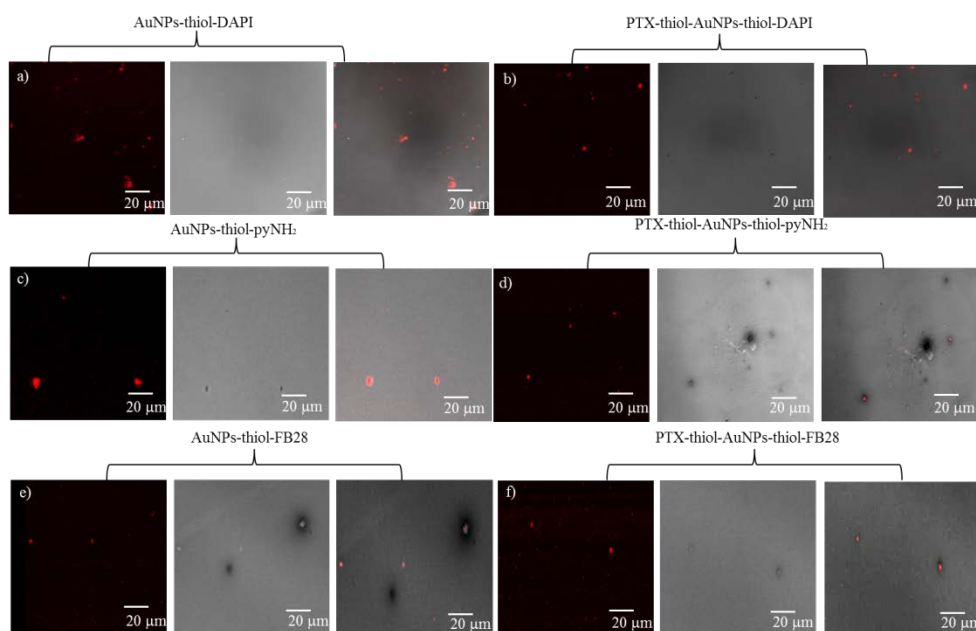


Figure 6.3 Fluorescence (left) ($\lambda_{\text{ex}} = 405 \text{ nm}$, $\lambda_{\text{em}} = 478\text{-}554 \text{ nm}$), bright field (middle) and overlaid (right) images of (a) AuNPs-thiol-DAPI direct conjugate (b) PTX-thiol-AuNPs-thiol-DAPI direct conjugate (c) AuNPs-thiol-pyNH₂ direct conjugate (d) PTX-thiol-AuNPs-thiol-pyNH₂ direct conjugate (e) AuNPs-thiol-FB28 hybrid and (f) PTX-thiol-AuNPs-thiol-FB28 direct conjugate at room temperature.

Table 6.2 Samples used for CLSM analysis in the presence or absence of cells.

AuNPs-thiol DAPI direct conjugate	PTX-thiol-AuNPs-thiol-DAPI direct conjugate
AuNPs-thiol-pyNH ₂ direct conjugate	PTX-thiol-AuNPs-thiol-pyNH ₂ direct conjugate
AuNPs-thiol-FB28 hybrid	PTX-thiol-AuNPs-thiol-FB28 direct conjugate

6.2.3 CLSM analysis of free fluorescent dyes on T47D cells

Figure 6.4 shows CLSM images for cells exposed to $30 \mu\text{g mL}^{-1}$ of free dyes solutions (DAPI, pyNH₂ or FB28) for a different period of times (1 h, 6 h and 24 h). Figure 6.4.a, b and c shows free DAPI stained the nuclei of T47D cells. For all time periods, DAPI was accumulated in the nuclei and stained them clearly. These results are in agreement with other findings from other research groups [420, 421]. For example, Manjili et al. [420] used free DAPI to stain nuclei in MCF-7 breast cancer living cells [420]. The cells were incubated with DAPI for 24 h. DAPI stained the cells nuclei clearly [420].

PyNH₂ stained the cytoplasm but not nuclei as shown in Figure 6.4.d, e and f. Figure 6.4.d shows an image was taken after 1 h of incubation of pyNH₂ with T47D cells. Low fluorescence was observed basically in cytoplasm and perinuclear region. No differences in fluorescence intensity were observed after longer period of incubation (6 h and 24 h as shown in Figure 6.4.e and f, respectively).

FB28 also stained the cytoplasm but not nuclei. Overall, free FB28 was internalised in T47D cells. However, no big increase in fluorescence intensity was observed after incubation for different periods of time (1 h, 6 h or 24 h) (see Figure 6.4.g, h and i). In contrast, when attached to the AuNPs the fluorescence intensity increased with time.

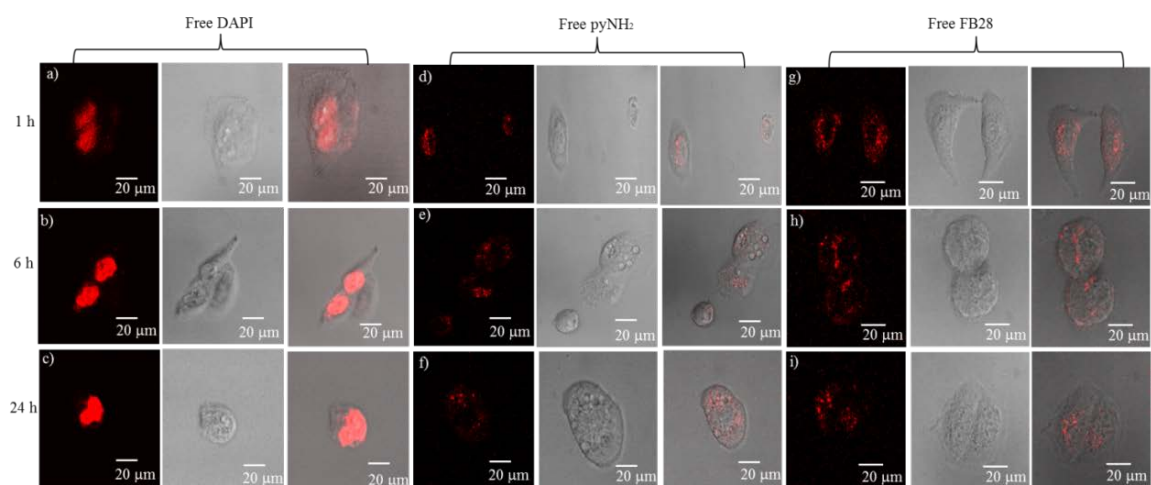


Figure 6.4 Fluorescence (left) ($\lambda_{\text{ex}} = 405 \text{ nm}$, $\lambda_{\text{em}} = 478 \text{ nm}$), bright field (middle) and overlaid (right) images of T47D human breast cancer cells treated with free DAPI, free pyNH₂ or free FB28 (a, d and g) after 1 h of incubation (b, e and h) after 6 h of incubation and (c, f and i) after 24 h of incubation at room temperature. Original magnification was 63 \times . Scale bars = 20 μm .

6.2.4 Intracellular distribution of fluorescently labelled AuNPs with different dyes analysed by CLSM

The intracellular distribution of AuNPs was investigated by exposing T47D cells to 30 μ L of each fluorescently labelled conjugate (see [Table 6.2](#) in this [Chapter](#), [Section 6.2.2](#)). Overall, all the conjugates were able to internalise and transport across the cell membrane. For conjugates containing a dye in the absence of the anticancer drug, PTX, after 1 h of incubation, low intensity fluorescence permeated throughout the membrane into the cytoplasm was observed in the cells ([Figure 6.6.a, d and g](#)). In AuNPs-thiol-pyNH₂ direct conjugate, most of the fluorescence was accumulated in perinuclear region ([Figure 6.6.d](#)). Images from free pyNH₂ stain imply that fluorescence was scattered across the cell ([Figure 6.4.d, e and f](#)). However, after conjugation pyNH₂ to the surface of AuNPs, the fluorescence looked more concentrated ([Figure 6.6.d, e and f](#)). This may be due to the fact that the dye attached to thiolated AuNPs behaves in different manner as it is part of AuNPs and tracks AuNPs transport inside cells. No fluorescence was found in the nucleus as clearly imaged in [Figure 6.6.d](#). After 6 h of exposure, a significant increase of intracellular fluorescence was observed in the conjugates containing DAPI or pyNH₂ dyes without the anticancer agent, PTX. However, for AuNPs-thiol-FB28 hybrid, no significant increase in fluorescence was noticed. The fluorescence was observed in all these conjugates in the cytoplasm, the cell periphery and near the perinuclear site ([Figure 6.6.b, e and h](#)). After 24 h of incubation, intracellular fluorescence was more intense and distributed across the cells compared to that observed after 1 h or 6 h of treatment. The reason for this could be because some of the fluorescent dye molecules are disconnected from the AuNPs after long time in the cells and the conjugate components are dissociated from each other. This allows some of free dye (in case of using DAPI as a probe as shown in [Figure 6.6.c](#)) to enter the nuclei and stain them. It was found that when DAPI conjugated to thiolated AuNPs, it did not behave same as when it was free. After conjugation, DAPI linked to AuNPs-thiol acted as a stain for AuNPs to detect their cellular uptake and internalisation and it did not act as nuclei stain as shown in [Figure 6.5.a and b](#). Images in [Figure 6.6](#) show the ability of all fluorescently labelled AuNPs conjugates to transport across the T47D cell membrane.

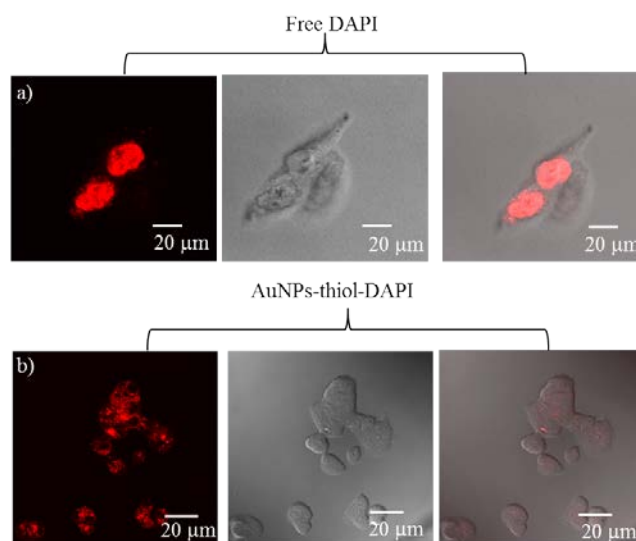


Figure 6.5 Fluorescence (left) ($\lambda_{\text{ex}} = 405 \text{ nm}$, $\lambda_{\text{em}} = 478 \text{ nm}$), bright field (middle) and overlaid (right) images of T47D human breast cancer cells treated with (a) free DAPI or (b) AuNPs-thiol-DAPI direct conjugate after 6 h of incubation at room temperature. Original magnification was 63 \times . Scale bars = 20 μm .

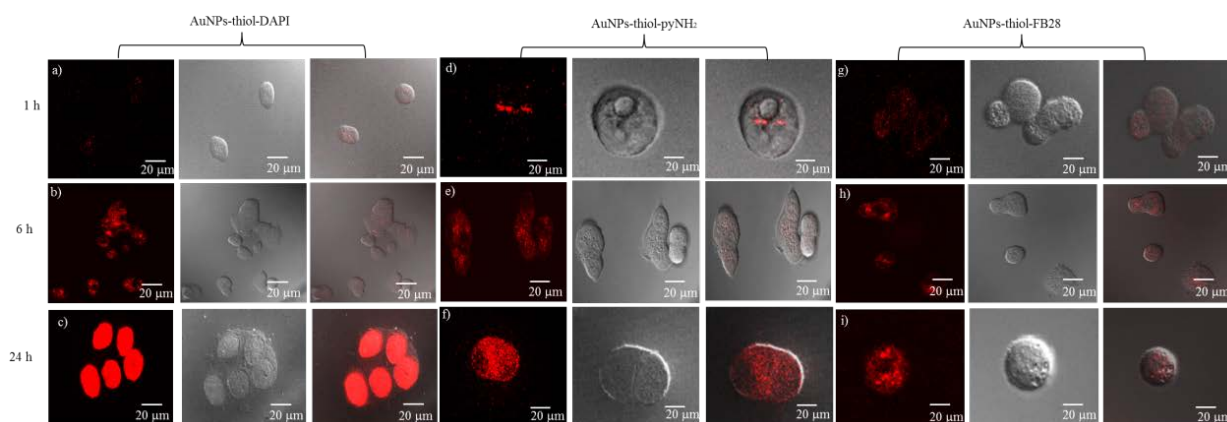


Figure 6.6 Fluorescence (left) ($\lambda_{\text{ex}} = 405 \text{ nm}$, $\lambda_{\text{em}} = 478 \text{ nm}$), bright field (middle) and overlaid (right) images of T47D human breast cancer cells treated with AuNPs-thiol-DAPI direct conjugate, AuNPs-thiol-pyNH₂ direct conjugate or AuNPs-thiol-FB28 hybrid (a, d and g) after 1 h of incubation (b, e and h) after 6 h of incubation and (c, f and i) after 24 h of incubation at room temperature. Original magnification was 63 \times . Scale bars = 20 μm .

Confocal luminescent images of T47D cells exposed to conjugates containing a fluorescent dye and PTX simultaneously (see [Table 6.2](#) in this [Chapter, Section 6.2.2](#))

were also recorded at room temperature and showed increase in fluorescence intensity over time as shown in [Figure 6.7](#).

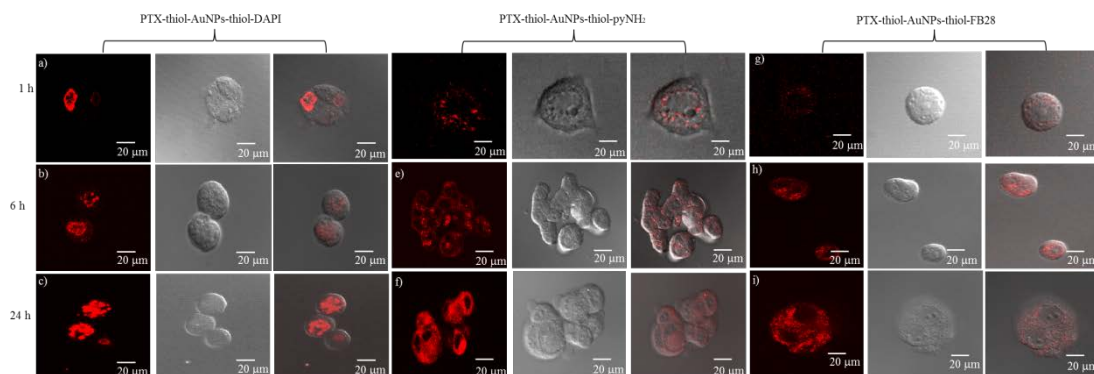


Figure 6.7 Fluorescence (left) ($\lambda_{\text{ex}} = 405 \text{ nm}$, $\lambda_{\text{em}} = 478 \text{ nm}$), bright field (middle) and overlaid (right) images of T47D human breast cancer cells treated with PTX-thiol-AuNPs-thiol-DAPI, PTX-thiol-AuNPs-thiol-pyNH₂ or PTX-thiol-AuNPs-thiol-FB28 direct conjugates (a, d and g) after 1 h of incubation (b, e and h) after 6 h of incubation and (c, f and i) after 24 h of incubation at room temperature. Original magnification was 63 \times . Scale bars = 20 μm .

After 1 h of exposure, cells treated with PTX-thiol-AuNPs-thiol-DAPI direct conjugate showed higher fluorescence compared to AuNPs-thiol-DAPI direct conjugate (see [Figure 6.8.a](#) and [b](#)). The probe fluorescence was concentrated close the cell's membrane inside the cells indicating the penetration of PTX-thiol-AuNPs-thiol-DAPI direct conjugate ([Figure 6.8.b](#)).

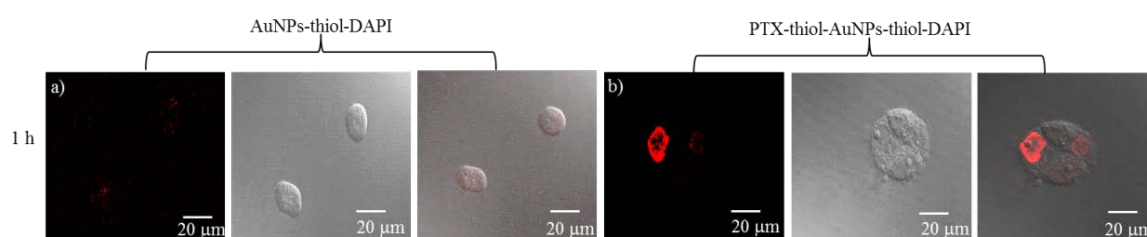


Figure 6.8 Fluorescence (left) ($\lambda_{\text{ex}} = 405 \text{ nm}$, $\lambda_{\text{em}} = 478 \text{ nm}$), bright field (middle) and overlaid (right) images of T47D human breast cancer cells treated with (a) AuNPs-thiol-DAPI and (b) PTX-thiol-AuNPs-thiol-DAPI direct conjugates after 1 h of incubation at room temperature. Original magnification was 63 \times . Scale bars = 20 μm .

Similarly, images for cells treated with PTX-thiol-AuNPs-thiol-pyNH₂ direct conjugate show more fluorescence compared to those treated with AuNPs-thiol-pyNH₂ direct conjugate (Figures 6.7.d and 6.6.d, respectively). The majority of fluorescence was found in perinuclear region in the cytoplasm. However, no difference in fluorescence intensity for PTX-thiol-AuNPs-thiol-FB28 direct conjugate compared to AuNPs-thiol-FB28 hybrid was observed. Most of fluorescence was located in the cytoplasm close to perinuclear region (see Figures 6.7.g and 6.6.g, respectively). After 6 h, intracellular fluorescence distributed in cytoplasm and near the perinuclear and slight signals at the cell periphery were observed in all the conjugates containing a fluorescent dye and PTX simultaneously. As the fluorescence accumulated close the perinuclear, it can be suggested that the particles transport through an endocytic pathway (see Figure 6.7.b, e and h). Lastly, after 24 h of incubation, an increase of cellular fluorescence was monitored. Intracellular uptake and transport of gold nanoparticles conjugates containing PTX and a fluorescent dye simultaneously are driven by an endocytosis mechanism. The endocytic pathway controls the cellular uptake of biomolecules. Images show fluorescence permeation into the nuclei in both conjugates (AuNPs-thiol-DAPI and PTX-thiol-AuNPs-thiol-DAPI direct conjugate) after 24 h of incubation. This can be attributed to the fact that since DAPI can stain nuclei, after 24 h the DAPI molecules are disconnected from the surface of AuNPs and became free and able to penetrate inside nuclei and stain them. However, in case of using pyNH₂ and FB28 as probes, it seems that the fluorescence could not internalise inside the nuclei and stain them as there was no fluorescence observed in nuclei images as shown in Figure 6.7.f and i. The higher intracellular fluorescence in PTX-thiol-AuNPs-thiol-DAPI direct conjugate and PTX-thiol-AuNPs-thiol-pyNH₂ direct conjugate (Figure 6.9.b & d, respectively) compared to AuNPs-thiol-DAPI and AuNPs-thiol-pyNH₂ direct conjugates (Figure 6.9.a & c, respectively) may ascribed to the interactions between conjugates containing PTX and a staining agent (DAPI or pyNH₂) with the biological media and the interactions between PTX and the staining agents on AuNPs surface facilitate cellular transference regardless of PTX particles' larger size (DLS intensity size distribution of both PTX-thiol-AuNPs-thiol-DAPI and PTX-thiol-AuNPs-thiol-pyNH₂ direct conjugates was 63 and 53 nm, respectively). These findings are similar to results reported by Lau et al. [422]. They synthesised a series of luminescent cyclometalated iridium (III) polypyridine indole complexes. They suggested that the use of longer

spacers, hydrophobic cyclometalating ligands and indole unit may facilitate the cellular uptake of these complexes [422].

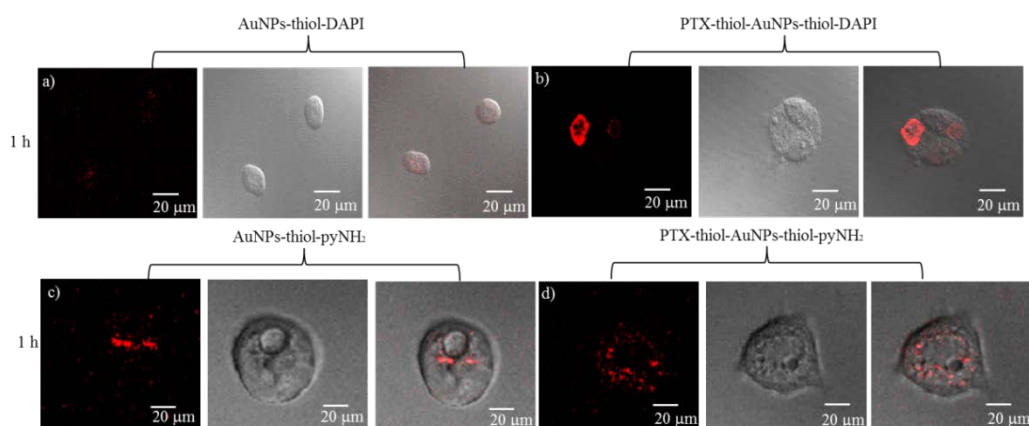


Figure 6.9 Fluorescence (left) ($\lambda_{\text{ex}} = 405 \text{ nm}$, $\lambda_{\text{em}} = 478 \text{ nm}$), bright field (middle) and overlaid (right) images of T47D human breast cancer cells treated with (a) AuNPs-thiol-DAPI (b) PTX-thiol-AuNPs-thiol-DAPI (c) AuNPs-thiol-pyNH₂ and (d) PTX-thiol-AuNPs-thiol-pyNH₂ direct conjugates after 1 h of incubation at room temperature. Original magnification was 63 \times . Scale bars = 20 μm .

Investigation cellular uptake of AuNPs in reverse conjugate containing DAPI in the presence and the absence of the anticancer agent, PTX was also carried out by CLSM. Likewise, the results of the reverse conjugate indicate that the AuNPs were internalised inside T47D cells and distributed in cytoplasm, near the perinuclear region and near cells membranes with an increase of intracellular fluorescence over time (Figure 6.10). In addition, fluorescence was found in some nuclei after treatment with AuNPs-16-MHDA-DAPI or PTX-16-MHDA-AuNPs-16-MHDA-DAPI reverse conjugates after 24 h which indicates DAPI disconnected from AuNPs conjugates after long time and became free and able to stain the nuclei.

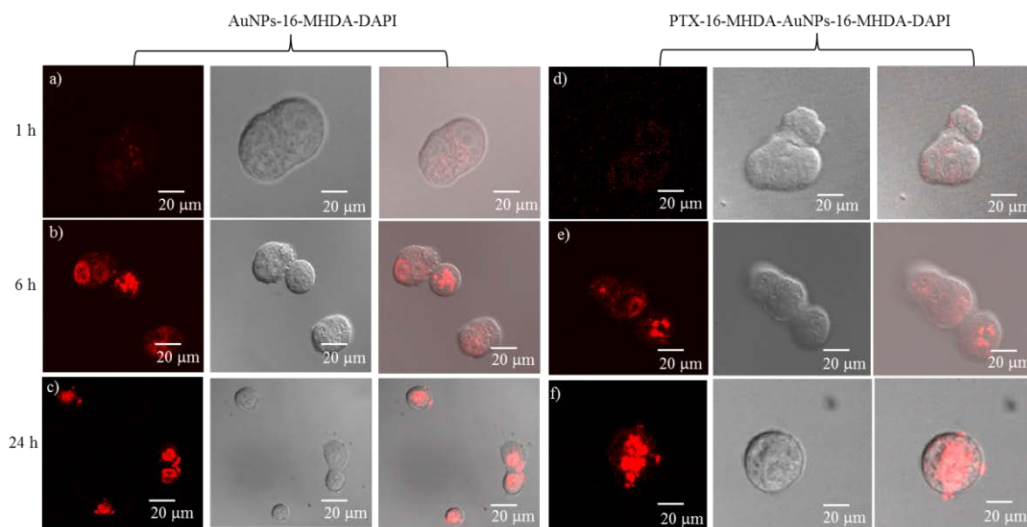


Figure 6.10 Fluorescence (left) ($\lambda_{\text{ex}} = 405 \text{ nm}$, $\lambda_{\text{em}} = 478 \text{ nm}$), bright field (middle) and overlaid (right) images of T47D human breast cancer cells treated with AuNPs-16-MHDA-DAPI or PTX-16-MHDA-AuNPs-16-MHDA-DAPI reverse conjugates (a and d) after 1 h of incubation (b and e) after 6 h of incubation and (c and f) after 24 h of incubation at room temperature. Original magnification was 63 \times . Scale bars = 20 μm .

The confocal microscopy results for T47D living cells treated with fluorescently labelled AuNPs direct and reverse conjugates revealed an increase of intracellular fluorescence over time as an indication of cellular uptake of AuNPs following the fluorophore's release (Figures 6.6 (c, f and i), 6.9 (c, f and i) and 6.10 (c and f)). According to different reports AuNPs are internalised the cells via a receptor-mediated endocytosis mechanism and trapped in small vesicles known as endosomes [423, 424]. Then, those endosomes fuse with lysosomes for processing followed by transferring them to the cell periphery for excretion [423, 424]. Different studies have confirmed the presence of AuNPs inside various sections of the endocytic pathway including endosomes and lysosomes [261, 424].

Cellular uptake of free RB and PTX conjugated to RB was also investigated by CLSM. The purpose of studying these two cases (free RB and PTX-RB conjugate) is to investigate the accumulation area of the fluorescence which may provide an idea about the localisation of PTX inside cells and to study if there are any differences in fluorescence intensities. Fluorescence images of free RB and PTX-RB conjugate in

the absence and in the presence of cells were obtained as shown in Figures 6.11 and 6.12, respectively. Essentially, all the images show no differences in fluorescence intensity between free RB or the PTX-RB conjugate. Figure 6.12 shows fluorescence in a ring shape surrounding the cells in both cases (cells treated with free RB or PTX-RB conjugate). After 1 h of incubation, significant fluorescence intensity was observed (Figure 6.12.a and d) indicating the RB agent with or without the anticancer drug, PTX was internalised inside cells through cell's membrane. However, the fluorescence intensity decreased after 6 h or 24 h of exposure. This can be attributed to the fact that the dye was secreted from the cells over longer times (Figure 6.12.b, c, e and f).

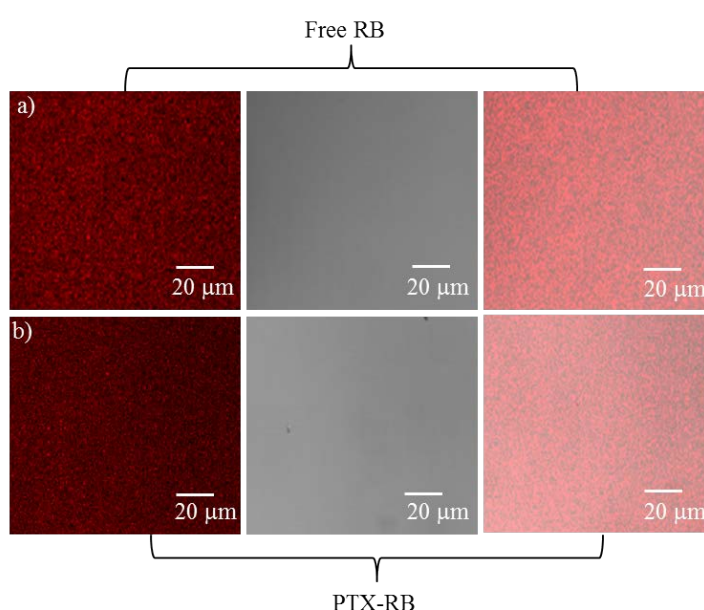


Figure 6.11 Fluorescence (left) ($\lambda_{\text{ex}} = 405 \text{ nm}$, $\lambda_{\text{em}} = 526\text{-}700 \text{ nm}$), bright field (middle) and overlaid (right) images of (a) free RB and (b) PTX-RB at room temperature.

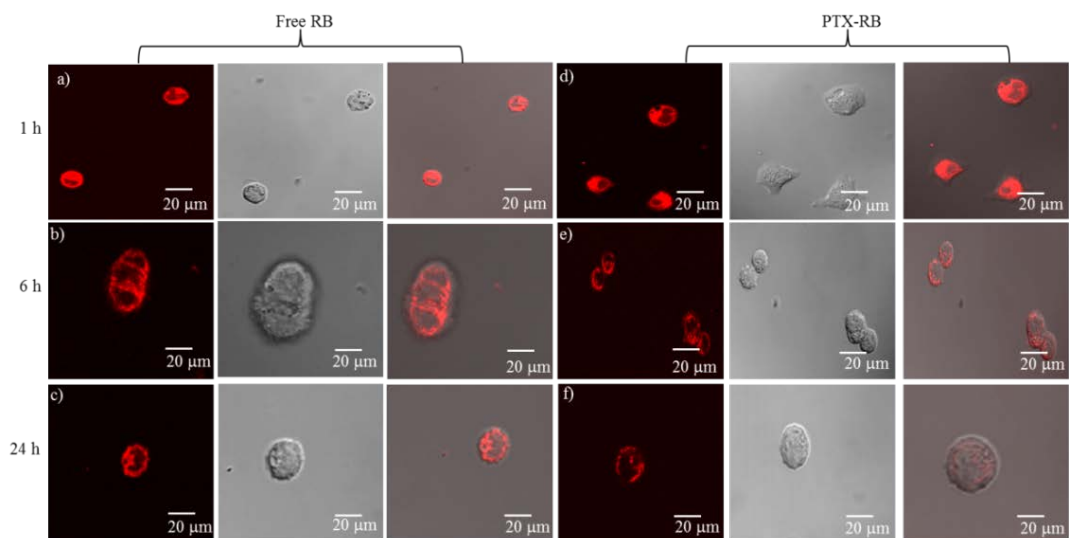


Figure 6.12 Fluorescence (left) ($\lambda_{\text{ex}} = 405 \text{ nm}$, $\lambda_{\text{em}} = 526\text{-}700 \text{ nm}$), bright field (middle) and overlaid (right) images of T47D human breast cancer cells treated with free RB or PTX-RB conjugate (a and b) after 1 h of incubation (b and e) after 6 h of incubation and (c and f) after 24 h of incubation at room temperature. Original magnification was $63\times$. Scale bars = $20 \mu\text{m}$.

6.2.5 TEM analysis of fluorescently labelled AuNPs

Transmission electron microscopy (TEM) was used to confirm the results obtained from CLSM in relation to intercellular uptake and localisation of AuNPs. TEM has been successfully used to recognise AuNPs in thin sections of cells and obtain high resolution images [425]. A high concentration of AuNPs was applied to simplify TEM imaging as it was difficult to detect low concentrations of AuNPs internalised cells. AuNPs appear as black spots in TEM due to their high atomic number. T47D cells were cultured and prepared for TEM imaging. TEM analysis of T47D cells exposed to as prepared AuNPs, a fluorescence dye (DAPI, pyNH₂ or FB28) loaded thiolated AuNPs or a fluorescence dye and the chemotherapeutic agent, PTX simultaneously loaded the thiolated AuNPs for 3-4 h have shown an efficient internalisation of AuNPs through cell membrane (Figure 6.13 where the white arrows identify gold nanoparticles).

To obtain detailed images of AuNPs internalised the cells, high magnification was applied. Cells treated with high concentrations of as prepared AuNPs or fluorescently labelled AuNPs conjugates (200 µL) were possibly taken up as groups of clusters. These clustered particles were found in the cytoplasm, probably indicating a later endocytosis mechanism [426] and were mainly localised in vacuoles (Figure 6.13.a). They were enclosed inside vesicles in cellular compartments (Figure 6.13.b). It was hypothesised that large clusters were absorbed by the plasma membrane and internalised the cells via endocytosis due to the presence of AuNPs inside cells near the cell's membrane (Figure 6.13.b). The aggregation of AuNPs is governed by their surface chemistry. The chemical properties of AuNPs such as the surface characteristics and charge may change after mixing the AuNPs with the biological media due to non-selective absorption of serum proteins on the surface of AuNPs. Proteins attached onto the surface of AuNPs may improve the endocytosis of the clustered AuNPs into the cells [426]. These findings are in agreement with other studies [249, 427]. For example, a study reported by Mustafa et al. [426] found that when exposing MC3T3-E1 osteoblastic cells to higher concentration (160 µg mL⁻¹) of AuNPs, the particles seem to internalise inside the cells mainly by endocytosis mechanism with one or more pathways such as clathrin- and caveolae-mediated endocytosis, macropinocytosis and pinocytosis [426, 428]. On the other hand, some

AuNPs were found to be freely dispersed in the cell cytoplasm (Figure 6.13.b). These individual particles may internalise the cells by a diffusion process unlike phagocytosis and endocytosis mechanisms. Geiser et al. [429] investigated the possibility of nanomaterials to pass the plasma membrane and go in cytoplasm by a non-phagocytic mechanism [429]. Rothen-Rutishauser et al. [430] found that 25 nm AuNPs and 22 nm titanium oxide nanoparticles may be internalised by the red blood cell membrane by a still unknown mechanism dissimilar to phagocytosis and endocytosis mechanisms [430]. However, the prime mechanism for internalisation and penetration of high concentration AuNPs inside the cells is expected via endocytosis.

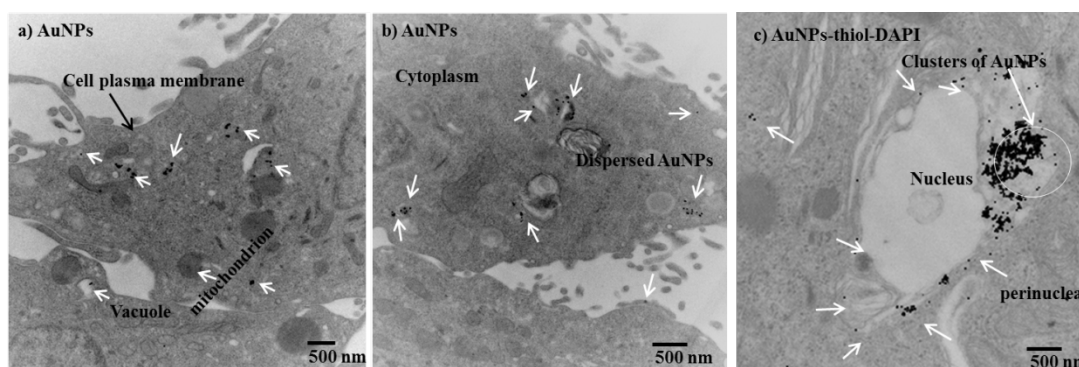


Figure 6.13 TEM images showing clusters and individual of AuNPs in cell cytoplasm of T47D cells exposed to 200 μ L of (a & b) AuNPs and (c) AuNPs-thiol-DAPI direct conjugate for 3-4 h. Scale bar = 500 nm.

The cellular uptake of AuNPs in AuNPs-thiol-DAPI direct conjugate was significantly higher than that for AuNPs without surface modifications (see Figure 6.13.c compared to Figure 6.13.a and b). The cells were treated with same concentrations in all conjugates and from TEM images (14 images for each) the total number of AuNPs taken up by cells treated with AuNPs-thiol-DAPI direct conjugate was higher than that for cells treated with as prepared AuNPs. This can be attributed to the ligand-receptor interactions in the cell membrane [431]. The electro-static interactions between the positively charged surfaces of nanoparticles and the negatively charged cell plasma membrane can facilitate internalisation the particles by cells [432]. Similar results have been reported by different groups [433-435]. For example, Harush-Frenkel et al. [434] investigated the difference of the endocytosis into HeLa cells of NPs having either a negative or positive charge on their surface.

They found that the positively charged NPs internalised the cells rapidly via the clathrin-mediated pathway whereas the negatively charged NPs were internalised slowly by endocytosis and did not use the clathrin-mediated endocytosis pathway [434]. The AuNPs in AuNPs-thiol-DAPI direct conjugate were localised in cytoplasm and near perinuclear region (see [Figure 6.13.c](#)). Likewise, PTX-thiol-AuNPs-thiol-DAPI direct conjugate penetrated inside the cells indicating transfer of the drug by the aggregated particles inside the cellular compartments which resembles endosomes in addition to few particles found near the cell membrane ([Figure 6.14.b](#)). The cellular uptake of this conjugate was higher than that for AuNPs (comparison between [Figure 6.14.b](#) and [Figure 6.13.a](#) and [b](#)). TEM data of T47D cells treated with AuNPs-thiol-pyNH₂ or PTX-thiol-AuNPs-thiol-pyNH₂ direct conjugates shows the cellular uptake of AuNPs in these conjugates was low compared to AuNPs-thiol-DAPI or PTX-thiol-AuNPs-thiol-DAPI direct conjugates as obtained from TEM images ([Figure 6.14.a-d](#)) indicating the number of cationic groups (one for pyNH₂ versus two for DAPI) contributes to facilitating the internalisation. The particles of AuNPs-thiol-pyNH₂ and PTX-thiol-AuNPs-thiol-pyNH₂ direct conjugates were found near the cell's periphery and in cytoplasm ([Figure 6.14.c](#) and [d](#)).

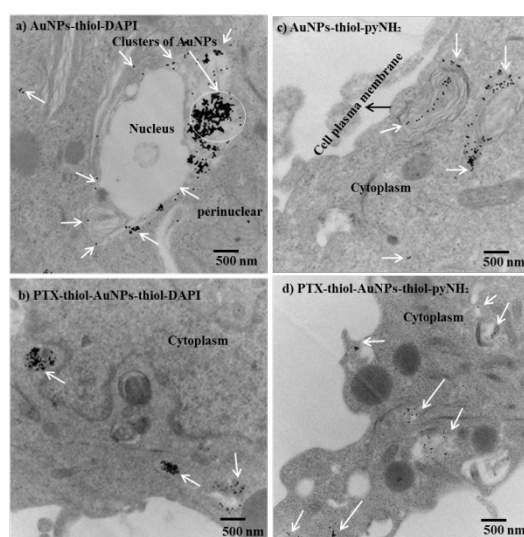


Figure 6.14 TEM images showing clusters and individual of AuNPs in cell cytoplasm of T47D cells exposed to 200 μ L of (a) AuNPs-thiol-DAPI (b) PTX-thiol-AuNPs-thiol-DAPI (c) AuNPs-thiol-pyNH₂ and (d) PTX-thiol-AuNPs-thiol-pyNH₂ direct conjugates for 3-4 h. Scale bar = 500 nm.

TEM images of T47D cells exposed to AuNPs-thiol-FB28 hybrid and PTX-thiol-AuNPs-thiol-FB28 direct conjugate for 3-4 h have shown an efficient internalisation of AuNPs through the cell membrane as well. Cellular uptake of AuNPs in AuNPs-thiol-FB28 hybrid and PTX-thiol-AuNPs-thiol-FB28 direct conjugate was lower than that for AuNPs-thiol-DAPI and PTX-thiol-AuNPs-thiol-DAPI direct conjugates (see [Figure 6.15.a, b, c and d](#) for comparison). This means that the presence of positively charged molecules on the NPs surface plays a role of facilitating the uptake of AuNPs by the cells. Images for cells exposed to AuNPs-thiol-FB28 hybrid or PTX-thiol-AuNPs-thiol-FB28 direct conjugate show that AuNPs were found mainly in cytoplasm (see [Figure 6.15.c and d](#), respectively).

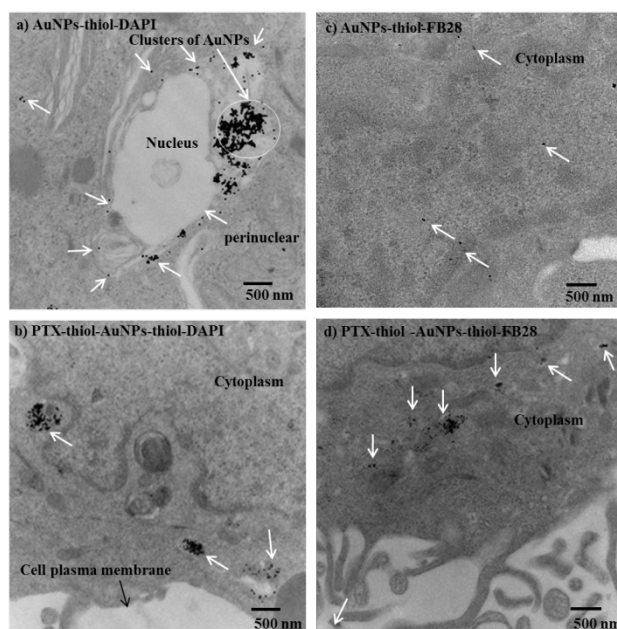


Figure 6.15 TEM images showing clusters and individual of AuNPs in cell cytoplasm of T47D cells exposed to 200 μ L of (a) AuNPs-thiol-DAPI direct conjugate (b) PTX-thiol-AuNPs-thiol-DAPI direct conjugate (c) AuNPs-thiol-FB28 hybrid and (d) PTX-thiol-AuNPs-thiol-FB28 direct conjugate for 3-4 h. Scale bar = 500 nm.

6.3 Concluding remarks

This chapter investigated the uptake of AuNPs by T47D breast cancer cells in different conjugates based on AuNPs using CLSM and TEM analysis. Cells treated with unlabelled AuNPs analysed by CLSM show no fluorescence while cells treated with fluorescently labelled AuNPs show fluorescence. The fluorescence intensity increases over time in all conjugates based on AuNPs. The cellular images obtained from CLSM and TEM suggested that the AuNPs were taken up by T47D cells and transport through endocytic pathways. TEM images show AuNPs were mainly localised in cytoplasm in addition to near the cell's periphery and near perinuclear region. Moreover, the surface chemistry of AuNPs plays an important role in facilitating their cellular uptake as TEM images for all conjugates containing DAPI show more AuNPs were internalised by the cells compared to their counterparts (AuNPs alone and conjugates containing pyNH₂ or FB28). These findings indicate that functionalisation the surface with positively charged ligands may facilitate the cellular uptake of AuNPs.

Chapter 7. Chemical conjugation of antibodies and PTX simultaneously to functionalised AuNPs nanocarriers

7.1 Introductory remarks

This chapter was directed to design a system comprised of antibodies used as active target, gold nanoparticles as carriers, PTX as a chemotherapy agent and alkanethiol acids as linkers; followed by, investigating the effectiveness of conjugation antibodies with AuNPs nanocarrier system to deliver the PTX to specific breast tumour sites.

There are two main strategies, which are passive and active targeting (see [Chapter 1, Sections 1.4.1](#) and [1.4.2](#), respectively for details), for delivering drug to tumour sites.

In current study, active targeting strategy was chosen for drug delivery in T47D breast cancer cells due to several reasons:

1. Active targeting is based on specific interactions between specific ligands functionalised the surface of nanocarriers and specific receptors over expressed on the targeted cells [111]. Therefore, this strategy can improve the tendency of nanocarriers to interact with tumour cell sites and can promote cellular uptake and permeation of nanocarriers via receptor mediated endocytosis while passive targeting function is limited to facilitating the localisation of nanocarriers in the tumour interstitium [111, 113, 436].
2. Active targeting may prevent multidrug resistance (MDR) via avoiding of P-glycoprotein-mediated drug efflux [437].
3. Active targeting strategy is used to improve recognition of the targeted cells. A variety of ligands such as antibodies, proteins, peptides, nucleic acids or sugars are

used to bind specifically to target molecules including proteins, sugars or lipids. The target molecules exist in diseased organs or on the surface of unhealthy cells [438].

Generally, there are two approaches for conjugation of a ligand to nanoparticles. These approaches are pre-conjugation and post-formulation methods.

In pre-conjugation method, small ligands, such as peptides or aptamers, are conjugated directly to the NPs before the assembly of the NP formulation [438].

On the other hand, post-formulation conjugation is applied for all types of molecules including antibodies, proteins, peptides and small molecules [439]. The strategy of formation of desired bonds between a ligand and the functionalised nanoparticles is simple and can be done in both aqueous and organic media [439]. Therefore, this method was preferred for current study. Coupling of antibodies with AuNPs can be achieved by using different approaches including ligand recognition, metal-mediated complexation, chemisorption, electrostatics interactions and covalent binding. Antibodies have amino acid polymers with reactive side chains can be used for covalent coupling [283]. However, concerns related to attachment of the functionalised AuNPs to the Fab region of the antibodies, where conjugation of the functionalised AuNPs block the antigen-binding site leading to loss of the functionality of the antibodies making them ineffective for targeted drug delivery, should be considered in the future when using the antibodies. If it is found that the antibodies have lost their activity, new experimental approaches for conjugation the antibodies to the functionalised AuNPs could be used [440]. However, different studies have used EDC/NHS coupling reaction with antibodies and have not reported the loss of the functionalities of the antibodies [441]. For example, Nghiem and co-workers [442] prepared a gold–HER2 antibody complex by attaching phage HER2 specific antibodies covalently to the bovine serum albumin (BSA) stabilised gold nanoparticles using EDC/NHS coupling. The bioactivity of the prepared complex was examined using enzyme-linked immunosorbent assay (ELISA test). The results show that the antibodies did not lose their functionalities and the Au–HER2 antibody complex was used as cancer marker [442].

7.1.1 Overview of EpCAM and TARP antibodies

Epithelial specific antigen, EpCAM/ CD326 Antibody, is a transmembrane glycoprotein with molecular weight of 40 kDa. It is also known as epithelial specific antigen (ESA) or epithelial cellular adhesion molecule (EpCAM). It is expressed on the surface of basolateral cell membranes in cancerous cells [443] and it is highly expressed in solid cancers [444]. EpCAM shows over-expression on colon, breast, pancreas and prostate cancerous cells [445-447]. EpCAM shows different biological functions including cell differentiation, cell-adhesion proliferation, cell migration and signalling [448]. EpCAM antigen can internalise and bind rapidly with specific EpCAM antibodies enabling successful delivery of anticancer therapeutics to targeted cancer cells [449, 450]. For example, Mitra et al. [451] designed a system consisting of EpCAM monoclonal antibody attached polyethyleneimine (PEI) capped gold nanoparticles (AuNPs) loaded with EpCAM-specific siRNA molecules to specific deliver siRNA to EpCAM-over expressing RB cells. The study concluded that this system has potential application as an operative gene therapy for retinoblastoma and as siRNA delivery system for treatment [451].

The epithelial cellular adhesion molecule, EpCAM antibody, has been chosen as an active target to specifically deliver PTX molecules due to the fact that EpCAM antigen is highly over-expressed in different types of cancers, among them breast cancer and on the surface of cancerous cells [444, 452]. In addition, after binding EpCAM antibodies to their antigens on tumour cells, they internalise and penetrate inside the cells rapidly improving the chemotherapeutics delivery to intracellular targeting [450, 453].

Anti-human TARP purified, also known as T cell receptor g chain alternate reading frame protein was also used. TARP antigens are highly expressed on human breast and prostate carcinoma [454-456]. Anti-human TARP purified was chosen to specifically bind to TARP antigen that is over-expressed on breast cancer. Anti-human TARP purified was used as an active target agent. EpCAM antibody (or TARP) and the anticancer drug, PTX, were simultaneously conjugated to thiol-AuNPs. The successful binding between the antibody and its receptor will allow to the anticancer agent, PTX, to reach the tumour cells then kill them.

In current study, after functionalisation of AuNPs using the two-step modification method, a carboxylic acid terminal end on AuNPs surface was obtained. An EDC/NHS coupling reaction was used to crosslink the antibody, EpCAM, (or TARP) and the anticancer agent, PTX, simultaneously to the AuNPs. Amino groups ($-\text{NH}_2$) of EpCAM (or TARP) and C_2 and C_7 hydroxyl groups of PTX with carboxyl groups of 16-MHDA or LA, used as linkers and stabilisers, amide and ester bonds were formed via using EDC/NHS coupling reaction (see [Schemes 2.13](#) and [2.14](#) in [Chapter 2, Section 2.8](#) for synthesis method of both antibodies). The formation of mixture of EpCAM (or TARP) and PTX molecules functionalised the thiol-AuNPs surface was investigated using UV-Vis, TEM, DLS and FT-IR techniques.

Using EDC/NHS coupling chemistry for loading antibodies to nanoparticles were carried out by other groups as well. For example, Pasqua et al. [287] reported a successful conjugation of anti-E. coli O157:H7 with AuNPs using EDC/NHS chemistry. The gold ions were first reduced via a mixture of carboxylic acid and alcohol terminated alkanethiols; followed by, attaching the antibody (anti-E. coli) with the carboxylic groups using EDC/NHS coupling reaction [287].

7.2 Characterisation of antibodies containing conjugates

7.2.1 UV-Vis analysis of antibodies containing conjugates

UV-Vis spectrophotometry was utilised to observe the maxima absorbance bands for thiolated AuNPs containing antibodies (EpCAM or TARP) before and after conjugation with the chemotherapy, PTX and compare them with thiol-AuNPs (see [Table 7.1](#)). [Figure 7.1.a](#) shows a distinctive band of thiol-AuNPs at 529 nm. After loading the antibodies (EpCAM or TARP) onto the functionalised AuNPs, a red shift to 538 nm was observed. The band was further red shifted after conjugation the anticancer agent, PTX, and the antibodies (EpCAM or TARP) simultaneously to the modified surface of AuNPs. The red shift indicates the successful conjugation of the molecules (antibodies and/or PTX) onto the thiol-AuNPs. The absorption bands for the antibodies were undetectable due to low amount of the antibodies attached thiol-AuNPs. Likewise, in case of conjugation PTX to antibodies containing conjugates, the signal of PTX at 228-230 nm was undetectable due to the low amount of PTX attached to the conjugates.

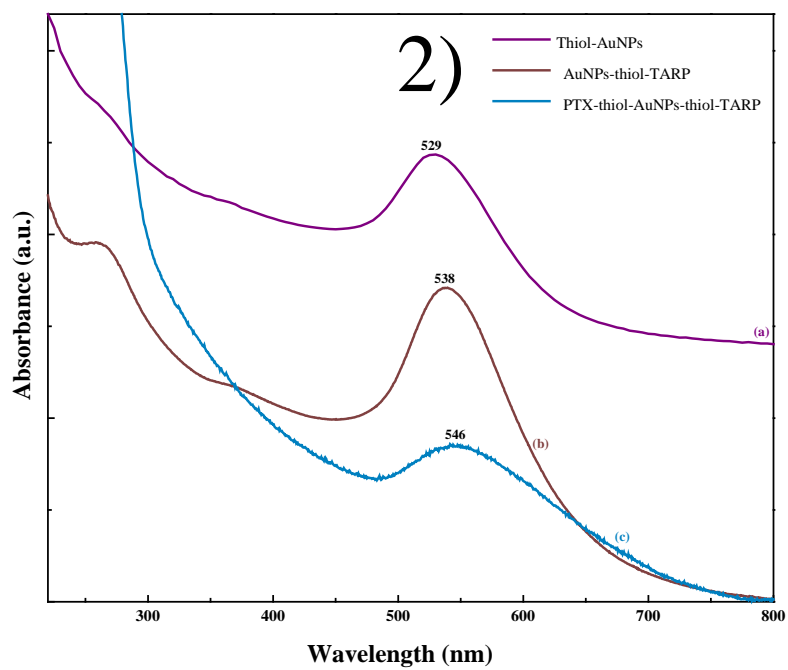
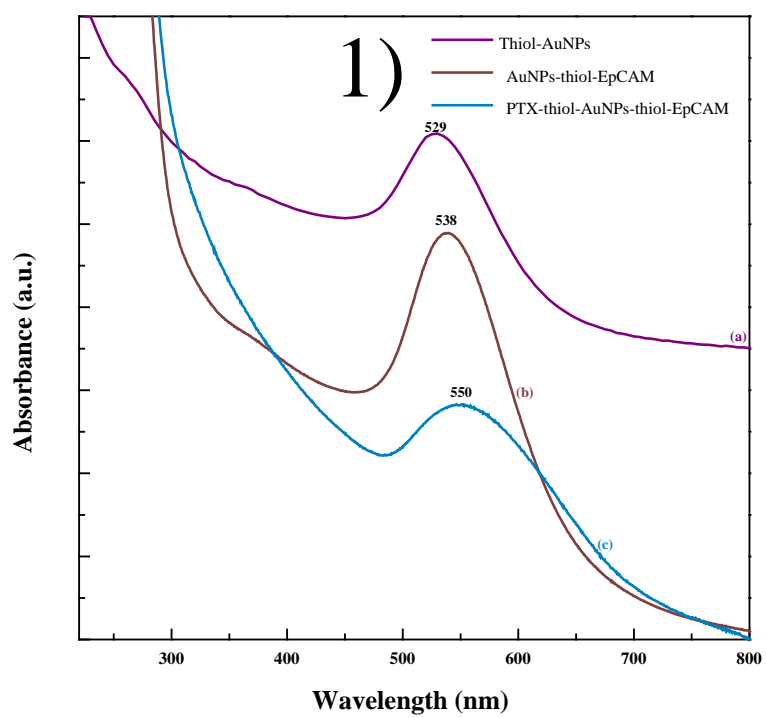


Figure 7.1 UV-Vis spectra of antibodies containing nanoparticles. 1) EpCAM and 2) TARP.

Table 7.1 Various samples based on AuNPs analysed using different techniques.

Thiol-AuNPs	
AuNPs-thiol-EpCAM direct conjugate	PTX-thiol-AuNPs-thiol-EpCAM direct conjugate
AuNPs-thiol-TARP direct conjugate	PTX-thiol-AuNPs-thiol-TARP direct conjugate

7.2.2 TEM analysis of antibodies containing conjugates

The direct conjugate (PTX-thiol-AuNPs-thiol-TARP) was characterised by transmission electron microscopy (TEM) to confirm the integrity of monodispersed gold nanoparticles. Figure 7.2 shows a typical TEM image of the conjugate. The size distribution histogram shows a narrow size distribution of the conjugate. Dark spots of AuNPs with size of approximately 18.7 ± 4.5 nm were observed. The increase of particle size, it was 17.13 ± 4.1 nm in PTX-thiol-AuNPs direct conjugate, suggests a slight potential aggregation of these particles. The TEM image indicates the formation of spherical shape of most AuNPs with some irregular particles.

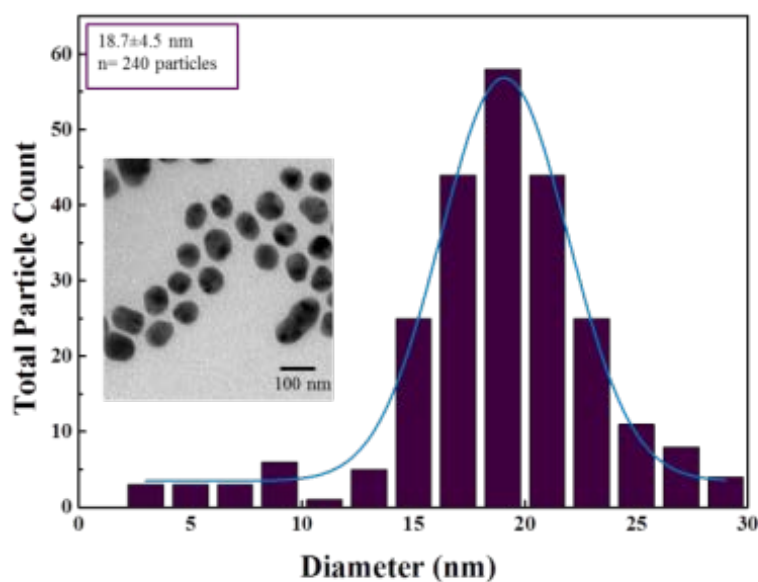


Figure 7.2 TEM image with size distribution histogram of PTX-thiol-AuNPs-thiol-TARP direct conjugate.

7.2.3 DLS analysis of antibodies containing conjugates

Intensity size distribution of thiolated AuNPs containing antibodies (EpCAM or TARP) before and after conjugation with the chemotherapy drug PTX was determined by DLS. In each case, an increase of the size after loading the PTX to the thiolated AuNPs containing antibodies samples was observed (see Figure 7.3). Narrow polydispersity indexes were recorded for all conjugates based on AuNPs indicating the formation of monodispersed nanoparticles (see Table 7.2).

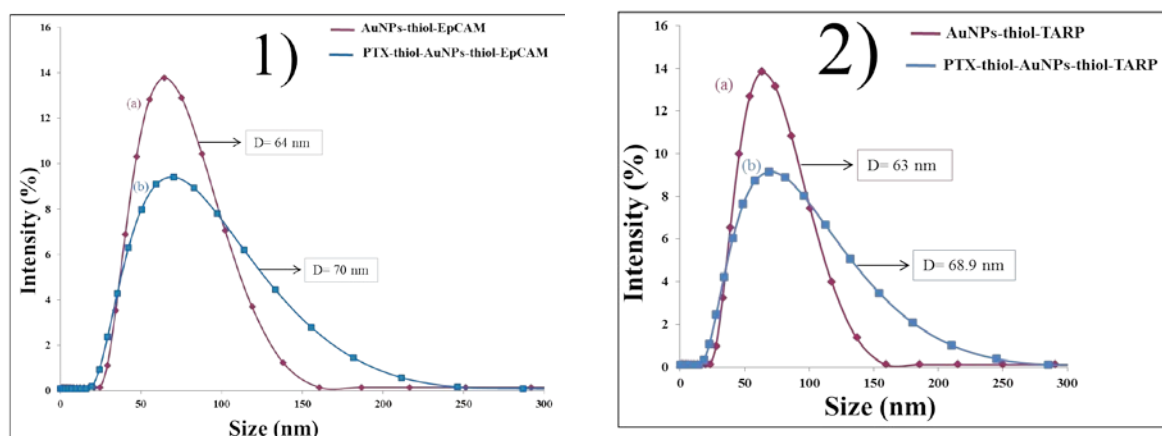


Figure 7.3 DLS measurements of antibodies containing nanoparticles. 1) EpCAM and 2) TARP.

Table 7.2 DLS measurements of various antibodies containing nanoparticles.

Sample	Size distribution by intensity (nm)	Polydispersity index
AuNPs-thiol-EpCAM direct conjugate	64	0.208
PTX-thiol-AuNPs-thiol-EpCAM direct conjugate	70	0.211
AuNPs-thiol-TARP direct conjugate	63	0.268
PTX-thiol-AuNPs-thiol-TARP direct conjugate	68.9	0.302

7.2.4 FT-IR analysis of antibodies containing conjugates

FT-IR spectroscopy was used to investigate the structural properties of the designed conjugate after attaching an antibody (Ab) (EpCAM or TARP) to the thiol-AuNPs. The use of FT-IR analysis to explore antibodies conjugation has been rarely applied [457]. Occhipinti et al. [457] synthesised trastuzumab-functionalised pegylated iron oxide nanoparticles (TMNP) and demonstrated the FT-IR analysis of covalent conjugated antibody to the nanoparticles. The results showed that the structural properties of mAb conjugated to the pegylated iron oxide nanoparticles surface did not change while when testing the physically adsorbed protein a broad absorption located at 1606 cm^{-1} was observed [457].

FT-IR spectra for (a) free antibodies (EpCAM or TARP), (b) AuNPs-thiol-Ab and (c) PTX-thiol-AuNPs-thiol-Ab direct conjugates were recorded to obtain information on protein secondary structure (see [Figures 7.4](#) and [7.5](#)). Both antibodies show similar FT-IR spectra. Therefore, EpCAM alone and EpCAM containing conjugates will be discussed and the same discussion can be applied for TARP antibody and its conjugates.

[Figure 7.4.a](#) shows the main characteristic bands of antibodies. The spectrum of the antibody alone shows the common characteristic peaks observed in the antibodies structures [457, 458]. An amide I band appeared at 1653 cm^{-1} associated with the C=O stretching vibration whereas amide II band resulted from the N-H bending vibration appeared at 1546 cm^{-1} and it is very weak [457, 459]. The band at 3427 cm^{-1} is assigned to N-H stretching vibration. [Figure 7.4.b](#) represents FT-IR spectra for AuNPs-thiol-EpCAM direct conjugate. The Amide I stretching vibration at 1653 cm^{-1} and N-H stretching vibration at 3427 cm^{-1} corresponding to the presence of EpCAM were observed. In addition, peaks in different stretching and bending modes of the carboxylic acids terminated alkanethiols were observed. The band at 1404 cm^{-1} is due to the C-H deformation of the alkyl group, the peaks at 2917 and 2849 cm^{-1} are assigned to C-H stretching of the alkyl groups, the peak at 1100 cm^{-1} corresponds to C-O stretching vibration, the peak at 1345 cm^{-1} is due to the out of-plane O-H

bending vibration in an intermolecular hydrogen-bonding structure [346, 347] were assigned to alkanethiols. [Figure 7.4.c](#) shows the FT-IR spectra of PTX-thiol-AuNPs-thiol-EpCAM direct conjugate. The Amide I stretching vibration at 1653 cm^{-1} , amide II band resulted from the N-H bending vibration appeared at 1546 cm^{-1} and it is very weak and N-H stretching vibration at 3427 cm^{-1} corresponding to the presence of EpCAM were observed. The main characteristic bands of PTX loaded to thiol-AuNPs were observed as well. The C=O band assigned to the formation of ester bond at 1736 cm^{-1} , the intense peaks at 1100 cm^{-1} corresponds to C-O stretching vibration, the peak at 1250 cm^{-1} is due to C-N stretching vibration, the peaks at 2923 and 2873 cm^{-1} are assigned to C-H stretching of the alkyl groups, at 1403 cm^{-1} is due to the C-H deformation of the alkyl group, at 1462 cm^{-1} is assigned to C-C in aromatic structure and the bands at 948 and 845 cm^{-1} are assigned to C-H in-plane deformation. The C-H stretching vibrations of the alkyl groups at 2923 and 2873 cm^{-1} show intense peaks due to addition of PTX molecules to EpCAP-thiol-AuNPs and the appearance of this peak is similar to that in free PTX. The results indicate the conjugation reaction occurred successfully.

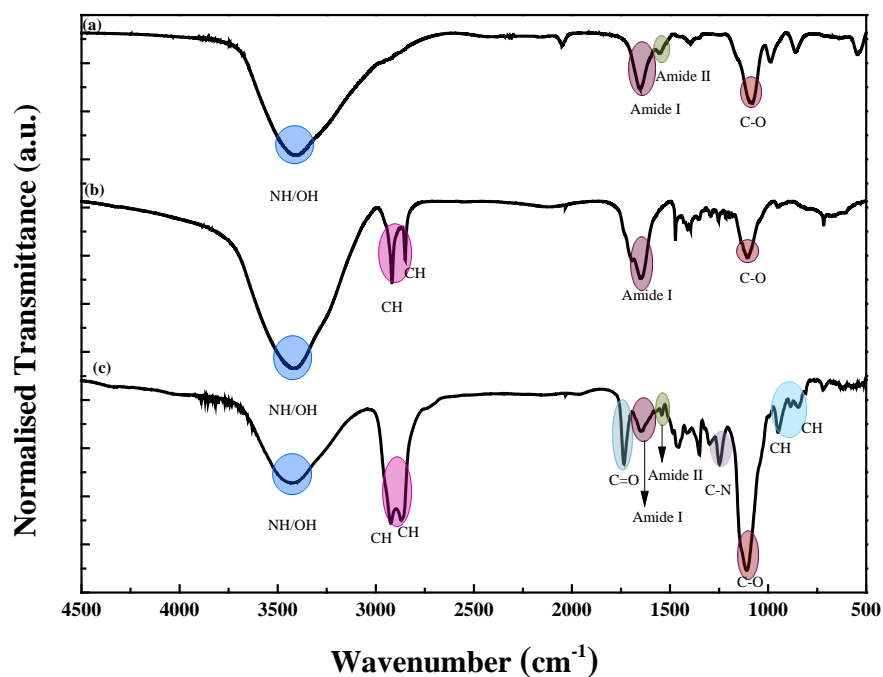


Figure 7.4 FT-IR spectra of (a) EpCAM antibody (b) AuNPs-thiol-EpCAM direct conjugate and (c) PTX-thiol-AuNPs-thiol-EpCAM direct conjugate.

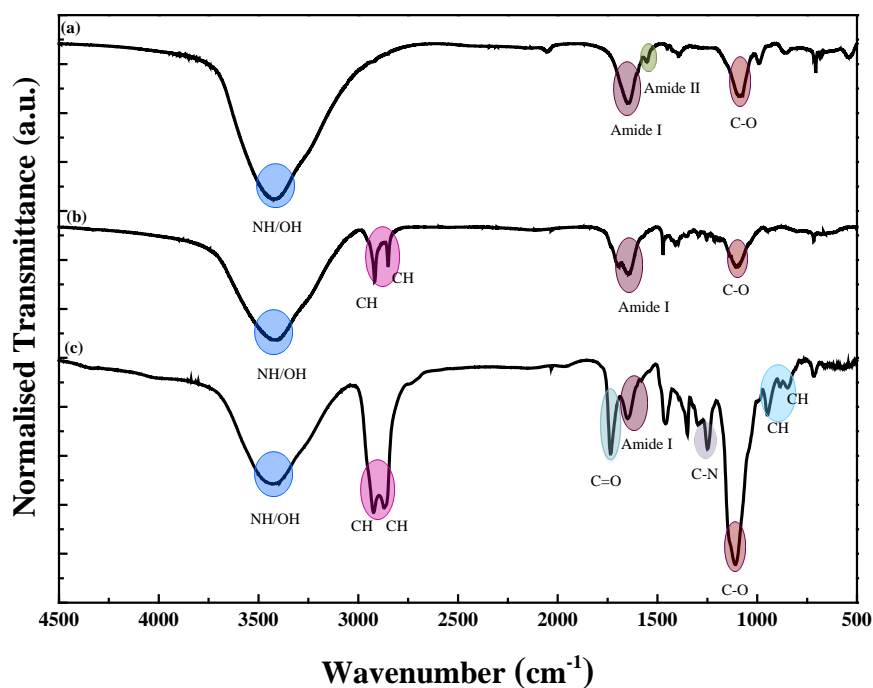


Figure 7.5 FT-IR spectra of (a) TARP antibody (b) AuNPs-thiol-TARP direct conjugate and (c) PTX-thiol-AuNPs-thiol-TARP direct conjugate.

7.2.5 Cytotoxicity assay of antibodies containing conjugates

Experiments on breast cancer cell lines to evaluate the *in vitro* effectiveness of the designed systems containing antibodies to improve drug delivery to target cancer cells were carried out. A description of the experiments is in [Appendix C](#). T47D cells were treated with AuNPs-thiol-TARP, PTX-thiol-AuNPs-thiol-TARP, AuNPs-thiol-EpCAM and PTX-thiol-AuNPs-thiol-EpCAM direct conjugates for 24 h. Five different concentrations were prepared for the experiment using serial dilutions starting with 0.1085 nM. As shown in [Figure 7.6](#). After exposing the cells to the AuNPs-thiol-TARP and AuNPs-thiol-EpCAM direct conjugates, no significant decrease in cell viability was induced at any concentrations tested. The results for AuNPs-thiol-TARP and AuNPs-thiol-EpCAM direct conjugates indicate that these two systems are nontoxic since the relative cell survival was 80 % or higher at all concentrations tested. After treating the cells with the same conjugates with PTX attached, at the first four concentrations the reduction of cell viability was not significant. This may be attributed to the low amounts of the anticancer PTX attached to the functionalised AuNPs. However, at the highest concentration tested (0.1085 nM), the reduction of cell viability was significant. In case of T47D cells treated with PTX-thiol-AuNPs-thiol-TARP direct conjugate, more than 95 % of cells were killed indicating the bioavailability of PTX and the effectiveness of TARP antibody to deliver the PTX to cancer sites. In case of the cells treated with PTX-thiol-AuNPs-thiol-EpCAM direct conjugate, more than 75 % of cells were killed indicating the effective action of EpCAM antibody to facilitate delivering PTX drug to specific sites of cancerous cells (see [Figure 7.6](#)). When comparing the cell viability between PTX-thiol-AuNPs and PTX-thiol-AuNPs-thiol-Ab (TARP or EpCAM) (see [Figure 7.7](#)), generally, at the first four low concentrations PTX-thiol-AuNPs direct conjugate was more effective at killing cancer cells than PTX-thiol-AuNPs-thiol-Ab (TARP or EpCAM) direct conjugates. This is likely due to the fact that the amount of PTX loaded on the functionalised AuNPs was much higher than the amount of PTX attached to conjugates containing antibodies. This means that at low concentrations there are not enough AuNPs to deliver a high enough dose of PTX to the cells to cause cell death. However, at high concentration the threshold of PTX dose is surpassed and significant cell death is observed. The cell viability for PTX-thiol-AuNPs-thiol-TARP direct conjugate was reduced to only 4 % while the cell viability

for PTX-thiol-AuNPs (no antibodies) was reduced to 60 % at the same concentration of the conjugate. In addition, cells treated with PTX-thiol-AuNPs-thiol-EpCAM direct conjugate showed significant reduction of cell viability up to 25 % whereas the reduction of cell viability for those treated with PTX-thiol-AuNPs direct conjugate was up to 60 % at the same concentration of the conjugates. The fact that the antibody containing particles will likely have a lower loading of PTX means the significantly lower cell viability observed when the cells are exposed these particles highlights the fact that the antibodies must lead to a more effective binding to the cells compared to particles without antibodies. This suggests lower doses of the conjugates will be effective thus reducing the drug side effects.

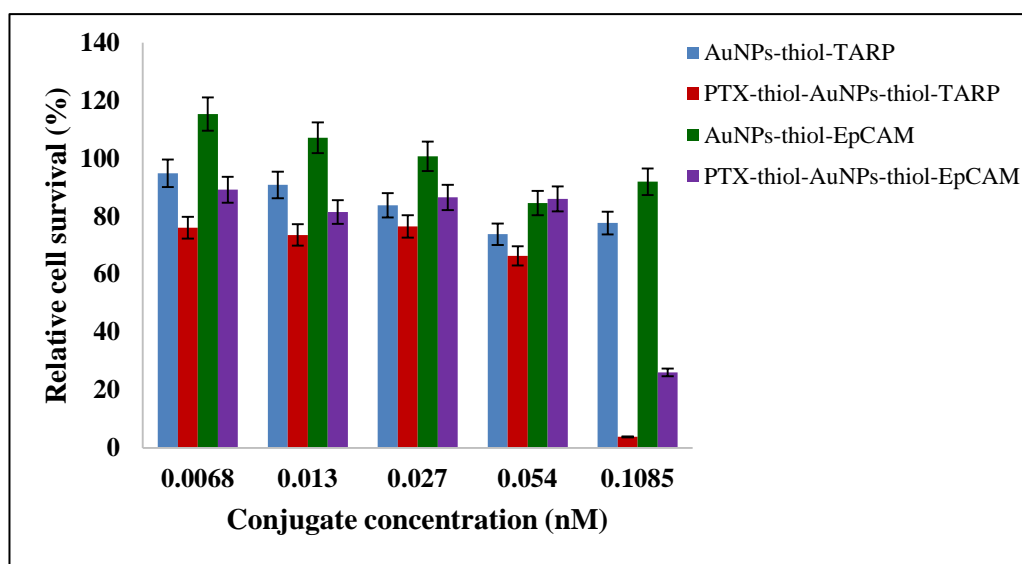


Figure 7.6 Comparison of response of T47D cell line to treatment with gold nanoparticles conjugates containing antibodies and/ or PTX using MTT assay. Shown in concentration of the direct conjugates (nM) versus relative survival (%) compared to untreated control. Data shown as mean, n:3, *: $p \leq 0.05$.

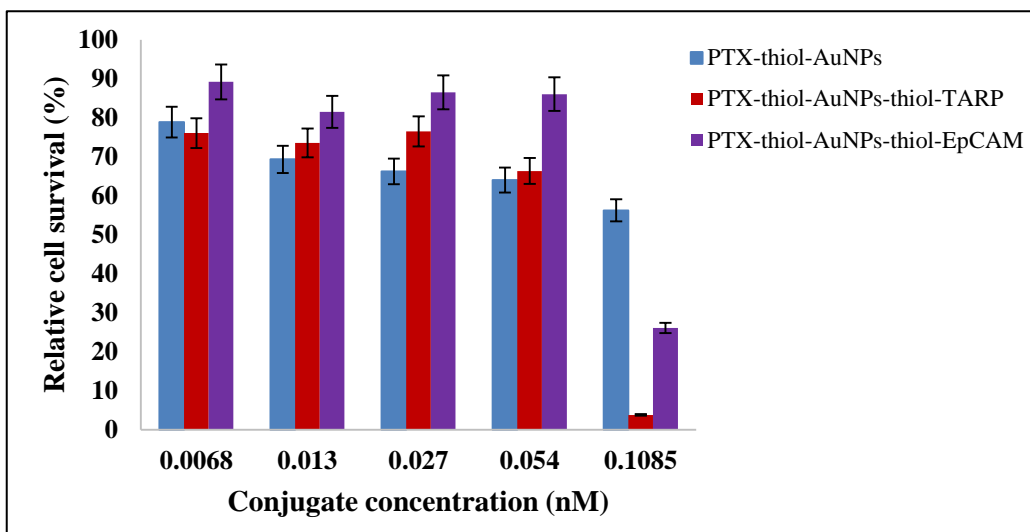


Figure 7.7 Comparison of response of T47D cell line to treatment with gold nanoparticles conjugates with and without antibodies using MTT assay. Shown in concentration of the direct conjugates (nM) versus relative survival (%) compared to untreated control. Data shown as mean, n:3, *: $p \leq 0.05$. The PTX-thiol-AuNP direct conjugate data is reproduced from [Figure 4.8](#) in [Chapter 4, Section 4.3.1.7](#).

7.3 Concluding remarks

This chapter focused on characterisation of antibodies covalently conjugated to thiolated gold nanoparticles using various characterisation techniques to show evidence of successful conjugation via EDC/NHS coupling. The results obtained from different characterisation techniques indicate the successful conjugation of antibodies and/ or PTX to thiolated AuNPs. The cytotoxicity assay of T47D cells treated with antibodies containing conjugates based on gold nanoparticles shows that the relative cell survival was 80 % and higher at the concentrations tested, indicating antibodies conjugated AuNPs systems are safe and nontoxic and can be used for biological research and for development of drug carrier systems. In addition, the cytotoxicity of T47D cells exposed to antibodies and PTX attached simultaneously to the functionalised AuNPs shows that at low concentrations no significant reduction in cell viability was induced. However, when using high concentrations (0.1085 nM) the reduction of cell viability was significantly high. The number of cells killed by antibodies and PTX attached simultaneously to the functionalised AuNPs systems was significantly higher than that for cells killed by PTX-thiol-AuNPs direct conjugate system where no antibodies were used. The results indicate the effectiveness of combining EpCAM or TARP antibodies with PTX-thiol-AuNPs system to target T47D breast cancer cells.

Chapter 8. Conclusions and recommendations

8.1 Synopsis

The aim of this thesis was to investigate the innovation of nanotechnology towards improving drug delivery system for breast cancer treatment. To achieve this aim, a drug delivery system comprised of gold nanoparticles as carriers and the anticancer agent, PTX, was designed using covalent and non-covalent methods. The cellular uptake of AuNPs containing conjugates was investigated using CLSM and TEM techniques. Two different antibodies were covalently coupled to the functionalised AuNPs to investigate their effectiveness of delivering the PTX specifically to breast cancerous cells by recognition their antigens and binding with them allowing PTX to be delivered in that specific site in a targeted way.

8.2 Conclusions

From the literature review in [Chapter 1](#) it was found that breast cancer is the most common cancer among women in the United States, accounting for nearly 1 in 3 cancers [5]. It is also the second leading cause of cancer-related death among women after lung cancer [6]. A number of treatments are used for breast cancer. Surgery, radiation therapy and chemotherapy are some of these therapies. The literature has shown that chemotherapy is a treatment of choice for most classes of breast carcinomas [39]. One of most commonly used chemotherapeutic agents for breast cancer treatment is paclitaxel [41]. However, its drawbacks including the lack of permeability into cells and poor water solubility has limited its utilisation in clinical applications [54, 56]. Literature has also shown combining drugs with nanoparticles could improve the drug solubility, permeability into cells and reduce other drawbacks such as high toxicity and short circulation half-life within the body that exist in standard anticancer therapeutic drugs [44, 66].

Gold nanoparticles have been extensively investigated for pharmaceutical and medical applications due to their unique properties such as high stability in physiological environments, high surface area, excellent biocompatibility and non-cytotoxicity properties [130, 131]. Literature has shown that the use of AuNPs as carriers in drug delivery systems is one of the most significant biomedical applications. Gold nanoparticles can improve delivering therapeutic agents within cancerous cells which leads to reduce the side effects of the therapeutic agents [2].

It was found that functionalisation the AuNPs surface with alkanethiol acids, which are one of the most commonly used ligands as linkers, through Au–S bond can facilitate binding with biomolecules and provide a stable linkage [160].

Literature has shown the importance of immunoglobulins for various applications in biological and clinical fields for diagnosis and treatments of diseases [270]. Antibodies conjugates can be used in targeted therapy for cancer and other diseases. It was found that developing antibody conjugates for cancer treatment is currently one of the most common approaches used to investigate new drugs. Successful development of defined monoclonal antibody conjugates leads to specific delivery of

a drug to diseased cells without harming normal cells [270]. This thesis covers the engineering of a novel drug delivery system by conjugation of the anticancer agent, PTX and antibodies as active targeting with the nanocarriers, AuNPs, through using carboxylic acids terminated alkanethiols as linker to link the PTX and antibodies to AuNPs.

[Chapter 2](#) described the experimental procedures for synthesis of gold nanoparticles, functionalisation their surfaces using carboxylic acids terminated alkanethiols and conjugation different molecules (the anticancer drug, PTX, fluorescence agents or antibodies) with the modified AuNPs. It also described the analytical instrumentation techniques used throughout this thesis.

[Chapter 3](#) focused on the mechanism of preparation AuNPs using trisodium citrate as a reducing agent. It also described modification the surface of AuNPs using carboxylic acids terminated alkanethiols and non-covalent coupling of PTX with the modified AuNPs to obtain an innovative drug delivery system. The prepared AuNPs based samples were characterised using UV-Vis spectrophotometry, DLS, TEM, FT-IR and NMR. It investigated the stability of the designed system (PTX-thiol-AuNPs hybrid) using UV-Vis spectrophotometry. It was found that there is a relationship between the time the AuNPs and PTX were mixed during the generation of the hybrid and the amount of PTX found to be present in the hybrid. This chapter also studied the response of T47D breast cancer cells treated with the thiol-AuNPs, free PTX and PTX-thiol-AuNPs hybrid. It was found that thiol-AuNPs were nontoxic at the concentrations tested indicating their potential use as safe system in drug delivery or other biological applications. However, after loading PTX to thiol-AuNPs, the cytotoxicity was significantly higher than PTX alone indicating the effectiveness of combining PTX with the AuNPs in one system.

[Chapter 4](#) described two covalent coupling methods to link PTX with the modified AuNPs. In the first approach, the anticancer drug, PTX, was covalently attached to thiolated AuNPs using EDC/NHS coupling reaction to synthesis the direct conjugate (PTX-thiol-AuNPs). In the second method, which was called reverse conjugate, the chemotherapy drug, PTX was first covalently bonded to the carboxylic acid terminated alkanethiol (16-MHDA) to form ester bonds using EDC/NHS coupling.

Then, the resulting conjugate was attached to AuNPs through chemisorption of thiols onto the AuNPs surface through Au-S bond to form the reverse conjugate (PTX-16-MHDA-AuNPs). Both conjugates were characterised using UV-Vis spectrophotometry, DLS, TEM, FT-IR and NMR to confirm the successful conjugation. This chapter also investigated the drug loading efficiency of PTX-thiol-AuNPs direct conjugate using UV-Vis spectrophotometry and it studied the response of T47D breast cancer cells to 24 h *in vitro* treatment with different concentrations of PTX-thiol-AuNPs direct conjugate and PTX-16-MHDA-AuNPs reverse conjugate. It was found that cells exposed to PTX-thiol-AuNPs direct conjugate were killed significantly and the killing of these cells was much higher than for the cells treated with PTX alone. However, no significant reduction of relative cell survival was observed in case of cells treated with PTX-16-MHDA-AuNPs reverse conjugate comparing to PTX alone or PTX-thiol-AuNPs direct conjugate. This is probably due to the fact that the reverse method is not as effective at loading the AuNP with PTX as the other conjugate methods. On the other hand, the response of T47D cancer cells to 24 h *in vitro* treatment with different concentrations of PTX-thiol-AuNPs direct conjugate and PTX-16-MHDA-AuNPs reverse conjugate at two different pHs (7.5 & 6.5) was tested. In case of T47D cells treated with PTX-thiol-AuNPs direct conjugate, significant reduction of cell viability at different pHs was observed. However, the decrease of cell viability was higher at pH 6.5 than at pH 7.4. In case of T47D cells exposed to PTX-16-MHDA-AuNPs reverse conjugate, also significant reduction of relative cell survival was observed. However, no significant difference of cell viability reduction was observed at different pHs.

Chapter 5 described the characterisation of various fluorescent dyes covalently attached (in case of using DAPI or pyNH₂ staining agents) or non-covalently interacted (in case of using FB28 staining agent) with thiol-AuNPs with or without the anticancer agent, PTX, using UV-Vis spectrophotometry, fluorescence spectroscopy, DLS, TEM, FT-IR and NMR techniques. It also described the characterisation of PTX chemically attached to RB staining agent using different characterisation techniques. This chapter discussed the response of T47D breast cancer cells to 24 h *in vitro* treatment with different concentrations of AuNPs-thiol-DAPI direct conjugate, AuNPs-thiol-pyNH₂ direct conjugate, AuNPs-thiol-FB28 hybrid, AuNPs-16-MHDA-DAPI reverse conjugate and free RB. It was found that

AuNPs-thiol-DAPI direct conjugate and AuNPs-thiol-FB28 hybrid were nontoxic at any concentration tested to investigate the cellular uptake and localisation of AuNPs and suggesting use of these conjugates will be possible in other medical applications. The AuNPs-thiol-pyNH₂ direct conjugate and AuNPs-16-MHDA-DAPI reverse conjugate can be considered safe products for intracellular applications when using low concentrations. Response of T47D cells to 24 h *in vitro* treatment with free RB showed that the free RB was nontoxic at any concentration tested, indicating its potential use for biomedical purposes.

Chapter 6 focused on investigation the uptake of AuNPs by T47D breast cancer cells in different conjugates based on AuNPs using CLSM and TEM analysis techniques. Cells treated with unlabelled AuNPs analysed by CLSM showed no fluorescence. Cells treated with fluorescently labelled AuNPs showed fluorescence. The fluorescence intensity increased over time in all conjugates based on AuNPs. The cellular images obtained from CLSM and TEM suggested that the AuNPs were taken up by T47D cells and penetrated inside cells by endocytosis mechanism. TEM images showed AuNPs were mainly localised in cytoplasm, near the cell periphery and near the perinuclear area. It was found that the surface chemistry of AuNPs may facilitate cellular uptake. TEM images for all conjugates containing DAPI showed more AuNPs were internalised by the cells compared to their counterparts (AuNPs alone and conjugates containing pyNH₂ or FB28). These findings indicate that functionalisation the surface with positively charged molecules may facilitate the cellular uptake of AuNPs.

Chapter 7 described the characterisation of two different antibodies (EpCAM and TARP) chemically attached to thiol-AuNPs in the presence and in the absence of PTX using different analytical techniques to evaluate their function as active targeting agents to deliver the chemotherapy drug, PTX, to breast tumour cells where the antigens of these antibodies are highly expressed. Response of T47D cells treated with antibodies containing conjugates based on gold nanoparticles in the absence of the anticancer PTX showed that the cell viability was always 80 % or higher at the concentrations tested indicating antibodies conjugated AuNPs systems are nontoxic and can be used in development of drug carrier systems and other pharmaceutical applications. Response of T47D cells exposed to gold nanoparticles conjugates

containing antibodies and PTX simultaneously showed that no significant reduction in cell viability was induced at low concentrations of the conjugates. However, when using high concentrations (0.1085 nM) the reduction of cell viability was significantly high. More than 95 % of the cells were killed after exposure to PTX-thiol-AuNPs-thiol-TARP direct conjugate and approximately 75 % of the cells were killed after treatment with PTX-thiol-AuNPs-thiol-EpCAM direct conjugate. The reduction of cell viability after exposure to antibodies and PTX attached simultaneously to the functionalised AuNPs systems was significantly higher than that when treating the cells with PTX-thiol-AuNPs direct conjugate and in the absence of antibodies at the same concentration. The findings indicate the effectiveness of combining EpCAM or TARP antibodies with PTX-thiol-AuNPs system to target T47D breast cancer cells.

8.3 Future research directions

Gold nanoparticles have attracted great attention due to their unique characteristics that can be exploited in various scientific fields. They have already shown successes in different areas including biomedical applications. Therefore, this research project has focused on using AuNPs with size of ~17 nm for development of an innovative drug delivery system for breast cancer therapy. This system used gold nanoparticles as nanocarriers, carboxylic terminated alkanethiols as spacers and the anticancer agent, PTX. It is the first system that combines these molecules in one construct and investigates their biological cytotoxicity *in vitro*. It would be interesting to expand the experimental work to investigate AuNPs as an anticancer drug delivery system using different parameters (size, shape, etc.) under various conditions. Some studies have shown that the gold nanoparticle shapes can have an effect in drug delivery applications. For example, Adnan et al. [460] have prepared hybrid gold nanoparticles with three shapes (spherical, rod-like and star-like particles). The nanoparticles were grafted with diblock copolymers (P(OEGMA)-b-P(VBA)) through the thiol moieties present on the polymer chain end. The other side of the polymer containing aldehyde groups was used to conjugate anticancer agent doxorubicin (DOX) via a Schiff base connection. The three prepared shapes of AuNPs were investigated as carriers for doxorubicin delivery and as photothermal agents. The grafting density of DOX conjugated polymer was the highest for spherical AuNPs compared to other particle shapes (rod-like and star-like particles). However, when testing the use of the three shapes of the hybrid AuNPs for photothermal therapy under near infrared (NIR) light, spherical nanoparticles showed the least toxicity to cancer cells whilst star nanoparticles had the highest toxicity. Also, when using these three shapes for drug delivery, spherical nanoparticles exhibited the least efficiency for drug delivery applications. The results suggest that gold nanoparticle shape influences the effectiveness of photothermal therapy and drug delivery applications based on AuNPs [460].

In this thesis, carboxylic terminated alkanethiol ligands (16-MHDA and LA) were used as linkers and stabilisers. It would be interesting to use these ligands with other new ligands to further functionalisation requirements with other biomolecules. For example, after preparation of AuNPs and functionalisation of their surface with

alkanethiol acids, the carboxylic ends of the alkanethiol ligands can be exploited to attach the amine group of chitosan and form amide bond. Then, the hydroxyl groups at the C₂, C₃ and C₆ positions of chitosan can be used to attach biomolecules or other functionalities. This may add more advantages to the system in terms of the longer chain helping to increase the circulation time of the NPs. Also, other molecules with positive charges can be used to facilitate the cellular uptake of AuNPs. This approach opens up the possibility of having a multifunctionised particles tuned to give the optimal drug delivery. It would be also interesting to use other molecules as linkers rather than using carboxylic terminated alkanethiols. However, it would still be important that the new linkers have thiols due to their good affinity to AuNPs. It would be worth combining various chemotherapeutics with thiolated AuNPs and study their efficiencies and study their cytotoxicity using different breast cancer cell lines such as MCF-7, SkBr3 or MDA-MB-231 cells. It is important to investigate the effects of the conjugation systems on normal cells. It would be interesting to conjugate an anticancer, DOX, to thiolated AuNPs and investigate its performance and efficiency using T47D cells *in vitro* then compare that to PTX conjugated thiolated AuNPs. DOX has different functional groups that may be used to covalently couple the drug to thiolated AuNPs using EDC/NHS coupling chemistry. DOX is used to treat liver (hepatic), breast and lymphoma cancers [461]. Free administration of the drug causes severe problems related to multidrug resistance and acute renal and cardiotoxicity. Combination of DOX agent with gold nanoparticles may improve the drug efficiency by exploiting the unique properties of gold nanoparticles (see [Chapter 1, Section 1.5.2](#) for more details related to the properties of gold nanoparticles). Guhagarkar et al. [462] have shown successful results of treating hepatic cancer using polyethylene sebacate (PES)–doxorubicin (DOX) nanoparticles (PES–DOX NP) and pullulan as asialoglycoprotein receptor (ASGPR) ligand for hepatic targeting. The results have shown only small dosages are required which will increase the cellular concentrations of the drug in specific tumour sites and will reduce the side effects [462, 463].

In [Chapters 3 and 4](#), the amount of the anticancer drug, PTX, loaded to the functionalised AuNPs was studied using UV-Vis spectrophotometry. It would be interesting to study the drug loading using another analytical technique such as thermogravimetric analysis (TGA) to further confirm the work in this thesis. Gibson

et al. [193] reported the preparation of PTX-AuNPs conjugate. PTX was first attached to hexaethylene glycol (HEG) linker at the C₇ position of PTX using carbodiimide-based esterification method. Then, the resulting analogue was attached to the mercaptophenol-terminated 2 nm gold nanoparticles (AuNPs) (refer to [Figure 1.11](#), [Chapter 1](#)). TGA was used to measure the weight of the organic shell. First, mercaptophenol-functionalised AuNPs was analysed by TGA to determine the amount of mercaptophenol ligands before linking to HEG-PTX. Approximately 23.1 % of the mass of mercaptophenol functionalised AuNPs sample was attributed to the mercaptophenol ligands. Each gold particle was found to contain 126 functional sites of mercaptophenol. Then, after coupling HEG-PTX with mercaptophenol functionalised AuNPs, the resulted conjugate AuNP (glutaratehexaethylene glycol glutarate-7-PTX) was also analysed by TGA. The composition of the conjugate was found to be 67.1 % organic, which corresponds to ~70 molecules of PTX per particle, and 32.9 % metallic Au ([Figure 8.1](#)). Their synthetic approach has allowed preparation of well characterised core-shell nanostructures [193].

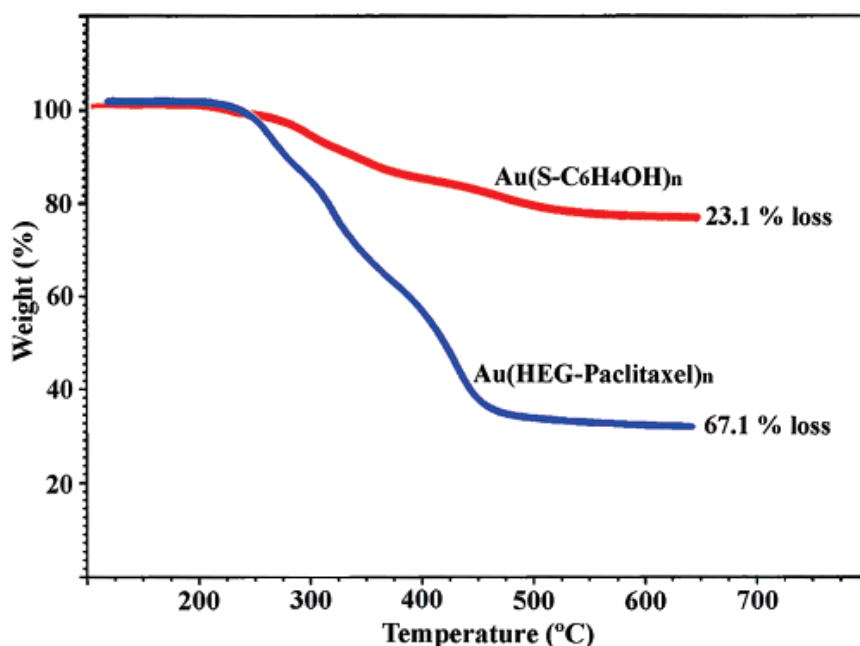


Figure 8.1 TGA data measuring the loss of organic material corresponding to 4-mercaptophenol-coated AuNPs (red) and hybrid structure (blue) [193].

In [Chapter 4](#), T47D breast cancer cell lines were treated with direct and reverse conjugates at two different pHs (pH 7.4 & 6.5) for 24 h to assess the possibility of using PTX loaded AuNPs *in vitro* to target cancerous cells. The cells treated with direct conjugate at pH 6.5 showed significant reduction of relative cell survival compared to the cells treated with the same conjugate at pH 7.4. Since acidity is a major feature of tumour tissues, it is important to investigate the effectiveness of drug delivery and release in tumour sites using different acidic pH values. It would be interesting to investigate the most efficient pH value for different engineered drug delivery systems (hybrid, direct and reverse conjugates) and compare it with the commercial formulation of PTX. Madhusudhan et al. [464] studied the effect of pH on the release of chemotherapeutic agent, doxorubicin (DOX) loaded AuNPs capped carboxymethyl chitosan (CMC) *in vitro* using different pH values (physiological pH 7.4 and acidic pH 5.3 and 4.6, where acetate buffer is used) for effective delivery to cancer cells. The results have shown that the released amount of DOX from DOX loaded AuNPs was dependent on the pH of the medium. The DOX release from DOX loaded AuNPs was significantly faster at pH 5.3 and 4.6 than at pH 7.4 (see [Figure 8.2](#)). The results reveal the potential effectiveness of pH dependent release on development of drug delivery to target cancer cells [464].

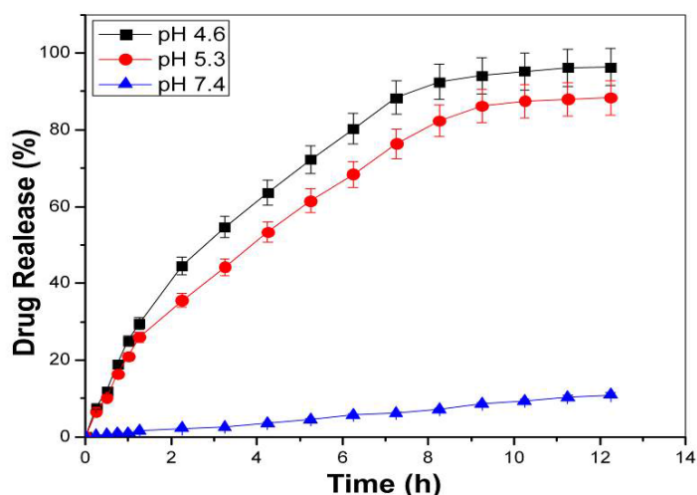


Figure 8.2 pH dependent release of DOX from DOX loaded nanoparticles [464].

[Chapter 5](#) and [6](#) investigated the cellular uptake of AuNPs using different fluorescent agents. The results collected from CLSM and TEM showed that the AuNPs were

internalised and taken up by T47D cells. It would be interesting to treat different cell lines with the fluorescently labelled AuNPs and study their uptake to investigate the interactions between the NPs and various cells. It would be valuable to prepare gold nanoparticles of different sizes, then functionalise their surface using the same carboxylic terminated alkanethiol ligands (16-MHDA and LA) followed by conjugation with different biomolecules (PTX, a fluorescence agent or antibodies) to study their effects and uptake by different cell lines. In addition, it would be useful to investigate the concentration of various sizes of gold nanoparticles in T47D cells after different periods of incubation using atomic absorption spectrometry (AAS) or inductively coupled plasma mass spectrometry (ICP-MS). For example, Trono et al. [465] investigated human pancreas cancer cell (PK-1, PK-45 and Panc-1) uptake of various sizes of gold nanoparticles using AAS. It was found that the cellular uptake is significantly size-dependent. The pancreas cancer cells uptake of 20 nm gold nanoparticles was higher compared to other gold nanoparticles sizes (5, 10, 30, 40 and 50 nm) (see Figure 8.3). In the same study, cellular uptake of 20 nm gold nanoparticles using different incubation times was carried out. The pancreas cancer cells were treated with 47.2 μM of AuNPs from 1 to 48 h. The results have shown that the cellular uptake of AuNPs increased by increasing the incubation time (see Figure 8.4) [465].

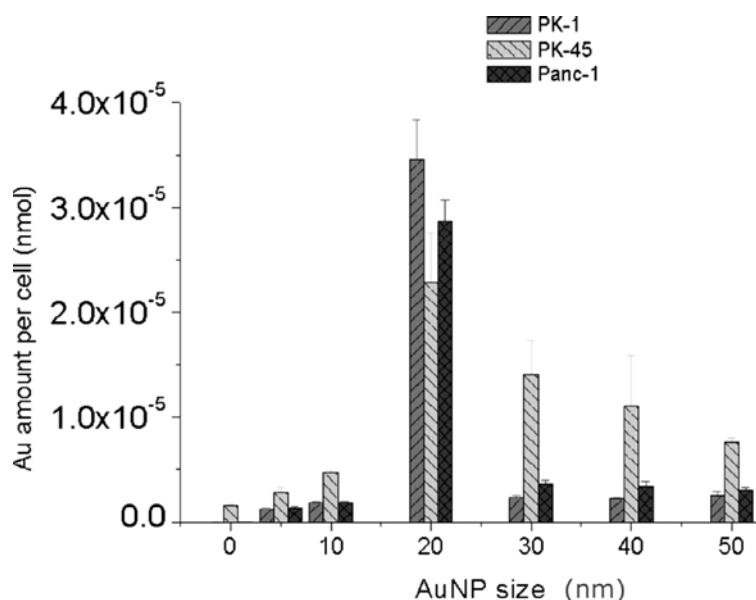


Figure 8.3 Intracellular uptake of AuNPs dependence on size [465].

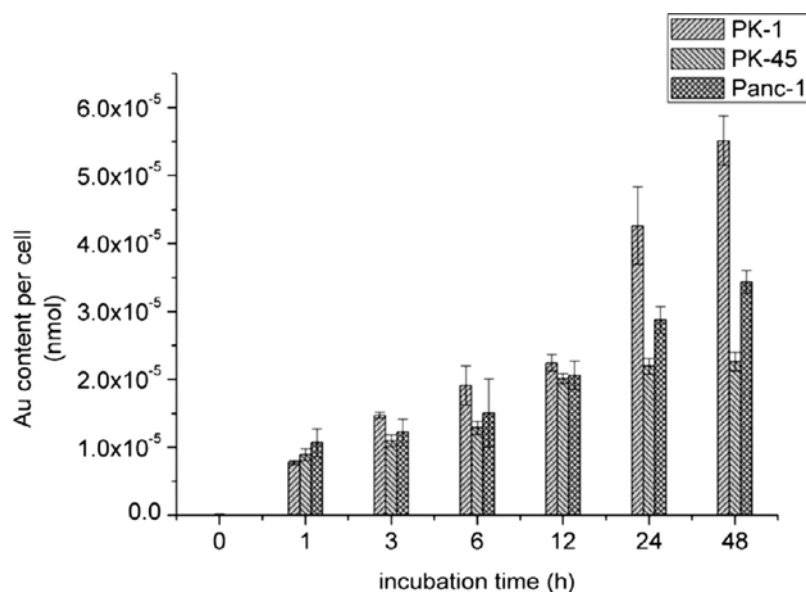


Figure 8.4 Intracellular uptake of 20 nm AuNPs dependence on incubation time [465].

In [Chapter 5](#), the cytotoxicity of rodamine B (RB) alone was examined against T47D cells. It would be important evaluate the cytotoxicity of PTX-RB conjugate as well. The lowest concentration tested for free PTX was 59 μM . However, the concentration of PTX in the prepared conjugate (PTX-RB) was very low (3.35 μM). Therefore, it would be interesting to increase the concentration of PTX in the conjugate and evaluate its cytotoxicity against T47D cells.

Different characterisation techniques were used through this thesis. It would be valuable to use zeta sizer to measure zeta potential as well. Colloidal nanoparticles are stabilised by electrostatic interactions specified by the zeta potential of the particles in solution, hence an electrical double layer on charged particles is formed [283]. Zeta potential value provides information whether the layer coated on the NPs is positively, negatively or neutrally charged. This information gives an indication if the NPs were successfully functionalised with other ligands or not.

In [Chapter 7](#), antibodies used were chemically conjugated to thiolated-AuNPs using EDC/NHS coupling to target specific receptors on breast cancer cells. It would be interesting to use another conjugation approach such as click chemistry. The

conjugation efficiency using click chemistry is approximately 100 %. The number of antibodies per particle conjugated to NPs via click chemistry is more than twice than EDC coupling [466]. In addition, improved coupling to target receptors was noticed in conjugates prepared by click chemistry [466]. Utilisation of click reaction with antibodies could lead to loss of functionality when using the reaction catalysts or the ligands for cross-linking. However, Thorek et al. [466] have used click chemistry to evaluate the coupling efficiency and the resulting product functionality after conjugating antibodies and superparamagnetic iron oxide nanoparticles together. The products obtained via click chemistry were compared to conjugates formed via using carbodiimide coupling. It was found that the production of antibody-NP conjugates by using CuI-catalysed terminal alkyne-azide cycloaddition (CuAAC) through click chemistry has a higher labelling efficiency than the products formed via EDC cross linking and the antibodies did not lose their functionality [466].

Another approach that can be considered is the use of gold nanoparticles-protein corona complex. The advantages of using corona proteins include an increase for specific cellular uptake because the misfolding of corona proteins triggers the nanoparticles to enter the cells or due to the presence of specific proteins in the corona that can target specific receptors over-expressed in the cells and the payload capacity of corona proteins is higher than covalently conjugated protein with nanoparticles [467]. Monopoli and co-workers [468] reported a study of plasma protein adsorption for two different nanoparticles which are sulfonated polystyrene nanoparticles and silica NPs to clarify the physicochemical properties and biological effects that influence the adsorption of hard protein corona. The results show that the surfaces on nanoparticles were covered with the proteins even in low plasma concentrations. The soft proteins with lower affinity to the NPs were exchanged by the harder ones that possess higher affinity to the NPs. The hard proteins layers were irreversible within the time of the experiments [468].

References

1. *What is cancer.* <https://canceraustralia.gov.au/affected-cancer/what-cancer> 2015 [cited 2015 18-02-2016].
2. Cai, W., et al., *Applications of gold nanoparticles in cancer nanotechnology.* Nanotechnology, science and applications, 2008. **2008**(1): p. 10.2147/NSA.S3788.
3. Siegel, R.L., K.D. Miller, and A. Jemal, *Cancer statistics, 2015.* CA: A Cancer Journal for Clinicians, 2015. **65**(1): p. 5-29.
4. *What is breast cancer.* <https://canceraustralia.gov.au/affected-cancer/cancer-types/breast-cancer/about-breast-cancer/what-breast-cancer> 2015 [cited 2016 07-03-2016].
5. DeSantis, C., et al., *Breast cancer statistics, 2013.* CA: A Cancer Journal for Clinicians, 2014. **64**(1): p. 52-62.
6. Key, T.J., P.K. Verkasalo, and E. Banks, *Epidemiology of breast cancer.* The Lancet Oncology. **2**(3): p. 133-140.
7. *Breast cancer in Australia.* <https://canceraustralia.gov.au/affected-cancer/cancer-types/breast-cancer/breast-cancer-statistics> 2016 [cited 2016 07-03-2016].
8. Sharma, G.N., et al., *Various types and management of breast cancer: an overview.* Journal of Advanced Pharmaceutical Technology & Research, 2010. **1**(2): p. 109-126.
9. *The normal breast.* <http://breastcancersurvivor.org/breastcancer.html> 2016 [cited 2016 13-03-2016].
10. *Non-invasive or invasive breast cancer.* <http://www.breastcancer.org/symptoms/diagnosis/invasive> 2015 [cited 2016 13-03-2016].
11. Virnig, B.A., et al., *Ductal carcinoma in situ of the breast: a systematic review of incidence, treatment, and outcomes.* Journal of the National Cancer Institute, 2010. **102**(3): p. 170-178.
12. Burstein, H.J., et al., *Ductal carcinoma in situ of the breast.* New England Journal of Medicine, 2004. **350**(14): p. 1430-1441.

13. Beckmann, M., et al., *Multistep carcinogenesis of breast cancer and tumour heterogeneity*. Journal of molecular medicine, 1997. **75**(6): p. 429-439.
14. Yerushalmi, R., M. Hayes, and K. Gelmon, *Breast carcinoma—rare types: review of the literature*. Annals of oncology, 2009: p. mdp245.
15. *ILC — Invasive Lobular Carcinoma*. <https://acrf.com.au/invasive-lobular-carcinoma/> 2016 [cited 2016 07-03-2016].
16. Bae, S.Y., Choi, M.Y., Cho, D.H., Lee, J., E., Nam, S.J., Yang, J.H., *Mucinous carcinoma of the breast in comparison with invasive ductal carcinoma: clinicopathologic characteristics and prognosis*. Journal of Breast Cancer, 2011. **14**(4): p. 308-313.
17. *IDC Type: Tubular Carcinoma of the Breast*. 2015 [cited 2016 07-03-2016].
18. *DCIS - ductal carcinoma in situ*. 2014 [cited 2016 13-03-2016].
19. Valero, V., A.U. Buzdar, and G.N. Hortobagyi, *Locally advanced breast cancer*. The Oncologist, 1996. **1**(1 & 2): p. 8-17.
20. *Metastatic breast cancer*. <http://www.nationalbreastcancer.org/metastatic-breast-cancer> 2015 [cited 2016 13-03-2016].
21. Chia, S.K., et al., *The impact of new chemotherapeutic and hormone agents on survival in a population-based cohort of women with metastatic breast cancer*. Cancer, 2007. **110**(5): p. 973-979.
22. Fossati, R., et al., *Cytotoxic and hormonal treatment for metastatic breast cancer: a systematic review of published randomized trials involving 31,510 women*. Journal of Clinical Oncology, 1998. **16**(10): p. 3439-3460.
23. Lopez, M.J., Porter, K.A., , *Inflammatory breast cancer* Surgical Clinics of North America, 1996. **76**(2): p. 411-429.
24. *What is inflammatory breast cancer?* 2016 [cited 2016 07-03-2016].
25. Foulkes, W.D., Smith, I.E., Reis-Filho, J.S., *Triple-negative breast cancer*. New England Journal of Medicine, 2010. **363**(20): p. 1938-1948.
26. *What is pagets disease of the nipple*. <https://canceraustralia.gov.au/affected-cancer/cancer-types/breast-cancer/about-breast-cancer/types-breast-cancer/what-pagets-disease-nipple> 2016 [cited 2016 07-03-2016].
27. Sandoval-Leon, A., Drews-Elger, K., Gomez-Fernandez, C., Yepes, M. Lippman, M. and *Paget's disease of the nipple*. Breast Cancer Research and Treatment, 2013. **141**(1): p. 1-12.

28. Fentiman, I.S., Fourquet, A., Hortobagyi, G.N., *Male breast cancer*. The Lancet, 2006. **367**(9510): p. 595-604.
29. *Breast cancer treatment*. <https://canceraustralia.gov.au/affected-cancer/cancer-types/breast-cancer/treatment> 2016 [cited 2016 07-03-2016].
30. *Surgical Treatment of Breast Cancer*. 2014 07-04-2014 [cited 2016 07-03-2016].
31. Association of Breast Surgery at, B., *Surgical guidelines for the management of breast cancer*. European Journal of Surgical Oncology (EJSO), 2009. **35**, **Supplement 1**: p. S1-S22.
32. Veronesi, U., Boyle, P., Goldhirsch, A., Orecchia, R. Viale, G., *Breast cancer*. The Lancet, 2005. **365**(9472): p. 1727-1741.
33. *Surgery to the armpit (axilla)*. <https://canceraustralia.gov.au/affected-cancer/cancer-types/breast-cancer/treatment/what-does-treatment-breast-cancer-involve/breast-cancer-surgery/surgery-armpit-axilla> 2016 [cited 2016 07-03-2016].
34. *Mastectomy*. <https://canceraustralia.gov.au/affected-cancer/cancer-types/breast-cancer/treatment/what-does-treatment-breast-cancer-involve/breast-cancer-surgery/mastectomy> 2016 [cited 2016 13-03-2016].
35. *Radiotherapy*. <http://www.cancer.org.au/about-cancer/treatment/radiotherapy.html> 2015 [cited 2016 07-03-2016].
36. Kamer, S. and B.M. Atasoy, *Mechanisms of Resistance to Radiation*, in *Principles and Practice of Modern Radiotherapy Techniques in Breast Cancer*, A. Haydaroglu and G. Ozyigit, Editors. 2013, Springer New York: New York, NY. p. 49-57.
37. *Radiotherapy*. 2015 10-11-2015 [cited 2016 07-03-2016].
38. *Chemotherapy*. 2014 01-08-2014 [cited 2016 07-03-2016].
39. Organisation, W.H. *Guidelines for management of breast cancer*. World Health Organisation 2006 [cited 2016 17 February 2016].
40. Findlay, M., G. von Minckwitz, and A. Wardley, *Effective oral chemotherapy for breast cancer: pillars of strength*. Annals of Oncology, 2008. **19**(2): p. 212-222.
41. Azim, H.A., et al., *Long-term toxic effects of adjuvant chemotherapy in breast cancer*. Annals of Oncology, 2011.

42. Xu, J., et al., *Design and characterization of antitumor drug paclitaxel-loaded chitosan nanoparticles by W/O emulsions*. International journal of biological macromolecules, 2012. **50**(2): p. 438-443.
43. Ding, Y., et al., *The performance of thiol-terminated PEG-paclitaxel-conjugated gold nanoparticles*. Biomaterials, 2013. **34**(38): p. 10217-10227.
44. Ma, P. and R.J. Mumper, *Paclitaxel Nano-Delivery Systems: A Comprehensive Review*. Journal of nanomedicine & nanotechnology, 2013. **4**(2): p. 1000164.
45. D. Yang, S.V., X. Jiang, L. Yu, *Novel free paclitaxel-loaded poly(L- γ -glutamylglutamine) paclitaxel nanoparticles*. International Journal of Nanomedicine, 2011. **6**: p. 85-91.
46. Harisa, G.I., et al., *Engineering erythrocytes as a novel carrier for the targeted delivery of the anticancer drug paclitaxel*. Saudi Pharmaceutical Journal, 2014. **22**(3): p. 223-230.
47. Brufsky, A., et al., *A Randomized Phase II Study of Paclitaxel and Bevacizumab With and Without Gemcitabine as First-Line Treatment for Metastatic Breast Cancer*. Clinical Breast Cancer, 2011. **11**(4): p. 211-220.
48. Larson, N., et al., *Biodegradable multiblock poly(N-2-hydroxypropyl)methacrylamide gemcitabine and paclitaxel conjugates for ovarian cancer cell combination treatment*. International Journal of Pharmaceutics, 2013. **454**(1): p. 435-443.
49. Lin, Z.-Z., et al., *Outcome of advanced nonsmall cell lung cancer patients receiving gemcitabine and weekly paclitaxel as first-line treatment*. Lung Cancer, 2008. **60**(2): p. 215-221.
50. Panchagnula, R., *Pharmaceutical aspects of paclitaxel*. International Journal of Pharmaceutics, 1998. **172**(1): p. 1-15.
51. Schiff, P.B., J. Fant, and S.B. Horwitz, *Promotion of microtubule assembly in vitro by taxol*. 1979.
52. Ochiai, E., *Chemicals for Life and Living*, 2011, Springer Canada. p. 288.
53. Rao, S., et al., *3'-(p-azidobenzamido) taxol photolabels the N-terminal 31 amino acids of beta-tubulin*. Journal of Biological Chemistry, 1994. **269**(5): p. 3132-3134.

54. Mo, R., et al., *The mechanism of enhancement on oral absorption of paclitaxel by N-octyl-O-sulfate chitosan micelles*. *Biomaterials*, 2011. **32**(20): p. 4609-4620.
55. Schiff, P. and S.B. Horwitz, *Taxol stabilizes microtubules in mouse fibroblast cells*. *Proceedings of the National Academy of Sciences*, 1980. **77**(3): p. 1561-1565.
56. Singla, A.K., A. Garg, and D. Aggarwal, *Paclitaxel and its formulations*. *International Journal of Pharmaceutics*, 2002. **235**(1-2): p. 179-192.
57. Fields, K., Partyka, J.S., Perkins, J.B., Elfenbein, G.J., *Optimization of high dose therapy for the treatment of patients with metastatic breast cancer*. *J. Oncol. Pharm. Practice.*, 1996. **2**(3): p. 11-17.
58. Yoncheva, K., et al., *Stabilized micelles as delivery vehicles for paclitaxel*. *International Journal of Pharmaceutics*, 2012. **436**(1-2): p. 258-264.
59. Gelderblom, H., et al., *Cremophor EL: the drawbacks and advantages of vehicle selection for drug formulation*. *European Journal of Cancer*, 2001. **37**(13): p. 1590-1598.
60. Sparreboom, A., et al., *Nonlinear pharmacokinetics of paclitaxel in mice results from the pharmaceutical vehicle Cremophor EL*. *Cancer Research*, 1996. **56**(9): p. 2112-2115.
61. Gallo, J.M., et al., *The effect of P-glycoprotein on paclitaxel brain and brain tumor distribution in mice*. *Cancer Research*, 2003. **63**(16): p. 5114-5117.
62. Ambudkar, S.V., et al., *P-glycoprotein: from genomics to mechanism*. *Oncogene*, 2003. **22**(47): p. 7468-7485.
63. Berg, S.L., et al., *Effect of R-verapamil on the pharmacokinetics of paclitaxel in women with breast cancer*. *J Clin Oncol*, 1995. **13**(8): p. 2039-42.
64. Fracasso, P.M., et al., *Phase I study of paclitaxel in combination with a multidrug resistance modulator, PSC 833 (Valspodar), in refractory malignancies*. *J Clin Oncol*, 2000. **18**(5): p. 1124-34.
65. Zhao, D., et al., *Preparation, characterization, and in vitro targeted delivery of folate-decorated paclitaxel-loaded bovine serum albumin nanoparticles*. *International journal of nanomedicine*, 2010. **5**: p. 669.
66. Desai, N., et al., *Increased antitumor activity, intratumor paclitaxel concentrations, and endothelial cell transport of cremophor-free, albumin-*

- bound paclitaxel, ABI-007, compared with cremophor-based paclitaxel.* Clinical Cancer Research, 2006. **12**(4): p. 1317-1324.
67. Panchagnula, R. and N.S. Thomas, *Biopharmaceutics and pharmacokinetics in drug research.* International Journal of Pharmaceutics, 2000. **201**(2): p. 131-150.
68. Kreuter, J., *Nanoparticles—a historical perspective.* International Journal of Pharmaceutics, 2007. **331**(1): p. 1-10.
69. Petricoin, E.F., et al., *Clinical proteomics: translating benchside promise into bedside reality.* Nature reviews Drug discovery, 2002. **1**(9): p. 683-695.
70. Cho, K., et al., *Therapeutic nanoparticles for drug delivery in cancer.* Clinical cancer research, 2008. **14**(5): p. 1310-1316.
71. Wang, X., et al., *Application of nanotechnology in cancer therapy and imaging.* CA: a cancer journal for clinicians, 2008. **58**(2): p. 97-110.
72. Nie, S., et al., *Nanotechnology applications in cancer.* Annu. Rev. Biomed. Eng., 2007. **9**: p. 257-288.
73. Jain, K.K., *Drug delivery systems-an overview.* Drug delivery systems, 2008: p. 1-50.
74. Allen, T.M. and P.R. Cullis, *Drug Delivery Systems: Entering the Mainstream.* Science, 2004. **303**(5665): p. 1818-1822.
75. Jain, S., D. Hirst, and J. O'sullivan, *Gold nanoparticles as novel agents for cancer therapy.* The British journal of radiology, 2014.
76. Ferrari, M., *Cancer nanotechnology: opportunities and challenges.* Nat Rev Cancer, 2005. **5**(3): p. 161-171.
77. Henglein, A., *Small-particle research: physicochemical properties of extremely small colloidal metal and semiconductor particles.* Chemical Reviews, 1989. **89**(8): p. 1861-1873.
78. Schmid, G., *Large clusters and colloids. Metals in the embryonic state.* Chemical Reviews, 1992. **92**(8): p. 1709-1727.
79. Niemeyer, C.M., *Nanoparticles, proteins, and nucleic acids: biotechnology meets materials science.* Angewandte Chemie International Edition, 2001. **40**(22): p. 4128-4158.

80. Chimene, D., D.L. Alge, and A.K. Gaharwar, *Two-dimensional nanomaterials for biomedical applications: emerging trends and future prospects*. *Advanced Materials*, 2015. **27**(45): p. 7261-7284.
81. Ventola, C.L., *The Nanomedicine Revolution: Part 2: Current and Future Clinical Applications*. *Pharmacy and Therapeutics*, 2012. **37**(10): p. 582-591.
82. Alivisatos, P., *The use of nanocrystals in biological detection*. *Nature biotechnology*, 2004. **22**(1): p. 47-52.
83. Alivisatos, A.P., W. Gu, and C. Larabell, *Quantum dots as cellular probes*. *Annu. Rev. Biomed. Eng.*, 2005. **7**: p. 55-76.
84. Navalakhe, R.M. and T.D. Nandedkar, *Application of nanotechnology in biomedicine*. *Indian journal of experimental biology*, 2007. **45**(2): p. 160.
85. Cai, W., et al., *Applications of gold nanoparticles in cancer nanotechnology*. *Nanotechnology, science and applications*, 2008. **2008**(1).
86. Prego, C., et al., *Chitosan-PEG nanocapsules as new carriers for oral peptide delivery: effect of chitosan pegylation degree*. *Journal of Controlled Release*, 2006. **111**(3): p. 299-308.
87. Mayer, C., *Nanocapsules as drug delivery systems*. *The International journal of artificial organs*, 2005. **28**(11): p. 1163-1171.
88. Maeda, H., *The enhanced permeability and retention (EPR) effect in tumor vasculature: the key role of tumor-selective macromolecular drug targeting*. *Advances in Enzyme Regulation*, 2001. **41**(1): p. 189-207.
89. Chiang, C.H., et al., *Improving drug loading efficiency and delivery performance of micro- and nanoparticle preparations through optimising formulation variables*. *International Journal of Nanotechnology*, 2013. **10**(10-11): p. 996-1006.
90. Storm, G., et al., *Surface modification of nanoparticles to oppose uptake by the mononuclear phagocyte system*. *Advanced Drug Delivery Reviews*, 1995. **17**(1): p. 31-48.
91. El-Shabouri, M.H., *Positively charged nanoparticles for improving the oral bioavailability of cyclosporin-A*. *International Journal of Pharmaceutics*, 2002. **249**(1-2): p. 101-108.

92. Hu, L., X. Tang, and F. Cui, *Solid lipid nanoparticles (SLNs) to improve oral bioavailability of poorly soluble drugs*. Journal of Pharmacy and Pharmacology, 2004. **56**(12): p. 1527-1535.
93. Arangoa, M.A., et al., *Gliadin nanoparticles as carriers for the oral administration of lipophilic drugs. Relationships between bioadhesion and pharmacokinetics*. Pharmaceutical research, 2001. **18**(11): p. 1521-1527.
94. Arbós, P., et al., *Nanoparticles with specific bioadhesive properties to circumvent the pre-systemic degradation of fluorinated pyrimidines*. Journal of Controlled Release, 2004. **96**(1): p. 55-65.
95. Orive, G., et al., *Drug delivery in biotechnology: present and future*. Current Opinion in Biotechnology, 2003. **14**(6): p. 659-664.
96. Mishra, B., B.B. Patel, and S. Tiwari, *Colloidal nanocarriers: a review on formulation technology, types and applications toward targeted drug delivery*. Nanomedicine: Nanotechnology, Biology and Medicine, 2010. **6**(1): p. 9-24.
97. Sahay, G., D.Y. Alakhova, and A.V. Kabanov, *Endocytosis of nanomedicines*. Journal of controlled release, 2010. **145**(3): p. 182-195.
98. Cai, W., Hsu, A.R., Li, ZB., *Are quantum dots ready for in vivo imaging in human subjects?* Nanoscale Res Lett., 2007. **2**: p. 265–281.
99. Liu, Z., et al., *In vivo biodistribution and highly efficient tumour targeting of carbon nanotubes in mice*. Nature nanotechnology, 2007. **2**(1): p. 47-52.
100. Thorek, D.L., et al., *Superparamagnetic iron oxide nanoparticle probes for molecular imaging*. Annals of biomedical engineering, 2006. **34**(1): p. 23-38.
101. Park, J.W., C.C. Benz, and F.J. Martin. *Future directions of liposome-and immunoliposome-based cancer therapeutics*. in *Seminars in oncology*. 2004. Elsevier.
102. Bisht, S., et al., *In vivo characterization of a polymeric nanoparticle platform with potential oral drug delivery capabilities*. Molecular cancer therapeutics, 2008. **7**(12): p. 3878-3888.
103. Huang, X., et al., *Gold nanoparticles: interesting optical properties and recent applications in cancer diagnostics and therapy*. 2007.
104. De Jong, W.H. and P.J. Borm, *Drug delivery and nanoparticles: applications and hazards*. International journal of nanomedicine, 2008. **3**(2): p. 133.

105. Miele, E., et al., *Albumin-bound formulation of paclitaxel (Abraxane® ABI-007) in the treatment of breast cancer*. International journal of nanomedicine, 2009. **4**: p. 99.
106. Pillai, G., *Nanomedicines for cancer therapy: an update of FDA approved and those under various stages of development*. SOJ Pharm Pharm Sci 2014. **1**(2): p. 13.
107. Duncan, R. and R. Gaspar, *Nanomedicine(s) under the Microscope*. Molecular Pharmaceutics, 2011. **8**(6): p. 2101-2141.
108. Deshpande, G.A., *Cancer nanotechnology: The recent developments in the cancer therapy*. Global Journal of Nanomedicine 2016. **1**(1).
109. Anselmo, A.C. and S. Mitragotri, *Nanoparticles in the clinic*. Bioengineering & Translational Medicine, 2016. **1**(1): p. 10-29.
110. Bazak, R., et al., *Passive targeting of nanoparticles to cancer: A comprehensive review of the literature*. Molecular and Clinical Oncology, 2014. **2**(6): p. 904-908.
111. Bae, Y.H. and K. Park, *Targeted drug delivery to tumors: myths, reality and possibility*. Journal of Controlled Release, 2011. **153**(3): p. 198.
112. Kunjachan, S., et al., *Theranostic systems and strategies for monitoring nanomedicine-mediated drug targeting*. Current pharmaceutical biotechnology, 2012. **13**(4): p. 609-622.
113. Lammers, T., et al., *Drug targeting to tumors: Principles, pitfalls and (pre-) clinical progress*. Journal of Controlled Release, 2012. **161**(2): p. 175-187.
114. Vasir, J.K. and V. Labhasetwar, *Targeted drug delivery in cancer therapy*. Technology in cancer research & treatment, 2005. **4**(4): p. 363-374.
115. Sahoo, S., S. Parveen, and J. Panda, *The present and future of nanotechnology in human health care*. Nanomedicine: Nanotechnology, Biology and Medicine, 2007. **3**(1): p. 20-31.
116. Torchilin, V.P., *Drug targeting*. European Journal of Pharmaceutical Sciences, 2000. **11**, **Supplement 2**: p. S81-S91.
117. Juweid, M., et al., *Micropharmacology of Monoclonal Antibodies in Solid Tumors: Direct Experimental Evidence for a Binding Site Barrier*. Cancer Research, 1992. **52**(19): p. 5144-5153.

118. Borsi, L., et al., *Selective targeting of tumoral vasculature: Comparison of different formats of an antibody (L19) to the ED-B domain of fibronectin*. International Journal of Cancer, 2002. **102**(1): p. 75-85.
119. Arap, W., R. Pasqualini, and E. Ruoslahti, *Cancer treatment by targeted drug delivery to tumor vasculature in a mouse model*. Science, 1998. **279**(5349): p. 377-380.
120. Neri, D. and R. Bicknell, *Tumour vascular targeting*. Nature Reviews Cancer, 2005. **5**(6): p. 436-446.
121. Johannsen, M., et al., *The tumour-targeting human L19-IL2 immunocytokine: Preclinical safety studies, phase I clinical trial in patients with solid tumours and expansion into patients with advanced renal cell carcinoma*. European Journal of Cancer, 2010. **46**(16): p. 2926-2935.
122. Kimball, K.J., et al., *A Phase I Study of a Tropism-Modified Conditionally Replicative Adenovirus for Recurrent Malignant Gynecologic Diseases*. Clinical Cancer Research, 2010. **16**(21): p. 5277-5287.
123. Lammers, T., W.E. Hennink, and G. Storm, *Tumour-targeted nanomedicines: principles and practice*. Br J Cancer, 2008. **99**(3): p. 392-397.
124. Mody, V.V., et al., *Introduction to metallic nanoparticles*. Journal of Pharmacy and Bioallied Sciences, 2010. **2**(4): p. 282-289.
125. Daniel, M.C. and D. Astruc, *Gold nanoparticles: Assembly, supramolecular chemistry, quantum-size-related properties, and applications toward biology, catalysis, and nanotechnology*. Chemical Reviews, 2004. **104**(1): p. 293-346.
126. Faraday, M., *The Bakerian lecture: experimental relations of gold (and other metals) to light*. Philosophical Transactions of the Royal Society of London, 1957. **147**: p. 145-181.
127. Schmid, G. and B. Corain, *Nanoparticulated Gold: Syntheses, Structures, Electronics, and Reactivities*. European Journal of Inorganic Chemistry, 2003. **2003**(17): p. 3081-3098.
128. Robenek, H., *Colloidal gold: Principles, methods, and applications vols. I and II (vol. III in preparation) Edited by M. A. Hayat Academic Press, Inc., New York, 1989 ISBN 0-12-333927-8, Vol. I, 536 pages ISBN 0-12-333928-6, Vol. II, 484 pages*. Scanning, 1990. **12**(4): p. 244-244.
129. Papavassiliou, G.C., *Optical properties of small inorganic and organic metal particles*. Progress in Solid State Chemistry, 1979. **12**(3): p. 185-271.

130. Huang, X. and M.A. El-Sayed, *Gold nanoparticles: optical properties and implementations in cancer diagnosis and photothermal therapy*. Journal of Advanced Research, 2010. **1**(1): p. 13-28.
131. Ghosh, P., et al., *Gold nanoparticles in delivery applications*. Advanced Drug Delivery Reviews, 2008. **60**(11): p. 1307-1315.
132. Murawala, P., et al., *In situ synthesized BSA capped gold nanoparticles: Effective carrier of anticancer drug Methotrexate to MCF-7 breast cancer cells*. Materials Science and Engineering: C, 2014. **34**: p. 158-167.
133. J. R. Blackborow, D.Y., *Metal vapour synthesis in organometallic chemistry*. 1979, New York: Springer Verlag.
134. Mafuné, F., et al., *Formation of Gold Nanoparticles by Laser Ablation in Aqueous Solution of Surfactant*. The Journal of Physical Chemistry B, 2001. **105**(22): p. 5114-5120.
135. Dong, S., et al., *Photochemical synthesis of gold nanoparticles by the sunlight radiation using a seeding approach*. Gold bulletin, 2004. **37**(3-4): p. 187-195.
136. Cioffi, N., et al., *Electrosynthesis and characterization of gold nanoparticles for electronic capacitance sensing of pollutants*. Electrochimica Acta, 2011. **56**(10): p. 3713-3720.
137. Ziegler, C. and A. Eychmüller, *Seeded Growth Synthesis of Uniform Gold Nanoparticles with Diameters of 15–300 nm*. The Journal of Physical Chemistry C, 2011. **115**(11): p. 4502-4506.
138. McCaffrey, R., et al., *Template Synthesis of Gold Nanoparticles with an Organic Molecular Cage*. Journal of the American Chemical Society, 2014. **136**(5): p. 1782-1785.
139. Alkilany, A.M., A.I. Bani Yaseen, and M.H. Kailani, *Synthesis of Monodispersed Gold Nanoparticles with Exceptional Colloidal Stability with Grafted Polyethylene Glycol-g-polyvinyl Alcohol*. Journal of Nanomaterials, 2015. **2015**: p. 9.
140. Frens, G., *Controlled nucleation for the regulation of the particle size in monodisperse gold suspensions*. nature physical science, 1973. **241**: p. 20-22.
141. Turkevich J, S.P., Hillier J., *A study of the nucleation and growth processes in the synthesis of colloidal gold*. Discuss. Faraday Soc., 1951. **11**: p. 55-75.
142. Tiwari, P., et al., *Functionalized Gold Nanoparticles and Their Biomedical Applications*. Nanomaterials, 2011. **1**(1): p. 31.

143. Enustun, B.V. and J. Turkevich, *Coagulation of Colloidal Gold*. Journal of the American Chemical Society, 1963. **85**(21): p. 3317-3328.
144. Ma, L.-N., D.-J. Liu, and Z.-X. Wang, *Synthesis and Applications of Gold Nanoparticle Probes*. Chinese Journal of Analytical Chemistry, 2010. **38**(1): p. 1-7.
145. Vigderman, L. and E.R. Zubarev, *Therapeutic platforms based on gold nanoparticles and their covalent conjugates with drug molecules*. Advanced drug delivery reviews, 2013. **65**(5): p. 663-676.
146. Akbarzadeh, A.Z., D.; Farhangi, A.; Mehrabi, M.R.; Norouzian, D.; Tangestaninejad, S.; Moghadam, M.; Bararpour, N., *Synthesis and characterization of gold nanoparticles by tryptophane*. American Journal of Applied Sciences, 2009. **6**(4): p. 691–695.
147. Ramezani, N., et al., *Screening of Medicinal Plant Methanol Extracts for the Synthesis of Gold Nanoparticles by Their Reducing Potential*, in *Zeitschrift für Naturforschung B*2008. p. 903.
148. Ravindra, P., *Protein-mediated synthesis of gold nanoparticles*. Materials Science and Engineering B-Advanced Functional Solid-State Materials, 2009. **163**(2): p. 93-98.
149. Brust, M., et al., *Synthesis of thiol-derivatised gold nanoparticles in a two-phase Liquid-Liquid system*. Journal of the Chemical Society, Chemical Communications, 1994(7): p. 801-802.
150. Jana, N.R., L. Gearheart, and C.J. Murphy, *Seeding Growth for Size Control of 5–40 nm Diameter Gold Nanoparticles*. Langmuir, 2001. **17**(22): p. 6782-6786.
151. Lee, J., et al., *Gold nanoparticles in breast cancer treatment: Promise and potential pitfalls*. Cancer Letters, 2014. **347**(1): p. 46-53.
152. Sun, Y. and Y. Xia, *Shape-controlled synthesis of gold and silver nanoparticles*. Science, 2002. **298**(5601): p. 2176-2179.
153. Zhu, J., et al., *Additive controlled synthesis of gold nanorods (GNRs) for two-photon luminescence imaging of cancer cells*. Nanotechnology, 2010. **21**(28): p. 285106.
154. Huang, X., et al., *Cancer Cell Imaging and Photothermal Therapy in the Near-Infrared Region by Using Gold Nanorods*. Journal of the American Chemical Society, 2006. **128**(6): p. 2115-2120.

155. Cho, E.C., Q. Zhang, and Y. Xia, *The effect of sedimentation and diffusion on cellular uptake of gold nanoparticles*. *Nat Nano*, 2011. **6**(6): p. 385-391.
156. Wang, H., et al., *Plasmonic Nanostructures: Artificial Molecules*. *Accounts of Chemical Research*, 2007. **40**(1): p. 53-62.
157. Conde, J., et al., *Revisiting 30 years of biofunctionalization and surface chemistry of inorganic nanoparticles for nanomedicine*. *Frontiers in Chemistry*, 2014. **2**: p. 48.
158. Yeh, Y.-C., B. Creran, and V.M. Rotello, *Gold Nanoparticles: Preparation, Properties, and Applications in Bionanotechnology*. *Nanoscale*, 2012. **4**(6): p. 1871-1880.
159. Fuentes, M., et al., *Preparation of inert magnetic nano-particles for the directed immobilization of antibodies*. *Biosensors and Bioelectronics*, 2005. **20**(7): p. 1380-1387.
160. Li, D., et al., *Immobilization of glucose oxidase onto gold nanoparticles with enhanced thermostability*. *Biochemical and biophysical research communications*, 2007. **355**(2): p. 488-493.
161. Zubarev, E.R., et al., *Amphiphilic Gold Nanoparticles with V-Shaped Arms*. *Journal of the American Chemical Society*, 2006. **128**(15): p. 4958-4959.
162. Gao, J., et al., *Colloidal Stability of Gold Nanoparticles Modified with Thiol Compounds: Bioconjugation and Application in Cancer Cell Imaging*. *Langmuir*, 2012. **28**(9): p. 4464-4471.
163. Gupta, R.K., M.P. Srinivasan, and R. Dharmarajan, *Synthesis of 16-Mercaptohexadecanoic acid capped gold nanoparticles and their immobilization on a substrate*. *Materials Letters*, 2012. **67**(1): p. 315-319.
164. Roux, S., et al., *Synthesis, Characterization of Dihydrolipoic Acid Capped Gold Nanoparticles, and Functionalization by the Electroluminescent Luminol*. *Langmuir*, 2005. **21**(6): p. 2526-2536.
165. Abad, J.M., et al., *Functionalization of Thioctic Acid-Capped Gold Nanoparticles for Specific Immobilization of Histidine-Tagged Proteins*. *Journal of the American Chemical Society*, 2005. **127**(15): p. 5689-5694.
166. Huff, T.B., et al., *Controlling the Cellular Uptake of Gold Nanorods*. *Langmuir*, 2007. **23**(4): p. 1596-1599.

167. Sharma, J., et al., *A facile in situ generation of dithiocarbamate ligands for stable gold nanoparticle-oligonucleotide conjugates*. Chemical Communications, 2008(18): p. 2140-2142.
168. Hoft, R.C., et al., *Adsorption of Amine Compounds on the Au(111) Surface: A Density Functional Study*. The Journal of Physical Chemistry C, 2007. **111**(37): p. 13886-13891.
169. Cheng, Y., et al., *Highly Efficient Drug Delivery with Gold Nanoparticle Vectors for in Vivo Photodynamic Therapy of Cancer*. Journal of the American Chemical Society, 2008. **130**(32): p. 10643-10647.
170. Ghosh, P.S., et al., *Efficient Gene Delivery Vectors by Tuning the Surface Charge Density of Amino Acid-Functionalized Gold Nanoparticles*. Acs Nano, 2008. **2**(11): p. 2213-2218.
171. Lee, S.H., et al., *Amine-functionalized gold nanoparticles as non-cytotoxic and efficient intracellular siRNA delivery carriers*. International Journal of Pharmaceutics, 2008. **364**(1): p. 94-101.
172. Wangoo, N., et al., *Synthesis and capping of water-dispersed gold nanoparticles by an amino acid: Bioconjugation and binding studies*. Journal of Colloid and Interface Science, 2008. **323**(2): p. 247-254.
173. Knop, K., et al., *Poly (ethylene glycol) in drug delivery: pros and cons as well as potential alternatives*. Angewandte Chemie International Edition, 2010. **49**(36): p. 6288-6308.
174. Tiwari, P.M., et al., *Functionalized gold nanoparticles and their biomedical applications*. Nanomaterials, 2011. **1**(1): p. 31-63.
175. Takae, S., et al., *Ligand density effect on biorecognition by PEGylated gold nanoparticles: Regulated interaction of RCA(120) lectin with lactose installed to the distal end of tethered PEG strands on gold surface*. Biomacromolecules, 2005. **6**(2): p. 818-824.
176. Otsuka, H., et al., *Quantitative and Reversible Lectin-Induced Association of Gold Nanoparticles Modified with α -Lactosyl- ω -mercapto-poly(ethylene glycol)*. Journal of the American Chemical Society, 2001. **123**(34): p. 8226-8230.
177. Shimmin, R.G., A.B. Schoch, and P.V. Braun, *Polymer size and concentration effects on the size of gold nanoparticles capped by polymeric thiols*. Langmuir, 2004. **20**(13): p. 5613-5620.

178. Zhang, G., et al., *Influence of anchoring ligands and particle size on the colloidal stability and in vivo biodistribution of polyethylene glycol-coated gold nanoparticles in tumor-xenografted mice*. *Biomaterials*, 2009. **30**(10): p. 1928-1936.
179. Biondi, O., S. Motta, and P. Mosesso, *Low molecular weight polyethylene glycol induces chromosome aberrations in Chinese hamster cells cultured in vitro*. *Mutagenesis*, 2002. **17**(3): p. 261-264.
180. Mitchell, A.D., et al., *The L5178Y/tk+/- mouse lymphoma specific gene and chromosomal mutation assay: A phase III report of the U.S. environmental protection agency Gene-Tox program I*. *Mutation Research/Genetic Toxicology and Environmental Mutagenesis*, 1997. **394**(1-3): p. 177-303.
181. Flora, S.J., et al., *Pharmacological perspectives of toxic chemicals and their antidotes*. 2004: Springer Science & Business Media.
182. Hatakeyama, H., H. Akita, and H. Harashima, *The polyethyleneglycol dilemma: advantage and disadvantage of PEGylation of liposomes for systemic genes and nucleic acids delivery to tumors*. *Biological and Pharmaceutical Bulletin*, 2013. **36**(6): p. 892-899.
183. Sun, L., D. Liu, and Z. Wang, *Functional Gold Nanoparticle-Peptide Complexes as Cell-Targeting Agents*. *Langmuir*, 2008. **24**(18): p. 10293-10297.
184. Wang, C., et al., *Gold nanoparticle-based colorimetric sensor for studying the interactions of β -amyloid peptide with metallic ions*. *Talanta*, 2010. **80**(5): p. 1626-1631.
185. Bastus, N.G., et al., *Peptides conjugated to gold nanoparticles induce macrophage activation*. *Molecular Immunology*, 2009. **46**(4): p. 743-748.
186. Tkachenko, A.G., et al., *Cellular trajectories of peptide-modified gold particle complexes: Comparison of nuclear localization signals and peptide transduction domains*. *Bioconjugate Chemistry*, 2004. **15**(3): p. 482-490.
187. Kang, B., M.A. Mackey, and M.A. El-Sayed, *Nuclear Targeting of Gold Nanoparticles in Cancer Cells Induces DNA Damage, Causing Cytokinesis Arrest and Apoptosis*. *Journal of the American Chemical Society*, 2010. **132**(5): p. 1517-1519.
188. Pellegrino, T., et al., *Gel electrophoresis of gold-DNA nanoconjugates*. *Journal of Biomedicine and Biotechnology*, 2007.

189. Javier, D.J., et al., *Aptamer-Targeted Gold Nanoparticles As Molecular-Specific Contrast Agents for Reflectance Imaging*. *Bioconjugate Chemistry*, 2008. **19**(6): p. 1309-1312.
190. Tomuleasa, C., et al., *Gold nanoparticles conjugated with cisplatin/doxorubicin/capecitabine lower the chemoresistance of hepatocellular carcinoma-derived cancer cells*. *J Gastrointest Liver Dis*, 2012. **21**(2): p. 187-196.
191. Oh, K.S., et al., *Gold/chitosan/pluronic composite nanoparticles for drug delivery*. *Journal of applied polymer science*, 2008. **108**(5): p. 3239-3244.
192. Brust, M., et al., *Synthesis and reactions of functionalised gold nanoparticles*. *Journal of the Chemical Society, Chemical Communications*, 1995(16): p. 1655-1656.
193. Gibson, J.D., B.P. Khanal, and E.R. Zubarev, *Paclitaxel-functionalized gold nanoparticles*. *Journal of the American Chemical Society*, 2007. **129**(37): p. 11653-11661.
194. Heo, D.N., et al., *Gold nanoparticles surface-functionalized with paclitaxel drug and biotin receptor as theranostic agents for cancer therapy*. *Biomaterials*, 2012. **33**(3): p. 856-866.
195. Skrabalak, S.E., et al., *Gold Nanocages: Synthesis, Properties, and Applications*. *Accounts of chemical research*, 2008. **41**(12): p. 1587-1595.
196. Lal, S., S.E. Clare, and N.J. Halas, *Nanoshell-Enabled Photothermal Cancer Therapy: Impending Clinical Impact*. *Accounts of Chemical Research*, 2008. **41**(12): p. 1842-1851.
197. Sau, T.K. and C.J. Murphy, *Seeded High Yield Synthesis of Short Au Nanorods in Aqueous Solution*. *Langmuir*, 2004. **20**(15): p. 6414-6420.
198. Mieszawska, A.J., et al., *Multifunctional Gold Nanoparticles for Diagnosis and Therapy of Disease*. *Molecular Pharmaceutics*, 2013. **10**(3): p. 831-847.
199. Cao, X., Y. Ye, and S. Liu, *Gold nanoparticle-based signal amplification for biosensing*. *Analytical Biochemistry*, 2011. **417**(1): p. 1-16.
200. Leduc, C., et al., *Chapter 2 - Single-molecule imaging in live cell using gold nanoparticles*, in *Methods in Cell Biology*, K.P. Ewa, Editor. 2015, Academic Press. p. 13-27.

201. Boisselier, E. and D. Astruc, *Gold nanoparticles in nanomedicine: preparations, imaging, diagnostics, therapies and toxicity*. Chemical society reviews, 2009. **38**(6): p. 1759-1782.
202. Crew, E., et al., *MicroRNA Conjugated Gold Nanoparticles and Cell Transfection*. Analytical Chemistry, 2012. **84**(1): p. 26-29.
203. Jain, S., D.G. Hirst, and J.M. O'Sullivan, *Gold nanoparticles as novel agents for cancer therapy*. The British Journal of Radiology, 2012. **85**(1010): p. 101-113.
204. You, C.-C., et al., *Detection and identification of proteins using nanoparticle-fluorescent polymer / 'chemical nose' sensors*. Nat Nano, 2007. **2**(5): p. 318-323.
205. Pingarrón, J.M., P. Yáñez-Sedeño, and A. González-Cortés, *Gold nanoparticle-based electrochemical biosensors*. Electrochimica Acta, 2008. **53**(19): p. 5848-5866.
206. Goyal, R.N., et al., *Differential pulse voltammetric determination of atenolol in pharmaceutical formulations and urine using nanogold modified indium tin oxide electrode*. Electrochemistry Communications, 2006. **8**(1): p. 65-70.
207. Qin, X., et al., *Amperometric biosensors based on gold nanoparticles-decorated multiwalled carbon nanotubes-poly(diallyldimethylammonium chloride) biocomposite for the determination of choline*. Sensors and Actuators B: Chemical, 2010. **147**(2): p. 593-598.
208. Pan, D., et al., *Multicolor Computed Tomographic Molecular Imaging with Non-crystalline High Metal Density Nanobeacons*. Contrast media & molecular imaging, 2014. **9**(1): p. 13-25.
209. Mieszawska, A.J., et al., *Multifunctional gold nanoparticles for diagnosis and therapy of disease*. Molecular pharmaceutics, 2013. **10**(3): p. 831-847.
210. Wang, H., et al., *Dendrimer-entrapped gold nanoparticles as potential CT contrast agents for blood pool imaging*. Nanoscale research letters, 2012. **7**(1): p. 1-8.
211. Cai, Q.-Y., et al., *Colloidal gold nanoparticles as a blood-pool contrast agent for X-ray computed tomography in mice*. Investigative radiology, 2007. **42**(12): p. 797-806.

212. Gu, Y.J., et al., *Nuclear penetration of surface functionalized gold nanoparticles*. Toxicology and Applied Pharmacology, 2009. **237**(2): p. 196-204.
213. Chithrani, D.B., et al., *Cellular uptake and transport of gold nanoparticles incorporated in a liposomal carrier*. Nanomedicine-Nanotechnology Biology and Medicine, 2010. **6**(1): p. 161-169.
214. Patra, C.R., et al., *Targeted Delivery of Gemcitabine to Pancreatic Adenocarcinoma Using Cetuximab as a Targeting Agent*. Cancer Research, 2008. **68**(6): p. 1970-1978.
215. Kawano, T., et al., *Stabilizing of plasmid DNA in vivo by PEG-modified cationic gold nanoparticles and the gene expression assisted with electrical pulses*. Journal of Controlled Release, 2006. **111**(3): p. 382-389.
216. Li, D., et al., *The enhancement of transfection efficiency of cationic liposomes by didodecyldimethylammonium bromide coated gold nanoparticles*. Biomaterials, 2010. **31**(7): p. 1850-1857.
217. Zhou, X., et al., *The effect of conjugation to gold nanoparticles on the ability of low molecular weight chitosan to transfer DNA vaccine*. Biomaterials, 2008. **29**(1): p. 111-117.
218. Grace, A.N. and K. Pandian, *Antibacterial efficacy of aminoglycosidic antibiotics protected gold nanoparticles - A brief study*. Colloids and Surfaces a-Physicochemical and Engineering Aspects, 2007. **297**(1-3): p. 63-70.
219. Colvin, V.L., *The potential environmental impact of engineered nanomaterials*. Nat Biotech, 2003. **21**(10): p. 1166-1170.
220. Maynard, A.D., et al., *Safe handling of nanotechnology*. Nature, 2006. **444**(7117): p. 267-269.
221. Nel, A., et al., *Toxic potential of materials at the nanolevel*. Science, 2006. **311**(5761): p. 622-627.
222. Helmus, M.N., *The need for rules and regulations*. Nat Nano, 2007. **2**(6): p. 333-334.
223. Fratoddi, I., Venditti, I., Cametti, C., Russo, M. V., , *How toxic are gold nanoparticles? The state-of-the-art*. Nano Research, 2015. **8**(6): p. 1771–1799.

224. Connor, E.E., Mwamuka, J., Gole, A., Murphy, C.J., Wyatt, M.D., *Gold nanoparticles are taken up by human cells but do not cause acute cytotoxicity*. *Small*, 2005. **1**(3): p. 325–327.
225. Villiers, C., et al., *Analysis of the toxicity of gold nano particles on the immune system: effect on dendritic cell functions*. *Journal of Nanoparticle Research*, 2010. **12**(1): p. 55-60.
226. Goodman, C.M., et al., *Toxicity of Gold Nanoparticles Functionalized with Cationic and Anionic Side Chains*. *Bioconjugate Chemistry*, 2004. **15**(4): p. 897-900.
227. Pan, Y., et al., *Gold nanoparticles of diameter 1.4 nm trigger necrosis by oxidative stress and mitochondrial damage*. *Small*, 2009. **5**(18): p. 2067-2076.
228. Shukla, R., et al., *Biocompatibility of Gold Nanoparticles and Their Endocytotic Fate Inside the Cellular Compartment: A Microscopic Overview*. *Langmuir*, 2005. **21**(23): p. 10644-10654.
229. Figueroa, D., *Potential of gold nanoparticles as drug delivery vehicles for breast cancer treatment*, in *Medical Biotechnology Department 2014*, Flinders University:
<http://trove.nla.gov.au/work/192581029?q&versionId=210661902>. p. 112.
230. Chuang, S.-M., et al., *Extensive evaluations of the cytotoxic effects of gold nanoparticles*. *Biochimica et Biophysica Acta (BBA)-General Subjects*, 2013. **1830**(10): p. 4960-4973.
231. Chen, Y.-S., et al., *Assessment of the In Vivo Toxicity of Gold Nanoparticles*. *Nanoscale Research Letters*, 2009. **4**(8): p. 858-864.
232. Bar-Ilan, O., et al., *Toxicity assessments of multisized gold and silver nanoparticles in zebrafish embryos*. *Small*, 2009. **5**(16): p. 1897-1910.
233. Ndolo, R.A., et al., *Intracellular distribution-based anticancer drug targeting: Exploiting a lysosomal acidification defect associated with cancer cells*. *Molecular and cellular pharmacology*, 2010. **2**(4): p. 131.
234. GM., C., *The cell: a molecular approach*, 2000, Sunderland (MA): Sinauer Associates.
235. Becker, W.M., Kleinsmith, L., Hardin, J., Bertoni, G., *The world of the cell*, 2009, Pearson/Benjamin Cummings. p. 912.

236. Iversen, T.-G., T. Skotland, and K. Sandvig, *Endocytosis and intracellular transport of nanoparticles: Present knowledge and need for future studies*. Nano Today, 2011. **6**(2): p. 176-185.
237. Battey, N.H., James, N.C., Greenland, A.J., Brownlee, C., *Exocytosis and endocytosis*. The Plant Cell, 1999. **11**: p. 643-659.
238. Oh, N. and J.-H. Park, *Endocytosis and exocytosis of nanoparticles in mammalian cells*. Int J Nanomedicine, 2014. **9**(Suppl 1): p. 51-63.
239. Brandenberger, C., et al., *Quantitative Evaluation of Cellular Uptake and Trafficking of Plain and Polyethylene Glycol-Coated Gold Nanoparticles*. Small, 2010. **6**(15): p. 1669-1678.
240. Mayor, S. and R.E. Pagano, *Pathways of clathrin-independent endocytosis*. Nature reviews Molecular cell biology, 2007. **8**(8): p. 603-612.
241. Conner, S.D. and S.L. Schmid, *Regulated portals of entry into the cell*. Nature, 2003. **422**(6927): p. 37-44.
242. Perrais, D. and C.J. Merrifield, *Dynamics of Endocytic Vesicle Creation*. Developmental Cell, 2005. **9**(5): p. 581-592.
243. Huotari, J. and A. Helenius, *Endosome maturation*. The EMBO Journal, 2011. **30**(17): p. 3481-3500.
244. Bogart, L.K., et al., *Nanoparticles for Imaging, Sensing, and Therapeutic Intervention*. ACS Nano, 2014. **8**(4): p. 3107-3122.
245. Gilleron, J., et al., *Image-based analysis of lipid nanoparticle-mediated siRNA delivery, intracellular trafficking and endosomal escape*. Nat Biotech, 2013. **31**(7): p. 638-646.
246. Dykman, L.A. and N.G. Khlebtsov, *Uptake of Engineered Gold Nanoparticles into Mammalian Cells*. Chemical Reviews, 2014. **114**(2): p. 1258-1288.
247. Chithrani, B.D., A.A. Ghazani, and W.C.W. Chan, *Determining the Size and Shape Dependence of Gold Nanoparticle Uptake into Mammalian Cells*. Nano Letters, 2006. **6**(4): p. 662-668.
248. Trono, J.D., et al., *Size, concentration and Incubation time dependence of gold nanoparticle uptake into pancreas cancer cells and its future application to X-ray drug delivery system*. Journal of Radiation Research, 2011. **52**(1): p. 103-109.

249. Schaeublin, N.M., et al., *Does Shape Matter? Bioeffects of Gold Nanomaterials in a Human Skin Cell Model*. Langmuir, 2012. **28**(6): p. 3248-3258.
250. Hutter, E., et al., *Microglial Response to Gold Nanoparticles*. ACS Nano, 2010. **4**(5): p. 2595-2606.
251. Hinde, E., et al., *Pair correlation microscopy reveals the role of nanoparticle shape in intracellular transport and site of drug release*. Nat Nano, 2016. **advance online publication**.
252. Scott, G.B., H.S. Williams, and P.M. Marriott, *The phagocytosis of colloidal particles of different sizes*. British Journal of Experimental Pathology, 1967. **48**(4): p. 411-416.
253. Hardonk, M.J., G. Harms, and J. Koudstaal, *Zonal heterogeneity of rat hepatocytes in the in vivo uptake of 17 nm colloidal gold granules*. Histochemistry. **83**(5): p. 473-477.
254. Sadauskas, E., et al., *Kupffer cells are central in the removal of nanoparticles from the organism*. Particle and Fibre Toxicology, 2007. **4**(1): p. 1-7.
255. Sadauskas, E., et al., *Protracted elimination of gold nanoparticles from mouse liver*. Nanomedicine: Nanotechnology, Biology and Medicine, 2009. **5**(2): p. 162-169.
256. Chithrani, B.D. and W.C.W. Chan, *Elucidating the Mechanism of Cellular Uptake and Removal of Protein-Coated Gold Nanoparticles of Different Sizes and Shapes*. Nano Letters, 2007. **7**(6): p. 1542-1550.
257. Fei, X. and Y. Gu, *Progress in modifications and applications of fluorescent dye probe*. Progress in Natural Science, 2009. **19**(1): p. 1-7.
258. Levy, R., et al., *Gold nanoparticles delivery in mammalian live cells: a critical review*. Nano reviews, 2010. **1**.
259. Landgraf, L., et al., *Comparative evaluation of the impact on endothelial cells induced by different nanoparticle structures and functionalization*. Beilstein journal of nanotechnology, 2015. **6**(1): p. 300-312.
260. Arvizo, R.R., et al., *Effect of Nanoparticle Surface Charge at the Plasma Membrane and Beyond*. Nano Letters, 2010. **10**(7): p. 2543-2548.
261. Gonciar, A., *Detection of intracellular gold nanoparticles*. Biotechnology, Molecular Biology and Nanomedicine, 2014. **2**(1): p. 21-25.

262. Han, G., P. Ghosh, and V.M. Rotello, *Functionalized gold nanoparticles for drug delivery*. 2007.
263. Sée, V., et al., *Cathepsin L Digestion of Nanobioconjugates upon Endocytosis*. ACS Nano, 2009. **3**(9): p. 2461-2468.
264. Fu, W., et al., *Biomedical applications of gold nanoparticles functionalized using hetero-bifunctional poly (ethylene glycol) spacer*, 2005, DTIC Document.
265. Fan, C.H., et al., *Beyond superquenching: Hyper-efficient energy transfer from conjugated polymers to gold nanoparticles*. Proceedings of the National Academy of Sciences of the United States of America, 2003. **100**(11): p. 6297-6301.
266. Jana, N.R., *Design and development of quantum dots and other nanoparticles based cellular imaging probe*. Physical Chemistry Chemical Physics, 2011. **13**(2): p. 385-396.
267. Arruebo, M., M. Valladares, and Á. González-Fernández, *Antibody-Conjugated Nanoparticles for Biomedical Applications*. Journal of Nanomaterials, 2009. **2009**: p. 24.
268. Arruebo, M., M. Valladares, and A. Gonzalez-Fernandez, *Antibody-Conjugated Nanoparticles for Biomedical Applications*. Journal of Nanomaterials, 2009.
269. Cohen, S., *Antibody structure*. J. clin. Path., 1975. **28**(6): p. 1-7.
270. Hermanson, G.T., *Chapter 20 - Antibody Modification and Conjugation*, in *Bioconjugate Techniques (Third edition)*. 2013, Academic Press: Boston. p. 867-920.
271. Burton, D.R., L. Gregory, and R. Jefferis, *Aspects of the molecular-structure of IGG Subclasses* Monographs in Allergy, 1986. **19**: p. 7-35.
272. Alberts, B., Johnson, A., Lewis, J., Raff, M., Roberts, K., Walter, P., *Molecular Biology of the Cell*, in *B Cells and Antibodies*, B. Alberts, Johnson, A., Lewis, J., Raff, M., Roberts, K., Walter, P., Editor 2002, Garland Science: New York.
273. Carter, P., L. Smith, and M. Ryan, *Identification and validation of cell surface antigens for antibody targeting in oncology*. Endocrine-related cancer, 2004. **11**(4): p. 659-687.

274. Ranade, V.V., *Drug Delivery Systems—2. Site-Specific Drug Delivery Utilizing Monoclonal Antibodies*. The Journal of Clinical Pharmacology, 1989. **29**(10): p. 873-884.
275. Scott, A.M., J.P. Allison, and J.D. Wolchok, *Monoclonal antibodies in cancer therapy*. Cancer Immunity, 2012. **12**: p. 14.
276. Jain, R.K., *Transport of molecules in the tumor interstitium: a review*. Cancer Res, 1987. **47**(12): p. 3039-51.
277. *Hematology/oncology (cancer) approvals & safety notifications*. 2016 [cited 2016 22-11-2016].
278. *Immunotherapy approvals in 2015*. <http://www.cancerresearch.org/news-publications/our-blog/december-2015/immunotherapy-approvals-in-2015> 2016 [cited 2016 22-11-2016].
279. Bhattacharyya, S., et al., *Nanoconjugation modulates the trafficking and mechanism of antibody induced receptor endocytosis*. Proceedings of the National Academy of Sciences of the United States of America, 2010. **107**(33): p. 14541-14546.
280. Reichert, J.M., *Antibodies to watch in 2016*. MAbs, 2016. **8**(2): p. 197-204.
281. Scott, A.M., J.D. Wolchok, and L.J. Old, *Antibody therapy of cancer*. Nature Reviews Cancer, 2012. **12**(4): p. 278-287.
282. Du, B.A., Z.P. Li, and Y.Q. Cheng, *Homogeneous immunoassay based on aggregation of antibody-functionalized gold nanoparticles coupled with light scattering detection*. Talanta, 2008. **75**(4): p. 959-964.
283. Ijeh, M., *Covalent gold nanoparticle—antibody conjugates for sensitivity improvement in LFIA*, 2011, Hamburg University.
284. Varshney, M., et al., *Magnetic nanoparticle-antibody conjugates for the separation of Escherichia coli O157 : H7 in ground beef*. Journal of Food Protection, 2005. **68**(9): p. 1804-1811.
285. Wartlick, H., et al., *Highly specific HER2-mediated cellular uptake of antibody-modified nanoparticles in tumour cells*. Journal of Drug Targeting, 2004. **12**(7): p. 461-471.
286. Dinauer, N., et al., *Selective targeting of antibody-conjugated nanoparticles to leukemic cells and primary T-lymphocytes*. Biomaterials, 2005. **26**(29): p. 5898-5906.

287. Di Pasqua, A.J., et al., *Preparation of antibody-conjugated gold nanoparticles*. Materials Letters, 2009. **63**(21): p. 1876-1879.
288. Selvaraj, V. and M. Alagar, *Analytical detection and biological assay of antileukemic drug 5-fluorouracil using gold nanoparticles as probe*. Int J Pharm, 2007. **337**(1-2): p. 275-81.
289. Gupta, B. and V.P. Torchilin, *Monoclonal antibody 2C5-modified doxorubicin-loaded liposomes with significantly enhanced therapeutic activity against intracranial human brain U-87 MG tumor xenografts in nude mice*. Cancer Immunology Immunotherapy, 2007. **56**(8): p. 1215-1223.
290. Kou, G., et al., *Preparation and characterization of paclitaxel-loaded PLGA nanoparticles coated with cationic SM5-1 single-chain antibody*. BMB Reports, 2007. **40**(5): p. 731-739.
291. Tyner, K.M., S.R. Schiffman, and E.P. Giannelis, *Nanobiohybrids as delivery vehicles for camptothecin*. Journal of Controlled Release, 2004. **95**(3): p. 501-514.
292. Eck, W., et al., *PEGylated gold nanoparticles conjugated to monoclonal F19 antibodies as targeted labeling agents for human pancreatic carcinoma tissue*. Acs Nano, 2008. **2**(11): p. 2263-2272.
293. Turkevich J, S.P., Hillier J., *A study of the nucleation and growth processes in the synthesis of colloidal gold*. Discussions of the Faraday Society., 1951. **11**(0): p. 55-75.
294. Grabar KC, F.R., Hommer MB, Natan MJ, *Preparation and characterization of Au colloid monolayers*. Analytical Chemistry 1995. **67**(4).
295. Haiss, W., et al., *Determination of size and concentration of gold nanoparticles from UV-Vis spectra*. Analytical Chemistry, 2007. **79**(11): p. 4215-4221.
296. Lin, S.Y., et al., *Two-step functionalization of neutral and positively charged thiols onto citrate-stabilized Au nanoparticles*. Journal of Physical Chemistry B, 2004. **108**(7): p. 2134-2139.
297. Schmid, F.X., *Biological macromolecules: UV-visible spectrophotometry*. Encyclopedia of Life Sciences, 2001: p. 1- 4.
298. Perkampus, H.-H., H.-C. Grinter, and T. Threlfall, *UV-VIS spectroscopy and its applications*. 1992: Springer.

299. Aldrich, S.-. *Gold Nanoparticles: Properties and Applications*. <http://www.sigmaaldrich.com/materials-science/nanomaterials/gold-nanoparticles.html> [2014 15-10-2014].
300. Musib, R., et al., *Effect of Polymerization on the Subdomain 3/4 Loop of Yeast Actin*. *Journal of Biological Chemistry*, 2002. **277**(25): p. 22699-22709.
301. Chemicals, A., *Kodak optical products*, Ajax Chemicals Australian Distributors: New York. p. 44-45.
302. Albani, J.R., et al., *Interaction between carbohydrate residues of α 1-acid glycoprotein (orosomucoid) and saturating concentrations of Calcofluor White. A fluorescence study*. *Carbohydrate Research*, 2000. **327**(3): p. 333-340.
303. Albani, J.R., *Effect of binding of Calcofluor White on the carbohydrate residues of α 1-acid glycoprotein (orosomucoid) on the structure and dynamics of the protein moiety. A fluorescence study*. *Carbohydrate Research*, 2001. **334**(2): p. 141-151.
304. Yildiz, I., et al., *Infusion of imaging and therapeutic molecules into the plant virus-based carrier cowpea mosaic virus: cargo-loading and delivery*. *Journal of controlled release : official journal of the Controlled Release Society*, 2013. **172**(2): p. 10.1016/j.jconrel.2013.04.023.
305. Green, H., et al., *Measurement of paclitaxel and its metabolites in human plasma using liquid chromatography/ion trap mass spectrometry with a sonic spray ionization interface*. *Rapid Communications in Mass Spectrometry*, 2006. **20**(14): p. 2183-2189.
306. Ma, H., Shieh, K. J., Qiao, T. X., *Study of transmission electron microscopy (TEM) and scanning electron microscopy (SEM)*. *Nature and Science*, 2006. **4**(3): p. 14-22.
307. Jin, L., et al., *Applications of direct detection device in transmission electron microscopy*. *Journal of Structural Biology*, 2008. **161**(3): p. 352-358.
308. Li, Z.M., et al., *The measurement system of nanoparticle size distribution from dynamic light scattering data*. *Optics and Lasers in Engineering*, 2014. **56**: p. 94-98.
309. Ahmed, E.A., Abdel Hafez, E. H., Ismail, A. F. M, Elsonbaty, S. M., Abbas, H. S., Salah El Din, R. A., *Biosynthesis of silver nanoparticles by spirulina*

- platensis* & *nostoc* sp. Global Advanced Research Journal of Microbiology, 2015. **4**(4): p. 36-49.
310. Barth, A., *Infrared spectroscopy of proteins*. Elsevier B.V.: Biochimica et Biophysica Acta, 2007. **1767**: p. 1073–1101.
311. Bobby, M.N.E., W.; Johnson, M., *FT-IR studies on the leaves of albizia lebbek benth*. International Journal of Pharmacy and Pharmaceutical Sciences 2012. **4**(3): p. 293-296.
312. Liotta, L.J.J.-P., M., *Identification of an unknown compound by combined use of IR, 1H NMR, 13C NMR, and mass spectrometry: a real-life experience in structure determination*. J. Chem. Educ, 2008. **85**(6): p. 832- 833.
313. Gerothanassis, I.P.T., A.; Exarchou, V.; Barbarossou, K., *Nuclear magnetic resonance (NMR) spectroscopy: basic principles and phenomena, and their applications to chemistry*. biology and medicine, , Chemistry Education Research and Practice 2002. **3**(2): p. 229-252.
314. Liu, X., et al., *Determination of monolayer-protected gold nanoparticle ligand-shell morphology using NMR*. Nature Communications, 2012. **3**.
315. Liu, Y. and B. Yan, *Characterizing the Surface Chemistry of Nanoparticles: An Analogy to Solid-Phase Synthesis Samples*. Combinatorial Chemistry & High Throughput Screening, 2011. **14**(3): p. 191-197.
316. Harvey, D., *Modern analytical chemistry*. Vol. 798. 2000: McGraw-Hill New York.
317. Zurek-Biesiada, D., S. Kedracka-Krok, and J.W. Dobrucki, *UV-activated conversion of Hoechst 33258, DAPI, and Vybrant DyeCycle fluorescent dyes into blue-excited, green-emitting protonated forms*. Cytometry Part A, 2013. **83A**(5): p. 441-451.
318. Kang, J.M. and N.Y. Cheong, *Nitrobenzene functionalized hexahomotrioxacalix 3 arene*. Bulletin of the Korean Chemical Society, 2002. **23**(7): p. 995-997.
319. Hussain, M., et al., *Synthesis of novel stilbene-alkoxysilane fluorescent brighteners, and their performance on cotton fiber as fluorescent brightening and ultraviolet absorbing agents*. Dyes and Pigments, 2012. **92**(3): p. 1231-1240.
320. Kristoffersen, A.S., et al., *Testing Fluorescence Lifetime Standards using Two-Photon Excitation and Time-Domain Instrumentation: Rhodamine B*,

- Coumarin 6 and Lucifer Yellow*. Journal of Fluorescence, 2014. **24**(4): p. 1015-1024.
321. Dey, V.R.N., *The Basics of Confocal Microscopy*.
322. Paddock, S.W., *Confocal laser scanning microscopy*. Biotechniques, 1999. **27**: p. 992-1007.
323. Westrøm, S., *Cellular interaction with polymeric nanoparticles: the effect of PEGylation and monomer composition*, in *Department of Physics 2013*, Norwegian University of Science and Technology.
324. Pawley, J. and B.R. Masters, *Handbook of biological confocal microscopy*. Optical Engineering, 1996. **35**(9): p. 2765-2766.
325. Murphy, D.B., *Fundamentals of light microscopy and electronic imaging*. 2002: John Wiley & Sons.
326. PECON®. *POC cell cultivation system*. 2012 [cited 1026 28-04-2016].
327. Alkilany, A.M., A.I.B. Yaseen, and M.H. Kailani, *Synthesis of Monodispersed Gold Nanoparticles with Exceptional Colloidal Stability with Grafted Polyethylene Glycol-g-polyvinyl Alcohol*. Journal of Nanomaterials, 2015.
328. Zhu, T., et al., *Surface modification of citrate-reduced colloidal gold nanoparticles with 2-mercaptop succinic acid*. Langmuir, 2003. **19**(22): p. 9518-9525.
329. Mikhlin, Y., et al., *Submicrometer intermediates in the citrate synthesis of gold nanoparticles: New insights into the nucleation and crystal growth mechanisms*. Journal of Colloid and Interface Science, 2011. **362**(2): p. 330-336.
330. Kumar, S., K.S. Gandhi, and R. Kumar, *Modeling of formation of gold nanoparticles by citrate method*. Industrial & Engineering Chemistry Research, 2007. **46**(10): p. 3128-3136.
331. Ojea-Jimenez, I., et al., *Small Gold Nanoparticles Synthesized with Sodium Citrate and Heavy Water: Insights into the Reaction Mechanism*. Journal of Physical Chemistry C, 2010. **114**(4): p. 1800-1804.
332. Akkas, S., et al., *Effects of lipoic acid supplementation on rat brain tissue: An FTIR spectroscopic and neural network study*. Food chemistry, 2007. **105**(3): p. 1281-1288.
333. Volkert, A.A., et al., *Salt-Mediated Self-Assembly of Thiocetic Acid on Gold Nanoparticles*. ACS Nano, 2011. **5**(6): p. 4570-4580.

334. Abdelhalim, M.A.K., M.M. Mady, and M.M. Ghannam, *Physical properties of different gold nanoparticles: ultraviolet-visible and fluorescence measurements*. J Nanomed Nanotechol, 2012. **3**(133): p. 2.
335. Jiang W., K.B.Y.S., Rutka J.T., Chan W.C.W., *Nanoparticle-medicated cellular response is size-dependent*. nature nanotechnology, 2008. **3**(0): p. 145-150.
336. Naill, M.C., M.E. Kolewe, and S.C. Roberts, *Paclitaxel uptake and transport in Taxus cell suspension cultures*. Biochemical engineering journal, 2012. **63**: p. 50-56.
337. Worldwide, M.I. *Dynamic light scattering common terms defined*. 2011 [cited 2016 6-04-2016]; 6].
338. Worldwide, M.I., *Dynamic light scattering common terms defined*. 2011: p. 1-6.
339. Tomaszewska, E., et al., *Detection Limits of DLS and UV-Vis Spectroscopy in Characterization of Polydisperse Nanoparticles Colloids*. Journal of Nanomaterials, 2013. **2013**: p. 10.
340. Thottoli, A. and A. Unni, *Effect of trisodium citrate concentration on the particle growth of ZnS nanoparticles*. Journal of Nanostructure in Chemistry, 2013. **3**(1): p. 1-12.
341. Park, J.-W. and J.S. Shumaker-Parry, *Structural study of citrate layers on gold nanoparticles: role of intermolecular interactions in stabilizing nanoparticles*. Journal of the American Chemical Society, 2014. **136**(5): p. 1907-1921.
342. Gasiorek, F., et al., *Effects of multivalent histamine supported on gold nanoparticles: activation of histamine receptors by derivatized histamine at subnanomolar concentrations*. Organic & Biomolecular Chemistry, 2015. **13**(39): p. 9984-9992.
343. Akkas, S.B., et al., *Effects of lipoic acid supplementation on rat brain tissue: An FTIR spectroscopic and neural network study*. Food Chemistry, 2007. **105**(3): p. 1281-1288.
344. Zhang, J., L. Dang, and H. Wei, *Thermodynamic analysis of lipoic acid crystallized with additives*. Journal of Thermal Analysis and Calorimetry, 2013. **111**(3): p. 2063-2068.

345. Deregowska, A.D., J.; Wojnarowska, R.; Polit, J.; Broda, D.; Nechai, H.; Gonchar, M.; Sheregii, E., *Study of optical properties of a glutathione capped gold nanoparticles using linker (MHDA) by fourier transform infrared spectroscopy and surface enhanced Raman scattering*. International Journal of Physical, Natural Science and Engineering, 2013. **7**(1): p. 47-50.
346. Mandal, T.K., M.S. Fleming, and D.R. Walt, *Preparation of Polymer Coated Gold Nanoparticles by Surface-Confined Living Radical Polymerization at Ambient Temperature*. Nano Letters, 2002. **2**(1): p. 3-7.
347. Di Pasqua, A.J., et al., *Preparation of antibody-conjugated gold nanoparticles*. Materials Letters, 2009. **63**(21): p. 1876-1879.
348. Ding, Y., et al., *The performance of thiol-terminated PEG-paclitaxel-conjugated gold nanoparticles*. Biomaterials, 2013. **34**(38): p. 10217-10227.
349. Garex, S.A. and A. Ghebaour, *FT-IR Spectroscopy and Thermogravimetric Characterization of Prodrugs Based on Different Dendritic Polymers and Antitumoral Drug*. Materiale Plastice, 2012. **49**(1): p. 1-4.
350. Doyen, M., K. Bartik, and G. Bruylants, *UV-Vis and NMR study of the formation of gold nanoparticles by citrate reduction: Observation of gold-citrate aggregates*. Journal of Colloid and Interface Science, 2013. **399**: p. 1-5.
351. Hostetler, M.J., et al., *Alkanethiolate gold cluster molecules with core diameters from 1.5 to 5.2 nm: Core and monolayer properties as a function of core size*. Langmuir, 1998. **14**(1): p. 17-30.
352. Ristig, S., et al., *An easy synthesis of autofluorescent alloyed silver-gold nanoparticles*. Journal of Materials Chemistry B, 2014. **2**(45): p. 7887-7895.
353. Badia, A., et al., *Structure and chain dynamics of alkanethiol-capped gold colloids*. Langmuir, 1996. **12**(5): p. 1262-1269.
354. Chen, J.Z., S.V. Ranade, and X.Q. Xie, *NMR characterization of paclitaxel/poly (styrene-isobutylene-styrene) formulations*. International Journal of Pharmaceutics, 2005. **305**(1-2): p. 129-144.
355. Chmurny, G.N., et al., *H-1-NMR AND C-13-NMR ASSIGNMENTS FOR TAXOL, 7-EPI-TAXOL, AND CEPHALOMANNINE*. Journal of Natural Products, 1992. **55**(4): p. 414-423.

356. Gangadevi, V., M. Murugan, and J. Muthumary, *Taxol Determination from Pestalotiopsis pauciseta, a Fungal Endophyte of a Medicinal Plant*. Chinese Journal of Biotechnology, 2008. **24**(8): p. 1433-1438.
357. Joshi, P., et al., *The anticancer activity of chloroquine-gold nanoparticles against MCF-7 breast cancer cells*. Colloids and Surfaces B: Biointerfaces, 2012. **95**: p. 195-200.
358. Everaerts, F., et al., *Biomechanical properties of carbodiimide crosslinked collagen: influence of the formation of ester crosslinks*. Journal of Biomedical Materials Research Part A, 2008. **85**(2): p. 547-555.
359. Ganesh, T., *Improved biochemical strategies for targeted delivery of taxoids*. Bioorganic & medicinal chemistry, 2007. **15**(11): p. 3597-3623.
360. Hwu, J.R., et al., *Targeted Paclitaxel by Conjugation to Iron Oxide and Gold Nanoparticles*. Journal of the American Chemical Society, 2009. **131**(1): p. 66-68.
361. Sanz, V., et al., *Effect of PEG biofunctional spacers and TAT peptide on dsRNA loading on gold nanoparticles*. Journal of Nanoparticle Research, 2012. **14**(6): p. 1-9.
362. Rudershausen, S., et al., *Multifunctional superparamagnetic nanoparticles for life science applications*. European Cells and Materials, 2002. **3**(supplement 2): p. 81-83.
363. Bartczak, D. and A.G. Kanaras, *Preparation of peptide-functionalized gold nanoparticles using one pot EDC/sulfo-NHS coupling*. Langmuir, 2011. **27**(16): p. 10119-10123.
364. Mojarradi, H., *Coupling of substances containing a primary amine to hyaluronan via carbodiimide-mediated amidation*, 2010: Uppsala University, Disciplinary Domain of Science and Technology, Chemistry, Department of Biochemistry and Organic Chemistry. p. 44.
365. Vukovic, V. and I. Tannock, *Influence of low pH on cytotoxicity of paclitaxel, mitoxantrone and topotecan*. British journal of cancer, 1997. **75**(8): p. 1167.
366. Gerweck, L.E. and K. Seetharaman, *Cellular pH gradient in tumor versus normal tissue: potential exploitation for the treatment of cancer*. Cancer research, 1996. **56**(6): p. 1194-1198.

367. Gao, A., et al., *Facile spectrophotometric assay of molar equivalents of N-hydroxysuccinimide esters of monomethoxyl poly-(ethylene glycol) derivatives*. Chemistry Central Journal, 2012. **6**: p. 142-142.
368. Devi, T.R. and S. Gayathri, *FTIR and FT-Raman spectral analysis of paclitaxel drugs*. International Journal of Pharmaceutical Sciences Review and Research, 2010. **2**(2): p. 106-110.
369. Kapuscinski, J., *DAPI - a DNA- specific fluorescent- probe*. Biotechnic & Histochemistry, 1995. **70**(5): p. 220-233.
370. Degtyareva, N.N., et al., *Hydration changes accompanying the binding of minor groove ligands with DNA*. Biophysical Journal, 2007. **92**(3): p. 959-965.
371. Zink, D., N. Sadoni, and E. Stelzer, *Visualizing chromatin and chromosomes in living cells*. Methods, 2003. **29**(1): p. 42-50.
372. Yang, X., et al., *The preparation of functionalized graphene oxide for targeted intracellular delivery of siRNA*. Journal of Materials Chemistry, 2012. **22**(14): p. 6649-6654.
373. Lodeiro, C., et al., *Intramolecular excimer formation and sensing behavior of new fluorimetric probes and their interactions with metal cations and barbituric acids*. Sensors and Actuators B: Chemical, 2006. **115**(1): p. 276-286.
374. Zollinger, H., *Color chemistry: synthesis, properties and applications of organic dyes and pigments*, 1991, VCH Publishers Inc.: New York. p. 496.
375. Davey, H.M. and D.B. Kell, *Fluorescent brighteners: novel stains for the flow cytometric analysis of microorganisms*. Cytometry, 1997. **28**(4): p. 311-315.
376. Darken, M.A., *Applications of fluorescent brighteners in biological techniques*. Science, 1961. **133**(3465): p. 1704-1705.
377. Allen, E.A., et al., *Influence of leaf surface features on spore deposition and the epiphytic growth of phytopathogenic fungi*, in *Microbial ecology of leaves*. 1991, Springer. p. 87-110.
378. Apoga, D. and H.-B. Jansson, *Visualization and characterization of the extracellular matrix of Bipolaris sorokiniana*. Mycological Research, 2000. **104**(5): p. 564-575.

379. Beija, M., C.A.M. Afonso, and J.M.G. Martinho, *Synthesis and applications of Rhodamine derivatives as fluorescent probes*. Chemical Society Reviews, 2009. **38**(8): p. 2410-2433.
380. Drexhage, K., *Fluorescence efficiency of laser dyes*. 1977.
381. Farinha, J., et al., *Picosecond fluorescence studies of the surface morphology of charged polystyrene latex particles*. Langmuir, 2001. **17**(9): p. 2617-2623.
382. Nicolas, J., et al., *Fluorescently tagged polymer bioconjugates from protein derived macroinitiators*. Chemical Communications, 2006(45): p. 4697-4699.
383. Zhou, Z., et al., *FRET-based sensor for imaging chromium(iii) in living cells*. Chemical Communications, 2008(29): p. 3387-3389.
384. Jaworska, A., et al., *Rhodamine 6G conjugated to gold nanoparticles as labels for both SERS and fluorescence studies on live endothelial cells*. Mikrochimica Acta, 2015. **182**: p. 119-127.
385. Jung, K.S., Kim, M.,S., Lee, GJ, Cho, TS, Kim, S.K., Yi, S.Y. , *Conformation of single stranded poly(dA) and its interaction with 4',6-diamidino-2-phenylindole*. Bull. Korean Chem. Soc., 1997. **18**(05): p. 510-514.
386. Kapuściński, J. and W. Szer, *Interactions of 4', 6-diamidine-2-phenylindole with synthetic polynucleotides*. Nucleic Acids Research, 1979. **6**(11): p. 3519-3534.
387. Ou, Y.-Y. and M.H. Huang, *High-Density Assembly of Gold Nanoparticles on Multiwalled Carbon Nanotubes Using 1-Pyrenemethylamine as Interlinker*. The Journal of Physical Chemistry B, 2006. **110**(5): p. 2031-2036.
388. Ding, S.-N., et al., *Electrochemical fabrication of novel fluorescent polymeric film: Poly(pyrrole-pyrene)*. Electrochemistry Communications, 2008. **10**(10): p. 1423-1426.
389. Praharaj, S., et al., *Size-Selective Synthesis and Stabilization of Gold Organosol in CnTAC: Enhanced Molecular Fluorescence from Gold-Bound Fluorophores*. The Journal of Physical Chemistry B, 2005. **109**(27): p. 13166-13174.
390. Yejun, Q., et al., *Synthesis of continuous boron nitride nanofibers by solution coating electrospun template fibers*. Nanotechnology, 2009. **20**(34): p. 345603.

391. Jao, M., Liao, M., Huang, C., Cheng, C., Chou, S. , *Studies on analytical method for determination of fluorescent whitening agents in paper containers for food*. Journal of Food and Drug Analysis 1999. **7**(1): p. 53-63.
392. Windsor, S.A., Harrison, N.J., Tinker, M.H., *Electro-fluorescence studies of the binding of fluorescent dyes to sepiolite* Clay Minerals, 1996. **31**: p. 81-94.
393. Pokhrel, M.R. and S.H. Bossmann, *Synthesis and characterization of poly (NIPAM-co-AA) polymers possessing perfluorinated side chains and chemically linked pyrene labels*. Journal of Nepal Chemical Society, 2012. **27**(1): p. 67-73.
394. Hashidzume, A., Y. Zheng, and A. Harada, *Interaction of cyclodextrins with pyrene-modified polyacrylamide in a mixed solvent of water and dimethyl sulfoxide as studied by steady-state fluorescence*. Beilstein Journal of Organic Chemistry, 2012. **8**: p. 1312-1317.
395. Garidel, P. and H. Schott, *Fourier-transform midinfrared spectroscopy for analysis and screening of liquid protein formulations*. BioProcess International, 2006. **48**.
396. Coates, J., *Interpretation of infrared spectra, a practical approach*. Encyclopedia of analytical chemistry, 2000.
397. Fontinha, I.R., et al., *EIS Study of Amine Cured Epoxy-silica-zirconia Sol-gel Coatings for Corrosion Protection of the Aluminium Alloy EN AW 6063*. Portugaliae Electrochimica Acta, 2013. **31**: p. 307-319.
398. Hansen, P.E. and A. Berg, *Infrared-spectra of pyrene derivatives-relation to the substitution pattern* Acta Chemica Scandinavica Series B-Organic Chemistry and Biochemistry, 1981. **35**(2): p. 131-137.
399. Guo, X.-X., et al., *Rapid analysis and quantification of fluorescent brighteners in wheat flour by Tri-step infrared spectroscopy and computer vision technology*. Journal of Molecular Structure, 2015. **1099**: p. 393-398.
400. Carpenter, J.S., Bai, C., Hwang, J-Y., Ikhmayies, S., Li, B., Monteiro, S. N., Peng, Z., Zhang, M., *Characterization of minerals, metals, and materials 2014*. 2014: Technology & Engineering. 680 pages.
401. Yu, G., et al., *Highly thermostable rigid-rod networks constructed from an unsymmetrical bisphthalonitrile bearing phthalazinone moieties*. Polymer Chemistry, 2012. **3**(4): p. 1024-1032.

402. Murthy, M. *Proton Conducting Membrane Fuel Cells III: Proceedings of the International Symposium*. 2005. The Electrochemical Society.
403. Trotta, E., et al., *¹H NMR study of [d(GCGATCGC)]₂ and its interaction with minor groove binding 4',6-diamidino-2-phenylindole*. J Biol Chem, 1993. **268**(6): p. 3944-51.
404. Trotta, E., et al., *Evidence for DAPI intercalation in CG sites of DNA oligomer [d(CGACGTCG)]₂: a ¹H NMR study*. Nucleic Acids Res, 1995. **23**(8): p. 1333-40.
405. Ossipov, D.A., et al., *Modular approach to functional hyaluronic acid hydrogels using orthogonal chemical reactions*. Chemical Communications, 2010. **46**(44): p. 8368-8370.
406. Okuom, M., et al., *Synthesis of a Fluorophore with Improved Optical Brightness*. International journal of organic chemistry, 2013. **3**(4): p. 256-261.
407. Platzer, G., Okon, M., McIntosh, L., *pH-dependent random coil ¹H, ¹³C, and ¹⁵N chemical shifts of the ionizable amino acids: a guide for protein pKa measurements*. J Biomol NMR, 2014. **60**: p. 109–129.
408. Trotta, E., et al., *Simultaneous and different binding mechanisms of 4',6-diamidino-2-phenylindole to DNA hexamer (d(CGATCG))₂*. Journal of Biological Chemistry, 1996. **271**(44): p. 27608-27614.
409. Kodak optical products, A. Chemicals, Editor: Australia
410. Ali, R.A., Abdul-Munem, O.M., Abd, A.N., *Study the spectroscopic characteristics of rhodamine b dye in ethanol and methanol mixture and calculation the quantum efficiency*. Baghdad Science Journal, 2012. **9**(2): p. 352-358.
411. Messenger, T.N., *Development and Characterization of a Multi-angle Dual Beam Thermal Lens Spectroscopy System*. 2008: ProQuest.
412. LI, J.-y., P.-x. LEI, and J.-c. ZHAO, *Detection of intermediates in the TiO₂-assisted photodegradation of Rhodamine B under visible light irradiation*. Journal of Environmental Sciences, 2007. **19**(7): p. 892-896.
413. Liu, G. and J. Zhao, *Photocatalytic degradation of dye sulforhodamine B: a comparative study of photocatalysis with photosensitization*. New Journal of Chemistry, 2000. **24**(6): p. 411-417.

414. Dukali, R.M., et al., *Electrospinning of laser dye Rhodamine B-doped poly (methyl methacrylate) nanofibers*. Journal of the Serbian Chemical Society, 2014. **79**(7): p. 867-880.
415. Dobrovolskaia, M.A., et al., *Interaction of colloidal gold nanoparticles with human blood: effects on particle size and analysis of plasma protein binding profiles*. Nanomedicine: Nanotechnology, Biology and Medicine, 2009. **5**(2): p. 106-117.
416. Lévy, R., et al., *Gold nanoparticles delivery in mammalian live cells: a critical review*. Nano Reviews, 2010. **1**: p. 10.3402/nano.v1i0.4889.
417. Khoobchandani, M., et al., *Cellular uptake and cytotoxic effect of broccoli phytochemical based gold nanoparticles (B-AuNPs): Enhanced cancer therapeutic efficacy*. *une*, 2016. **13**: p. 15.
418. Ankamwar, B., *Size and shape effect on biomedical applications of nanomaterials in Biomedical Engineering - Technical Applications in Medicine*, D.R. Hudak, Editor 2012, InTech:
<http://www.intechopen.com/books/biomedical-engineering-technical-applications-in-medicine/size-and-shape-effect-on-biomedical-applications-of-nanomaterials>.
419. Zhao, F., et al., *Cellular uptake, intracellular trafficking, and cytotoxicity of nanomaterials*. Small, 2011. **7**(10): p. 1322-1337.
420. Manjili, H.K., Ma'mani, L., Tavaddod, S., Mashhadikhan, M., Shafiee, A., Naderi-Manesh, H., *D, L-sulforaphane loaded Fe₃O₄@ gold core shell nanoparticles: a potential sulforaphane delivery system*. PLOS ONE, 2016: p. 20.
421. Rastogi, S., et al., *Prohibitin facilitates cellular senescence by recruiting specific corepressors to inhibit E2F target genes*. Molecular and cellular biology, 2006. **26**(11): p. 4161-4171.
422. Lau, J.S.-Y., et al., *Luminescent cyclometalated iridium (III) polypyridine indole complexes ~~its synthesis, photophysics~~, protein-binding properties, cytotoxicity, and cellular uptake*. Inorganic chemistry, 2008. **48**(2): p. 708-718.
423. Lim, J.P. and P.A. Gleeson, *Macropinocytosis: an endocytic pathway for internalising large gulps*. Immunology and cell biology, 2011. **89**(8): p. 836-843.

424. Franzen, S., *A comparison of peptide and folate receptor targeting of cancer cells: from single agent to nanoparticle*. Expert opinion on drug delivery, 2011. **8**(3): p. 281-298.
425. Chen, X., et al., *High-Resolution 3D Imaging and Quantification of Gold Nanoparticles in a Whole Cell Using Scanning Transmission Ion Microscopy*. Biophysical Journal, 2013. **104**(7): p. 1419-1425.
426. Mustafa, T., Watanabe, F., Monroe, W., Mahmood, M., Xu, Y., Saeed, L., M., Karmakar, A., Casciano, D., Ali, S., Biris, A., S., , *Impact of gold nanoparticle concentration on their cellular uptake by MC3T3-E1 mouse osteoblastic cells as analyzed by transmission electron microscopy J* Nanomedic Nanotechnol, 2011. **2**(6): p. 7.
427. Geiser, M., et al., *Cellular uptake and localization of inhaled gold nanoparticles in lungs of mice with chronic obstructive pulmonary disease*. Particle and fibre toxicology, 2013. **10**(1): p. 1.
428. Oh, N. and J.-H. Park, *Endocytosis and exocytosis of nanoparticles in mammalian cells*. International Journal of Nanomedicine, 2014. **9**(Suppl 1): p. 51-63.
429. Geiser, M., et al., *Ultrafine Particles Cross Cellular Membranes by Nonphagocytic Mechanisms in Lungs and in Cultured Cells*. Environmental Health Perspectives, 2005. **113**(11): p. 1555-1560.
430. Rothen-Rutishauser, B.M., et al., *Interaction of Fine Particles and Nanoparticles with Red Blood Cells Visualized with Advanced Microscopic Techniques*. Environmental Science & Technology, 2006. **40**(14): p. 4353-4359.
431. Bale, S.S., et al., *Nanoparticle-Mediated Cytoplasmic Delivery of Proteins To Target Cellular Machinery*. ACS Nano, 2010. **4**(3): p. 1493-1500.
432. Wang, J., et al., *More Effective Nanomedicines through Particle Design*. Small (Weinheim an Der Bergstrasse, Germany), 2011. **7**(14): p. 1919-1931.
433. Harush-Frenkel, O., Y. Altschuler, and S. Benita, *Nanoparticle-cell interactions: drug delivery implications*. Critical Reviews™ in Therapeutic Drug Carrier Systems, 2008. **25**(6).

434. Harush-Frenkel, O., et al., *Targeting of nanoparticles to the clathrin-mediated endocytic pathway*. Biochemical and Biophysical Research Communications, 2007. **353**(1): p. 26-32.
435. Harush-Frenkel, O., et al., *Surface Charge of Nanoparticles Determines Their Endocytic and Transcytotic Pathway in Polarized MDCK Cells*. Biomacromolecules, 2008. **9**(2): p. 435-443.
436. Yu, B., et al., *Receptor-targeted nanocarriers for therapeutic delivery to cancer*. Molecular membrane biology, 2010. **27**(7): p. 286-298.
437. Dong, X. and R.J. Mumper, *Nanomedicinal strategies to treat multidrug-resistant tumors: current progress*. Nanomedicine, 2010. **5**(4): p. 597-615.
438. Bertrand, N., et al., *Cancer nanotechnology: The impact of passive and active targeting in the era of modern cancer biology*. Advanced Drug Delivery Reviews, 2014. **66**: p. 2-25.
439. Valencia, P.M., et al., *Effects of ligands with different water solubilities on self-assembly and properties of targeted nanoparticles*. Biomaterials, 2011. **32**(26): p. 6226-6233.
440. Le, H.T., et al., *Antibody functionalization with a dual reactive hydrazide/click crosslinker*. Analytical Biochemistry, 2013. **435**(1): p. 68-73.
441. Ayers, B.C., *Conjugation of anti-CD47 antibody to gold nanoparticles via click chemistry for cancer therapy*, in *The Department of Chemistry and Biochemistry*2014, Middlebury College. p. 42.
442. Nghiem, T.H.L., et al., *Synthesis, capping and binding of colloidal gold nanoparticles to proteins*. Advances in Natural Sciences: Nanoscience and Nanotechnology, 2010. **1**(2): p. 025009.
443. Scientific, T.F. *EpCAM / CD326 Antibody (323/A3)*. 2016 [cited 2016 31-03-2016]; <https://www.thermofisher.com/order/genome-database/antibody/EpCAM-CD326-Antibody-clone-323-A3-Monoclonal/MA5-12436>].
444. Winkler, J., et al., *EpCAM-targeted delivery of nanocomplexed siRNA to tumor cells with designed ankyrin repeat proteins*. Molecular Cancer Therapeutics, 2009. **8**(9): p. 2674-2683.

445. Al-Hajj, M., et al., *Prospective identification of tumorigenic breast cancer cells*. Proceedings of the National Academy of Sciences, 2003. **100**(7): p. 3983-3988.
446. O'Brien, C.A., et al., *A human colon cancer cell capable of initiating tumour growth in immunodeficient mice*. Nature, 2007. **445**(7123): p. 106-110.
447. Ricci-Vitiani, L., et al., *Identification and expansion of human colon-cancer-initiating cells*. Nature, 2007. **445**(7123): p. 111-115.
448. Trzpis, M., et al., *Epithelial Cell Adhesion Molecule: More than a Carcinoma Marker and Adhesion Molecule*. The American Journal of Pathology, 2007. **171**(2): p. 386-395.
449. Paolo, C.D., Willuda, J., Kubetzko, S., Lauffer, I., Tschudi, D., Waibel, R., Plu'ckthun, A, Stahel, R.A., Zangemeister-Wittke, U. , *A recombinant immunotoxin derived from a humanized epithelial cell adhesion molecule-specific single-chain antibody fragment has potent and selective antitumor activity* Clinical Cancer Research, 2003. **9**: p. 2837–2848.
450. Hussain, S., et al., *Chemosensitization of carcinoma cells using epithelial cell adhesion molecule-targeted liposomal antisense against bcl-2/bcl-xL*. Molecular cancer therapeutics, 2006. **5**(12): p. 3170-3180.
451. Mitra, M., Kandalam, M., Rangasamy, J., Shankar, B., Maheswari, U.K., Swaminathan, S., Krishnakumar, S., *Novel epithelial cell adhesion molecule antibody conjugated polyethyleneimine-capped gold nanoparticles for enhanced and targeted small interfering RNA delivery to retinoblastoma cells*. Molecular Vision, 2013. **19**: p. 1029-1038.
452. Osta, W.A., et al., *EpCAM is overexpressed in breast cancer and is a potential target for breast cancer gene therapy*. Cancer research, 2004. **64**(16): p. 5818-5824.
453. Di Paolo, C., et al., *A Recombinant Immunotoxin Derived from a Humanized Epithelial Cell Adhesion Molecule-specific Single-Chain Antibody Fragment Has Potent and Selective Antitumor Activity*. Clinical Cancer Research, 2003. **9**(7): p. 2837-2848.
454. Epel, M., et al., *Targeting TARP, a novel breast and prostate tumor-associated antigen, with T-cell receptor-like human recombinant antibodies*. European journal of immunology, 2008. **38**(6): p. 1706-1720.

455. Essand, M., et al., *High expression of a specific T-cell receptor γ transcript in epithelial cells of the prostate*. Proceedings of the National Academy of Sciences of the United States of America, 1999. **96**(16): p. 9287-9292.
456. Wolfgang, C.D., et al., *TARP: A nuclear protein expressed in prostate and breast cancer cells derived from an alternate reading frame of the T cell receptor γ chain locus*. Proceedings of the National Academy of Sciences of the United States of America, 2000. **97**(17): p. 9437-9442.
457. Occhipinti, E., et al., *Investigating the structural biofunctionality of antibodies conjugated to magnetic nanoparticles*. Nanoscale, 2011. **3**(2): p. 387-390.
458. Reiter, G., et al., *In situ FTIR ATR spectroscopic study of the interaction of immobilized human tumor necrosis factor- α with a monoclonal antibody in aqueous environment*. Biochimica et Biophysica Acta (BBA) - Proteins and Proteomics, 2004. **1699**(1–2): p. 253-261.
459. Gallagher, W., *FTIR analysis of protein structure*. Course manual Chem, 2009. **455**.
460. Adnan, N.N.M., et al., *Effect of gold nanoparticle shapes for phototherapy and drug delivery*. Polymer Chemistry, 2016. **7**(16): p. 2888-2903.
461. Khan, A., et al., *Gold nanoparticles: synthesis and applications in drug delivery*. Trop J Pharm Res, 2014. **13**(7): p. 1169-1177.
462. Guhagarkar, S.A., et al., *Polyethylene sebacate–doxorubicin nanoparticles for hepatic targeting*. International Journal of Pharmaceutics, 2010. **401**(1–2): p. 113-122.
463. Syed, A., et al., *Extracellular biosynthesis of monodispersed gold nanoparticles, their characterization, cytotoxicity assay, biodistribution and conjugation with the anticancer drug doxorubicin*. Journal of Nanomedicine & Nanotechnology, 2012.
464. Madhusudhan, A., et al., *Efficient pH dependent drug delivery to target cancer cells by gold nanoparticles capped with carboxymethyl chitosan*. Int J Mol Sci, 2014. **15**(5): p. 8216-34.
465. Trono, J.D., et al., *Size, concentration and incubation time dependence of gold nanoparticle uptake into pancreas cancer cells and its future application to X-Ray Drug Delivery System*. J Radiat Res, 2011. **52**(1): p. 103-9.

466. Thorek, D.L. and A. Tsourkas, *Comparative analysis of nanoparticle-antibody conjugations: carbodiimide versus click chemistry*. *Molecular imaging*, 2009. **8**(4): p. 7290-2009. 00021.
467. Brun, E. and C. Sicard-Roselli, *Could nanoparticle corona characterization help for biological consequence prediction?* *Cancer Nanotechnol*, 2014. **5**(1): p. 7.
468. Monopoli, M.P., et al., *Physical– chemical aspects of protein corona: relevance to in vitro and in vivo biological impacts of nanoparticles*. *Journal of the American Chemical Society*, 2011. **133**(8): p. 2525-2534.
469. Strekalova, E., et al., *Methionine Deprivation Induces a Targetable Vulnerability in Triple-Negative Breast Cancer Cells by Enhancing TRAIL Receptor-2 Expression*. *American Association for Cancer Research*, 2015. **21**(12): p. 2780-2791.

Appendices

The appendices include supplementary data which has been referenced within the body of text in the results/discussion sections of this thesis.

Appendix A.1: FT-IR spectral data for Chapter 3

FT-IR spectroscopy characterisation of pure 16-MHDA and LA exchanged by 16-MHDA functionalised AuNPs (thiol-AuNPs) shows S-H band in free 16-MHDA (Figure A.1.a) whereas the disappearance of this band after exchanging LA by 16-MHDA ligands is shown in Figure A.1.b.

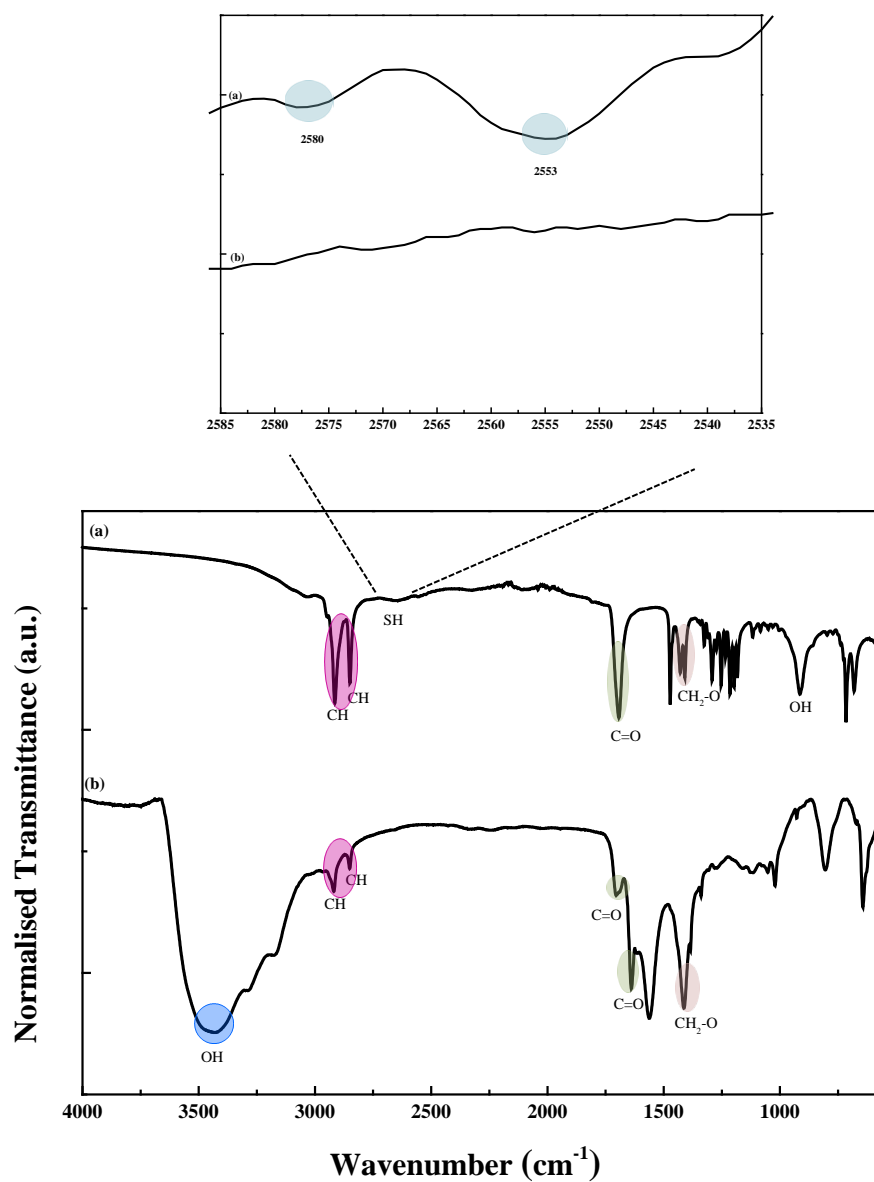


Figure A.1 FT-IR spectra of (a) pristine 16-MHDA and (b) LA exchanged by 16-MHDA functionalised AuNPs (thiol-AuNPs).

Appendix A.2: ^1H NMR spectral data for free PTX, Chapter 3

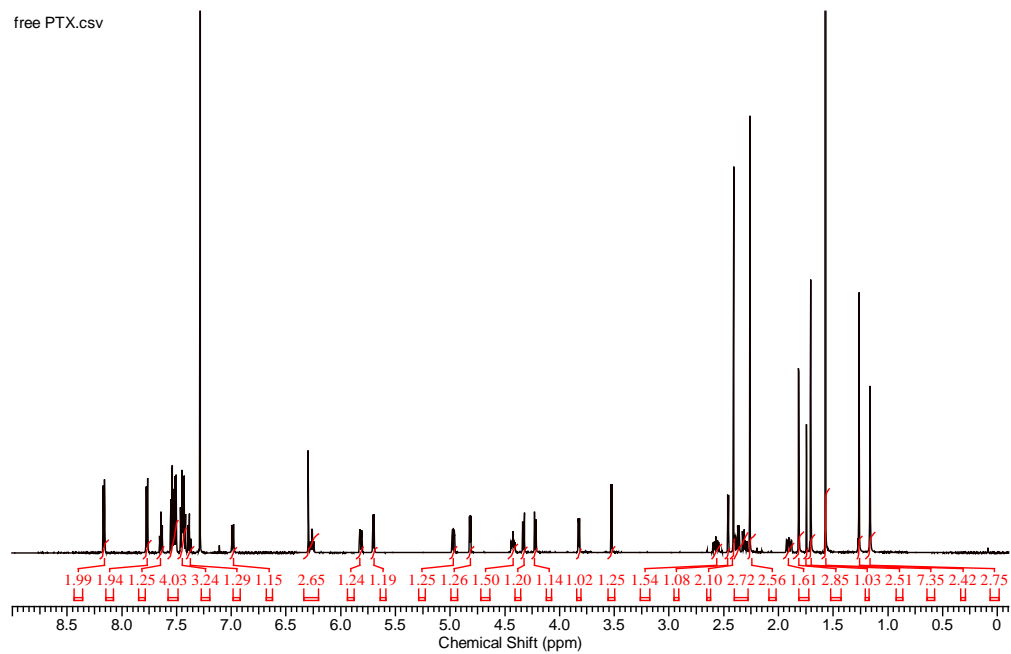


Figure A.2 ^1H NMR spectra of free PTX.

Appendix A.3: UV-Vis spectral data for Chapter 3

Hybrid samples of the chemotherapy drug, paclitaxel, PTX, and the functionalised AuNPs (thiol-AuNPs) were stirred at different mixing times (1 h, 2 h, 6 h, 10 h, 15 h, 20 h and 24 h). Therefore, 7 samples were obtained. Then, the mixtures were centrifuged at 15700 g for 15 minutes and washed with Milli-Q water. The pellets and the supernatants were collected and diluted to conform to UV-Vis measurement limitations. The data acquired were plotted as presented in Figures (A.3.a-g). The background calculations for all samples displayed the concentrations acquired based on Beer-Lambert Law ($A = \epsilon \ell c$, where ϵ of PTX = $29.8 \text{ mM}^{-1} \text{ cm}^{-1}$, $\ell = 1 \text{ cm}$, volume used for diluting the pellets was 15 mL and the molecular weight of PTX is $853.91 \text{ g mol}^{-1}$).

The calculations of concentrations for the pellets and supernatants of the hybrid (PTX-thiol-AuNPs) stirred for an hour

For the pellets of sample 1: The hybrid was stirred for an hour.

$$C = A/\epsilon$$

$$C = 0.078 / 29.8 \text{ mM}^{-1} \text{ cm}^{-1}$$

$$C = 2.6 \times 10^{-3} \text{ mM}$$

Therefore: $m = c \times v \times Mw$:

$$m = 2.6 \times 10^{-3} \text{ mM} \times 0.015 \text{ L} \times 853.91 \text{ g mol}^{-1} = 0.033 \text{ mg.}$$

For the supernatant in sample 1: The hybrid was stirred for an hour.

$$C = A/\epsilon$$

$$C = 0.29 / 29.8 \text{ mM}^{-1} \text{ cm}^{-1}$$

$$C = 9.7 \times 10^{-3} \text{ mM}$$

Therefore: $m = c \times v \times Mw$:

$$m = 9.7 \times 10^{-3} \text{ mM} \times 0.015 \text{ L} \times 853.91 \text{ g mol}^{-1} = 0.124 \text{ mg}$$

Then, the total mass for PTX in both the pellets and supernatant is 0.158 mg.

Other calculations data for the remaining samples can be found in [Table 3.7](#) in [Chapter 3, Section 3.3.6](#).

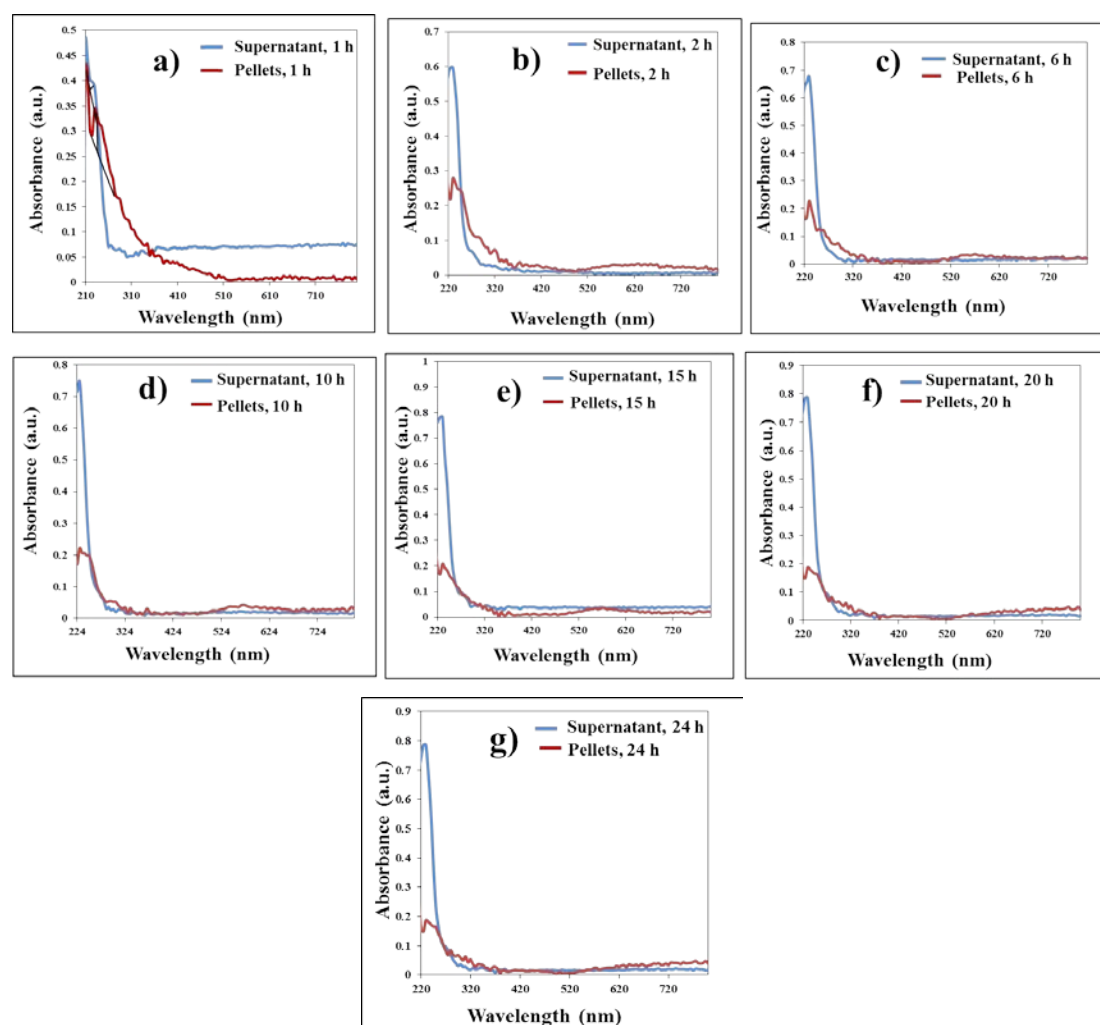


Figure A.3 Absorption spectra of PTX-thiol-AuNPs hybrid stirred for (a) 1 h (b) 2 h (c) 6 h (d) 10 h (e) 15 h (f) 20 h and (g) 24 h.

The calculations of concentrations for the pellets and supernatants of the hybrid (PTX-thiol-AuNPs) stirred for different periods of time (2 h, 6 h, 10 h, 15 h, 20 h and 24 h) are exactly equivalent to the hybrid stirred an hour.

Appendix B: Selective 1D NMR COSY spectra of PTX-16-MHDA-AuNPs reverse conjugate for Chapter 4

A selective 1D NMR Correlation Spectroscopy (COSY) experiment was used to confirm the locations of ester coupling. The (COSY) experiment was carried out by Prof. Martin Johnston at Flinders Centre for NanoScale Science and Technology, School of Chemical and Physical Sciences, Flinders University, Adelaide. As shown in Figure B.1.A, selective excitation (using a shaped pulse) of the C₂' proton resonance at 4.83 ppm in the PTX-thiol-AuNP reverse conjugate reveals only coupling to the proton C₃' signal at 5.83 ppm with no signal at 3.57 ppm demonstrating that the C₂'-OH proton is no longer present. In Figure B.1.B, selective excitation (using a shaped pulse) of the C₇ proton resonance at 4.38 ppm in the PTX-thiol-AuNP direct conjugate reveals only coupling to the proton C₆ signal at 2.60 and 1.90 ppm demonstrating that the C₇-OH proton is no longer present given the absence of any signal at 2.46 ppm.

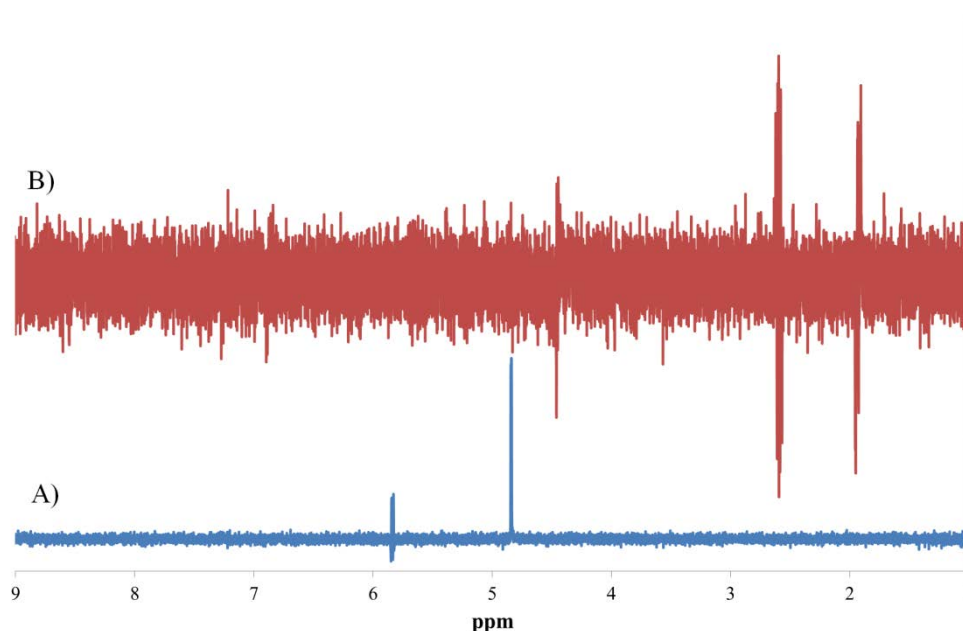


Figure B.1 Selective 1D NMR COSY spectra of (A) the PTX-16-MHDA-AuNPs reverse conjugate tuning the excitation to the C₂' proton resonance at 4.83 ppm and (B) PTX-thiol-AuNPs direct conjugate tuning the excitation to the C₇ proton resonance at 4.45 ppm.

Appendix C: Cytotoxicity assessment data for Chapters 3, 4, 5, 6 and 7

Experiments and results relevant to cell culture and treatment were carried out in the School of Medical Science and Technology, Flinders University, South Australia, by collaborating with Assoc.Prof. Barbara Sanderson, a PhD student, Daniela Figueroa, Master students, Abeer Zaila and Nur Hikmatul Auliya.

C.1 Cell cultures

All experiments were completed aseptically in a laminar flow hood to avoid contamination.

C.1.1 Cell line

Human ductal breast epithelial tumour cell line (T47D) used in all experiments in this thesis, was obtained from the America Type Culture Collection (ATTC). Cells were grown in RPMI media 10 % Foetal bovine serum and passaged every 3 days when cells reached around 80 % of viability. Frozen aliquots of 1×10^6 cells mL^{-1} were stored in liquid nitrogen in Flinders Medical Centre (FMC) until needed.

C.1.2 Thawing cells

Before defrosting cells from liquid nitrogen, 8 mL of RPMI media was transferred into a sterile 10 mL centrifuge and equilibrated to room temperature. Vials of cells were collected placed on ice, then tube submerged several times into the water bath at 37 °C until the cells were almost thawed. Cells were completely thawed by adding RPMI media drop by drop to the cryotube from warm media. The cells were collected into a 10 mL sterile centrifuge tube, which was centrifuged for 5 minutes at 312 x g. After centrifugation, supernatant was removed and the pellets were resuspended gently in 5 mL of media. This was transferred to a 25 cm^2 sterile culture flask incubated at 37 °C with 5 % CO_2 for 2-3 days until the cells reached ~80 % confluence and when they were subculture into a 75 cm^2 flask.

C.1.3 Subculture

Before subculturing T47D cells, 75 cm² flasks were observed under an inverted microscope to assess confluence and morphology. Then media was removed and remaining attached cells were washed twice with 5 mL of 1X phosphate buffered saline (PBS). Cells were detached by adding 1.5 mL of trypsin-ethylene diamine tetra acetic acid (EDTA) to the flask and incubated for 10-15 minutes at 37 °C with 5 % CO₂. Then 4 mL of RPMI was added to the flask to inactivate the trypsin, detached cells were resuspended then transferred to a 10 mL centrifuge tube. Cells were centrifuged for 5 minutes at 612 x g. The supernatant was aspirated. Cells were gently resuspended in 1 mL of media which was adjusted to a final volume of 5 mL. To determine the cell concentration, a trypan blue assay was performed. Seeding concentration was 1x10⁶ cells per 20 mL for a 75 cm² flask.

C.1.4 Freezing cells

Cells were stored in liquid nitrogen. To do so, cells were trypsinised to harvest. After centrifugation, the pellet was kept on ice for 10 minutes while the media was aspirated and replaced with 4.5 mL of cold freezing media. Resuspended cells (at ~2x10⁶ cells mL⁻¹) were aliquoted in 1 mL fractions added to cryovials and kept on ice for 10 minutes, then transferred to -20 °C for 1 h, followed by -80 °C for 24 h and ultimately stored in liquid nitrogen.

C.1.5 MTT assay

C.1.5.1 MTT Standard curve for T47D cell line

A standard curve was used for each experiment performed. Serial dilutions of the cells were performed using RPMI media starting from 40,000 cells well⁻¹ and ending with 625 cells well⁻¹. Halving dilutions were performed in the 96-well flat bottom plate in replicates of four. Plates were incubated for 20-22 h in a humidified 37 °C with 5 % CO₂ incubator. Media was then aspirated and 200 µL of a 0.5 mg mL⁻¹ of MTT solution in RPMI was added. The plates were incubated for further 4 h in the incubator and then 80 µL of 20 % sodium dodecyl sulfate solution (SDS) in 0.02 mM of HCl, was added. Plates were incubated in the dark overnight at room temperature

and then the absorbance (O.D.) was read using a spectrophotometer at 570 nm, with a reference wavelength of 630 nm.

C.1.5.2 MTT interference assay

To determine if there was any interaction between the gold nanoparticles and the components of the MTT assay, an interference assay was performed. Three standard curve plates (1, 2 and 3) were seeded as described in [Section C1.5.1](#) in [Appendix C](#) and 0.02 nM AuNPs were used for treating plates 2 and 3. Plate 1 was a control MTT standard curve set up unaltered except that after the attachment period of the cells, 190 μL of 0.5 mg mL^{-1} MTT and 10 μL of 0.1 X PBS was added. Plate 2 was used to test the interaction between AuNPs and the MTT solution, by adding 190 μL of 0.5 mg mL^{-1} MTT and 10 μL of a 0.02 nM AuNPs solution. Plate 3 evaluated the interaction between AuNPs and SDS solubilising solution. After addition of the MTT, the three plates were incubated for 4 h in a humidified 37 °C with 5 % CO_2 incubator. Then, 80 μL of SDS was added to the plates 1 and 2 and to plate 3 a mix of 70 μL of SDS and 10 μL of a 0.02 nM AuNPs solution was added per well. All plates were incubated in the dark overnight and read on the spectrophotometer with a wavelength of 570 nm and a reference wavelength of 630 nm.

C.1.5.3 Cytotoxicity assay: T47D cell line treated with AuNPs or PTX

Treatment was in 96-well flat bottom plates, using a dose-response curve to treat the cells in four replicate wells (see [Table C.1](#)). Dilutions of the particles and PTX were made in RPMI after 1 minute sonication of the AuNPs stock solutions. A MTT standard curve was set. Treatment plates were seeded with 100 μL of a cell suspension at 10,000 cells well^{-1} and incubated for 24 h at 37 °C with 5 % CO_2 to allow adherence. Then, the media was removed and 200 $\mu\text{L well}^{-1}$ of each treatment added and was incubated for further 24 h in a humidified 37 °C with 5 % CO_2 incubator. Excess of AuNPs and PTX were then removed and cells were washed with 1X PBS. Subsequently, 200 μL of 0.5 mg mL^{-1} MTT solution was added to the plates, which were incubated for 4 h at 37 °C with 5 % CO_2 . Then, 80 μL of 10 % SDS/0.1 M HCl was added to each well and plates were incubated overnight in the dark at room temperature. O.D was at 570 nm with a reference wavelength of 630

nm. The Stock solution of the AuNPs and an aliquot of PTX (5 mg mL⁻¹) was stored at 4 °C and retested later.

Table C.1 Treatment agents and concentrations used for cytotoxicity assay.

Treatment agent	Doses tested week (0)	Doses tested after storage
Thiol-AuNPs	0.008 nM 0.015 nM 0.030 nM 0.060 nM 0.125 nM	0.008 nM 0.015 nM 0.030 nM 0.060 nM 0.125 nM
PTX-thiol-AuNPs hybrid, PTX-thiol-AuNPs direct conjugate or PTX-16-MHDA-AuNPs reverse conjugate	0.0068 nM 0.014 nM 0.027 nM 0.054 nM 0.109 nM	0.0068 nM 0.014 nM 0.027 nM 0.054 nM 0.109 nM
Free PTX	0.005 µg mL ⁻¹ 0.05 µg mL ⁻¹ 0.5 µg mL ⁻¹ 5 µg mL ⁻¹ 50 µg mL ⁻¹	0.005 µg mL ⁻¹ 0.05 µg mL ⁻¹ 0.5 µg mL ⁻¹ 5 µg mL ⁻¹ 50 µg mL ⁻¹

C.1.5.4 Cytotoxicity assay for T47D cells treated with PTX-thiol-AuNPs direct conjugate and PTX-16-MHDA-AuNPs reverse conjugate at different pHs

Experiments on cytotoxicity assay in different pHs (7.4 & 6.5) and different concentrations relevant to cell culture and treatment were carried out. The treatments of plates at different pH ranges were also performed in same way as described in [Section C.1.5.3](#) in [Appendix C](#) (see [Table C.2](#)). pH of RPMI media which supplemented with 10 % of FBS was modified using acetic acid. A pH response standard curve was also made with the range pH between 3 and 7.4 using the MTT assay.

Table C.2 Treatment agents and concentrations used for cytotoxicity assay at different pHs (7.4 & 6.5).

Inhibitor	Concentration of PTX (nM)
PTX-thiol-AuNPs direct conjugate	1.5 7.6 15.2 30.4 76 152 303.5
PTX-16-MHDA-AuNPs reverse conjugate	10.97 54.85 109.7 219.4 548.5 1097 2194

C.1.5.5 Cytotoxicity assay for T47D cells treated with free RB

Experiments on cytotoxicity assay relevant to cell culture and treatment with free RB at different concentrations were carried in same way as described in Section C.1.5.3 in Appendix C (see Table C.3).

C.1.5.6 Crystal violet interference assay for cells treated with fluorescently labelled AuNPs

Crystal violet assay was carried out for cells treated with fluorescently labelled AuNPs conjugates. The experiments were performed in 2 × 96-well flat-bottom plates, one as standard curve and the other as treatment plate. Serial dilutions of cells were prepared in 100 µL volume and cells were seeded from 20,000 cells well⁻¹ to 312.5 cells well⁻¹. Plates were incubated in a humidified 37 °C, 5 % CO₂ incubator for 20-22 h. The following day, medium was removed and 50 µL well⁻¹ of crystal violet stain was placed in standard curve plate and incubated for 10 minutes at RT, prior to washing with Milli-Q water. Plates were then left to dry at RT overnight. For treatment plates, cells were treated with 50 µL crystal violet mixed with 30 µL of four concentrations of (DAPI, pyNH₂ and FB28) (see Table C.3). The next day, 50 µL acetic acid was added to each well and the plates were incubated at RT for 10 minutes before reading with a spectrophotometer [469].

Table C.3 Concentrations of fluorescent agents conjugated gold nanoparticles in addition to free RB used for cytotoxicity assay.

Fluorescent agent	Concentration (nM)
AuNPs-thiol-DAPI direct conjugate	41850 nM 4185 nM 418.5 nM 41.85 nM
AuNPs-thiol-pyNH ₂ direct conjugate	7300 nM 730 nM 73 nM 7.3 nM
AuNPs-thiol-FB28 direct conjugate	15300 nM 1530 nM 153 nM 15.3 nM
AuNPs-16-MHDA-DAPI reverse conjugate	39600 nM 396 nM 3.96 nM 0.0396 nM
Free RB	1000,00 nM 10,00 nM 1,000 nM 100 nM

C.1.5.7 Preparation of live cells for CLSM imaging

After determination of optimised cell concentration for the 6-well plate as 0.3×10^5 cells/well/2mL, this concentration was seeded and incubated for 20-22 h in a humidified 37 °C with 5 % CO₂ incubator. Then, plates were treated with 30 µL of fluorescently labelled AuNPs in the presence or in the absence of the anticancer agent, PTX. For cells treated with RB alone or the PTX-RB conjugate, 15 µL of RB was mixed with 3 mL of fresh media, then 2 mL of this mixture was treated cells for 1 h, 6 h and 24 h. Cell treated coverslips were washed twice with media then cells were harvested and placed carefully in a POC chamber. 150 µL of fresh media was added to the chamber after sealing and observed under fluorescence microscopy.

C.1.5.8 Statistical analysis

Statistical analysis was carried out using one-way ANOVA and all experiments were performed in triplicate and repeated at least three times.

C.1.5.9 Cytotoxicity assay for T47D cells treated with antibodies containing conjugates

Experiments on cytotoxicity assay relevant to cell culture and treatment with antibodies containing conjugates at different concentrations (see [Table C.4](#)) were carried in same way as described in [Section C.1.5.3](#) in [Appendix C](#).

Table C.4 Antibodies containing nanoparticles and the concentrations used for cytotoxicity assay.

Inhibitor	Concentration of PTX (nM)
AuNPs-thiol-Ab direct conjugate (Ab= EpCAM or TARP)	0.0068 0.013 0.027 0.054 0.1085
PTX-thiol-AuNPs-thiol-Ab direct conjugate (Ab= EpCAM or TARP)	0.0068 0.013 0.027 0.054 0.1085

C.2 Results

C.2.1 MTT standard curve assay results

Results of the MTT standard curve showed a linear correlation between the optical density (OD) readings and the cell number per well (R^2 between 0.92- 0.98). Values of OD were consistent in each experiment, with readings ~ 0.1 for media without cells and approximately 0.5 for 20,000 cells well⁻¹. The coefficient of variation for each set of 4 technical replicate wells was also consistent in the range of 2-10 %. An example of a standard curve is shown in [Figure C.1](#).

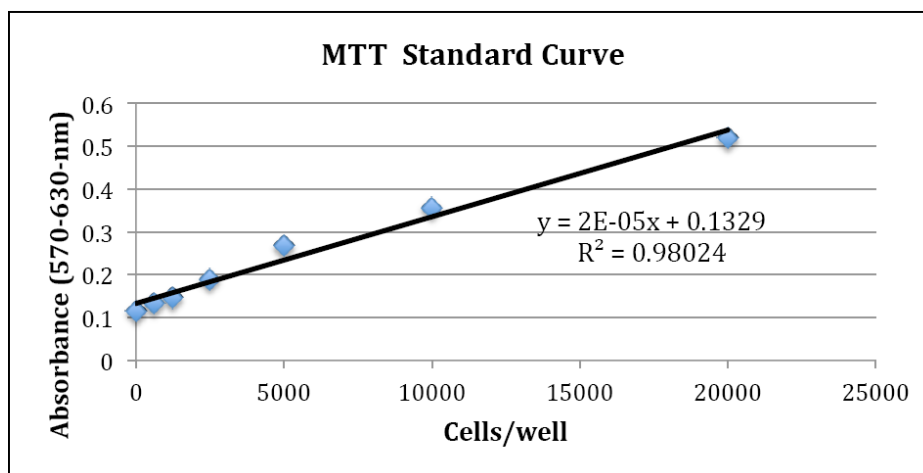


Figure C.1 MTT standard curve. X-axis shows the number of cells per well and Y-axis shows the absorbance values. The equation of the line and the value of R^2 are represented in the figure.

C.2.2 MTT interference assay

To assess whether the AuNPs interfered with the MTT assay, three different standard curve plates were prepared as described in Section C.1.5.2 in Appendix C. Plate 1 was set up as a normal standard curve (untreated control), plate 2 was used for assessing the interaction between AuNPs and the MTT dye and plate 3 was set up to evaluate the interaction between AuNPs and SDS solubilising solution. As shown in Figure C.2, no significant difference was observed between any curves, indicating that AuNPs have no significant effect over the parameters of the MTT assay.

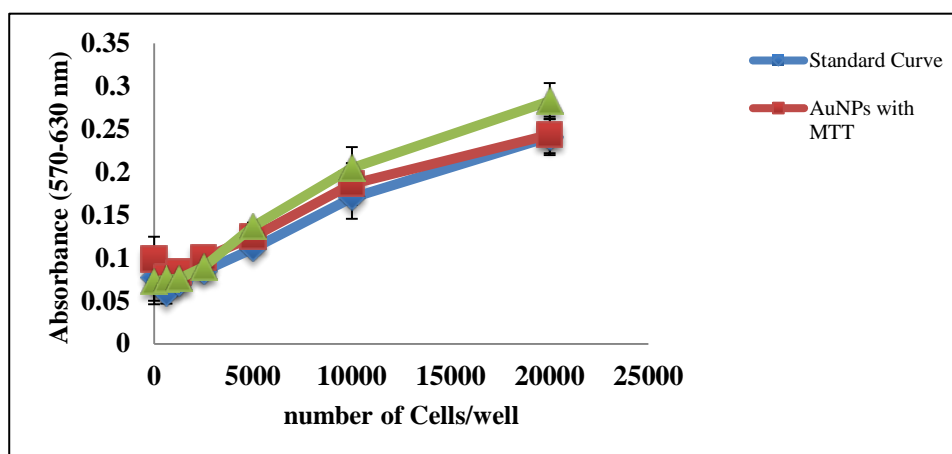


Figure C.2 MTT nanoparticles interference assay. AuNPs (0.02 nM) added with different components of the MTT standard curve assay. Blue line = the normal standard curve; red line = AuNPs added with MTT dye; green line = AuNPs added with SDS. Data shown as the mean \pm S.E.M; n=3; * = $p \leq 0.05$.

C.2.3 Crystal violet assay standard curve

Results of the crystal violet standard curve showed a linear correlation between the optical density (OD) readings and the cell number per well ($R^2 = 0.9898$). T47D was used at the concentration of 2×10^5 cell well⁻¹ in four replicates. Values of OD were consistent in each experiment. An example of a standard curve is shown in [Figure C.3](#).

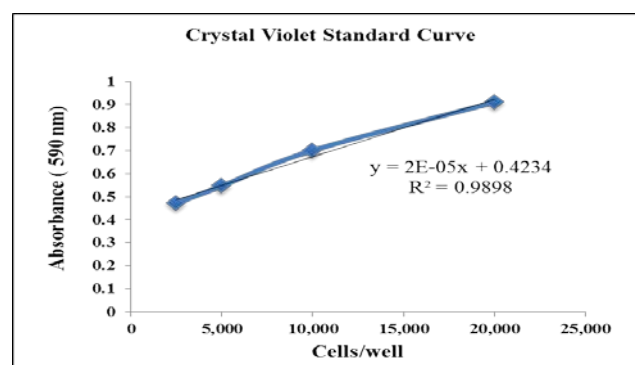


Figure C.3 Crystal violet assay standard curve.

C.2.3.1 Crystal violet interference assay with fluorescent agents

The crystal violet interference assay was prepared using five standard curve plates for each fluorescent dye. The first plate was a normal control standard curve. Plates two, three, four and five contained the crystal violet stain and different concentrations of fluorescent agents (DAPI, pyNH₂ or FB28). As shown in Figures C.4, C.5 and C.6, there was no or slight interference with colorimetric development in the crystal violet assay with the fluorescent agents, which shows nearly the same OD values. Therefore, this assay was used for further investigations with the fluorescent agents.

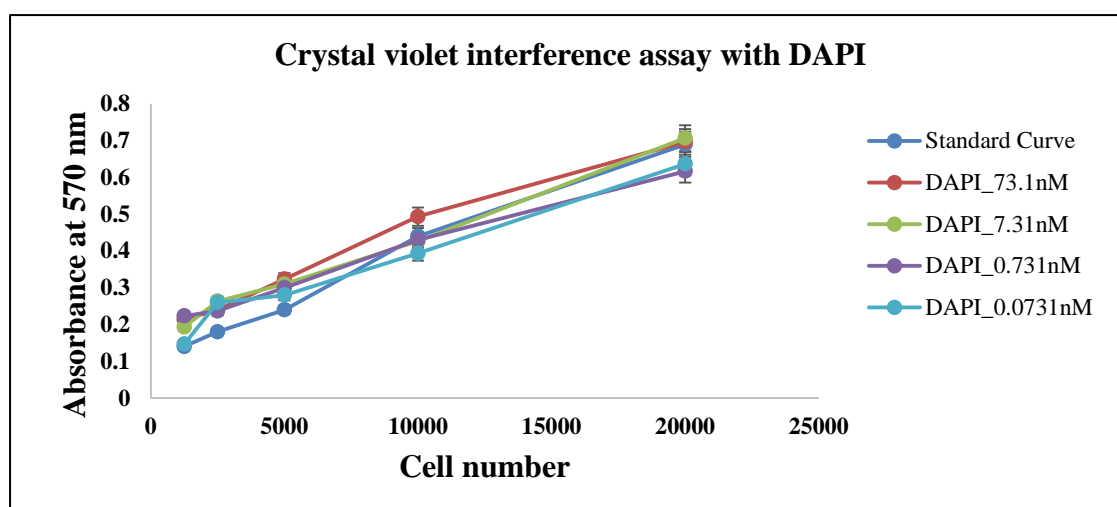


Figure C.4 Crystal violet interference assay with DAPI.

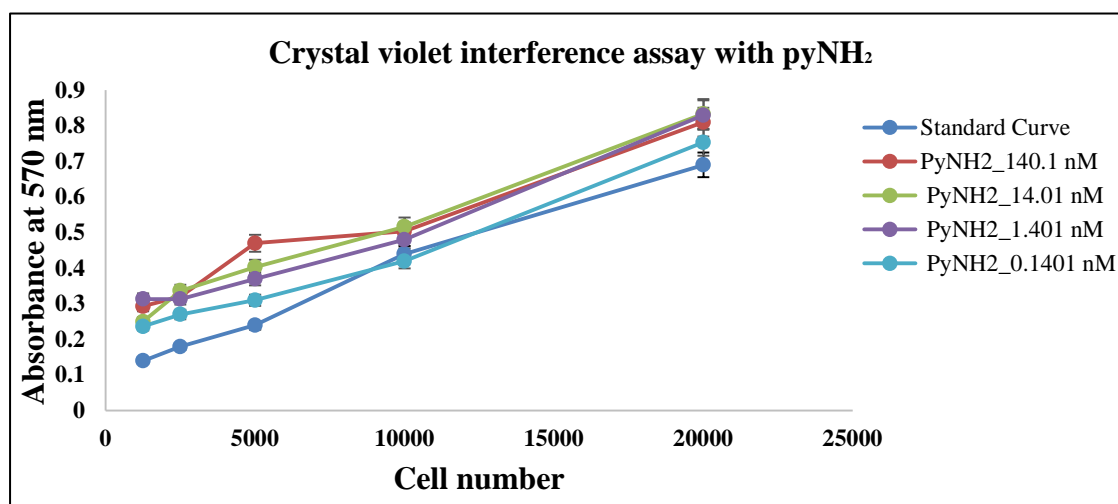


Figure C.5 Crystal violet interference assay with pyNH₂.

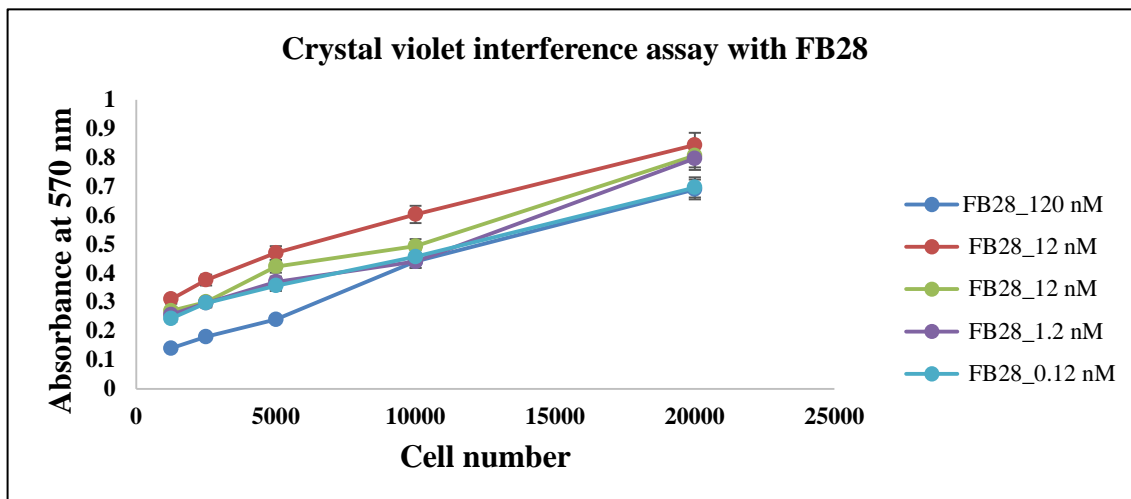


Figure C.6 Crystal violet interference assay with FB28.

The results were tested for significance by One-way ANOVA and statistical significance showing *, $P < 0.05$.

C.2.3.2 MTT interference assay with rhodamine B

In order to identify the interaction between RB and MTT assay, the MTT interference assay was performed using various concentrations of RB in triplicate. The tested concentrations of RB were 45.928, 0.45928, 0.0045928 and 0.000045928 nM mixed with MTT and SDS to determine interaction and relevant stage. Plate 1 was prepared as a normal standard curve (control); plate 2 was set up to evaluate the interaction between RB and MTT dye and plate 3 was set up to assess the interaction between RB and SDS. [Figure C.7](#) shows that line curves almost align with each other. This suggests no interactions between RB and MTT or between RB and SDS. Thus, the MTT assay is the suitable assay to detect cell cytotoxicity of RB agent.

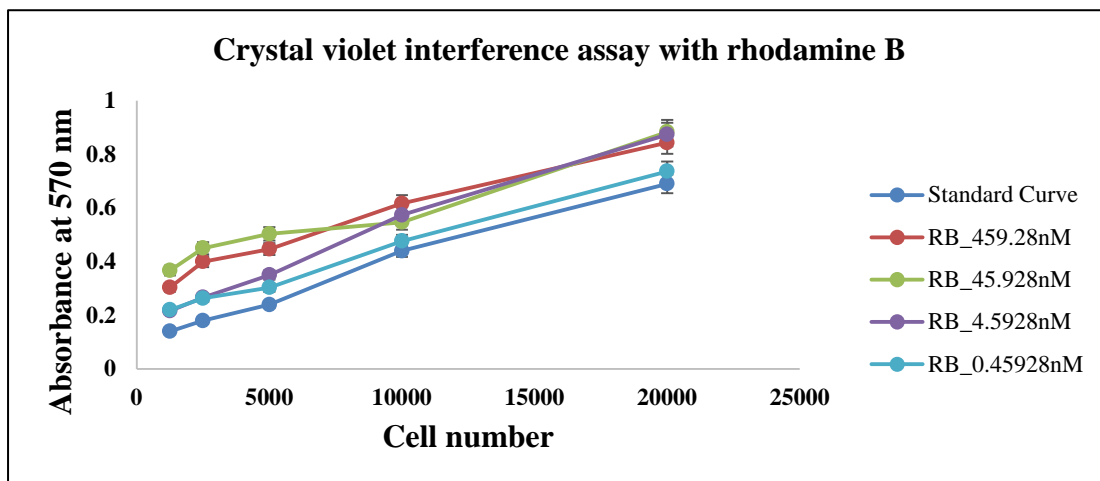


Figure C.7 MTT interference assay with rhodamine B.